OBSERVATIONAL AND THEORETICAL STUDIES OF MESOSPHERIC DYNAMICS AND BORES USING AIRGLOW IMAGERS AT MID-LATITUDES

A Dissertation

Presented to the Faculty of the Graduate School

of Cornell University

in Partial Fulfillment of the Requirements for the Degree of

Doctor of Philosophy

by

Pamela Jane Loughmiller

August 2008

OBSERVATIONAL AND THEORETICAL STUDIES OF MESOSPHERIC DYNAMICS AND BORES USING AIRGLOW IMAGERS AT MID-LATITUDES

Pamela Jane Loughmiller, Ph.D.

Cornell University 2008

This dissertation focuses on the study of coupling-dynamics in the mesosphere. Interesting airglow phenomena - primarily internal bores occurring mid-latitude at mesospheric altitudes – have been observed and studied in a multifaceted approach, combining the analysis of experimental data with modelling and theory.

After the initial mesospheric bore sighting by the scientific community in 1993, the next recorded events were observed by Cornell University. To gain additional insight, this investigation effectively pursued more data by installing imaging equipment as part of a collaborative, multi-instrument campaign involving lidar. While coincident lidar data eluded us, we did expand our database allowing us to develop the first classification system to categorize mesospheric bore observations. We also verify for the first time that a mesospheric inversion layer would support bore formation as proposed.

Some of the bore data exhibits features unexpected and new. Most intriguing is that the brightness relationship between airglow layers is reversed and accompanied by a lateral shift! This was the first such ”inverse” event reported in the scientific community, and its seemingly contradictory nature fails to support the existing basic theory. Working with researchers at the Air Force Research Laboratory, we propose a new theory extending the original numerical model. We also compare the data to another non-linear theory and find both

that: (1) neither theory explains all the observable features, and (2) each theory succeeds in explaining some characteristics not addressed by the competing theory. This theory development suggests that mesospheric bores likely are nonlinear structures propagating within upper atmospheric waveguides such as thermal-inversion layers or wind-shear ducts.

Well into this thesis, we realized the critical and complicated role calibration plays in ensuring the condition of our data. Calibration reduces the discrepancies between the raw error-prone data and a true portrayal of the phenomena, facilitating the generation of congruent, accurate data for analysis. To address some of the calibration challenges and to alleviate some of the confusion for future graduate students, a portion of this dissertation is devoted to providing the first, comprehensive presentation of calibration – detailing topics, techniques, methodologies, and results, as they pertain to airglow imagers.

BIOGRAPHICAL SKETCH

Explore – "My life is like a stroll on the beach... as near to the edge as I can go." - Thoreau

A true native Texan, Pamela was born in Austin, but grew up in Houston. From her early years on, Pamela's sense of adventure was instilled via annual family vacations camping throughout all forty-nine contiguous United States, AK, and the provinces of Canada. When not on one of these family excursions, Pamela's early play often involved piloting Barbie – with the Hot Wheels land cruiser in tow – off to some exotic land for safari, or rocketing with a stuffed elephant to outer space. In the real world, she kept busy outside of school taking baton and dance lessons, organizing neighborhood kids' clubs to build things, involving herself in church activities (choir, softball, service groups), playing clarinet and twirling in the band, competing in academic contests, and very actively participating in the Girl Scouts of America. As a Senior Girl Scout, she earned the GS First Class Award. Pamela graduated Summa Cum Laude from Bellaire Senior High School as one of only five inaugural International Baccalaureate Diploma recipients.

After much deliberation, Pamela turned down "elite" universities to continue the Longhorn tradition at The University of Texas at Austin. Completing her bachelors degree in three years in mathematics with a minor in computer science, and having taken electives in engineering, she returned to Houston expecting to continue her education uninterrupted to a doctorate degree. Instead, she accepted a full-time engineering job in the semiconductor industry which afforded her many treasured, global experiences: making life-long friends, negotiating commitments from diverse cultures, and seeing sites around the world. It also allowed her the means to pursue many interests on the side. During her

years at TI, she: went skydiving; worked towards her private pilot's license; bicycled cross-state for charity; participated in educational outreach programs (e.g., Expanding Your Horizons) to inspire young women in STEM curricula; organized a Society of Women Engineers National Conference; trekked in Nepal; rappelled near the Grand Canyon; learned to sail; continued canoeing; played tennis; saw many of the wonders of the world; worked on a masters degree in electrical engineering at Rice University; attended NASA JSC's first industry-partnership open house; and volunteered as an elephant keeper at the Houston Zoological Gardens. Pamela's participation in these activities profoundly impacted her life by introducing her to pivotal mentors and influences, including NASA officials, retired military commanders, the planet's premiere elephant researchers and the International Elephant Foundation's Elephant Research Symposium (a forum for global exchange of in-situ and ex-situ elephant research). As a result of meeting the elephant researchers, she funded her first independent trip to Africa upon the invitation of one scientist to support his elephant research and conservation efforts. While the worldwide travel courtesy of TI was intoxicating, Pam did not abandon her dream to pursue a doctorate full-time. To this end, she transitioned to a research position, working on a NASA-funded telemedicine image-processing project at The University of Texas M. D. Anderson Cancer Center Levit Radiologic-Pathologic Institute.

Driven by her passions in space and elephant bioacoustics/conservation, influenced by her introduction to upper atmospheric research from NASA, and encouraged by her mentors, Pamela sought to pursue her Ph.D. at Cornell University... much to the chagrin of her southern family. Her venture north was colored by more than just intellectual stimulation and an introduction to fall leaves and seasons. In addition to the vast opportunities offered by her work in the

Space Plasma Physics research group, Pamela also involved herself in a variety of classes and projects with the National Science Foundation, the College of Engineering Teaching Fellows, the Cornell Graduate School's Center for Learning and Teaching, the Bioacoustics Laboratory, the Space Sciences and Astronomy Department including the MER project, the Natural Resources Department, the Earth and Atmospheric Science's Oceanography group, the Paleontological Research Institute with the Museum of the Earth, and the Discovery Channel. To round out her truly rewarding time in "gorges" Ithaca, Pamela enjoyed many extracurricular activities including hiking, rock climbing, Tae Kwon Do, yoga and a variety of dance classes.

Her next stop on life's journey is a return south for a National Science Foundation CEDAR Postdoctoral Research Fellowship at Embry-Riddle Aeronautical University in Daytona Beach, FL. Life's a beach... go there!!!

To Momma,

my sister Lauri,

my family... both in Heaven on Earth and above.

ACKNOWLEDGEMENTS

We don't accomplish anything in this world alone... and whatever happens is the result of the whole tapestry of one's life and all the weavings of individual threads from one to another that creates something." - Sandra Day O'Connor

Earning a Ph.D. has always held a prominent place on my personal "bucket" list, but upon completion of my bachelors degree, the mission took a detour as life intervened. During this interim, the vision became clearly focused with the opportunities at Cornell University resolutely in the target. While I never intended to fill such a lengthy chapter of my life on this quest north of the Mason-Dixon line, or to fall so completely for this idyllic academic and cultural utopia centrally isolated in gorgeous Upstate NY, that is the way it played out. As such, there are innumerable people to thank for making this unbelievable dream become a reality. As it takes a village to rear a child, so it does to shepherd a post-baccalaureate through graduate school and the accompanying experiences. I'd like to express my sincere gratitude to the entire village!

First and foremost, I'd like to thank my committee – each of whom I am greatly indebted to – for their vision, inspiration, enthusiasm, guidance, insight, feedback, confidence in me, acceptance, latitude, compassion, and patience. Without these gentlemen – Michael C. Kelley, Charles E. Seyler, and Peter J. Gierasch – none of this would have been possible!! Special thanks to Mike, my graduate advisor, for believing in the interdisciplinary dream and going for it; it was always a win-win choice, and I think the result was the winningest outcome. I especially want to thank you and Pat for welcoming me and being like family. Thanks to Charlie for spying me among the masses, and everything after... including the many in depth bore (not "boring") discussions. Thanks,

Peter, for bringing your invaluable comparative-planetary-aeronomy perspective to the mix providing fodder for many interesting discussions, as well as for your thoughtful opinions. You all know how much I loved my experience at Cornell University, and this had everything to do with my interactions with each of you!

In the same breath, I owe a great deal of thanks to Edmond Dewan of AFRL who became practically an adjunct member of my committee, as well as a dear mentor and friend. Edmond exemplified scientific passion for me with many a fiery phone conversation or the occasional animated discussion over a tropical sunset and a frothy drink, punctuated by an equally frothy debate. I appreciate your support and confidence in me more than words can say.

I want to thank everyone in SPP and ECE for providing such a stimulating and welcoming atmosphere. Special thanks to Don Farley, Wes Schwartz, David Hammer, David Hysell, Cliff Pollack, John Belina, Steven Powell, and Bernie Hutchins. I have enjoyed many fascinating conversations on a wide variety of topics with each of you. Special thanks, in particular, to Don for his thoughtful and detailed review of several chapters in this dissertation, and for directing me towards my intended audience.

Whenever a group appears to function seamlessly, you know there is someone behind the scenes tirelessly supporting everyone's efforts. For our SPP research group, that person is Laurie Shelton. With her vigilance and diligence, neither lack of supplies nor faulty equipment ever sabotaged a scramble to complete a presentation! And, often as not, she was there with you late at night to offer support, or work side-by-side as we did making our way through the chapters on that first round of Mike's book. I thank Laurie for her help both in navigating and shepherding paperwork through the system at Cornell. I also thank

her for sharing her green thumb with our corner of Rhodes Hall to brighten the long winter season, for including us in her bell choir concerts, and for being a friend always willing to lend an ear. Lastly, I both thank and blame her for introducing me to Edy's Swiss Orange sherbet!

My other administrative and support heros include: Scott Coldren, Anne Haessner, Barb Edinger, Linda Frady, Pattie Place, Jamie DalCero, Lisa Gould, Sally Bird, and the ECE IT marvels Bob Beaver, Paul Shuh, and Jason Seymour. In addition to their routine help, each one of these folks came through for me in a pinch at one time or another. Not a one let me down or failed me in a minor crisis, even those inadvertently orchestrated by me. These people were my buffer to any bureaucracy that existed at Cornell. I'm eternally grateful that they all like and excel at their jobs; and I count them amongst my friends.

I owe special thanks to many folks at the Maui Space Surveillance Complex for their help in maintaining our airglow imager equipment through the years. Particularly vital to this effort were Russ Taft, Spence Ah You, and Ken Dutton; thank you gentlemen!

During the course of the research for this dissertation, two "formidable" periods of frustration were encountered. One was an elongated period of duelling mentors. While this stymied progress, it also stimulated thought-provoking and lively discussions which led to advances in this dissertation. Additionally, it expanded my negotiating skills to the scientific arena, teaching me to find common ground between passionate experts with contrary visions. The second detour was a seemingly routine task – calibration – that took on a life of its own. A whole host of people lent their talents and resources to help me through the process and to each of them I am indebted.

SRI was generous enough to let us borrow their PCLS – twice. I thank

Mary McCready, Rick Doe, John Kelly, Craig Heinselman, Eggert Gudmundsson, Nathan Eldridge, Henrik Sandin, and Claus Johannsen at SRI for all their assistance and support: loaning the PCLS, hosting me in Greenland, and fielding questions. I thank Rick, in particular, for all the time he devoted to our discussions and data review. Special thanks to Eggert for performing a post-mission sanity check on the PCLS! And thanks Nathan for the hike! It was a highlight!

In Maui, Rick Harris was indispensable in helping me trouble-shoot equipment. Some of the most fun I've had in the field was differentiating between tricks-of-the-mind and equipment malfunctions with Rick. Jake Barros was a godsend in Maui in all manner of ways. I also thank Paul Bernhardt, along with Mike Martin, for working with me to cut through both the sacred-ground and cross-branch-military red tape to facilitate a calibration source comparative study. Timing, unfortunately, thwarted our efforts to see this to fruition that trip. Next time, Paul! Another Paul – Paul Sydney – also helped me immensely, generously offering his input, guidance, and friendship. I enjoyed working with both him and Rainer Dressler on the MAUI (Maui Analysis of Upper Atmospheric Injections) space shuttle engine-burn project sponsored by the AFRL and DoD Space Test Program (STP). I also thank both of them for reviewing chapters of this dissertation. At one point in Maui, site personnel and procedural changes abruptly impacted my visit. While this was by no means the only time these friends and colleagues came through for me, I owe a debt of gratitude to John Africano, Paul Kervin, Kelly Hammett, and Ron Lambert for their hand up during these unexpected obstacles. Another silver lining during the calibration ordeal was the aloha spirit of "my Hawaiian family", the Bettendorfs – Jeff, Leslie, Katie, and Elisa. Thanks for the use of your basement o'hana, and

for including me in your circle of friends. Mahalo to the girls for the sidewalk messages which brightened some frustrating days of data collection.

Additionally, I owe very special thanks to four more folks who contributed extensively to the calibration process. I thank my former officemate Jon Makela for sharing his experience and write-up with me from when he calibrated our other imager at NRL. As always, our discussions enlightened and entertained us both. Thanks to Susan Nossal for her feedback, and for helping to champion the calibration cause. I thank Raju (D. Pallamraju) for providing both clarity on error analysis and tons of encouragement, and for becoming a friend in the process. Lastly, I thank Jeff Baumgardner – a calibration guru in our science community! This is one of those cases where there just are not enough words to thank him for his generous mentoring and tutoring – in calibration, as well as in filter and imager design. He answered my barrage of questions unwearingly and with a smile. I enjoyed our many lengthy discussions, and I appreciate immensely his thorough review and detailed feedback of the related chapters. Jeff really served as my surrogate optical lab guy, and I thank him for filling this gap for me!

Until my introduction to CEDAR, I had never met a community which so fully and genuinely supports each other, particularly its students. I thank and treasure the community for this investment in the future, and in individuals. One of my most gratifying and valuable graduate-school experiences was serving on the CSSC. The committee allowed me to run with my ideas, fully supporting my endeavors and never failing to volunteer for and to assist with any functions I organized. I'm especially grateful that they valued my contributions and sought to extend my tenure with them to an unprecedented second year, and in so doing expanded the role for future student participation. I thank each

of my fellow committee members: Roger Smith, Graham Bailey, Leroy Cogger, John Foster, Sixto Gonzales, Tim Kane, John Kelly, Delores Knipp, Erhan Kudeki, Art Richmond, Jan Sojka, Jeng-Hwa (Sam) Yee, Lars Dyrud, Philip Erickson, Marina Galand, Larry Paxton, Joshua Semeter, Robert Vincent, Sunanda Basu, Rich Behnke, Bob Robinson, and Paul Bellaire. Special thanks to Barb Emery for her exceptional support during my time on the committee and beyond!

I also thank the others in the community who obliged every request I made, generously giving of their time and knowledge to support the CEDAR and AGU student programs I organized: Marie Boyko, Alan Burns, Jim Clemmons, Greg Earle, Maura Hagan, Don Hampton, Matt Heavner, Tim Killeen, Frank Lind, Suzanne Moon, Susan Nossal, and Stan Solomon.

One special opportunity provided by the CEDAR community was the chance to visit the Arecibo Observatory. I cherish this experience, and thank Sixto Gonzales for championing and sponsoring me.

Special thanks is owed to my NSF representatives for many of these opportunities through the years, as well as for their individual support, guidance, and encouragement offered to me. I feel fortunate to count them – Rich Behnke, Bob Robinson, Sunanda Basu, Bob Kerr, Paul Bellaire, and Cassandra Fessen – as my friends and colleagues, and thank them for my post-doc funding. The work for this graduate research at Cornell University was supported by the National Science Foundation under grant ATM-0000196 and by the Air Force Office of Scientific Research under grant F49620-01-1-0064.

Throughout the years, there has been a core few who have served as informal mentors, offering me friendship, feedback, and advice. I value their input and appreciate the many discussions we have shared. While many have

already been mentioned above, this list also includes: Mike Taylor, Gary Swenson, Bob Eather, Jack Drummond, Dick Picard, Jeremy Winick, Larry Paxton, Frank Hughes, and John Otten.

Thanks to the folks in Space Sciences at Cornell for your friendship and enlightenment. Special thanks to Steve Squyres for allowing me the rare and wonderful opportunity of sitting in on the Mars rover planning meetings, and for the many space-related talks and NASA insights. Thanks to Jim Bell and Jason Soderblom for your advice on image contrast analysis. I am grateful to Yervant Terzian for promoting critical thinking with Carl Sagan, and for his thoughtful conversation during the difficult 911 period.

Many thanks to the wonderful folks associated with both the College of Engineering TA Fellow program, as well as the University-Wide TA Development Workshop administered through the Graduate School's Center for Learning and Teaching. I thoroughly enjoyed my years developing curriculum for and working as an instructor in these programs. Particular thanks goes to Virleen Carlson, Pat Spencer and my many TA Fellow friends and cohorts: Mark Smith, Connie Lew, Aaron Sin, Kathryn Hollar, Vatsa Srivatsa, Yogesh Potdar, Wendy Foels, Tina Jayaweera, Daisy Fan, Chris Roth, Jitendra (Jeetu) Balakrishnan, Kathy Chandler, Mayur Khandelwal, Aditya Bhandari, Charlie Chen, and Jon Makela.

Thanks to my friends/instructors/mentors on the Dark Side, particularly Warren Allmon for stealing me away for awhile for the chance of a lifetime – searching for and excavating the Hyde Park mastodon. Many thanks, Warren, for the opportunity to take a leadership role in that effort! Thanks also to you and Rob Ross for introducing me to paleobiology, and for making the Paleontological Research Institute a fun and fascinating place to volunteer. Additional thanks go to Evan Cooch, Thomas Gavin, and Steve Ellner for letting me camp

out with natural resources for a bit and learn about conservation biology, population dynamics, matrix modelling, and theoretical ecology. The folks in the Bioacoustics Research Program within the Cornell Lab of Ornithology helped introduce me to Cornell in the first place. My thanks to Katy Payne, Chris Clark, and Kurt Fristrup for their ongoing guidance and inspiration!

Thanks to all my many fellow graduate students, as well as a few postdocs, who encouraged and supported me through the years, especially: Francisco Garcia, Craig Kruschwitz, Eric Klatt, Jon Makela, Mike Nicolls, Camilo Ramos, Rudy Cuervas, Esayus Shume, Fabiano Rodrigues, Alex Cerruti, Brent Ledvina, Hasan Bahcivan, Jason and Tami Franz, Nester Aponte, Ken Wu, Ed Hua, Kathy Chandler, Kerri Cahoy, Lisa Larrimore, Jami Meteer, Christina Tavoularis, Xiaofei Clement Wang, Aimee Merkel, Mercedes Huaman, Lynette Gelinas, Elizabeth Kendall, Fei Lu, and Asti Bhatt. You became great friends along the way, and I truly miss seeing you all every day! Very special thanks to Eric, Jon, Mike, and Craig... I love you guys; you're the best!!

One of the great things about living in Ithaca was that there was a host of people who kept the daily grind anything but. Friends were around every corner... at my apartments (especially Rebecca and Robbie Daniel), the post office, the grocery store (especially Ron at P&C), and even the health center with its caring and fun-loving nurses and staff (especially Julienne, Gale, and Penny). When inevitably life got a bit frustrating, I thank my friends and instructors who helped me redirect my focus and hula it off, shimmy it off, waltz it off, tap it off, climb it off, and kick it off: Mapuana, June, Larry, Leslie, Julie, Lisa, Alison, and Sue. Also many, many thanks to my vigilant neighbors back home – Jenna Weikel, Margaret Swartz, and Mary Thayer – for keeping a watchful eye on things while I was away!

Through thick and thin, and through the years, my friends back in Texas have seen me through it all! I hope they each know the special place they have in my heart. Thanks to my girlfriends – Mary Kuse, Lisha Doucet, and Debra Guillemaud – for their friendship, love, and support! And thanks to John Knoblauh for pushing and challenging me through the years while always lending a helping hand, for providing a stable presence in the unstable times, and for hauling my stuff around!

I'd like to give a shout out to my "imaginary" friends who kept me entertained throughout: Jåck, Såm, Dåniel, Teål'c, Jonås, Cåmeron, and Våla. Thanks team!

I am eternally grateful to my whole family for their steadfast love and support. Thanks to Momma, Dad, and Lauri for always believing in me, encouraging me, and allowing me to pursue my dreams. Thanks to Lauri, Clay, and Karen for loving and caring for Grizzly and Polar Bear. And a huge thanks to Mom and Lar for all your drudgery behind the scenes; I truly do appreciate all your efforts! You are the wind beneath my wings!

TABLE OF CONTENTS

LIST OF TABLES

LIST OF FIGURES

LIST OF ABBREVIATIONS

ACH *Automated Clearing House*.

AEOS *Advanced Electro-Optical System*.

AFOSR *Air Force Office of Scientific Research*.

AFRL *Air Force Research Laboratory*.

AGW *Acoustic Gravity Wave*.

ALARA *As Low As Reasonably Achievable*.

ALOHA-93 *Airborne Lidar and Observations of Hawaiian Airglow*.

AMOS *Air-Force Maui Optical and Supercomputing*.

AOI *Angle of Incidence*.

ATA *French: Admission Temporaire; English: Temporary Admission*.

C14 *Carbon-14,* ^{14}C*, or radiocarbon*.

CARI *Cornell All-sky Roving Imager*.

CASI *Cornell All-Sky Imager*.

CCD *Charge Coupled Device*.

CDAS *Camera Data Acquisition Software*.

CEDAR *Coupling, Energetics, and Dynamics of Atmospheric Regions*.

CEU *Camera Electronics Unit*.

CFC *Chlorofluorocarbons*.

CNFI *Cornell Narrowfield Imager*.

CSSC *CEDAR Science Steering Committee*.

CU-WINS *Cornell University Worldwide Imager Network System*.

CU-WINS URT *Cornell University Worldwide Imager Network System Undergraduate Research Team*.

CWL *Center Wave Length*.

DOD *Department of Defense*.

EIN *Employer Identification Number*.

EUV *Extreme Ultraviolet*.

FOV *Field of View*.

FWHM *Full-Width Half-Maximum*.

GEODSS *Ground-based Electro-Optical Deep Space Surveillance*.

GGS *Global Geospace Science*.

GW *Gravity Wave*.

IGW *Internal Gravity Wave*.

IGY *International Geophysical Year*. 1957–1958.

IMF *Interplanetary Magnetic Field*.

ISR *Incoherent Scatter Radar*.

ISTP *International Solar-Terrestrial Physics*.

LANL *Los Alamos National Laboratory*.

LBD *Laser Beam Detector*.

LCU *Liquid Cooling Unit*.

LIDAR *Light Detection and Ranging*.

LT *Local Time*.

MAUI *Maui Analysis of Upper Atmospheric Injections*.

Maui-MALT *Maui Mesosphere and Lower Thermosphere*.

MHPCC *Maui High Performance Computing Center*.

MIL *Mesospheric Inversion Layer*.

MLT *Mesosphere and Lower Thermosphere*.

MPP *Multi-Pinned Phasing*.

MSDS *Material Safety Data Sheet*.

MSIS-86 *Mass-Spectrometer-Incoherent-Scatter model*.

MSSC *Maui Space Surveillance Complex*.

MSSS *Maui Space Surveillance System*.

NAS *National Academy of Sciences*.

NASA *National Aeronautics and Space Administration*.

NRAO *National Radio Astronomy Observatory*.

NRC *Nuclear Regulatory Commission*.

NRL *Naval Research Laboratory*.

NSF *National Science Foundation*.

NSTP *National Solar Terrestrial Program*.

PCLS *Portable Calibrated Light Source*.

POC *Point of Contact*.

PSU *Pennsylvania State University*.

PVC *Polyvinyl chloride*.

RAM *Radioactive Material*.

REU *Research Experience for Undergraduates*.

RME *Remote Maui Experiment*.

RPS *Remote Power Switch*.

RSO *Radiation Safety Officer*.

SNR *Signal to Noise Ratio*.

SOFDI *Second-Generation Optimized Fabry-Perot Doppler Imager*.

SOR *Starfire Optical Range*.

SPP *Space Plasma Physics*.

SRI *SRI International (formerly, Stanford Research Institute)*.

SSH *Secure Shell*.

STP *Space Test Program of DoD*.

TECA *ThermoElectric Cooling America*.

TID *Travelling Ionospheric Disturbance*.

TLD *Thermoluminescent Dosimeters*.

UARS *Upper Atmosphere Research Satellite*.

UCAR *University Corporation for Atmospheric Research*.

UIUC *University of Illinois Urbana-Champaign*.

UPS *Universal Power Supply*.

USCIB *U.S. Council for International Business*.

USU *Utah State University*.

UT *Universal Time*.

VE *Visiting Experimenter*.

VLA *Very Large Array*.

VNC *Virtual Network Computing*.

CHAPTER 1

INTRODUCTION

1.1 Motivation

It was a dark and stormy night. [1] A few hundred kilometers from paradise, out over the Pacific, a storm was brewing in the troposphere. Back over the islands, however, as twilight fell and the splendor of the tropical sunset faded, the stars emerged twinkling and bright on this moonless night. High atop the volcano tiny red lights flickered on, preserving night vision and signaling the start of the work shift. The Menehune [2] and bugs [3] were at bay, and here at the summit of the House of the Sun [4], conditions were prime for nature to reveal her secrets, with *all eyes on the sky... nowhere to hide* [5]. While Pele [6] slept, thunder rumbled in the distance barely disrupting the tranquility of this peaceful night. And yet, inaudibly, a disruption had occurred. Emanating outward from the storm cell, much like a ripple leaving a stone tossed in a pond, a gravity wave had been launched. Immediately it began to climb, leaving the storm clouds of the homo-

[1] A common narrative cliché made famous by comic strip artist Charles M. Schulz, but originally penned by Victorian novelist Edward Bulwer-Lytton, 1rst Baron Lytton, as the beginning of his 1830 novel *Paul Clifford*.

[2] Also known as Nawao. Menehune are the legendary, mystical, 'little people' of Hawaii, similar to pixies or trolls, who roam the forests at night with mischievous intent and industrious, engineering prowess.

[3] Refers to the bug infestation of 2002.

[4] Translation of the Hawaiian name *Haleakalā* for the entire shield of the East Maui volcano. Early Hawaiians applied the name only to the summit area, the site where the demigod Maui snared the Sun and forced it to slow its journey across the sky.

[5] Also in Hawaiian: *Nā maka ́i ka laní Nā wahí ‘ ole ́i ka pe’e*. The motto of Detachment 15 of the Air Force Research Laboratory's Directed Energy Directorate. Included as a nod to Detachment 15 which conducts the research and development mission on the Maui Space Surveillance System (MSSS) at the Maui Space Surveillance Complex (MSSC).

[6] Hawaiian goddess of volcanoes currently thought to reside in Kilauea on the Big Island. The remnants of Pele still remain on her former residence, the summit of Haleakala, which lies within the Land of Pele as part of Hawaii National Park.

geneous atmosphere far behind as it forged its way out of the cold, upper troposphere and on through the heated stratosphere. Discharging its energy upward while throwing off phase disturbances orthogonally downward, it continued to ascend growing in amplitude as it advanced. No sooner had it burst past the mesopause in the coldest region of Earth's atmosphere, than it encountered a formidable barrier at a critical level, halting its journey upward. The intrigue began to escalate. The gravity waves behind it kept coming, piling up in a turbulent jam providing the forcing – like a piston driving the gravity wave down the corridor of an inversion layer – until it reached its nonlinear breaking point and like a sonic boom transformed into a hydraulic jump forming the leading edge of a mesospheric bore. And now close to a hundred kilometers below, the Valley Island was in sight, as this trapped mysterious phenomenon surged along making constant progress through the guiding tunnel. In the pitch black of this moonless night, as the tourists and kamaaina [7] alike slumbered serenely, the bore found itself in a glowing region of dim light, poised for the cameras below.

Thus, our research study unfolds with a natural phenomenon to investigate, ensconced in a medium to explore, supported by instruments deployed to record it, and laid on a theoretical foundation ready to incorporate new findings expanding as needed. However, before embarking on this study, as with any scientific journey, we need to address the age-old adage of universal concern: "Why should we care?" To answer this question validating the inherent worth of the research, it is useful to place the study in general context.

The event described anecdotally above occurred in the lower reaches of the upper portion of the Earth's atmosphere. The terrestrial atmosphere is a

[7] A long-term Hawaiian resident.

relatively thin, spherical envelope encircling the Earth, extending out beyond 1000 km, and characterized by both neutral and ionized gases. According to temperature-differentiated designations, the lower sections of the upper atmosphere are known as the "mesosphere" and "lower thermosphere" – together referred to in the literature as the "MLT" region. The *mesosphere*, distinguished as the coldest region in the terrestrial environment, straddles the boundary between the neutral atmosphere and the first signs of ionization. The densities of neutral gases fall off exponentially with altitude from the Earth's surface, and eventually the ionized gases take over. The Earth's *ionosphere* is delineated as the ionized portion of the terrestrial upper atmosphere. The story really begins farther out in the solar system, however, with the relationship between the Sun and the Earth – the solar-terrestrial system. The Earth, with its strong, protective magnetic field, is situated within the interplanetary magnetic field in direct line-of-fire of the constant bombardment of the supersonic solar wind. The plasma in the Earth's atmosphere at midlatitudes originates primarily with this extreme ultraviolet radiation from the Sun, which results in photoionization of neutral particles. Both the newly formed charged particles, as well as the neutral particles, are then affected by a myriad of processes, including: chemical reactions, diffusion, wave disturbances, plasma instabilities, and transport due either to electric and magnetic fields or wave ducting. In the highly interconnected atmospheric system of the Earth, these processes affect and are affected by the couplings between both different vertical layers and geographic areas, whereby the dynamics and energetics of one region can dramatically impact other regions.

The opening narrative illustrates the development of a bore phenomenon originating in a localized region of the lower atmosphere, yet resulting in more

global impact as energy and momentum flux are transported across regions both vertically to higher altitudes and horizontally through a wave-guiding structure to distant latitude-longitude locations where the flux is then deposited through dissipative effects. Upward vertical transport of even small amounts of energy and momentum can have disproportionately large effects on the upper-atmospheric global budgets as a result of wave-associated dynamics, such as exponential growth in amplitude due to the decrease in atmospheric density with height. These vertical amplification effects allow energy, momentum, and chemical processes, coupled from the lower atmosphere, to serve as sensitivity indicators of small changes. Chemical reactions, occurring at a specific altitude based on the intrinsic constituent profile resulting from diffusive stratification, can illustrate the coupling effects by producing chemiluminescent light which then serves as a dynamical tracer as it is transported by wave disturbances driving momentum flux deposition.

Once discarded as hard-to-reach quiet areas, the middle regions in both the vertical and horizontal (lat-lon) dimensions have both been revealed in recent years as accessible, active, important, and interesting sectors of the atmosphere. Spatial irregularities, such as wavelike or undulatory structures created in the atmosphere by events impacting mesospheric dynamics – while interesting in their own right for the purpose of basic scientific advancement to gain an understanding of the still vast geophysical unknown – are of particular interest to many in the scientific and military communities who view these distortions as obstacles to their own specific goals. Structured small-scale and large-scale plasma disturbances in the ionosphere are known to impact satellite communication and navigation signals. The influence of waves and tides on the structure and brightness of airglow layers, infrared in particular, along with diurnal and

seasonal variations in these layers, can all impact the military's efforts in surveillance, imaging, and missile defense. In general, structured formations, turbulent regions, and gradients, that is, variations from the ambient background, even in neutral gases, can hinder the efforts of those looking past the MLT region, those maneuvering equipment through the MLT region, and those focusing directed energy within the MLT region. Ecologically speaking, it is imperative to understand the climatology of the region so that secular variations or sudden impacts, arising from possible human influences upon the environment, might be detected, recognized as potential harbingers of global change, and addressed. Anthropogenic CFC gases deteriorating the effectiveness of the stratospheric ozone layer is a well-known illustration of this point. As studies of the upper atmosphere continue, ever more is understood of this highly interconnected system. Each new study, such as this one, provides incremental insight into this important atmospheric region and our environment as a whole.

1.2 Research Context

In an effort to understand further the bore phenomena, this dissertation follows the development of an observational and theoretical study of bores in the mesosphere and lower thermosphere using airglow imagers at mid-latitudes. Sighting bores near the mesopause is a relatively new phenomenon – the first such observation occurred a little over a decade ago, late in 1993, during the Airborne Lidar and Observations of Hawaiian Airglow (ALOHA-93) campaign. One particularly spectacular gravity-wave event from this campaign resembled aerial views of tidal bores in river channels. This striking resemblance inspired *Dewan and Picard* [1998] to coin the term "mesospheric bore" when they proposed

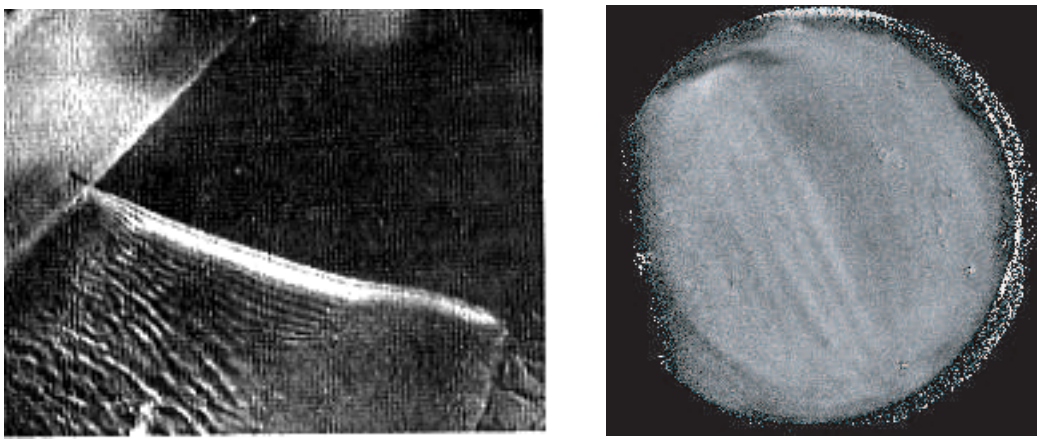

(a) (b)

Figure 1.1: (a) Tidal bore on the River Mersey from the air (From *Tricker* [1965]). (b) Internal bore in the mesosphere at 96-km altitude over Peru. This 557.7-nm wavelength airglow image was taken by the Cornell All-sky Roving Imager (CARI).

the first basic mathematical model for an atmospheric bore at mesospheric altitudes. Panel (a) of Figure 1.1 shows the river channel inspiration for *Dewan and Picard* [1998] – an aerial view of a tidal bore on the River Mersey – revealing the striking similarity to airglow images of mesospheric sharp fronts, such as the one shown in panel (b).

After this initial ALOHA-93 observation, the next recorded mesospheric bores were registered by researchers at Cornell University, first in Puerto Rico [*Garcia*, 1999], and later in Peru. To gain more insight into mesospheric bores, this investigation started with pursuing more data by installing imaging equipment at a long-term field site. Beginning in 2001, this strategy proved effective as even more occurrences of bores were recorded using the Cornell University imager fielded in Maui, HI, as part of a collaborative, multi-instrument campaign. One of the ambitions for this campaign was to obtain simultaneous airglow image data and lidar data, if a mesospheric bore should happen to occur

during one of the scheduled lidar runs. While we were unlucky with regard to obtaining complementary lidar data to provide a corresponding vertical atmospheric profile, we did collect additional and varied bore data from this field site. Building from this expanded database, we developed the first classification system to categorize mesospheric bore observations. We also evaluated temperature profile data corresponding to a mesospheric inversion layer (MIL) to investigate the bore formation hypothesis proposed by *Dewan and Picard* [2001], and verified for the first time that the MIL would support bore formation.

All of the Cornell University airglow observations were made over multiple emission layers. While the images from most of the new datasets display the same anti-correlated brightness patterns between upper and lower altitudes as the original ALOHA-93 data, the data from Peru, in particular, exhibits something unexpected and new – the brightness relationship between airglow layers is reversed and accompanied by a lateral shift! This was the first such inverse event reported in the scientific community, and this seemingly contradictory data failed to support the existing basic theory. Working with researchers at the Air Force Research Laboratory (AFRL), we proposed the possibility of two coexisting bores to explain both the inverse contrast pattern and the accompanying horizontal phase shift between emission layers. We also compared the data to an alternative non-linear theory [*Seyler*, 2005], and found both that: (1) neither theory explains all the observable features, and (2) each theory succeeds in explaining some characteristics not addressed by the competing theory. Evaluating the various theories in the context of only the two-dimensional image data available underscores the inherent limitations and the need to obtain corresponding parametric vertical profile data in order to ascertain the validity of either hypothesis.

Late in the development of this thesis came the realization of the critical and complicated role calibration plays in ensuring the condition of our data for achieving the goals of the scientific community – goals of allowing effective data comparisons, using data to constrain numerical models, and monitoring data trends. Impacting all of these are the inherent errors which exist in the data-collection process. Overall, calibration reduces the discrepancies between raw data and true phenomenon, facilitating the generation of congruent, accurate data for analysis. In actuality, "calibration" breeds confusion, as it is a semantically complicated term with multiple meanings, addressing many processes, each with numerous methods of implementation. The challenges associated with calibration are readily acknowledged by the scientific community. To address some of these challenges and alleviate some of the confusion for future graduate students, in particular, a portion of this dissertation is devoted to presenting the first, comprehensive presentation of calibration, detailing topics, techniques, methodologies, and results, as they pertain to airglow imagers.

1.3 Dissertation Organization

The organization of this dissertation is as follows: To motivate the bore study further – beyond the narrative interpretation of the evolution of a mesospheric bore event and the general geophysical context described in the opening section – Appendix A.1 provides a more detailed description of the environmental fabric in which the studied phenomena are ensconced. In the same vein, Appendix A.2 gives a brief historical perspective from ancient times through the present to add chronological context. Section 1.2 provides the framework for the specific work done as part of this dissertation, and defines the basic scien-

tific questions being addressed.

Chapter 2 lays the experimental foundation for the project. Section 2.1 describes the primary long-term field site established and maintained for our observational studies, as well as an historical log of other short-term field sites operated. Section 2.2 concentrates on the equipment tasked with making airglow observations, providing a thorough description at the component level of the imaging systems deployed. Operating procedures for the remote AC power switch are included in Appendix B, as the command-line instructions for this device, in particular, are very detailed and nonintuitive. For more details on fundamental filter construction, design, performance, and care-protocol concepts than provided within Section 2.2.1.3, the reader is referred to Appendix C. A detailed equipment inventory for each imager is provided in Appendix D for reference. Appendix E chronicles field-site information for each imager system, and offers some sample shipping documents. Finally, in Section 2.3, a mathematical model – incorporating contributions from both external, environmental sources and internal, equipment sources – is derived to describe the digital representation of the airglow data for analysis. Error types contributing to this mathematical airglow model are highlighted and categorized in Section 2.3.2, motivating the need for calibration discussed in Chapter 3. Methods for isolating our airglow signal of interest are presented and analyzed in Section 2.3.4.

Calibration is the key for translating raw optical data into an effective mathematical-model format most closely depicting the true natural phenomenon. Chapter 3 is intended to highlight some of the challenges of calibration readily acknowledged by the scientific community, and to alleviate some of the associated confusion through discussions of these topics and presentation

of relevant methodologies. To begin, a foundation is laid in Section 3.1 with the definition of the signal-to-noise ratio for our airglow signal, which serves as the context for the ensuing sections. Types of calibration sources are presented in Section 3.3. In Sections 3.4 – 3.5, the types of calibration are introduced under two broad categories: radiometric calibration and geometric calibration. Methods used in radiometric calibration are covered in Sections 3.4.1 – 3.4.4, with procedures for a specific calibration study also detailed in these sections. Additional results from the calibration study can be found in Appendix F.

Chapter 4 lays the theoretical foundation for the dissertation. Section 4.1 details the chemistry behind specific photochemical reactions producing airglow, which, in turn, acts as a dynamical tracer for wave phenomena, providing the means for our observations. In Section 4.2, atmospheric wave theory is introduced with a brief overview of different types of waves occurring in the atmosphere. The basic wave equations which provide the framework for studies of the dynamics and energetics of the upper atmosphere are derived in this section. Finally, gravity waves, which play a crucial role in bore development, are introduced. From here, bore theory and generation are described in Section 4.3.

Chapter 5 relates observational bore data, and introduces a new classification system. As this chapter has been submitted for publication, some effort was made to preserve the original format while maintaining continuity within the dissertation. As mentioned earlier, in the decade plus since the initial spectacular gravity wave events were observed, additional examples of sharp airglow fronts have been recorded by imaging systems at a variety of locales. Some of these subsequent bore observations are narratively recounted in Section 5.3. Parameters of each event are summarized in Section 5.3.1. Building from our new

database of events, we present, in Section 5.3.2, the classification system developed to categorize mesospheric bore observations based on the variability of the brightness as demonstrated in the collective observations. In Section 5.4, we analyze the bore observations and compare them to the basic, analytical bore model. Chapter 5 concludes in Section 5.5 with a discussion and summary.

Chapter 6 proposes a theoretical explanation for, and analysis of, new bore observations. This chapter has also been submitted for publication; as such, the same effort was made to preserve the original format while maintaining continuity within the dissertation. The possibility of two or more coexisting bores is proposed in Section 6.2. This inverse bore theory accounts for the new bore observations (presented in Chapter 5) with inverted brightness patterns and accompanying horizontal phase shifts between the emission layers. In Section 6.3, characteristics of the new bore observations are compared to the predictions of another nonlinear theory which extends the symmetric bore theory and offers additional insights to explain the data [*Seyler*, 2005]. This chapter is concluded in Section 6.4 with a discussion and summary.

Finally, Chapter 7 highlights future directions to expand this line of research. A new investigation, as described in Section 7.1, is planned as a postdoctoral study to model optical emissions using a robust, time-dependent chemical dynamics model to explore both the airglow response to ducted gravity waves, and, in turn, the associated geographical and vertical coupling relationships which may exist. Some concluding remarks are given in Section 7.2.

Unless otherwise specified, all photographs contained within this dissertation were taken by Pamela Loughmiller.

CHAPTER 2

INSTRUMENTATION

To set the stage for the data presented subsequently in this dissertation, this chapter provides basic descriptions of the equipment used to collect the data, as well as the campaigns for which the instruments were deployed. The focus of this chapter is the primary campaign site since late 2001, and the equipment deployed for this mission. Additionally, however, an attempt is made to provide an exhaustive historical account, chronicling the various worldwide field sites where the Cornell University imagers have been deployed. The last section in this chapter contains the derivation of the airglow model which describes our digital representation of the airglow signal depicting the underlying geophysical phenomenon.

2.1 Campaign Field Sites

As shown in Figure 2.1, the Cornell University airglow imagers have been operated at many locations worldwide. Since the first deployment of a Cornell airglow imager to collect data in 1997, the longest-running, highest-profile imager installation conducted by Cornell University has been the collaborative Maui-MALT campaign. For over five years now, the Maui site has been home to two of Cornell's three airglow imagers, delivering an abundance of provocative new data, and providing the primary focus for many resulting studies. In this section, the description of this primary field site includes not only an overview of the various facilities collectively comprising the site and their respective functions, but also a report of the evolution of the personnel team supporting the campaign. In addition to providing an historical record of the support structure

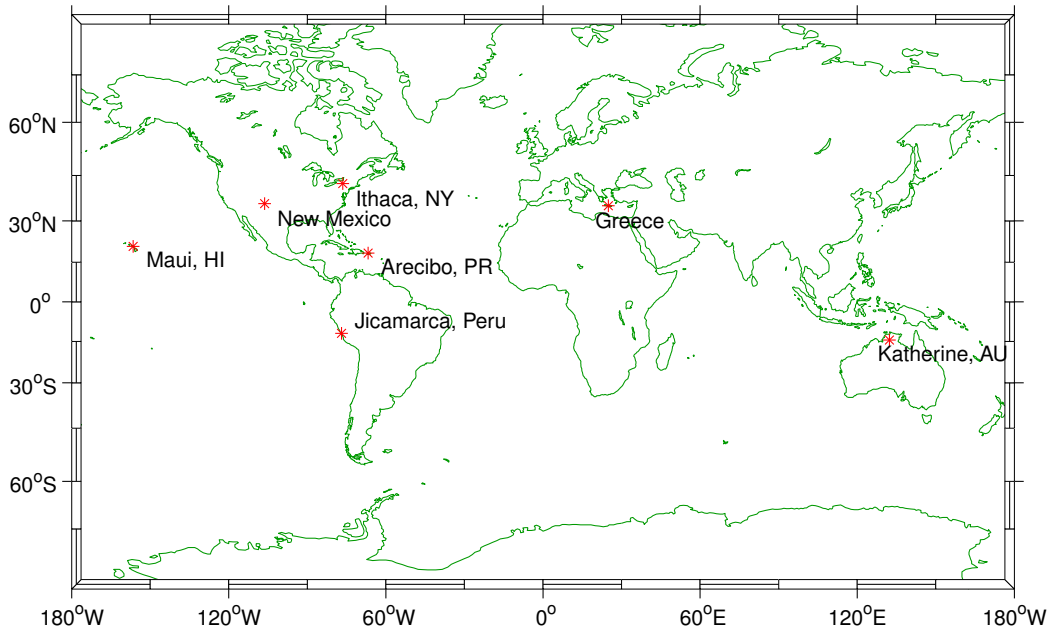

Figure 2.1: World-wide locations where Cornell University imagers have been fielded.

for this specific campaign, the information regarding the site personnel team may also serve as a template for future graduate students for interfacing with a long-term field site on a collaborative campaign.

2.1.1 Maui-MALT Campaign Site

The Maui-MALT initiative is a scientific data collection campaign jointly-sponsored by the National Science Foundation (NSF) and the Air Force Office of Scientific Research (AFOSR) to promote upper atmospheric studies of the mesosphere and lower thermosphere (hence, MALT). The program is comprised of scientists from Cornell University, the University of Illinois at Urbana-Champaign, Utah State University, Pennsylvania State University, and the Aerospace Corporation. The program has been in operation since the late fall of 2001, initially centered around the use of a giant 3.67-meter telescope as the op-

Figure 2.2: Pamela poses at the entrance sign to the Maui Space Surveillance Complex on top of Haleakala Volcano in Maui, HI.

tics for two different LIDAR (Light Detection and Ranging) systems. Multiple imagers have been deployed at the site by Maui-MALT participants to provide corollary data, as well as coverage when the telescope is not available.

The Maui Space Surveillance Complex (MSSC), part of the United States Air Force Research Laboratory (AFRL) operations, provides an ideal location to study the mid-latitude mesosphere and lower thermosphere. This restricted Air Force facility shown in Figure 2.2 has served as our on-going field campaign site since October 2001. In this section, publicly-accessible, non-classified information about the site is presented to describe the facilities and their function, including their operating environment, capabilities and organization. The information included in this site overview is drawn primarily from the facility's website (http://www.maui.afmc.af.mil) and covers: the viewing environment, optical assets, visitor experiments, management and operation, and administrative and technical assistance.

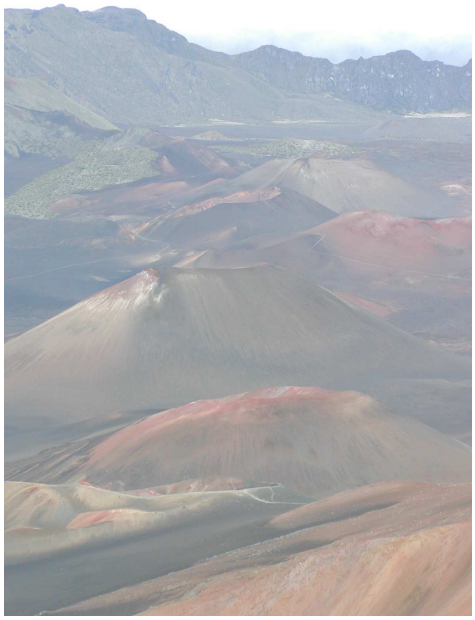

Figure 2.3: The caldera of the dormant Haleakala volcano on the island of Maui in Hawaii.

2.1.1.1 Viewing Environment

Sitting at over 10,000 feet above sea-level, the site – located 20.7°N latitude, and 156.3°W longitude – rises above the clouds at the crest of the dormant Haleakala volcano (see Figure 2.3) on the island of Maui, Hawaii. Shown in Figure 2.4, the site is situated far away from and high above any city lights, thus minimizing scattered light from surface sources. Combining this feature with the dry, clean air quality, and with the relatively stable climate of the region, the observatory offers wonderful seeing conditions virtually year-round providing for excellent data collection.

(a)

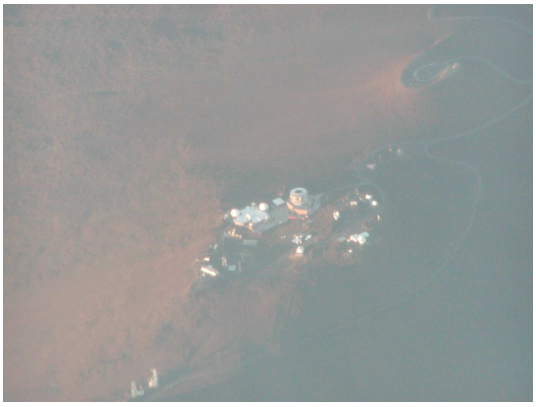

(b)

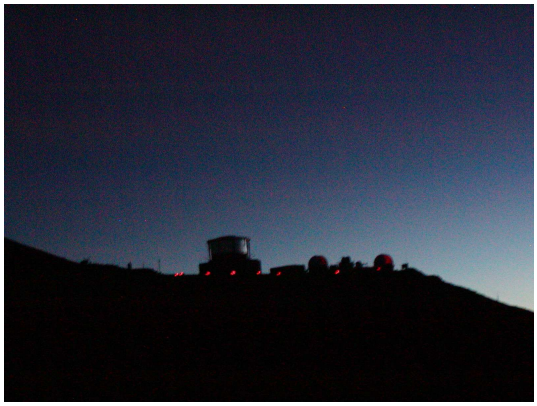

(c)

(d)

(e)

(f)

Figure 2.4: Various views of the U.S. Air Force's Maui Space Surveillance Complex. (Panel (a)–(e) photographs by P.J. Loughmiller. Panel (f) photograph courtesy of AMOS.)

2.1.1.2 AFRL Mission

AFRL operations on Maui currently address a two-fold mission from the AFRL's Directed Energy Directorate. First, AFRL Detachment 15 conducts the research and development mission on the Maui Space Surveillance System (MSSS) at the Maui Space Surveillance Complex (MSSC). Second, AFRL Detachment 3 oversees operation of the Maui High Performance Computing Center (MHPCC). Formerly, the term AMOS (Air Force Maui Optical & Supercomputing) was used to indicate both a mission and a collection of facilites. Specifically, AMOS referred to the AFRL's research and development mission on Maui, as well as a collection of operating facilities including the MHPCC and a portion of the facilities housed at the MSSC. The use of the term AMOS has been widespread throughout the technical community for over thirty years, and is still used today at many technical conferences, including the increasingly-prominent, annual AMOS Technical Conference.

The accessibility and capability of the Maui Space Surveillance System provides an unequaled opportunity to the scientific community by combining state-of-the-art satellite tracking and lidar capability with a facility supporting research and development. As such, it is routinely involved in numerous observing programs. Overall, the Air Force's objectives at the MSSC facility atop Haleakala volcano include conducting operations, integration and testing, and research and development in support of their missions targeting atmospheric science, astronomy, and space surveillance (per the United States Space Command's Space Object Identification Statement of Need). The site is the largest United States Air Force optical space tracking facility in existence.

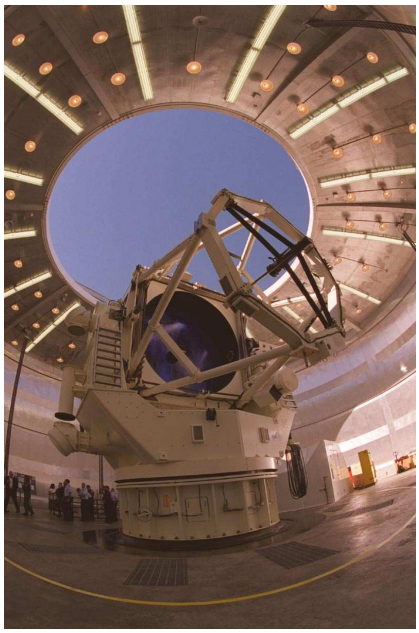

Figure 2.5: A close-up view of the Advanced Electro-Optical System (AEOS) telescope located at the U.S. Air Force's Maui Space Surveillance Complex. (Photograph courtesy of AMOS.)

2.1.1.3 Optical Assets

Spanning over 30 years, the evolution of the Maui Space Surveillance Complex has demonstrated several stages in the history of space object tracking telescopes. Currently, through its primary mission for Air Force Command, the Maui Space Surveillance Complex combines large-aperture tracking optics with visible and infrared sensors to collect data on near Earth and deep-space objects.

The star of the suite of instruments on site at the complex is the nations largest optical telescope designed for tracking satellites – the Advanced Electro-Optical System (AEOS) telescope – shown in Figure 2.5. This 3.67-meter telescope, owned by the Department of Defense, is optimized for speed to facilitate satellite tracking and space object identification applications. The 75-ton AEOS telescope points and tracks very accurately, while simultaneously en-

dowed with speed capabilities fast enough to track both low-Earth satellites and missiles. AEOS can be used simultaneously by many groups or institutions because its light can be channelled through a series of mirrors to seven independent coud rooms below the telescope. Employing sophisticated sensors that include an adaptive optics system, radiometer, spectrograph, and long-wave infrared imager, the telescope tracks man-made objects in deep space and performs space object identification data collection. The entire configuration is housed in a 40,000 square foot, four-level facility under a retractable dome. The telescope with its adaptive optics system is structurally isolated within the facility to minimize vibration. AEOS is equipped with an adaptive optics system, the heart of which is a 941-actuator deformable mirror that can change its shape to remove the atmospheres distorting effects. With this capability, scientists are expected to get near diffraction-limited images of space objects.

The work-horse within the MSSS building is the Ground-based Electro-Optical Deep Space Surveillance system (GEODSS). Additional Air Force instruments at the MSSS include the following: a 1.6-meter telescope, two 1.2-meter telescopes on a common mount, a 0.8-meter beam director/tracker, and a 0.6-meter laser beam director. The telescopes accommodate a wide variety of sensor systems, including imaging systems, conventional and contrast mode photometers, infrared radiometers, low light level video systems, and acquisition telescopes. In addition to these assets, the site has a machine shop, optics laboratories, and electronics laboratories. The Remote Maui Experimental (RME) site at sea level houses additional optics and electronics laboratories.

2.1.1.4 Visiting Experiments

The Air Force Research Laboratory has a long history of partnering with various military and civilian organizations in diverse fields. Visiting experiment programs are generally divided into two main classes: measurement programs and development programs. Measurement programs have little or no direct on-site involvement, and are usually characterized by scientific measurements. Development programs are scientific investigations that may require modifications or additions to the facilities and direct personnel involvement on the island.

Typical visiting experiments include the following:

- complex space missions
- astronomical observations
- laser development
- observation campaigns
- detection and tracking of orbital debris
- observation of missile experiments out of both Vandenburg Air Force Base (AFB) and Barking Sands Missile Range on the island of Kauai

As an observation campaign, Maui-MALT has primarily been a measurement program with direct involvement of site personnel requisite only during the initial setup phases requiring equipment installations. The Maui-MALT campaign was initially a two-year program jointly funded by the NSF and AFOSR, with the imager systems beginning operation in late fall of 2001 and with quarterly lidar data runs commencing in 2002. Additional funding extended the full program another two years through 2004. Following this ex-

tension, the lidar participation was removed, and at this time, only the imager and meteor radar components remain. Overall, the Maui-MALT instruments, principal investigators, and participating entities included:

- Airglow Imagery & Spectroscopy
  - Cornell University, Michael Kelley
  - University of Illinois, Gary Swenson
  - Utah State University, Mike Taylor
  - The Aerospace Corporation, Jim Hecht
- Meteor Radar
  - University of Illinois, Steve Franke
  - University of Western Ontario, Wayne Hocking
- Na Wind/Temperature Lidar
  - University of Illinois, Chet Gardner, George Papen, Xinzhao Chu
- Rayleigh Temperature Lidar
  - Pennsylvania State University, Tim Kane
  - Clemson University, John Meriwether

For Cornell University's participation, two cameras have been fielded at this location. The first is our "standard" all-sky imager located in the LBD trailer on the roof of the MSSS building as shown in Figure 2.6. This imager provides a nighttime, horizon-to-horizon snapshot of the state of the ionosphere at different heights, and is useful for observing atmospheric waves, mesospheric bores,

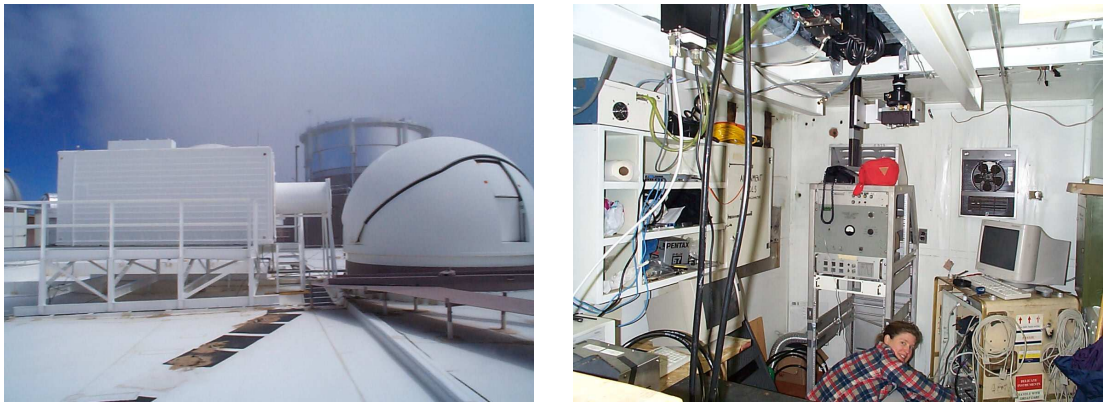

(a) (b)

Figure 2.6: Panel (a) shows the LBD trailer housing CASI on the roof of the MSSS (Maui Space Surveillance Site) building, and panel (b) shows Pamela working inside the LBD trailer on the CASI equipment.

meteor trains, and equatorial spread-F. The second camera, shown in Figure 2.7, is a narrow-field-of-view camera (approximately 40 degrees), which is pointed approximately towards the south. The purpose of this camera is to observe the state of the equatorial F-region in hopes of better understanding the causes of the equatorial spread-F phenomenon. Detailed descriptions of these camera systems will follow in Section 2.2.

Broad scientific research goals were defined for the overall campaign to include:

- to develop instrument capabilities to measure atmospheric temperature and winds from the Earth's surface to the edge of space (110 km),
- to characterize the generation, propagation, and dissipation of gravity waves from the troposphere through the mesosphere.

Additionally, specific research goals were defined to address distinct needs of the Air Force. These are listed below, with the relevant Air Force programs

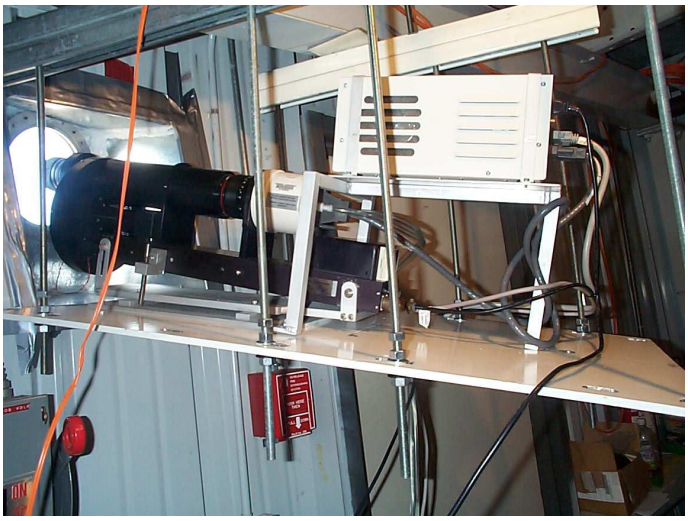

Figure 2.7: CNFI is shown mounted on a semi-permanent structure in the dog-house at the MSSC (Maui Space Surveillance Complex).

impacted noted in parentheses:

- to develop models for predicting winds and temperature at all atmospheric levels (flight ops)
- to determine the relationship between breaking gravity waves, tides, and clear air turbulence (imaging, flight ops, directed energy weapons)
- to determine the influence of waves and tides on the structure and brightness of infrared airglow layers (surveillance, imaging, missile defense)
- to characterize and model diurnal and seasonal variations of the Na layer (laser-guided adaptive imaging, surveillance, directed energy weapons).

2.1.1.5 Management and Operation

The MSSC, managed by the Air Force Research Laboratory's Directed Energy Directorate, operates 24/7 responding rapidly to perform its vital space surveillance mission. Scientists, engineers and technical staff design experiments,

build sensor systems, perform measurements, and analyze data in support of advanced space surveillance research and space object identification.

The designated procedure for any interactions with the Maui site personnel is for communications to be channelled through the primary point of contact (POC), who is a Boeing CTR employee assigned as project manager for the Maui-MALT program. The POC is charged with three principle functions: coordinating any required support issues, interfacing with Air Force personnel, and organizing site visits including obtaining the necessary clearance approvals, as well as arranging for escorts and scheduling the obligatory security briefings. In this role, the Boeing POC is part of the technical administrative staff located at the base of the mountain in Premier Place. Additionally, the Maui-MALT program was supported by an "on-site" POC located atop the mountain at the MSSC. This Boeing technical support staffer was the chief contact for any equipment-specific requests regarding the Cornell computers or imagers. Also available on-site in a support capacity are electrical technicians and computer systems personnel. The specified hierarchy is for requests to be funnelled through the primary POC, who then coordinates with other support personnel as needed. As close working relationships evolved in the first few years, requests could be made directly to the on-site POC, while keeping the primary POC in the loop. Note that charge accounts are assigned for the various projects facilitated at the complex, and the primary POC tracks the material and time charged to his assigned accounts. In this regard, one important point to keep in mind, and must at times be reminded to the local Maui support group, is that Cornell's source of funding is different from the rest of the Maui-MALT team. Cornell's participation is supported through separate Air Force funding tied to its own unique charge account.

Lastly, there is another Boeing site down in Kahului which is responsible for receiving shipments and approving equipment to be transported up top the mountain. This second function is an important step to remember in order to avoid unnecessary delays in installing equipment – even small items such as external hard drives. When the POC system is working as designed, this approval is negotiated and obtained as if in a black-box; when the POC system fails, we must step in to ensure the appropriate paperwork is obtained as this approval is still required to locate equipment at the site. Originally, our equipment was shipped to the following address on 10/11/01: (Figure E.3 in Appendix E shows a sample shipping label.)

Maui-MALT Russ Taft
The Boeing Company
358 Papa Place #3
Kahului, Maui, HI 96732

In constrast, our POC's (Russ') office building address was:

Maui-MALT Russ Taft
The Boeing Company
535 Lipoa Parkway, Suite 200
Kihei, Maui, HI 96753
(808) 874-1557

Since late 2004, a lot of changes and turnovers have occurred in the Air Force and Boeing management and staff structures supporting the Maui-MALT program. Of largest consequence was the retirement of both our primary POC (Russell Taft) and our on-site POC (Spence Ah You). Russell was replaced by John Ross, who left the island within three months having made a lateral move

within Boeing to a stateside position. John Ross was then replaced by Juan Cabanilla who took over the position in 2005. Early in 2006, Boeing signed a new contract with the Air Force impacting project assignments. As a result, Juan's tenure in the position was also temporary. Spence's position as on-site POC is not planned to be refilled. Instead, support staff on-site who have worked with Cornell in the past, and are familiar with our equipment and project, have filled in to assist with any on-site requests. The main support has been provided by the system administrators, in particular Ken Dutton. Unfortunately, in February 2006, Ken transferred stateside after eight years on the island. In Ken's absence, we have been working with Jerry Mizomi, also a member of the system administration team led by Dean Ikioka. In 2005, a new Boeing position (VE POC) was created on-site at the MSSC to act as the primary POC for all visiting experimenters. This person would have served as our replacement for Spence's on-site POC position, but the short-lived post was dissolved within the year. In 2006–2007, Jacob Barros, who maintains the RME site and provided support during the last calibration of Cornell imagers in 2005, has been tapped by Boeing to fill an intermediary role between the primary POC and MSSC on-site support. The MSSC VE POC position was resurrected (filled by Jacob Burger), along with creating a new accompanying VE POC position down below at Premier Place (filled by Capt. Virginia Wright). Overseeing all the Boeing employees, John Africano[1] is the manager in charge. John's responsibilities also include two other Boeing sites stateside, so he is only periodically in residence on the island. Given his position, John is included on some, but not all, related communications. He has on occasion intervened to expedite procedures. On the Air Force side of things, Paul Kervin has served as our Air Force POC since the

[1]John Africano died in late summer 2006. By late 2007, two Boeing employees were tapped to fill his role in Maui. One is Tamara Payne.

campaign's inception. Similar to John Africano, Paul's support is primarily in a managerial capacity, receiving regular briefings from the primary POC, but Paul has also become directly involved upon request to facilitate the process. In late 2004, a new Director of Research position was created at the top of the Air Force hierarchy. This post, filled by Jim Riker[2], has dual responsibility with the Air Force Site Commander for overseeing the entire site.

2.1.1.6 Administrative and Technical Assistance

The technical and administrative facility is located at Premier Place in the Maui Research and Technology Park in Kihei, Maui. MSSC organizations with office space at this location include AFRL, Boeing CTR (prime contractor, previously Boeing RTS), as well as Textron and Trex (subcontractors).

The Maui High Performance Computing Center (MHPCC) is also located in the Maui Research and Technology Park. As one of the worlds largest IBM SP installations chartered to sustain a broad base of users in the Department of Defense (DOD), government, academic, and commercial communities, the MHPCC provides access to parallel computing hardware, advanced software tools and applications, high bandwidth communications, and high performance storage technologies. In addition, MHPCC offers a variety of services, including application support, parallel code development, large system management, and training and education programs.

Another key point that often gets forgotten in connection with the Maui-MALT campaign is that the network supporting the Maui-MALT computers is

[2]Jim was promoted, and his Director of Research responsibilities have also been divided between two new replacements.

provided by the MHPCC. However, due to physical logistics, the on-site MSSC system administrators – not associated with the MHPCC – provide the personnel support for our system connections. The on-site system administrators do not always have visibility of changes made or outage occurrences incurred by the MHPCC staff. When Maui-MALT related system issues occur, the first-line response from the MSSC system administrators is often that there are no system outages or malfunctions, so the problem must reside with the Cornell University equipment. As such, it is often necessary to remind everyone that the system in question is maintained by MHPCC.

2.1.2 Other Campaign Sites

In addition to this now 5-year-plus long-term field site participation involving two imagers, Cornell University imagers have been deployed to a number of locations for short-term projects. Currently Cornell University maintains three imager systems for airglow studies. Collectively, these imagers in their far-reaching field sites are known as "CU-WINS" – the Cornell University Worldwide Imager Network System. For many years, data obtained from CU-WINS was processed by an ever-evolving undergraduate research team. In 2002, graduate students Pamela Loughmiller and Jonathan Makela generated a manual called "CU-WINS URT Manual (or the Handy-Dandy Guide to Processing Airglow Data from Cornell University's Worldwide Imager Network System)" [*Loughmiller and Makela*, 2002]. While written to direct the efforts of the undergraduate researchers for the Maui-MALT campaign specifically, the document has general applicability as it contains descriptions of the science and computer software involved, definitions of relevant acronyms, procedures for

(a) (b)

Figure 2.8: Panel (a) shows the Arecibo radar observatory in Puerto Rico, and panel (b) shows the airglow facility at the site.

data cataloging and processing, as well as further references and useful contact information.

CU-WINS began with the original Cornell imager, an all-sky camera system assembled by former graduate student F. J. Garcia in 1996, and deployed to the Arecibo site in Puerto Rico (see Figure 2.8) from January 1997 through March 1998. This portable camera system was originally named "CASI", short for Cornell *A*ll-*S*ky *I*mager. In July of 1998, CASI was fielded in Kauai and Maui, HI, as a feasibility test for the anticipated future Maui-MALT campaign (see Figure 2.9). In between official campaigns, CASI has been intermittently set up locally in Ithaca, NY. During the Leonids meteor shower in November of 1999, CASI was transported to Los Alamos, NM, to support the lidar campaign run from the Starfire Optical Range on Kirtland Air Force Base (see Figure 2.10). The next stop for CASI was the Jicamarca radar site in Colan-Piura, Peru, in December 2000. In 2001, CASI's name was changed to CARI (Cornell *A*ll-sky *R*oving *I*mager) as a new all-sky imager brought on board from Los Alamos National Laboratory assumed the name CASI . From September 2001 through June 2002,

(a)

(b)

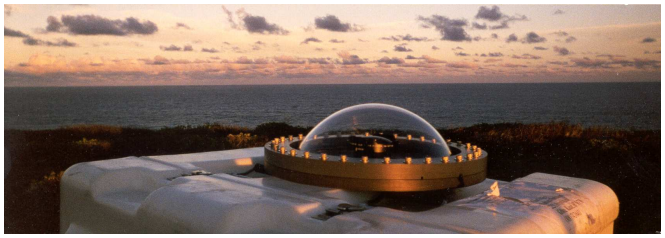

(c)

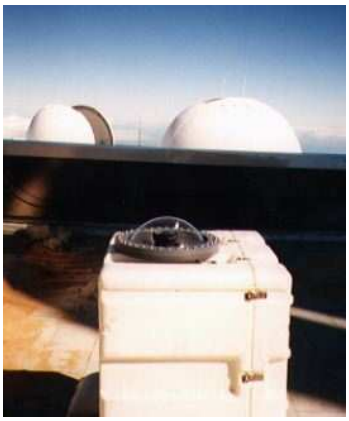

(d)

Figure 2.9: Panel (a)-(c) show CASI (now CARI) "roving" Kauai in a pickup truck to escape clouds and light contamination. Data was collected from behind a stable at the coast, on a golf course, at a tourist lookout in Waimea Canyon, and in a sugar cane field. Panel (d) shows CASI (now CARI) on the roof of the AEOS building at the MSSC.

Figure 2.10: Starfire Optical Range at Kirtland Air Force Base in Albuquerque, NM.

Figure 2.11: Mike Nicolls working on CARI in Greece. CARI was fielded to the islands of Crete and Milos.

CARI resided downunder at the RAAF Base Tindal, N.R., in Australia. Upon return to NY, the system was immediately checked out, repackaged, and shipped to the University of Crete, for deployment in the summer of 2002 to the islands of Crete and Milos in Greece (see Figure 2.11). In 2003, some design changes were incorporated into the portable mounting structure, using the now defunct

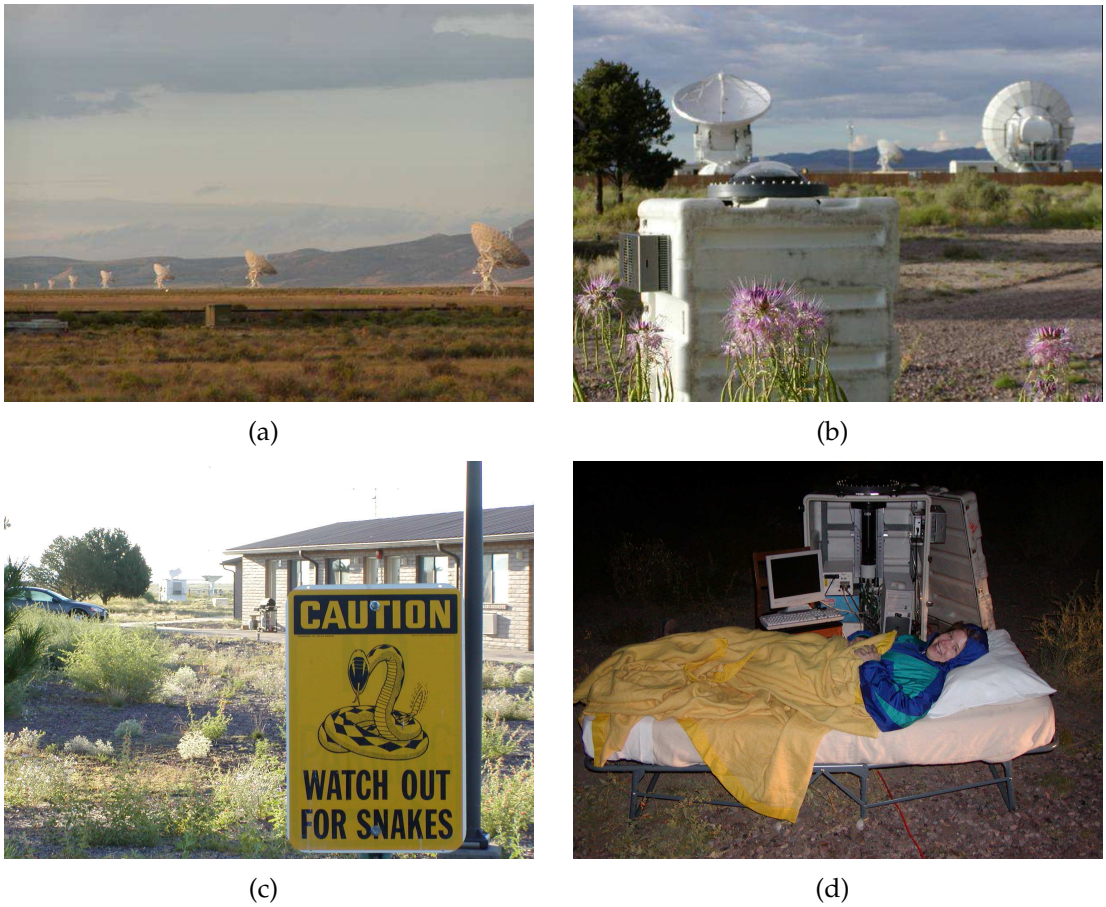

(a) (b)

(c) (d)

Figure 2.12: Panel (a) shows one of the three arms of the VLA. Panel (b) shows CARI with three prototype radar in the immediate background and the VLA radar in the distance. Panel (c) shows the on-site housing for visiting scientists. Panel (d) shows Pamela manning the operation of CARI overnight for a special NRL campaign.

machine shop in Rhodes Hall. From June 2003 through August 2003, CARI made a pit stop in Washington, DC, for radiometric calibration at the Naval Research Laboratory (NRL). Upon completion of calibration procedures, CARI was shipped to the Very Large Array (VLA) operated by the National Radio Astronomy Observatory (NRAO) in Socorro, NM, in support of an NRL short-term campaign in late August 2003 (see Figure 2.12). CARI was shipped directly from the VLA in NM to the Michigan Aerospace Corporation in Ann Arbor, MI,

Figure 2.13: CARI is shown mounted on a semi-permanent structure in the SOFDI trailer in Andrew Gerrard's backyard located upstate in Oneida, NY.

for re-outfitting to allow it to be mounted in a specially-designed trailer housing a suite of instruments in support of SOFDI. The SOFDI trailer was transported to its field site in Oneida, NY, where it has remained deployed from late 2003 through today (see Figure 2.13). The SOFDI suite of instruments is slated for eventual deployment to Peru.

During the Leonids meteor shower of 1998, a second all-sky imager was added to the Cornell University group through a temporary loan from Los Alamos National Laboratory. During this campaign, the imager was known only as the LANL imager. It was fielded at a "remote" site set up in Las Placitas, NM, in support of the meteor campaign headquartered at the Starfire Optical Range on Kirtland Air Force Base in Albuquerque, NM. For this campaign, low-intensity video cameras, on loan from Clemson University, were positioned both in Las Placitas and at the SOR to complement the suite of instruments. The purpose of these cameras was to provide additional data for triangulating meteor positions. The remote site video camera with its special configuration is

(a) (b)

Figure 2.14: Panel (a) shows Pamela with one of the low-intensity video cameras employed during the 1998 Leonids Meteor Campaign. This camera was fielded on the roof at the "remote" site in Las Placitas, NM; another was positioned at the Starfire Optical Range at Kirtland Air Force Base in Albuquerque, NM. Panel (b) shows a closeup of the rigging used to determine the az-el alignment of the camera for tracking long-lived meteor trails.

shown in Figure 2.14. Later, in 2001, when the Maui-MALT campaign became a reality, LANL once again supplied the imager on a loan basis. Upon installation in the trailer on the roof of the MSSS at the MSSC in October 2001, the imager was christened "CASI", and the original CASI was renamed "CARI". At some point during this long-term campaign, the loan arrangement was dissolved, and CASI is now Cornell University property.

The last imager in the CU-WINS is a narrow-field imager assembled in 2001 to support the Maui-MALT campaign. This campaign has been the sole deployment for CNFI, the *C*ornell *N*arrow-*F*ield *I*mager.

On an operational note, when transporting an imager and its supporting

equipment to a foreign locale, an international customs document called a "Carnet" or "ATA Carnet" is highly recommended as part of the shipping arrangements to facilitate temporary importation of research equipment sans duties and taxes. The shipping carrier uses this document containing very detailed inventory and shipping information to process the equipment through customs both in the foreign country and upon return to the USA without payment of duties and taxes due to the temporary nature of the relocation. Note that the Carnet document is good for only one year; i.e., it can only be used if the equipment will be re-exported within the given 12 month period. Information about the Carnet document and application process is included in Appendix E as reference. A sample checklist for shipping an imager out of USA is provided:

- Air bill – like Fedex packing list with quantities included
- Envoice – like pack list, but with prices included
- Carnet – international passport for equipment providing ease through customs as described above
- Letter stating: "The above items are a temporary import in support of a scientific campaign. They are not for resale."
- Letter requesting "Application for waiver of security for given Carnet number". A sample letter is provided in Figure E.1 included in Appendix E.
- Shipment Weight – needed for Air bill and Carnet; requires that the shipping containers be palletized and weighed at the Phillips Hall shipping/receiving dock. Note that time must be allotted in the shipping schedule for this additional step.

The field deployment locations for all of the Cornell University imagers are shown in Figure 2.1. Table E.1 in Appendix E provides a summary of the campaigns supported. Tables D.1– D.3 in Appendix D provide an inventory list for each of the imagers.

2.2 Airglow Imagers

As demonstrated in each of these campaigns, imagers have proven to be useful assets to the suite of scientific diagnostic tools used to study the upper atmosphere. While irrefutably worthwhile as stand-alone instruments, or as part of an ensemble study, imagers are not entirely without drawbacks. As will be shown in Chapter 3, radiometric calibration, in and of itself, as well as the cross-calibration of imagers which it potentially allows, can be very difficult, sometimes limiting the usefulness of imager data to qualitative studies. Another disadvantage is that operation times are limited to avoid saturating and damaging the electronic components; hence, nightglow data-collection is restricted to whenever the sun and moon have set below the horizon. Overall, however, the benefits of fielding imagers more than outweigh these negatives.

One such benefit is the relatively low cost associated with imagers as compared to other ionospheric instruments such as radars, lidars, and satellite systems. Following the general trend identified with all electronic components, the increased quality and capacity of charge-coupled devices has increased dramatically in recent years, while the cost has summarily decreased. With charge-coupled devices at the heart of airglow imagers, this trend has spurred many researchers to incorporate these systems into their suites of instruments, and

allowed novice researchers to break into the field. Another major advantage is that the imagers with their support electronics are highly portable, and hence relocatable – conducive both to short-term and semi-permanent studies around the globe. Finally, while many instruments used to study the ionosphere permit only a single look-direction, imagers offer a real spatial context with their two-dimensional, wide field of view. This perspective is expanded to three dimensions when factoring in the altitude-range coverage allowed by taking data with multiple filters corresponding to multiple atmospheric airglow layers. This increased two- and three-dimensional spatial perspective, coupled with the temporal progression rendered by time-lapse imaging, is extremely favorable to studies of the dynamics of the region.

As noted in the previous section, the Cornell University Worldwide Imager Network System (CU-WINS) currently includes three airglow imagers. Each of these imagers was designed by Keo Consultants, formerly an independent company operating out of Brookline, MA, with Robert (Bob) Eather at the helm. Recently, Keo Consultants has been acquired by Keo Scientific Ltd., of Calgary, Canada. Founded in January 2004 by a group of science and engineering personnel from the University of Calgary, Keo Scientific Ltd. has experience with the design and use of specialized scientific optical instrumentation going back to the mid 1970s. Through a "spin off" agreement, Keo shares some personnel and lab space with the University of Calgary's Institute for Space Research, but Keo Scientific Ltd. is an autonomous and independent company. Dr. Eather's expertise remains available through his current role as Keo Scientific's Senior Consultant. Combined with the founders' expertise ranging from space and atmospheric research to electrical engineering to the deployment and maintenance of distributed imaging arrays, Keo Scientific Ltd. is now the principal

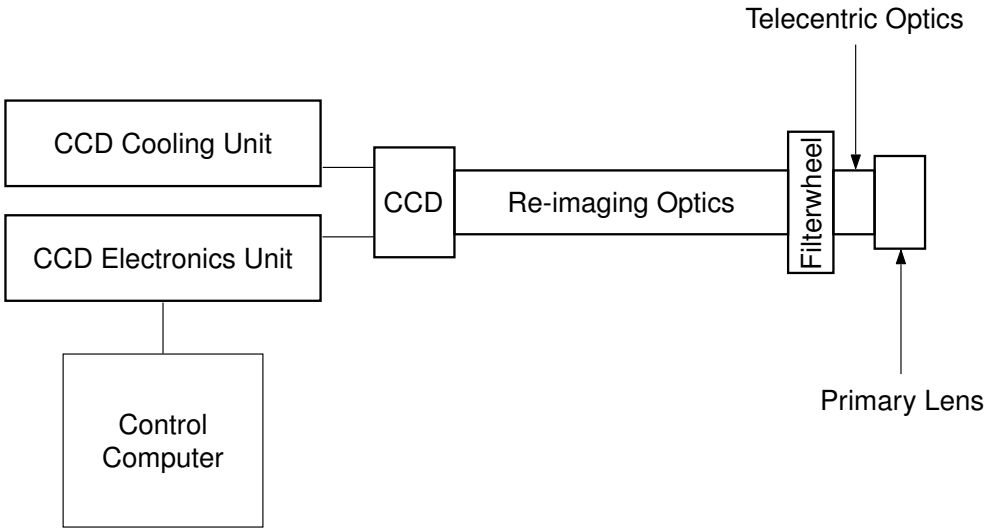

Figure 2.15: Block diagram of typical airglow imager components.

resource for in-depth instrument support for the overall imager systems. The component manufacturers (noted below) are also key technical resources.

Airglow imager designs fall into two major categories – collimating and telecentric – distinguished by the ray angles crossing the image plane, which in turn are governed by the lens selection within the optical train. Keo Consultants was for many years the primary supplier of telecentric lens systems to the ionospheric science community, including having manufactured all three of the imagers operated by Cornell University. Built from this core telecentric design, all three Cornell imagers share the same basic features, as illustrated in the block diagram of a typical airglow imager shown in Figure 2.15. The hardware configuration for each system is comprised of a scientific-grade, charge-coupled device (CCD) fronted by fast telecentric optics, a five-position filter wheel, and a primary optics lens which defines the field of view for that system. An electronics unit controls each camera, and a liquid circulation unit removes heat from the thermo-electrically cooled CCD chip. The entire system runs on a PC and is controlled by a Windows-based program that was developed at Cornell

University by graduate students. These basic hardware components are organized into four basic subsystems – optical system, CCD camera, control system, and mounting structure – described below, with differences between the three imagers highlighted where appropriate.

Detailed inventory lists for each of the imagers are provided in Tables D.1–D.3 in Appendix D. These reference lists include: part #, manufacturer #, model #, serial #, and - where known - P.O. #, contact and purchase date.

2.2.1 Optics System

The optical system is comprised of the objective, or primary, lens, the telecentric optics, the filter wheel, and the re-imaging optics. Each of these four components are described below.

2.2.1.1 Primary Lens

The primary, or objective, lens determines the field of view for the imager. Two of the Cornell imagers, CASI and CARI, are all-sky systems, each employing a Mamiya Sekor 24mm/F4.0 wide-angle (180°) fisheye lens to provide a horizon-to-horizon view of the sky. In reality, the field of view is limited to 150 – 160° as trees and buildings often obstruct approximately the first 10° above the horizon. Compared to these all-sky systems – the typical imager used for upper atmospheric studies – the newest addition to the Cornell imager group, CNFI, is a "narrow-field" system with a 47° field of view. Still considered quite a large field of view by the astronomy community, this so-called narrow field uses a

Mamiya 80mm/F1.9 lens. During normal operations, the primary lens on each of these imagers should always be focused at ∞ with the F-stop fully open. While the objective lens remains set at ∞, critical focusing of the overall system is controlled by a separate camera lens located just in front of the CCD; this function is discussed in the section to follow on re-imaging optics. Having the F-stop of the primary lens set to the fully open position is vital to allow as much light as possible into the system; a partially-closed F-stop, particularly given the very low intensity of airglow, will result in a darkened image.

2.2.1.2 Telecentric Optics

Telecentric optics are a critical design component permitting proper filtering of radiation incident on CCD cameras with low-light-level imaging capabilities. The goal these optics help achieve is collection of spatial atmospheric data represented by a monochromatic signal which can be related to specific physical excitation processes. Note that here "monochromatic" refers to the usually-preferred single wavelength of incident airglow light captured by the imager; in the context of atmospheric waves, some of the physical phenomena observed via images of integrated monochromatic airglow light are, themselves, nearly monochromatic wave features. Monochromatic airglow images are achieved by directing the incoming light through narrow-band interference filters. This effort would be thwarted, however, if the primary lens were used in *direct* conjunction with narrow-band filters. Part of the problem lies in the fact that the principal light rays exiting the primary lens are not parallel, and, further, normal camera lenses have large ray angles to the principal ray throughout their optical path. The basic design and construction of interference filters is such

that the wavelength of light transmitted through the filter depends extensively on the incident angle. The transmitted wavelengths shift with increased angle of incidence to the filter. This shift increases as the angle squared, resulting in larger ray angles rapidly requiring much wider-band filters. To combat this issue, telecentric optics are inserted into the system design to redirect the incident light so that the principal rays of all image-forming cones – across the entire field of view – cross the image plane parallel to the optical axis. With this design, the maximum ray angles through the filter are determined only by the F number of the lens. For our all-sky systems, that translates to 7.1° for the primary lens with F4.0.

The elements of the telecentric optics, inserted between the primary lens and the filter wheel, include two plano-convex lenses, selected and positioned to coordinate with the primary lens. This configuration of two plano-convex lenses was found to be optimal by the manufacturers, allowing reasonable surface curvature to enable the required focal length, reducing further spherical aberration, and refracting the principal rays of all image-forming cones parallel to the principal axis of the camera lens [*Eather*, 1993].

2.2.1.3 Filter Wheel

All three Cornell University imagers incorporate a five-position filter wheel, which can be cycled to allow for the study of up to four different layers of the atmosphere. Filters for four of the available filter-wheel positions are chosen to correspond to different chemical emissions that occur naturally in the Earth's ionosphere. Since chemiluminescent reactions emit radiation of specific wavelengths, and these correlate fairly well to specific altitudes, we choose various

narrow-band filters to isolate each wavelength, and hence, its corresponding altitude for study. To inspect mesospheric altitudes relevant to this dissertation, the two primary filters employed to isolate the corresponding range of airglow emissions were: a 589.0-nm wavelength narrow-band filter which captures sodium (Na) emissions peaking at 90 km; and a 557.7-nm narrow-band filter which captures greenline (OI) emissions at 96 km. Exposure times for both these narrow-band filters are 90 s – typical duration integration times for line-emission filters.

The fifth position in the filter wheel routinely houses a "background" filter with the same bandwidth as the narrow-band line filters, but centered at 541.0 nm, considered to be a "quiet" part of the airglow spectrum such that only the background airglow continuum is present. Background images are taken using the same exposure time as line-emission images, resulting in a comparable image, only without the desired airglow contribution. Pre-processed background images are subtracted from line-emission images as part of the overall data-processing procedure required prior to beginning scientific analysis of the image data. For broadband OH images, for which no comparable background filter exists, the recommendation is to subtract a value corresponding to the constant electronic bias [*Garcia*, 1999]. This bias level can be represented in a dark-current image taken in close temporal proximity, or estimated by observing intensity values near the edge of the OH image. Note that background images are typically collected with every cycle of the filter wheel, as they, as with the dark-current images, need to represent close temporal proximity conditions.

Each filter position within each of the Cornell imager filter wheels is designed to hold a 3" interference filter. Typically, the filters used in the Cornell im-

agers are narrow-band (short for "narrow bandpass") interference filters. "Narrow bandpass" describes the function of the filters, while "interference" refers to their construction. As the first term implies, narrow-band filters transmit a well-defined, narrow (~ 2 nm) band of wavelengths of optical radiation, while rejecting all other unwanted radiation. The filters, themselves, play such a crucial role in the overall functionality of the optical system and the integrity of the resultant data, that it is an extremely worthwhile exercise to examine - at length - some fundamental aspects pertaining to filter construction, design, performance, and care. A treatise on filters is provided in Appendix C to address these concerns which ultimately drive the requirements for filter calibration.

Most of the Cornell filters were manufactured prior to year 2000 by Barr Associates. Due to service and pricing issues encountered with this company in 1999, alternate suppliers were sought. As a result, the most recent purchases, in 2002, were made through Andover Corporation. Over the past five years within the entire industry, manufacturing procedures have changed, significantly driving up the costs of high-performance narrow-band interference filters.

The filter wheel is controlled by the computer system via an adjustable software interface which may be modified remotely allowing the filters to be rotated into alignment with the optics for any specified sequence of filters. While the filters are usually cycled per a standard routine, this discretionary sequencing feature, which allows more data collection to be concentrated at specific altitudes upon request, is very advantageous during short-term studies focused on a particular region. Such studies can occur, for example, during meteor showers or space shuttle missions. Altering the filter-cycle sequence to target specific emissions and layers benefits the study by providing more data with higher

temporal resolution in these regions of interest.

2.2.1.4 Re-imaging Optics

While telecentric optics resolve the issue of reducing the ray angles incident on the narrow-band filters, a further complication arises. A trade-off emerges as low-light-level imaging, required for airglow studies, requires operation at the lowest possible F numbers, which, in turn, drives higher ray angles through the filter, again requiring wider-band filters. To combat this issue, telecentric imaging systems make use of the fact that narrow-band (2.0 nm) filters are readily available with large diameters compared to the size of the CCD detector. Pairing the use of these "large" (3") filters together with re-imaging optics in the same system allows high F-number images from the primary lens to be re-imaged to low F-number images at the detector. It is the re-imaging optics – as the name attests – that take the telecentric image passing through the filter, having filled the entire filter area, and reduce it in size through the re-imaging process to fit onto the CCD detector. The re-imaging optics provide the means for monochromatic images of wide-angle fields to be fashioned onto detectors at low effective F numbers.

The re-imaging optics consist of two achromatic lenses situated inside the long tube structure connecting the filter wheel to the CCD camera lens. The achromatic field lens is located near the filter wheel; the achromatic close-up lens is found near the camera lens.

2.2.2 CCD Camera

The charge-coupled device, or CCD, is the heart of today's electronic imaging systems, and is the imager of choice for use in quantitative acquisition systems such as airglow imagers. Each CCD camera in the Cornell suite is composed, at a minimum, of a CCD camera head and a liquid cooling system. The camera electronics units will be discussed forthcoming in Section 2.2.3.

2.2.2.1 Camera Head

Camera heads are composed of a sealed CCD enclosure housing the thermo-electrically (Peltier effect) cooled detector, a shutter assembly, and a lens. Based on the properties of silicon when exposed to electromagnetic radiation in the visible spectrum, CCD imagers are typically silicon devices with electronic charge produced by incident photons collected and stored in potential wells, until finally brought out to an output amplifier by charge transfer techniques. The charge first collects in the potential wells, accumulating when the shutter is open and the CCD imager is exposed to light over an extended period of time. The charge pattern which results from this charge accumulation, or integration, corresponds to the focused image. On occasion, charge from adjacent pixels or potential wells are combined during the readout process. This technique, called *binning*, improves the signal-to-noise ratio and extends the dynamic range of the CCD imager, but at the expense of spatial resolution. For the Cornell imagers, pixels are binned on-chip by a factor of 2, producing 512×512 images from the 1024×1024 CCD. As discussed in Section 2.3 to follow, the sensitivity of the CCD to light is determined by the system noise level and quantum efficiency. *Quantum efficiency* measures the efficiency of the CCD sensor in generating electronic

charge from incident photons through the production of electron-hole pairs in the region from 400 to 1100 nm. Within the visible spectrum, this conversion factor from photon to electron varies as a function of wavelength, and, for a given wavelength, is intrinsically linear for scientific grade CCDs such as these. This linearity is illustrated in Chapter 3 in the determination of the G-factor for intensity calibration. In general, in comparison to commercial-grade CCDs, the scientific-grade CCDs have fewer defects, image with better resolution, and have low noise so they can detect weak signals. Additional features included to improve the performance of the CCDs are: (1) multi-pinned phasing (MPP) allowing the CCD to collect fewer dark current electrons per pixel per second, translating to lower noise per integration, and (2) Metachrome II coating – a proprietary, permanent coating which extends the sensitivity of the CCD to below 200 nm.

As denoted in Tables D.1– D.3, the camera equipment varies among the Cornell imagers. Both CARI and CNFI incorporate CCDs manufactured by Photometrics, Ltd. – CARI employs a CH250 model CCD, while CNFI utilizes a series 300 CCD (CH350/L). CASI operates with an older model Princeton Instruments CCD (TEA/CCD-1024TKB/1). A few years back, Photometrics, Ltd. became Roper Scientific, and, in fact, Roper Scientific now provides technical support for all three camera systems, though some technical documentation still carries the Photometrics, Ltd. name.

Each CCD camera head has a lens associated with it to focus the re-imaged telecentric image onto the CCD. Connected to CARI is a Canon 50mm/F1.2 lens; a similar lens is utilized in CASI. The camera head in CNFI uses a Canon 85mm/F1.2 lens. For each camera, this is the lens used to focus the system,

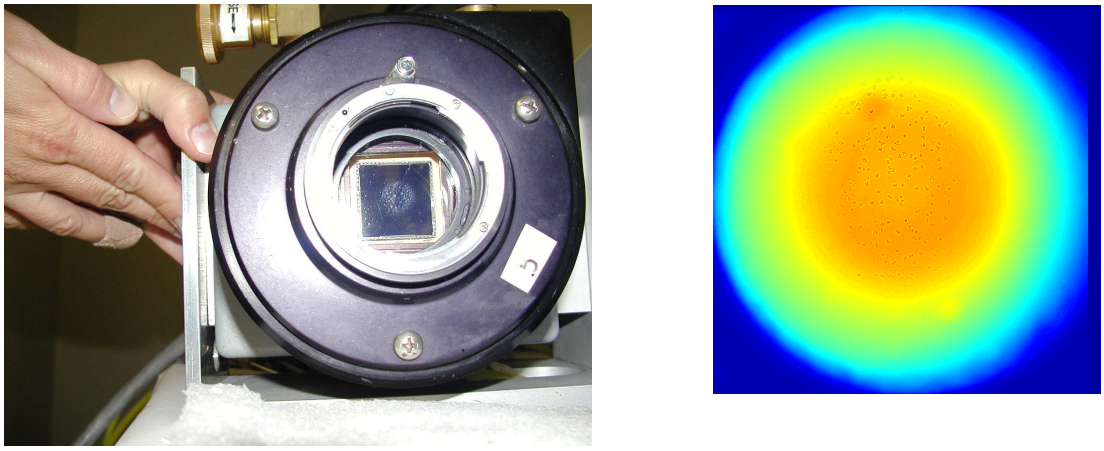

(a) (b)

Figure 2.16: Panel (a) shows ice crystal contamination inside CASI's vacuum chamber. The photograph was taken with the shutter open to reveal the inside of the chamber. Panel (b) shows the spots which can result on images when contamination is present within the sealed chamber. This image of a calibration light source was exposed using the 5577-nm filter.

beginning with the F-stop completely open, and backing down from that position as required. Focusing a system employing a variety of filters is tricky business as each filter has a slightly different focal length. While it is impossible to achieve perfect focus for all of the filters, a suitable compromise is usually attainable if one concentrates on the narrow-band filter with a center wavelength in the middle of the collective set of filters. Avoid using a broad-band filter (e.g. OH) to focus the system. Quite often if the broad-band filter is in focus, the narrow-band filters may be entirely out of focus.

The vacuum seal surrounding the camera head is a critical component. If the vacuum chamber becomes compromised allowing moisture to penetrate the seal, ice crystals can form on the CCD or on the pane behind the shutter as shown in panel (a) of Figure 2.16. This contamination can translate to temporary or permanent spots appearing on the images, as shown in panel (b) of

Figure 2.16, resulting in tainted data. The vacuum chambers can be flushed to remedy the situation; the manufacturers' documentation recommends periodic servicing to maintain the integrity of the system.

2.2.2.2 Liquid Cooling Unit

Each of the three cameras has been thermo-electrically cooled with additional cooling provided by a liquid cooling system, called an LCU, or liquid circulation unit. The liquid circulation functions as a heat exchanger drawing heat away from the thermo-electric (Peltier effect) cooler, allowing operating temperatures close to -40° C at the CCD, thus resulting in significant reductions in noise levels. Although the three liquid circulation units are all different models made by different manufacturers, as described in Tables D.1– D.3, the basic design and operation are the same. The LCU connects to ports on the camera head via flexible hoses used to circulate a coolant mixture of 50% ethylene glycol (antifreeze[3]) and 50% distilled water. The coolant reservoir should never drain below half full; to avoid this, the reservoir should be checked periodically (every 3 months) to see if coolant needs to be added. For proper operation, the LCU should be run in the upright position in order to keep the pump primed. Special care should be taken when connecting and disconnecting the hoses to avoid spilling coolant into the camera. Most importantly, the LCU must always be connected to the camera head and operating properly *prior* to turning on the camera. The ***camera*** should be the ***last*** item powered ***on*** after the power-up sequence of all supporting equipment; and likewise, when powering down the system, the ***camera*** should be the ***first*** item powered ***off***. Note that the CCD

[3]Note that at sites, e.g. the MSSC, where hazardous material control procedures are in place, the specific approved antifreeze must be determined and obtained. Check the MSDS (Material Safety Data Sheet) on record, and consult the local safety officer before purchase.

camera has been replaced with one that does not need liquid cooling in CARI, the imager unit slated to go to Peru.

2.2.3 Control System

The overall control system for each camera includes the camera electronics unit, the interface hardware, and the host computer system.

2.2.3.1 Camera Electronics Unit

The electronics control unit controls the CCD and serves as an interface between the control computer and the CCD head. Known as the camera electronics unit, or CEU, this hardware contains signal processing, camera control, and temperature control systems. It produces CCD clocking signals for the camera head and manages the transfer of raw data to the host interface hardware. The analog processor card within the CEU governs the tradeoff between speed and dynamic range.

The CEU for CASI is unique; the Princeton Instruments ST-138S CEU contains an additional adjustment knob for setting the CCD-head operating temperature. Care should be taken not to disturb this knob as it will disrupt the cooling process and can result in over-saturated images if the CCD operates outside the limits of acceptable temperature specifications. The "Princeton Instruments TE/CCD Detector" Manual, Version 1.H, published as Roper Scientific document 4411-0012 [*Roper-Scientific*, 1999], provides valuable operating and trouble-shooting information, particularly in Chapters 2, 3, and Appendix

C. Although Appendix C of the *Roper-Scientific* [1999] document refers to the MTE/CCD detector (a modified version of CASI's CCD), the cooling power control section related to overdriving the cooler is applicable. That is, if a temperature lock cannot be achieved in a reasonable amount of time (~ 10 minutes), set the temperature control knob to a warmer setting until a lock is obtained, then proceed to reduce the temperature setting in 1°C increments every few minutes, continuing in this step-wise manner until the target temperature is attained. At the end of Chapter 2 in the *Roper-Scientific* [1999] manual, another seemingly misplaced, yet important reference is found. This note states that if the CCD is cooled to low temperatures (< -50°C), exposure to ambient light will oversaturate the detector. As a result, dark current may increase significantly. If the detector remains saturated after all light sources are removed, bring the detector back to room temperature to restore dark charge to its original level, then attempt to set the cooling lock again.

2.2.3.2 Interface Hardware

The interface hardware consists of specially-designed cables and the host interface hardware. An AIA cable with a 68-pin, high-density, I/O connector with standard AIA format connects the CEU to the host interface hardware – a PCI card installed in the host computer. A camera head cable with DB37 connector at the CEU connects via another DB37 connector to the CH350/L camera head. These expensive, specialized cables come in to play particularly when the camera must be positioned some distance from the supporting electronics due to field-environment constraints. Lead time and funds must be allotted to obtain appropriate length cables. Additionally, a remote power switch produced

by Western Telematic, Inc. has been installed on each of the imager systems to allow hard-boot capability for the camera from a remote internet connection to the control computer. While the installation of the remote power switches is not overly complex, the operating control procedures and required key-stroke sequences are anything but intuitive. Given this, detailed information on this component – including product description, installation, installation verification check, and operating procedures – is included in Appendix B. Additional information can be found in the product user's guide [*Western-Telematic-Inc.*, 2000].

2.2.3.3 Control Computer

Cornell imager systems are all currently controlled by PCs running the Microsoft Windows 2000 operating system. The camera data acquisition software ("CDAS") which was developed and modified by previous graduate students [*Garcia*, 1999; *Makela*, 2003], provides a user-friendly graphical interface to acquire images and to schedule data runs; "Viewer" software provides some basic capability to analyze data. Secure Shell Client and VNC packages position the computer to be internet-ready for remote controlling of the camera – provided an internet connection is available.

2.2.4 Mounting Structure

All three Cornell imagers were originally designed as portable systems mounted in durable, modified research trunks for field deployment. However, differences do exist among the various field-box designs. Only CARI can be

Figure 2.17: Inside view of CARI's portable, self-contained, field research box housing the camera along with all the supporting electronic equipment.

deployed in a single self-contained unit. The supporting electronic equipment for CARI can be positioned under the camera entirely within the field box as shown in Figure 2.17. Note that although the field box contains a weighted metal mounting structure to prevent the box from tipping over, in high wind conditions it can still become necessary to tie down the entire structure. One should plan accordingly and have tie-downs on-hand.

Several design improvements have been made through the years – some small innovative adjustments, as well as some major changes. Black cloth has been added as "collars" around the various primary lenses to block reflected light from getting into the system. The collars can be attached using velcro, an improvised curtain rod, or merely tension from "stuffing" the material around. Note that tape alone will usually not suffice to hold the material in place for long deployments. To further reduce stray light, it is ***always*** necessary to cover ***all*** indicator lights on any of the equipment contained within whatever enclosure holds the imager. Black electrical tape is used for this purpose. The very reflec-

tive, slick white material that the research crates are constructed of is also found on the inside surfaces. This causes a great deal of light contamination. One recommendation to reduce this effect in the future is to coat the inside of the field boxes with black matte paint. One potential problem with implementing this fix is that there is question as to whether the paint would adhere to the box surface. What we found when researching this option was that some preparation lead time would be required as the internal surfaces would have to be "roughened" before applying any paint.

To combat moisture condensation within the box, coat-hangers have been used to affix a hairdryer operating on a cold setting, so that it aims at the inside of the dome. In the summer of 2003, we went to the next step and purchased a thermo-electric air conditioner with built-in condensate removal. The AHP-1200XE NEMA-4 model (P/N 0-3080-4-000) was purchased from ThermoElectric Cooling America Corporation (TECA). This through-mount unit is attached to one side of the field box as shown in Figure 2.18, and includes a drip pan and condensate wick with PVC tubing system for moisture removal. Device specifications can be found on the company's website: www.thermoelectric.com. To cool the interior even further, another recommended to minimize heat flux into box by segregating the electronic equipment via: (i) create a separate pull-out internal compartment with an exterior exhaust fan, or (ii) purchase separate research box.

In the summer of 2003, another design improvement was made to allow for easier and safer mounting of the camera into the field box. In the original CARI camera-mount design, the clearance was very tight when inserting the fisheye lens up through the cutout into the dome while lifting the heavy camera assem-

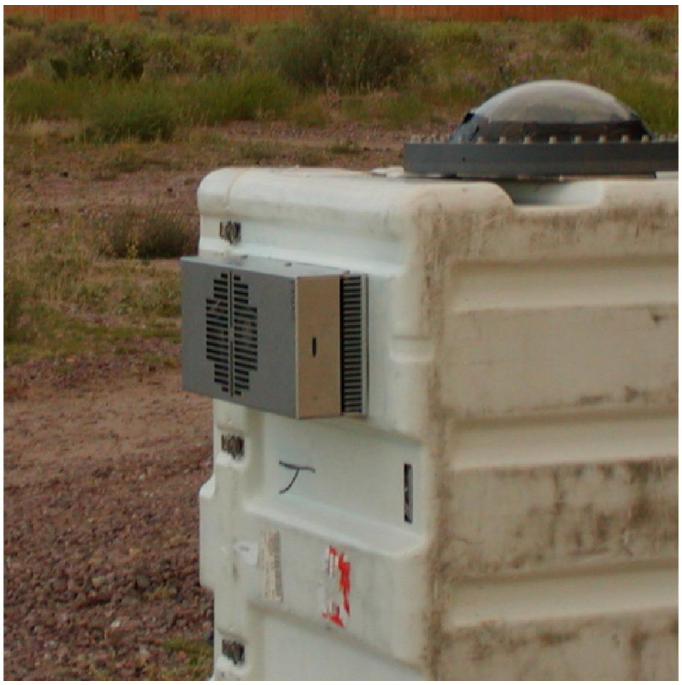

(a)

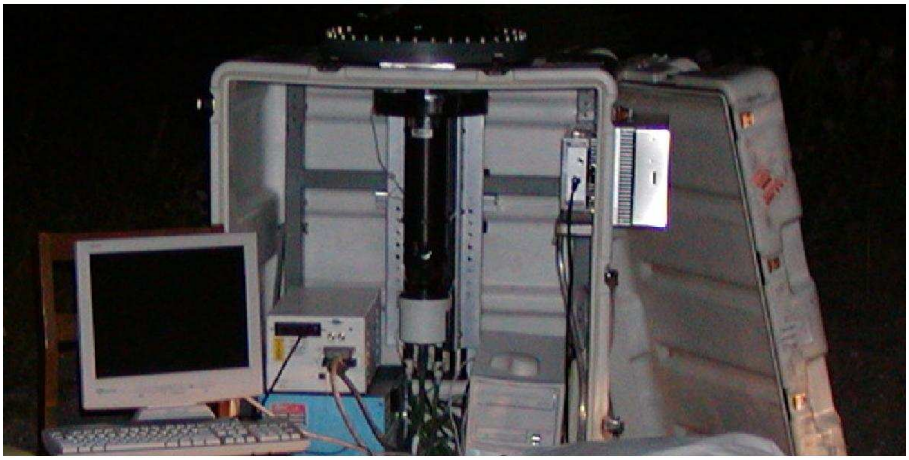

(b)

Figure 2.18: Panel (a) shows an outside view of the TECA a/c unit protruding from CARI's portable field box. Panel (b) highlights the through-mount design of TECA's AHP-1200XE NEMA-4 model visible on the right-hand side of CARI's portable field box.

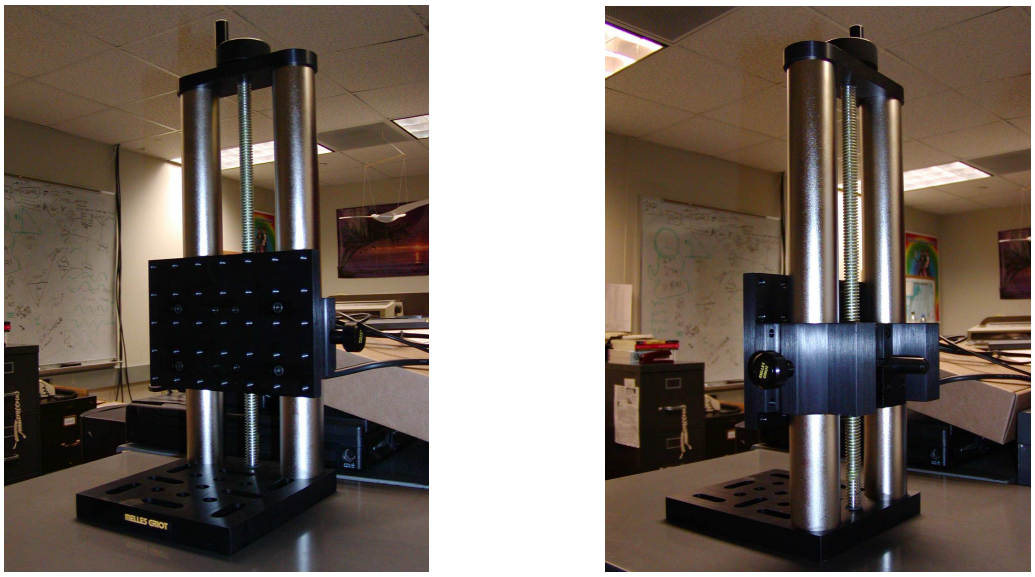

(a) (b)

Figure 2.19: Panels (a) and (b) show the dual-StableRod system manufactured by Melles Griot. This system was modified and installed in an upside down configuration inside CARI's portable field box to improve both the method of mounting the camera in the box and the means of raising and lowering the camera. It has since been further adapted to mount the camera inside the SOFDI trailer.

bly into place. Great care was required to avoid scratching the primary lens, particularly if doing this maneuver without the assistance of someone to help guide the equipment. Even then, this is still a difficult task due to space constraints with two people trying to reach up inside the box at the same time, since the dome should already be fastened in place and overhead access is no longer available. The modification made was to add a dual-StableRod system to the existing internal framework, so that the camera assembly could ***first*** be lifted into the box and fastened to the support structure, and ***then*** smoothly raised into position using a mechanical crank which controls the adjustable mounting platform running along optical rails. A dual-StableRod system with a vertical mounting plate (P/N 07 DPP 013/501) was purchased from Melles Griot for

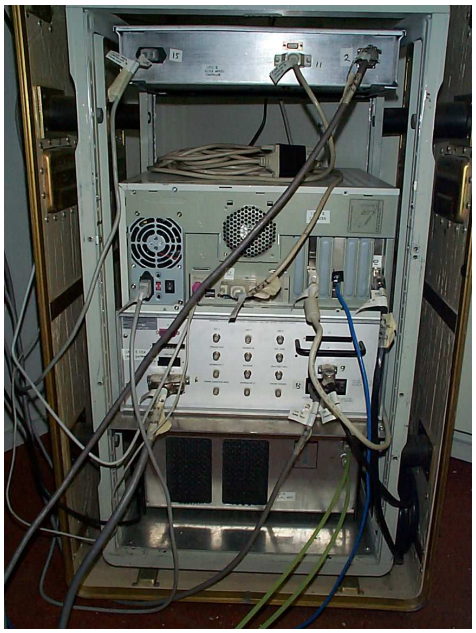

Figure 2.20: CASI's 2^{nd} portable research box housing the electronic support equipment affixed to a rack. This photo is from CASI's current, semi-permanent, field site at the MSSC where the box remains uncovered on an ongoing basis. CASI's 1^{rst} research box designed to hold the camera is stored downstairs in the MSSS while the camera is mounted in the LBD Trailer.

this redesign. Note that for our application, the dual-StableRod system (see Figure 2.19) was installed upside down from its advertised usage. Additional recommendations for future consideration to achieve easier access into the box, are either to modify the box such that the "top" (when positioned for data collection) can be lifted or hinged completely off and then sealed back in place with water-tight clamps, or to modify the dome attachment such that it is attached with quick-release water-tight clamps. The first scenario may have potential drawbacks to consider. The stress impact of cutting the research box to allow the top portion either to hinge or to lift off may affect the overall strength integrity of the box too much, especially during shipment.

CASI's portable configuration includes two of the large field boxes – one housing the imager and one housing the electronics arranged on an internal

(a) (b)

(c) (d)

Figure 2.21: Panels (a) and (b) show CNFI's temporary arrangement inside the cathouse at the Maui Space Surveillance Complex (MSSC). Panels (c) and (d) show the semi-permanent structure built inside the doghouse for CNFI for this long-term deployment as part of the Maui-MALT campaign.

equipment rack as shown in Figure 2.20. However, this imager has not been deployed in this "mobile" manner since the Leonid's meteor campaign of 1998, before Cornell University acquired it. CNFI, intended for horizontal viewing, was designed for field deployment within a smaller research box (shown in Figure 2.21 panels (a) and (b)) which is not large enough to contain all the supporting equipment. However, sometime after arrival at its first field site (MSSC), a

(a) (b)

Figure 2.22: Panel (a) shows the CASI imager mounted on the rail in the roof of the LBD trailer on the MSSS building at the MSSC. The pink bubble-wrap is to protect people from hitting their heads on the rail. Panel (b) shows the arrangement for the computer and electronic support equipment for CASI inside the LBD trailer.

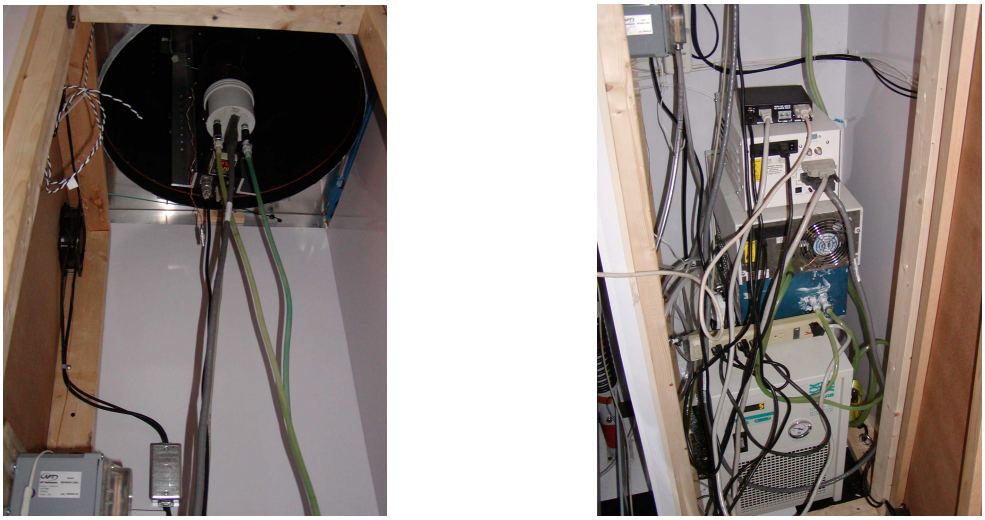

(a) (b)

Figure 2.23: Panel (a) shows the CARI imager mounted on the rail in the roof of the SOFDI trailer on Andrew Gerrard's property in Oneida, NY. Panel (b) shows the arrangement for the electronic support equipment for CARI inside the SOFDI trailer.

special apparatus was constructed to house the equipment within a fixed facility (see Figure 2.21 panels (c) and (d)). Likewise, CASI has been mounted in a semi-permanent structure at its current location for over the past five years (see Figure 2.22). Even CARI, the touted "roving" imager, has spent time out of its box – installed, rather, in a semi-permanent arrangement within a large trailer as part of the collaborative SOFDI campaign (see Figure 2.23). The bottom line is that, although each imager is designed to function in its own self-contained housing in a stand-alone fashion, the mounting structures may be modified as-needed to support specific field deployments.

2.3 Airglow Image Model

2.3.1 Target Airglow Signal

In research studies conducted using airglow imagers such as those described above, our aim is to specify, as accurately as possible, the amount of airglow for a specific wavelength(s) produced during an observed phenomenon. Physical production of airglow is discussed quantitatively in terms of volume emission rates in units of photons per cubic centimeter per sec, or $[ph/cm^3/s]$. However, volume emission rate is not a measurable quantity. Usually in radiometry and photometry, the quantity measured for an extended source, such as airglow, is the integrated intensity, also called *surface brightness*, expressed for airglow in units of photons per square centimeter per second per steradian, $[ph/cm^2/s/sr]$, rather than in units of energy, $[erg/cm^2/s/sr]$, as is typical.

Fortunately, the surface brightness is directly related to the integrated emis-

sion rate over an entire column along the observational line of site. Specifically, given the measurable monochromatic surface brightness, I_λ, in units of $[10^6 ph/cm^2/s/sr]$,

$$I_\lambda = \frac{1}{4\pi} \int_0^\infty \mathcal{F}_\lambda(z) dz \tag{2.1}$$

where z is the distance from the source to the observer, and $\mathcal{F}_\lambda(z)$ is the volume emission rate $[ph/cm^3/s]$ for a specific wavelength(s) in an arbitrary direction from the observer, then

$$4\pi I_\lambda = \int_0^\infty \mathcal{F}_\lambda(z) dz \tag{2.2}$$

is the emission rate integrated over the whole column along the line of site. To describe this emission rate, aeronomers back in the early 1900's coined their own term, the Rayleigh (R), naming it after the fourth Lord Rayleigh (R. J. Strutt), who made the first measurement of the absolute brightness of night airglow [*Chamberlain*, 1995], and whose father the third Lord Rayleigh is known for "Rayleigh Scattering". The *Rayleigh*, then, is defined as the emission rate in a column of unit cross-section oriented along the line of site. In deriving Eq.2.2 (see *Chamberlain* [1995] for details), two assumptions were made: (1) isotropic radiation, and (2) no subsequent backscatter or reabsorption of radiation back into the source. Given that these are not always justifiable assumptions, the literature often refers to the Rayleigh as the *apparent* emission rate. *Chamberlain* [1995] notes that the word "column" is generally included in the units to emphasize that the quantity is an integrated emission rate, not a flux.

$$1R = \ apparent\ emission\ rate\ of\ 10^6 photons/cm^2(column)/s \tag{2.3}$$

Simply put, the apparent emission rate in rayleighs is the measured brightness multiplied by a factor of $\frac{4\pi}{10^6}$; if the surface brightness is measured in units of $[10^6 ph/cm^2/s/sr]$, the conversion factor to rayleighs is merely 4π. Note that this

apparent emission rate, described by the observed photon flux, will generally be less than the emitted flux due to the inevitable attenuation of the photons through absorption and scattering – both of which were ignored through the second assumption above.

In reality, what we actually observe are the incident photons discerned as pixel counts, N, detected by the CCD. This quantity of counts is our measured value representing the observed surface brightness, I, of the source along with a host of unwanted signal contributions and distortions including, I_c, the background airglow continuum. Note that the total desired airglow surface brightness, I, is actually composed of a mean airglow signal, $\bar{I}$, and the airglow perturbation signal, δI. Given the adulterated state of the raw data in N, our goal becomes to isolate I, as best we can, for study. To achieve this, we must first identify the offending contaminations. In the next section, we investigate the various contributions which taint the target signal.

2.3.2 Airglow Signal Contamination

As mentioned above, within the raw count data collected by airglow imagers, the target signal is shrouded by contamination. This camouflage is produced both by external influences from nature, and by internal factors inherent in the equipment, itself, – inescapable byproducts, if you will, of the equipment design and operation. Contamination, with regard to the target signal, can include contributions from additional signal sources, as well as variations and distortions in the data. In some cases, actions can be taken to avoid the signal impurities, but in most cases, schemes must be developed to remove the undesired signal com-

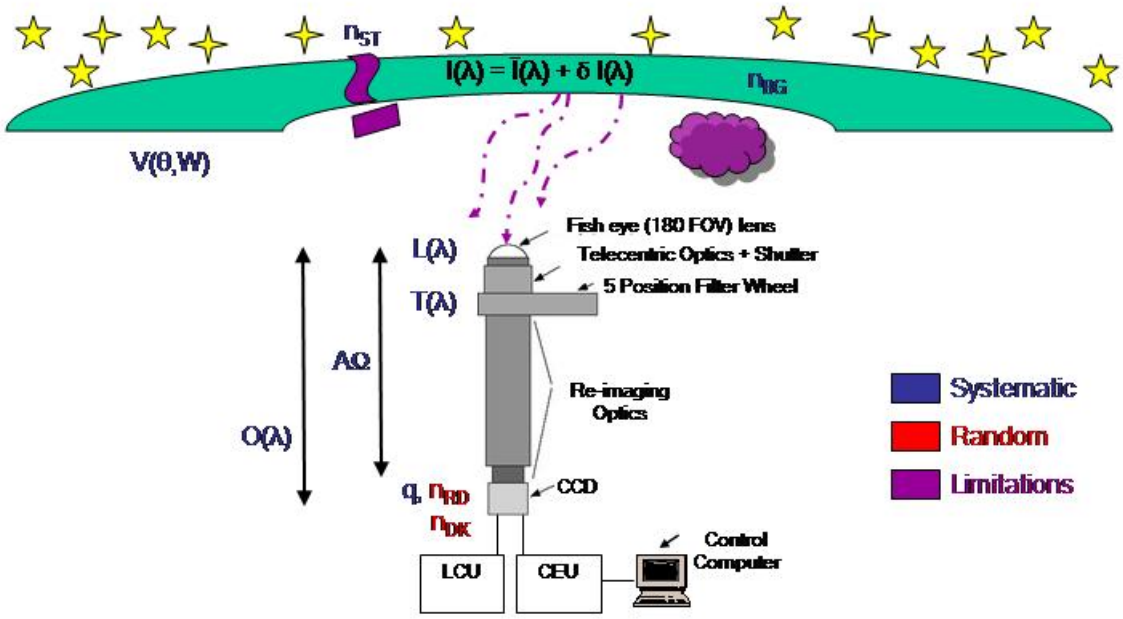

Figure 2.24: Schematic summarizing airglow signal contamination contributions both from the external influences of nature, as well as from the internal factors inherent in the equipment.

ponents. For our purposes, all of the various factors, illustrated in Figure 2.24, which contribute towards concealing the target signal can be considered as errors.

Errors affecting airglow brightness measurements can be classified into the following main categories:

- systematic or determinate
- random or indeterminate
- miscellaneous
  - dynamic
  - illegitimate
- limitations

Systematic errors impact the "accuracy" of the data, that is, the variation of the measured value from the truth. *Random* errors, on the other hand, affect the "precision" from measurement to measurement, that is, the repeatability of an experiment. *Dynamic* errors, as the name alludes, relate to the dynamic properties of the instrumentation. *Illegitimate* errors include mishaps with different units, computational glitches such as rounding off and double precision, et cetera.

2.3.2.1 Systematic Errors

Systematic errors stem both, externally, from the natural environment and, internally, from the research equipment. Externally, systematic errors originate from the stars, the "noisy" sky, and artifacts of the geometry of the viewing environment. Internally, they can manifest from a number of sources including the CCD, filters, as well as variations and distortions in the optical path intrinsic to the overall imager design. Each potential error is noted and described below.

Unwanted sky contributions come from stars, the continuum emission, and aerosol scattering. Stars – considered noise, n_{ST}, in airglow images – are prominent features with respect to the low intensity airglow emissions, and, therefore, are easily identified and removed. Star-removal routines are now standard features in the airglow data-processing software. The collective effects, n_{BG}, from both the continuum emission, I_c, and aerosol scattering are identified by imaging a quiet part of the airglow spectrum to discern the ambient background conditions. As stated earlier in Section 2.2.1.3, we cycle a "background" filter centered at 541.0 nm, as part of routine operations, for this purpose. Like the line-emission filters, the background filter has a narrow bandwidth and is oper-

ated at long exposure times, thus resulting in background images comparable to line-emission images, but without the targeted airglow contribution. These background images can then be used in conjunction with data processing procedures to help isolate the targeted airglow data by removing the background effects from the line-emission images.

The CCD quantum efficiency, q, is the measure of the effectiveness of an imager to produce electronic charge from incident photons. This process is based on the material properties of silicon - the basic component of the CCD - interacting with light. Light normally enters a CCD through parallel register gates, as is the case in the usual front-illuminated CCDs. This design has an inherent drawback at short wavelengths, however, as these gates, comprised of very thin polysilicon, exhibit transparency properties associated with this material. While reasonably transparent at long wavelengths, polysilicon becomes opaque at shorter wavelengths ($< 400\,nm$); that is, at short wavelengths the gate structure attenuates incoming light. To combat this inherent design disadvantage, acid-etching techniques can be used to thin CCDs uniformly such that an image can be focused on the backside of the parallel register where no gate structure exists. These thinned, or backside-illuminated, CCDs exhibit high sensitivity to photons ranging from the soft xray to the near-infrared regions of the spectrum [*Photometrics*, 1998]. Data integrity can be affected if the CCD quantum efficiency varies over time; if moisture condenses on the chip either due to a high-humidity field environment or due to a vacuum loss in the CCD chamber; if flaws such as hot pixels develop on the CCD; or if structures such as dust, bugs, et cetera are found within the instrument. To avoid data degradation, proactive actions can be taken such as fielding equipment in dry climates, installing a cold-blowing hairdryer to alleviate condensation, protecting vacuum seals, pe-

riodically cleaning the system, and housing equipment in bug-infestation-proof buildings. Apart from efforts to minimize the impacts, each of these effects discernable on the detector is best addressed by periodic brightness calibrations and routine flat-fielding, which are described in Chapter 3.

Interference filters used to isolate specific wavelengths of airglow can impact the airglow data in a number of ways through their transmission characteristics, $T(\lambda)$. Some inherent spatial variation in the filter transmission is expected as a result of the filter manufacturing process itself. The filter design specifies operating temperature and angle of incidence, so temperature variations and tilting can affect the specified transmission characteristics. Filters can wear out over time degrading their transmission properties. As with CCD errors described above, filter transmission error effects can be mitigated by periodic brightness calibrations and flat-fielding techniques. As additional notes on filter transmission, it is important to remember the following: for broadband filters, contributions may arise from other wavelengths; for narrowband filters, off-axis ray angles can easily fall outside the passband, reducing the light throughput as a result. As discussed in Appendix C, for telecentric imager systems, even though the principal ray of all image-forming cones, across the entire field of view, all intersect the image plane (and the filter) parallel to the optical path, we must still accommodate the maximum ray angles for each cone as governed by the F number of the lens. In collimating systems – used by some in the scientific community as an alternative to systems designed with telecentric optics – the problem worsens as, by design, every part of the filter receives light waves impacting the lens from all angles of incidence, including high angles of incidence (i.e., at low angles to the horizon). Light striking the filter at varying angles of incidence in either system type affects the light propagation characteristics

through the material layers of the filter, resulting in an overall shift of the spectral characteristics of the incident light to shorter wavelengths; the upshot of this pervasive blue shift when coupled with the passband constraints of narrowband filters is a potential reduction of transmission of light from a given spectral line for rays more than $\sim 5^\circ$ [*Baumgardner*, personal communication] from filter normal. In telecentric systems, it is important to know the exact transmission characteristics of the filter as a function of wavelength. For collimating systems, it is important to carry this further by having a clear spatial perspective of the transmission characteristics of the filter, as all parts of the image use all parts of the filter – contrary to telecentric systems which have a one-to-one mapping between the location of a point on an image and the corresponding point for small regions on the filter. In either case, periodic characterization of the filters will reveal the current conditions and allow for corrective methods.

Vignetting is an innate property of optical systems, such as airglow imagers, whereby illumination decreases away from the optical axis of the total system, that is, near the edge of the field of view. The vignetting function, $L(\lambda)$, can be determined for a particular imager system during laboratory calibration procedures as described in Chapter 3, and is defined for the entire length of the optical path from the objective lens through to the detector. Effects of the optical vignetting function can be removed from airglow images by dividing by a vignetting correction array.

Conversely to optical vignetting which results in an inherent reduction in light throughput at the edge of the field of view, the van Rhijn effect, $V(\theta, H)$, results in brightening at the edge of the field of view. The van Rhijn effect is an artifact of the 2-D limitations of the imagers. Masking height, the column-

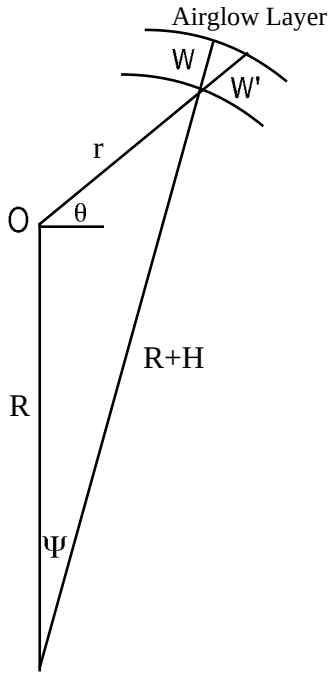

Figure 2.25: Schematic of the van Rhijn effect illustrating the increased path length through the airglow layer for off-zenith viewing.

integrated emissions vary with elevation angle due to the inherent geometry as illustrated in Figure 2.25. The van Rhijn effect, then, is the line-of-sight enhancement of the airglow signal resulting from an increase in the optical path length through the emission layer when viewed at increasing angles from zenith. As shown in Figure 2.26, the plot of relative brightness as a function of distance along the airglow layer portrays an increase in airglow brightness of almost six times that at zenith [*Garcia*, 1999]. Correcting for this external effect of brightening at the horizon has been implemented by two methods: (1) incorporating the effects in with off-setting errors addressed via a flat-fielding scheme, then removing their effects through image processing algorithms, or (2) assuming a uniform emission layer and geometrically calculating brightness at a given elevation based on brightness overhead at zenith.

Given the large fields of view common in today's airglow imaging systems

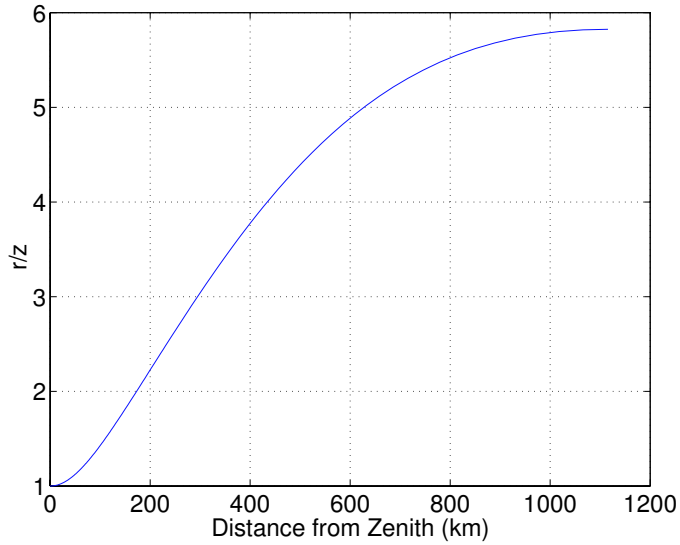

Figure 2.26: Plot of relative brightness as a function of distance along the airglow layer. The dependence is due to the van Rhijn effect.

often used to study large-scale phenomena, and given the necessity to place the observed phenomena in a meaningful physical context, accurate spatial information is required. The actual physical alignment and orientation of any airglow system varies each time it is deployed to the field. Furthermore, some camera characteristics, such as the vertical and horizontal scales, can drift over time [*Oznovich et al.*, 1994], or change if the system is jarred. Additionally, standard spectral analysis techniques require uniform sampling of data. However, due to effects of the wide-angle lenses, airglow imaging systems (all-sky systems, in particular) project the curved surface of the field of view of the sky onto the planar CCD with one of five projection systems. The all-sky lenses in use by Cornell University imagers incorporate the equidistant projection scheme which is preferred for measurements of zenith and azimuth angles because of the linear relationship whereby each pixel subtends an equal angle of the sky. In employing one of the projections schemes, distortions in the data are introduced, clearly evident at low elevations, that is, near the horizon. Large scale

wave patterns, such as bores, illustrate this problem with all-sky optics. Linear wave patterns appear curved and compressed at low elevations. To correct for these geographical and lens-induced spatial variations, all-sky images depicted by $\mathcal{N}^{(i,j)}$ are converted from the original image coordinate system with arbitrary orientation to the uniformly-spaced geographic coordinate system represented by latitude and longitude.

2.3.2.2 Random Errors

We think of random, or indeterminate, errors as the true noise in a system. Airglow imaging systems, like all electronic circuitry, generate undesirable noise. The primary sources of noise in a CCD camera include photon noise (or photonic or photon-shot noise), read noise (or pre-amplifier noise), thermal noise (or dark noise), and quantization noise.

Photon noise, $\sqrt{I(\lambda)}$, refers to the inherent natural variation in the radiant energy flux, or photon flux, incident on the imager, specifically the CCD. This noise contribution is a fundamental property of the quantum nature of light. Photons incident on the CCD convert to photoelectrons via the photoelectric effect within the silicon layer of the detector. These photoelectrons comprise the signal, but also include a statistical variation of fluctuations collected by the CCD. This unavoidable statistical variation is known as photon noise, and is the bottom-line uncertainty in the data. As such, it is customarily excluded from typical equations describing theoretical airglow models. Exhibiting a Poisson distribution, photon noise is dependent on the strength of the signal and can be described in terms of the square root of the signal. As photon noise is not additive, a large signal, large integration times, and/or high CCD sensitivity

can all reduce its effect.

In contrast to photon noise, read noise, n_{RD}, or pre-amplifier noise, is not dependent on the strength of the signal, but rather is generated by the on-chip output amplifier and is related to read-out rates. Read noise refers to the uncertainty introduced when the signal is quantified on the detector, and is typically on the order of 3 e^- rms [*Baumgardner*, personal communication]. Whereas photon noise is governed by the Poisson distribution, read noise is described by the Gaussian distribution. Using a small number of co-adds during data acquisition is recommended to reduce read noise [*Pallamraju*, 2003].

Within the field-of-view portion of airglow images, thermal noise, n_{DK}, is indistinguishable from signal photoelectrons, resulting in the contamination of the airglow signal. Outside the data field of view, thermal noise appears as specs on the image. This thermal or dark noise arises from the Poisson statistical variation of thermally generated electrons within the CCD silicon layers. The production rate of the thermal electrons, defined as the dark current, increases exponentially with temperature. When the detector is not cooled properly to the specified ranges, these increasing thermal electrons fill the wells of the CCD even before the signal is received thus resulting in the reduction of the dynamic range of the detector.

Quantization noise is caused by roundoff errors in the analog-to-digital converter when converting the amplitude of the electronic signal into a binary representation. General practice assumes this contribution to be insignificant and as a result ignores it.

2.3.2.3 Miscellaneous Errors

In addition to determinate and indeterminate errors, there always exists the possibility of miscellaneous errors relating to dynamic properties of the instruments (e.g., setting time, et cetera) or human error (e.g., blunders, different units, computational glitches, et cetera).

2.3.2.4 Limitations

Some limitations are inherent in the study of optical emission measurements. Environmental situations over which we have little or no control include sky transmission, clouds, moonlight, emission height variation, and lack of vertical resolution. Intrinsic to fielding ground-based instruments to observe upper-atmospheric phenomena is the issue that the emissions of interest must propagate through the lower atmosphere to be detected by our imagers. This path can be obstructed by tropospheric scattering and general transmission properties of the sky if thin clouds, haze, fog, mist, dust, or the like are present. The presence of anthropogenic lights magnifies these ill effects. Compounding these issues is the fact that, given that we are viewing over wide fields of view, conditions can vary from one part of the sky to another. Operating airglow imagers from high altitudes, above much of the lower atmosphere, in dry locales can mitigate the impact of these conditions. In addition, observing stars of known brightness provides a comparative standard which can be important for spatial calibration. For the 630.0-nm line, another limitation, emission height variation, can occur with vertical movement of the F-layer. As the F-layer moves down or up, more or less emissions are produced. Lastly, the lack of any layer height information is a real limiting factor inherent in two-dimensional airglow imag-

ing. However, in the F-region when both 630.0-nm and 777.4-nm emissions are measurable, the height can be determined [*Makela et al.*, 2001]. As stated earlier in the discussion on the van Rhijn effect, the line-of-site nature of the 2-D image representation of the 3-D physical geometry restricts the information which can be realized. Column-integrated emissions preclude any knowledge of the vertical structures. The impact of both of the last two limitations can be lessened by expanding the available instrument suite to include equipment such as digisondes, lidars, et cetera, as well as models, to provide complementary measurements allowing the derivation of accurate physical parameters.

2.3.3 Airglow Model Equations

To combine comprehensively all of the contributing effects described above in Section 2.3.2, the designated factors are multiplied or added to the target airglow signal, $I(\lambda)$, as appropriate. We represent the theoretical image of raw airglow field-data for line-emission λ_0 as an array of pixel intensity counts in the form:

$$\mathcal{N}^{(i,j)} = t \cdot \left[\int_{\lambda_0} T(\lambda)\, L(\lambda)\, O(\lambda)\, [V(\theta, W) \cdot I(\lambda) + n_{BG} + n_{ST}] \frac{10^6}{4\pi} A\Omega\, q\, d\lambda + n_{DK} \right] + n_{RD} \tag{2.4}$$

where the variables with respective units and definitions are tabulated as follows:

$\mathcal{N}$	$[counts]$	image data array for emission wavelength(s)
(i, j)		indices into this data array, $\mathcal{N}$, of measured counts
t	$[s]$	exposure time

$V_{\theta,W}$	dimensionless	elevation and height-dependent van Rhijn effect
L_λ	dimensionless	λ-dependent lens-vignetting function
O_λ	dimensionless	λ-dependent flat-fielding function
I_λ	$[R/nm]$	λ-dependent source signal strength
n_{BG}	$[R/nm]$	λ-dependent surface brightness of the continuum emission, I_c, combined with aerosol scattering effects
n_{ST}	$[R/nm]$	λ-dependent surface brightness of the stars
$10^6/4\pi$	$[ph/cm^2/s/sr/R]$	factor to convert from $[R]$ to $[ph/cm^2/s/sr]$
$A\Omega$	$[cm^2 sr]$	system throughput (or Etendue) of the imager
T_λ	dimensionless	λ-dependent optical transmittance of the filter
q	$[count/ph]$	detector quantum efficiency incorporating gain
n_{DK}	$[counts/s]$	dark current signal contribution
n_{RD}	$[counts]$	read noise contribution.

Based on our assumption that the line emission signal is superposed on the continuum emission signal, we can break the integral into the sum of two integrals and distribute the t, to get:

$$\begin{aligned} \mathcal{N}^{(i,j)} &= t \cdot \int_{\lambda_0} T(\lambda)\, L(\lambda)\, O(\lambda)\, [V(\theta, W) \cdot I(\lambda)] \frac{10^6}{4\pi} A\Omega\, q\, d\lambda + \\ & \quad t \cdot \int_{\lambda_0} T(\lambda)\, L(\lambda)\, O(\lambda)\, [n_{BG} + n_{ST}] \frac{10^6}{4\pi} A\Omega\, q\, d\lambda + (t \cdot n_{DK}) + n_{RD}. \end{aligned} \tag{2.5}$$

This separation of integrals rearranges Eq. 2.4 into four overall additive terms – each conveniently representing a conceptual component of the signal and noise contained in the raw-data image. We consider the "signal", S, to originate from the targeted source, represented in this case by $I(\lambda)$ in the first term of Eq. 2.5, such that:

$$S = S^{(i,j)} = t \cdot \int_{\lambda_0} T(\lambda)\, L(\lambda)\, O(\lambda)\, [V(\theta, W) \cdot I(\lambda)] \frac{10^6}{4\pi} A\Omega\, q\, d\lambda. \tag{2.6}$$

Similarly, we let:

$$N_{BG} = B^{(i,j)} = t \cdot \int_{\lambda_0} T(\lambda)\, L(\lambda)\, O(\lambda)\, [I_c + n_{ST}] \frac{10^6}{4\pi} A\Omega\, q\, d\lambda \tag{2.7}$$

represent the "sky noise", including contributions from both the continuum emission and stars. We further define the "dark current noise", D, more accurately called the "dark signal", as:

$$N_{DK} = D^{(i,j)} = t \cdot n_{DK}, \tag{2.8}$$

where n_{DK} is the dark current rate. Finally, the "read noise", R, is defined as:

$$N_{RD} = R^{(i,j)} = n_{RD}. \tag{2.9}$$

Substituting these terms into Eq. 2.4, we dramatically reduce the notation to:

$$\mathcal{N}^{(i,j)} = S^{(i,j)} + B^{(i,j)} + D^{(i,j)} + R^{(i,j)}. \tag{2.10}$$

Dropping the indexing notation, which is quite cumbersome to carry throughout despite that it clarifies that each term is an indexed array of measured values, we attain the succinct forms:

$$\mathcal{N} = S + B + D + R, \tag{2.11}$$

or

$$\mathcal{N} = S + N_{BG} + N_{DK} + N_{RD}, \tag{2.12}$$

which neatly convey that the image data is composed of the target signal combined with noise contributions from background sky elements, dark current, and digital readout effects. To isolate our target signal – disguised within S and further imbedded in $\mathcal{N}$ – we must first eliminate the various noise contributions. To enable us to peel off the layers of noise during data analysis, we take additional images to monitor the noise effects. It should be noted, however, that B (or N_{BG}) above – the background noise contribution to the raw-data image for line-emission λ_0 – is NOT explicitly the same as the "background image", $\mathcal{B}$, which is introduced next.

As stated previously in Section 2.2.1.3, background images are collected routinely throughout an overnight data-run to record the continuum emission. Typically, the background filter is exposed once during each filter wheel cycle. Note that the continuum emission captured in a background image is impacted by the effects of the background filter, while the continuum emission component found in a line-emission image is influenced by the properties of that specific line-emission filter. A theoretical background image, where λ_c = 541.0 nm, can be expressed as follows:

$$\mathcal{B}^{(i,j)} = \mathcal{N}_c^{(i,j)} = t \cdot \left[\int_{\lambda_c} T(\lambda)\, L(\lambda)\, O(\lambda)\, [I_c + n_{ST}] \frac{10^6}{4\pi} A\Omega\, q\, d\lambda + n_{DK} \right] + n_{RD} \qquad (2.13)$$

where the variables with respective units and definitions are tabulated as follows:

$\mathcal{B}$	$[counts]$	image data array for backgnd emission wavelength(s)
(i, j)		indices into this data array, $\mathcal{B}$, of measured counts
t	$[s]$	exposure time
L_λ	dimensionless	λ-dependent lens-vignetting function
O_λ	dimensionless	λ-dependent flat-fielding function
I_λ	$[R/nm]$	λ-dependent source signal strength
I_c	$[R/nm]$	λ-dependent continuum emission surface brightness
n_{ST}	$[R/nm]$	λ-dependent surface brightness of the stars
$10^6/4\pi$	$[ph/cm^2/s/sr/R]$	factor to convert from $[R]$ to $[ph/cm^2/s/sr]$
$A\Omega$	$[cm^2 sr]$	system throughput (or Etendue) of the imager
T_λ	dimensionless	λ-dependent optical transmittance of the filter
q	$[count/ph]$	detector quantum efficiency incorporating gain
n_{DK}	$[counts/s]$	dark current signal contribution
n_{RD}	$[counts]$	read noise contribution.

Given an exposed image integrated over the background filter bandwidth,

we can eliminate t and the integral in Eq. 2.13, and reduce the overall format to:

$$\mathcal{B} = \mathcal{N}_c = T_c\, L_c\, O_c\, [I_c + N_{ST}] \frac{10^6}{4\pi} A\Omega\, q\ + N_{DK} + N_{RD}. \tag{2.14}$$

Periodically throughout a night of observing, closed-shutter dark-count images are collected to discern the level of remnant thermal noise present in the system after initiatives have been taken to minimize its production. It is preferable for the dark images used in noise-calibration data-processing procedures to originate in somewhat close temporal proximity as the airglow images to be analyzed. As the dark current typically does not vary over the night to the extent the background sky conditions do, it is unnecessary to collect dark images with every filter-wheel cycle, as required for background images; a number of dark images interspersed from the same overnight data-run will suffice as representative. Thermal noise reduction is discussed in more detail in Section 3.4.1. For now, we merely note the basic notation for a dark-current image:

$$\mathcal{D}_{(i,j)} = t \cdot n_{DK}. \tag{2.15}$$

While equations 2.11 and 2.12 succinctly represent the composition of the airglow image data, more detail is required to evaluate the data accurately. Given an exposed line-emission image, a more useful representation is one which maintains the impact of the equipment on the data, such as the following simplification of Eq. 2.4:

$$\mathcal{N}_{\lambda_0} = T_{\lambda_0}\, L_{\lambda_0}\, O_{\lambda_0}\, [V \cdot I_{\lambda_0} + I_c + N_{ST}] \frac{10^6}{4\pi} A\Omega\, q\ + N_{DK} + N_{RD} \tag{2.16}$$

2.3.4 Signal Isolation Methods

2.3.4.1 Historical Approximations

Historically for the Cornell airglow image data-analysis system, "Viewer", the method used to segregate the targeted airglow signal is approximate and originally estimated the fractional intensity change, $\delta I/\bar{I}$, in the airglow data, using the fact that the target airglow signal, I, is actually composed of a mean airglow signal, $\bar{I}$, and the airglow perturbation signal, δI. The algorithm applies to a series of line-emission images and their associated background images, and starts by removing the brightest stars (i.e., the systematic "noise" contribution from stars) from every image in both series. We indicate these images after the stars have been removed as: $\acute{\mathcal{N}}_{\lambda_0}$ and $\acute{\mathcal{B}}$. The dark noise and read noise together are considered to be a bias, and the remaining sky noise after the stars have been removed – i.e., contributions from the continuum emission alone – is assumed to be the same in both images for each pair of line-emission and background images. To remove these noise effects, the background images are subtracted from their partner line-emission images, to generate a series of "background-corrected" images. An example background-corrected image, $\mathcal{BC}$, for one pair of line-emission and background images – *as portrayed by this scheme* [*Garcia*, 1999] – but using notation based on the previous section, is given as:

$$\mathcal{BC} = \acute{\mathcal{N}}_{\lambda_0} - \acute{\mathcal{B}} = L \cdot O \cdot V \cdot (\bar{I} + \delta I). \tag{2.17}$$

As an aside, if we were to consider the assumptions correct up to this point in the argument, we would still actually be left with the following for our background-corrected example image:

$$\mathcal{BC} = \acute{\mathcal{N}}_{\lambda_0} - \acute{\mathcal{B}} = T \cdot L \cdot O \cdot V \cdot (\bar{I} + \delta I)\frac{10^6}{4\pi} A\Omega\, q. \tag{2.18}$$

Continuing with the presentation of the algorithm, a new term is introduced to simplify the notation. Representing the competing impacts of the van Rhijn effect versus lens vignetting coupled with the influence of the optical train, the array H is defined to be:

$$H \equiv L \cdot O \cdot V, \tag{2.19}$$

so that Eq. 2.17 simplifies to:

$$\mathcal{BC} = H \cdot (\bar{I} + \delta I). \tag{2.20}$$

Now, making use of the fact that the airglow perturbation, δI, is not spatially stationary, a series of background-corrected images are averaged together to remove the effects of the variation, creating the reported average image, $\mathcal{AV}$:

$$\mathcal{AV} = \overline{\mathcal{BC}} = H \cdot \bar{I}. \tag{2.21}$$

The software routine goes a step further and takes into account the gradual changes in the mean airglow signal, $\bar{I}$. With this approach, the single average image, $\mathcal{AV}$, is replaced by a series of average images, $\mathcal{AV}(t)$, with each entry in the series generated by averaging background-corrected images over roughly $\sim$ 30 minute intervals. Finally, by dividing a background-corrected image by its associated average image, this algorithm claims to separate out the intensity differential as follows:

$$\frac{\mathcal{BC}}{\mathcal{AV}(t)} = \frac{\bar{I} + \delta I}{\bar{I}}, \tag{2.22}$$

then,

$$\frac{\delta I}{\bar{I}} = \frac{\mathcal{BC}}{\mathcal{AV}(t)} - 1. \tag{2.23}$$

Within the past few years, the software – still based on this overall algorithm – has been revised to calculate the perceived total intensity, rather than the fractional intensity change. To accommodate this total-intensity calculation, the average airglow intensity, $\bar{I}$, is estimated by using the fact that H, from Eq. 2.19

above, equals unity at zenith. So averaging a few pixels ($\sim 5 \times 5$ box) at zenith provides the necessary approximation for $\bar{I}$, so that the total intensity, I, is given by:

$$I = \bar{I} + \delta I = \frac{\mathcal{BC}}{\mathcal{AV}(t)} \cdot \bar{I}. \tag{2.24}$$

The main impact to the accuracy of this method described in detail above is the assumption that the continuum emission is represented the same in both the line-emission and background images. It is, indeed, safe to assume that the continuum emission was likely the same when both datasets were imaged; that is the point in taking the background images in the first place. However, the numerical representations of the continuum emission will differ between the line-emission and background images due to the disparate effects of the two filters used. As pointed out in Eq. 2.17, the filter transmission effects and the associated system throughput variations are omitted from Eq. 2.18. Beyond that, it the basic assumption requiring the need for the misleading generic non-subscripted variables used in Eq.s 2.17-2.19, that is at fault. As forewarned in Section 2.3.3, while the values for I_c can be considered equal in both equations, $\mathcal{B} \neq B$. To determine the consequences of this inequality, we compare equations representing the contributions stemming from the continuum emission only. For a line-emission image, we label this $\mathcal{N}_{c\lambda_0}$, such that:

$$\mathcal{N}_{c\lambda_0} = T_{\lambda_0} L_{\lambda_0} O_{\lambda_0} I_c \left(\frac{10^6}{4\pi} A\Omega\, q \right)_{\lambda_0}. \tag{2.25}$$

For the background image with the star, dark count, and read noises all removed, we get:

$$\grave{\mathcal{N}}_c = \grave{\mathcal{B}} = T_c L_c O_c I_c \left(\frac{10^6}{4\pi} A\Omega\, q \right)_c. \tag{2.26}$$

Note that while the values in

$$\frac{10^6}{4\pi} A\Omega\, q$$

are not explicitly wavelength dependent, the term is evaluated through intensity calibration methods described in Chapter 3, and *is* directly indicated by both a specific filter and imager system. For this reason of filter and system dependency, the subscripts are included to emphasize that the term will vary between the line image and background image.

Assuming that I_c, itself, is the same in both Eq.s 2.25 and 2.26, these respective continuum emission inputs would be the same if

$$T_{\lambda_0} L_{\lambda_0} O_{\lambda_0} \left(\frac{10^6}{4\pi} A\Omega q \right)_{\lambda_0} = T_c L_c O_c \left(\frac{10^6}{4\pi} A\Omega q \right)_c . \tag{2.27}$$

As mentioned earlier, at zenith the lens vignetting effects coupled with optical train imperfections are unity, so setting $L_{\lambda_0} O_{\lambda_0} = L_c O_c = 1$, and looking at this best-case example, we can reduce Eq. 2.27 to:

$$T_{\lambda_0} \left(\frac{10^6}{4\pi} A\Omega q \right)_{\lambda_0} = T_c \left(\frac{10^6}{4\pi} A\Omega q \right)_c . \tag{2.28}$$

Evaluating the ratio, $\mathfrak{R}$, of the factors impacting the line-emission image to the those impacting the background image, using values determined through calibration procedures discussed in Chapter 3, we find for CASI:

$$\mathfrak{R}_{CASI} = \frac{T_{\lambda_0} \left(\frac{10^6}{4\pi} A\Omega q \right)_{\lambda_0}}{T_c \left(\frac{10^6}{4\pi} A\Omega q \right)_c} = \frac{(2.11)(0.0044)}{(0.93)(0.0087)} = 1.15 \tag{2.29}$$

and for CARI:

$$\mathfrak{R}_{CARI} = \frac{T_{\lambda_0} \left(\frac{10^6}{4\pi} A\Omega q \right)_{\lambda_0}}{T_c \left(\frac{10^6}{4\pi} A\Omega q \right)_c} = \frac{(1.61)(0.0656)}{(1.51)(0.0337)} = 2.07 \tag{2.30}$$

These results indicate that interchanging $\mathcal{B}$ for B, can introduce errors into the image processing scheme.

2.3.4.2 Accurate Method

A more accurate method for isolating the target signal is a two-stage approach based on our assumption of superposition; i.e., the line-emission signal, I_{λ_0}, is superposed onto the continuum emission signal, I_c. In this approach, we first determine the intensity term I_c using the background image, $\mathcal{B} = \mathcal{N}_c$, with the noise elements removed, forcing the altered notation $\grave{\mathcal{B}} = \grave{\mathcal{N}}_c$. The read noise is considered negligible here and may be omitted; dark count noise can be removed by subtracting a temporally-related dark image, $\mathcal{D}$; and the stars are removed using the star-removal software routine [*Garcia*, 1999] which identifies the sharp, localized changes in intensity associated with stars and replaces them with a linear fit of the surrounding pixels. Eq. 2.14 now becomes

$$\grave{\mathcal{B}} = \grave{\mathcal{N}}_c = T_c\, L_c\, O_c\, I_c \left(\frac{10^6}{4\pi} A\Omega\, q\right)_c , \tag{2.31}$$

and I_c can be defined as

$$I_c = \frac{\grave{\mathcal{N}}_c}{T_c\, L_c\, O_c \left(\frac{10^6}{4\pi} A\Omega\, q\right)_c}. \tag{2.32}$$

Next we substitute the value obtained for I_c into Eq. 2.16 and evaluate the intensity terms piecewise. After removing the noise through the same methods used on the background image, Eq. 2.16 becomes

$$\grave{\mathcal{N}}_{\lambda_0} = T_{\lambda_0}\, L_{\lambda_0}\, O_{\lambda_0} \left[V \cdot I_{\lambda_0} + I_c\right] \left(\frac{10^6}{4\pi} A\Omega\, q\right)_{\lambda_0} . \tag{2.33}$$

Separating the two intensity terms and distributing, we get:

$$\grave{\mathcal{N}}_{\lambda_0} = T_{\lambda_0}\, L_{\lambda_0}\, O_{\lambda_0} \left[I_c\right] \left(\frac{10^6}{4\pi} A\Omega\, q\right)_{\lambda_0} + T_{\lambda_0}\, L_{\lambda_0}\, O_{\lambda_0} \left[V \cdot I_{\lambda_0}\right] \left(\frac{10^6}{4\pi} A\Omega\, q\right)_{\lambda_0} . \tag{2.34}$$

The first term on the right-hand side of Eq. 2.34 represents the effect of the line filter on the continuum emission, and can be designated as $\grave{\mathcal{N}}_{c\lambda_0}$, where

$$\grave{\mathcal{N}}_{c\lambda_0} = T_{\lambda_0}\, L_{\lambda_0}\, O_{\lambda_0} \left[I_c\right] \left(\frac{10^6}{4\pi} A\Omega\, q\right)_{\lambda_0} . \tag{2.35}$$

Evaluating Eq. 2.35 numerically using the value obtained for I_c above in Eq. 2.32, we then substitute into Eq. 2.34 to complete the piecewise analysis.

$$\grave{\mathcal{N}}_{\lambda_0} = \grave{\mathcal{N}}_{c\lambda_0} + T_{\lambda_0} L_{\lambda_0} O_{\lambda_0} [V \cdot I_{\lambda_0}] \left(\frac{10^6}{4\pi} A\Omega q \right)_{\lambda_0}. \tag{2.36}$$

Finally, we solve for I_{λ_0} to get:

$$I_{\lambda_0} = \frac{\grave{\mathcal{N}}_{\lambda_0} - \grave{\mathcal{N}}_{c\lambda_0}}{T_{\lambda_0} L_{\lambda_0} O_{\lambda_0} V \left(\frac{10^6}{4\pi} A\Omega q \right)_{\lambda_0}}. \tag{2.37}$$

2.3.4.3 Error Analysis

In order to evaluate the impact the approximations in Section 2.3.4.1 have on the accuracy of the line-emission intensity results calculated, we can perform some basic error analysis to determine the potential percent error introduced. We first address the algorithm as it is advertised in Eq.s 2.21 and 2.22, and let $I^{'}_{\lambda_0} = \bar{I}_{\lambda_0} + \delta I_{\lambda_0}$, so that:

$$I^{'}_{\lambda_0} = \bar{I}_{\lambda_0} + \delta I_{\lambda_0} = \frac{\mathcal{BC}}{\mathcal{AV}(t)} \cdot \bar{I}_{\mathcal{AV}} = \frac{\mathcal{BC}}{H \cdot \bar{I}_{\mathcal{AV}}} \cdot \bar{I}_{\mathcal{AV}}. \tag{2.38}$$

The prime notation, $I^{'}_{\lambda_0}$ is used in this section to differentiate the approximated results from those calculated using the method in Eq. 2.37. As will be shown, the approximate method defined by Eq. 2.38 *appears* to give us our desired results for I_{λ_0}; however, upon closer inspection, we show where a faulty assumption leads us astray.

Proceeding with the evaluation of Eq. 2.38, we note that $\mathcal{BC}$ is actually $\acute{\mathcal{N}}_{\lambda_0} - \acute{\mathcal{N}}_c$, using our notation introduced earlier in Eq. 2.17 to indicate the stars have been removed from each image. Specifying each image after star removal, we have:

$$\acute{\mathcal{N}}_{\lambda_0} = T_{\lambda_0} \cdot L_{\lambda_0} \cdot O_{\lambda_0} \cdot (V I^{'}_{\lambda_0} + I_c) \left(\frac{10^6}{4\pi} A\Omega q \right)_{\lambda_0} + N_{DK} + N_{RD}, \tag{2.39}$$

and

$$\acute{\mathcal{N}}_c = T_c \cdot L_c \cdot O_c \cdot I_c \left(\frac{10^6}{4\pi} A\Omega\, q \right)_c + N_{DK} + N_{RD}. \tag{2.40}$$

To simplify the notation, we define

$$G_c \equiv \left(\frac{10^6}{4\pi} A\Omega\, q \right)_c, \tag{2.41}$$

and

$$G_{\lambda_0} \equiv \left(\frac{10^6}{4\pi} A\Omega\, q \right)_{\lambda_0}. \tag{2.42}$$

G will be derived in Section 3.4.4; for now we merely introduce it as a substitution. Continuing with the algorithm specified in Eq. 2.38, we utilize the G notation, neglect the read noise, and subtract to get:

$$\acute{\mathcal{N}}_{\lambda_0} - \acute{\mathcal{N}}_c = T_{\lambda_0} L_{\lambda_0} O_{\lambda_0} G_{\lambda_0} (V I^{'}_{\lambda_0}) + [T_{\lambda_0} L_{\lambda_0} O_{\lambda_0} G_{\lambda_0} - T_c L_c O_c G_c] I_c. \tag{2.43}$$

Before proceeding we can simplify this a bit by assuming the best-case scenario at zenith where $L_{\lambda_0} O_{\lambda_0} = L_c O_c = 1$. We can also substitute in H using the definition in terms of our nomenclature, i.e. $H = L_{\lambda_0} O_{\lambda_0} V$. Lastly, we can estimate the coefficient of I_c using real values calculated in Section 3.4.4 for CASI; i.e., $T_{\lambda_0} G_{\lambda_0} - T_c G_c = 0.00928 - 0.00809 = 0.00119 \approx 0.0012$. Incorporating all this, we have:

$$\frac{\mathcal{BC}}{\mathcal{AV}(t)} \cdot \bar{I}_{\mathcal{AV}} = \frac{\acute{\mathcal{N}}_{\lambda_0} - \acute{\mathcal{N}}_c}{H \cdot \bar{I}_{\mathcal{AV}}} \cdot \bar{I}_{\mathcal{AV}} = \frac{T_{\lambda_0} G_{\lambda_0} H I^{'}_{\lambda_0} + 0.0012 I_c}{H \cdot \bar{I}_{\mathcal{AV}}} \cdot \bar{I}_{\mathcal{AV}}. \tag{2.44}$$

The $\bar{I}_{\mathcal{AV}}$'s cancel. Solving the remaining equation algebraically for $I^{'}_{\lambda_0}$, gives us:

$$I^{'}_{\lambda_0} = \frac{\acute{\mathcal{N}}_{\lambda_0} - \acute{\mathcal{N}}_c}{T_{\lambda_0} G_{\lambda_0} H} - \frac{0.0012 I_c}{T_{\lambda_0} G_{\lambda_0} H}. \tag{2.45}$$

Substituting back in for H and rearranging yields the following form similar to that in Eq. 2.37:

$$I^{'}_{\lambda_0} = \frac{\acute{\mathcal{N}}_{\lambda_0} - [\acute{\mathcal{N}}_c + 0.0012 I_c]}{T_{\lambda_0} G_{\lambda_0} L_{\lambda_0} O_{\lambda_0} V}. \tag{2.46}$$

To complete the comparison with Eq. 2.37, we need to determine $\acute{\mathcal{N}}_c + 0.0012I_c$ in terms of $\acute{\mathcal{N}}_{c\lambda_0}$. We know that $I_c = \acute{\mathcal{N}}_{c\lambda_0}/T_{\lambda_0}G_{\lambda_0}L_{\lambda_0}O_{\lambda_0}$. To find $\acute{\mathcal{N}}_c$ in terms of $\acute{\mathcal{N}}_{c\lambda_0}$, we solve both for I_c and then equate the two solutions for I_c, as shown:

$$\frac{\acute{\mathcal{N}}_c}{T_cG_cL_cO_c} = \frac{\acute{\mathcal{N}}_{c\lambda_0}}{T_{\lambda_0}G_{\lambda_0}L_{\lambda_0}O_{\lambda_0}}. \tag{2.47}$$

Following our assumption again to consider zenith conditions where $L_{\lambda_0}O_{\lambda_0} = L_cO_c = 1$, rearranging terms to solve for $\acute{\mathcal{N}}_c$, and substituting values from Section 3.4.4, we show that for CASI:

$$\acute{\mathcal{N}}_c = \frac{\acute{\mathcal{N}}_{c\lambda_0}T_cG_c}{T_{\lambda_0}G_{\lambda_0}} = \frac{\acute{\mathcal{N}}_{c\lambda_0}(0.93)(0.0087)}{(2.11)(0.0044)} = 0.87\acute{\mathcal{N}}_{c\lambda_0}. \tag{2.48}$$

Returning to Eq. 2.46, and making these substitutions for $\acute{\mathcal{N}}_c$ and I_c, we now have:

$$I'_{\lambda_0} = \frac{\acute{\mathcal{N}}_{\lambda_0} - [0.87\acute{\mathcal{N}}_{c\lambda_0} + 0.0012\frac{\acute{\mathcal{N}}_{c\lambda_0}}{(1)(0.0093)}]}{T_{\lambda_0}G_{\lambda_0}L_{\lambda_0}O_{\lambda_0}V} = \frac{\acute{\mathcal{N}}_{\lambda_0} - \acute{\mathcal{N}}_{c\lambda_0}}{T_{\lambda_0}G_{\lambda_0}L_{\lambda_0}O_{\lambda_0}V} = I_{\lambda_0}, \tag{2.49}$$

so that it appears that everything checks out appropriately. *However*, the problem arises with the improper definition that $\mathcal{AV}(t) = H \cdot \bar{I}_{\mathcal{AV}}$. Actually, the average image impacted by H, i.e., by LOV, is also influenced by the equipment transmission and etendue along with the difference in the background continuum contribution given that different filters are used in obtaining line and background images. So in truth,

$$\mathcal{AV}(t) = (H \cdot \bar{I}_{\lambda_0} \cdot T_{\lambda_0}G_{\lambda_0}) - 0.13\acute{\mathcal{N}}_{c\lambda_0}, \tag{2.50}$$

which follows from the definition of $\bar{I}_{\mathcal{AV}}$, derived from

$$\mathcal{BC} = \acute{\mathcal{N}}_{\lambda_0} - \acute{\mathcal{N}}_c = (\bar{I}_{\lambda_0} + \delta I_{\lambda_0})(T_{\lambda_0}G_{\lambda_0}L_{\lambda_0}O_{\lambda_0}V) + \acute{\mathcal{N}}_{c\lambda_0} - 0.87\acute{\mathcal{N}}_{c\lambda_0}, \tag{2.51}$$

then

$$\overline{\mathcal{BC}} = \langle\acute{\mathcal{N}}_{\lambda_0} - \acute{\mathcal{N}}_c\rangle = \bar{I}_{\lambda_0}T_{\lambda_0}G_{\lambda_0}L_{\lambda_0}O_{\lambda_0}V + 0.13\acute{\mathcal{N}}_{c\lambda_0}, \tag{2.52}$$

and finally,

$$\bar{I}_{\lambda_0} = \frac{\langle \acute{\mathcal{N}}_{\lambda_0} - \acute{\mathcal{N}}_c \rangle - 0.13 \acute{\mathcal{N}}_{c\lambda_0}}{T_{\lambda_0} G_{\lambda_0} L_{\lambda_0} O_{\lambda_0} V}. \tag{2.53}$$

A more rigorous percent error analysis is attained by basing the comparison – of the accurate method (proposed in Eq. 2.37) to the approximate method given below in Eq. 2.54 – on using the actual substitutions corresponding to the variables in the historical algorithm, shown as:

$$\frac{\mathcal{BC}}{\mathcal{AV}(t)} \cdot \bar{I}_{\lambda_0} = \frac{\acute{\mathcal{N}}_{\lambda_0} - \acute{\mathcal{N}}_c}{\langle \acute{\mathcal{N}}_{\lambda_0} - \acute{\mathcal{N}}_c \rangle} \cdot \bar{I}_{\lambda_0}. \tag{2.54}$$

Using this rigorous approach employing values consistent with the actual representations of the image data, and letting $\Upsilon = T_{\lambda_0} G_{\lambda_0} L_{\lambda_0} O_{\lambda_0} V$, we have the following:

$$\frac{I_{\lambda_0} - I'_{\lambda_0}}{I_{\lambda_0}} = \left[\frac{\acute{\mathcal{N}}_{\lambda_0} - \acute{\mathcal{N}}_{c\lambda_0}}{\Upsilon} - \frac{\left(\frac{\acute{\mathcal{N}}_{\lambda_0} - \acute{\mathcal{N}}_c}{\langle \acute{\mathcal{N}}_{\lambda_0} - \acute{\mathcal{N}}_c \rangle} \right) \cdot \langle \acute{\mathcal{N}}_{\lambda_0} - \acute{\mathcal{N}}_c \rangle}{\Upsilon} \right] \cdot \frac{\Upsilon}{\acute{\mathcal{N}}_{\lambda_0} - \acute{\mathcal{N}}_{c\lambda_0}} \tag{2.55}$$

$$= \frac{\left[\acute{\mathcal{N}}_{\lambda_0} - \acute{\mathcal{N}}_{c\lambda_0} - \acute{\mathcal{N}}_{\lambda_0} + \acute{\mathcal{N}}_c - 0.13 \acute{\mathcal{N}}_{c\lambda_0} \left(\frac{\acute{\mathcal{N}}_{\lambda_0} - \acute{\mathcal{N}}_c}{\langle \acute{\mathcal{N}}_{\lambda_0} - \acute{\mathcal{N}}_c \rangle} \right) \right]}{\acute{\mathcal{N}}_{\lambda_0} - \acute{\mathcal{N}}_{c\lambda_0}} \tag{2.56}$$

$$= \frac{\left[-\acute{\mathcal{N}}_{c\lambda_0} + 0.87 \acute{\mathcal{N}}_{c\lambda_0} - 0.13 \acute{\mathcal{N}}_{c\lambda_0} \left(\frac{\acute{\mathcal{N}}_{\lambda_0} - \acute{\mathcal{N}}_c}{\langle \acute{\mathcal{N}}_{\lambda_0} - \acute{\mathcal{N}}_c \rangle} \right) \right]}{\acute{\mathcal{N}}_{\lambda_0} - \acute{\mathcal{N}}_{c\lambda_0}} \tag{2.57}$$

$$= \frac{\acute{\mathcal{N}}_{c\lambda_0}}{\acute{\mathcal{N}}_{c\lambda_0}} \frac{-0.13}{\left(\frac{\acute{\mathcal{N}}_{\lambda_0}}{\acute{\mathcal{N}}_{c\lambda_0}} - 1 \right)} \left[1 + \left(\frac{\acute{\mathcal{N}}_{\lambda_0} - \acute{\mathcal{N}}_c}{\langle \acute{\mathcal{N}}_{\lambda_0} - \acute{\mathcal{N}}_c \rangle} \right) \right] \tag{2.58}$$

$$= \frac{-0.13}{\left(\frac{\acute{\mathcal{N}}_{\lambda_0}}{1.15 \acute{\mathcal{N}}_c} - 1 \right)} \left[1 + \left(\frac{\acute{\mathcal{N}}_{\lambda_0} - \acute{\mathcal{N}}_c}{\acute{\mathcal{N}}_{\lambda_0} - \acute{\mathcal{N}}_c} \right) \right] \tag{2.59}$$

$$= \frac{-0.13}{(1.74 - 1)} \left[1 + \left(\frac{1}{0.5} \right) \right] \tag{2.60}$$

$$= 0.53 \tag{2.61}$$

based on historical 557.7-nm line-emission data and 541.0-nm background data, for which the ratio of counts for $\acute{N}_{\lambda_0}/\acute{N}_c$ has typically approximated 2/1.

CHAPTER 3

CALIBRATION

Widely accepted in the space physics science community, ground-based airglow measurements are an effective and relatively inexpensive method for remote-sensing the behavior of the upper atmosphere. As evidence to this notion, ever more ionospheric physicists today are incorporating airglow imagers into their instrument portfolios. This increase is fortuitous to the community as a whole, producing an ever larger dataset for comparison and study.

The condition of our data can have critical consequences in achieving the scientific community's goals of: (1) comparing observational data from different instruments, (2) using data from multiple instruments as constraints to modelling, and (3) recording and monitoring possible long-term trends due to natural variability and climatic influences [*Nossal*, 2005]. As a pointed example, a recent corroborative study making use of the availability of different sets of long-term solar spectral irradiance measurements allowed scientists to examine the mutual consistency of this data and to study the solar activity in dissociation and ionization rates of atmospheric species. As a result, while scientists confirmed consistency among a variety of newer space-borne instruments for overlapping observations, the evaluation revealed a disconnect between this new satellite data source and both model parameters and airglow values, with implications that ionospheric photochemistry and airglows might warrant re-examination [*Yee et al.*, 2005].

In order to ensure the validity of comparisons such as these, however, we need to have congruent data; and, in order to produce meaningful studies, we need to have accurate data. Confounding our goals of comparison and study is

the fact that our raw data are collected in terms of pixel counts relevant to the particular imager recording the observations; in addition, there exists a myriad of factors which impact how closely our observations come to a true representation of the airglow phenomenon. Given these conditions, some modifications must be made both to translate this optical data into a format for effective comparisons, as well as to reduce the discrepancies between the data and the true phenomenon. Calibration, in all its many facets, is the means to this end.

The term "calibration" has broad, abundant coverage, applying semantically to everything from determining the caliber of the equipment used as a measurement standard; to that standard's application towards specifying the caliber of our research instruments, the components of our optical instruments, as well as, various parameters of the data collected by the instruments. With so many meanings, the terminology can get confusing and one must rely on context to clarify the semantics. Compounding things even further, in addition to the many processes covered by the term calibration, there are numerous methodologies for implementing each, with a variety of instruments from which to choose to accomplish each task. Consistent calibration techniques are critically important when multiple observers contribute to a long-term dataset and when there are upgrades to the instrument(s) acquiring the dataset. Exacerbating all this, the evolution of the field of optics has spawned its own layer of confusion with its basic terminology. The scientific community readily acknowledges the challenges associated with calibration and recognizes the need to optimize methods for brightness and spectral calibration, as well as inter-calibration between instruments [*Nossal*, 2005].

The intent of this chapter is to highlight some of the challenges and to allevi-

ate some of the confusion through discussions of these topics and presentation of relevant methodologies. To begin, a foundation is laid in Section 3.1 with the definition of the signal-to-noise ratio for our airglow signal which will serve as the context for the ensuing sections. Error types were highlighted and categorized previously in Section 2.3.2, motivating the need for calibration. Before continuing with details concerning calibration, types of calibration sources are presented in Section 3.3. In Sections 3.4 – 3.5, the types of calibration are introduced under two broad categories: radiometric calibration and geometric calibration. Methods used in radiometric calibration are covered in Sections 3.4.1 – 3.4.4, with procedures for a specific calibration study also detailed in these sections.

Realization of the importance and difficulty of calibration unfortunately came too late in this thesis research to contribute much to the thesis, per se. Nonetheless, it seems worthwhile to present this topic in the hopes that future students may benefit.

3.1 Signal-to-Noise Ratio

Based on our fundamental goals of data comparison and study, four objectives drive the need for calibration:

1. to characterize the capability and performance of the overall instrumentation system allowing for, among other things, calculations based on true brightness values rather than limiting calculations to perturbations from the background mean;
2. to monitor the system to recognize drift from the original performance

characterization;

3. to eliminate or minimize errors in the data wherever possible; and
4. to enable certain types of calculations and interpretations by modifying the raw data into a more productive representation.

In general, the idea behind calibration is to make periodic measurements of either bureau-certified standards or measurable contamination, and to incorporate the results into an image processing scheme which, when applied to the raw images obtained from data campaigns, results in the best possible database of images for analyzing the natural phenomena observed.

Many of the numerous aspects to calibration address potential error sources which could otherwise contaminate one's data. By characterizing the signal contribution from all the measurable error sources, we can incorporate these into the overall correction scheme. For this reason, it is a worthwhile endeavor to review suspected error types and the associated calibration procedures for avoiding or correcting for such errors, noting that not all errors can be addressed by calibration. A useful context for evaluating the relationship among all the signal and contamination components is the signal-to-noise ratio. The first step is to define this ratio for our systems.

Revisiting the airglow signal introduced in Section 2.3, we recall that one representation of the recorded image was first given in Eq. 2.4, and is repeated here for proximity:

$$\mathcal{N}^{(i,j)} = t \cdot \left[\int_{\lambda_0} T(\lambda)\, L(\lambda)\, O(\lambda)\, [V(\theta, W) \cdot I(\lambda) + n_{BG} + n_{ST}] \frac{10^6}{4\pi} A\Omega\, q\, d\lambda + n_{DK} \right] + n_{RD} \tag{3.1}$$

where the variables with respective units and definitions are tabulated as follows:

$\mathcal{N}$	$[counts]$	image data array for emission wavelength(s)
(i, j)		indices into this data array, $\mathcal{N}$, of measured counts
t	$[s]$	exposure time
$V_{\theta,W}$	dimensionless	elevation and height-dependent van Rhijn effect
L_λ	dimensionless	λ-dependent lens-vignetting function
O_λ	dimensionless	λ-dependent flat-fielding function
I_λ	$[R/nm]$	λ-dependent source signal strength
n_{BG}	$[R/nm]$	λ-dependent surface brightness of the continuum emission, I_c, combined with aerosol scattering effects
n_{ST}	$[R/nm]$	λ-dependent surface brightness of the stars
$10^6/4\pi$	$[ph/cm^2/s/sr/R]$	factor to convert from $[R]$ to $[ph/cm^2/s/sr]$
$A\Omega$	$[cm^2 sr]$	system throughput (or Etendue) of the imager
T_λ	dimensionless	λ-dependent optical transmittance of the filter
q	$[count/ph]$	detector quantum efficiency incorporating gain
n_{DK}	$[counts/s]$	dark current signal contribution
n_{RD}	$[counts]$	read noise contribution.

Segregating our signal of interest from the noise contributions and combining terms, we were able to reduce Eq. 2.4 to the succinct representation given in Eq. 2.11, and repeated here:

$$\mathcal{N} = S + B + D + R, \tag{3.2}$$

where $\mathcal{N}$ is the raw image data, S represents the target signal, B includes noise contributions from background sky elements, D is the dark current, and R represents digital readout effects.

Owing that the genesis of the airglow signal is photon-counting, Poisson statistics can be invoked to discuss the uncertainty of the signal and system.

Table 3.1: Poisson Statistics

Poisson distribution	$p_\mu(\nu)$	=	$e^{-\mu}\frac{\mu^\nu}{\nu!}$
mean	$<\nu>$	=	μ
standard deviation	σ	=	$\sqrt{\mu}$
final count		=	$\mu \pm \sqrt{\mu}$
fractional uncertainty		=	$\frac{\sqrt{\nu}}{\nu} = \frac{1}{\sqrt{\nu}}$
signal-to-noise	SNR	=	$\frac{1}{fractional\ uncertainty} = \frac{\nu}{\sqrt{\nu}} = \sqrt{\nu}$

The Poisson distribution describes the results of experiments where one counts events that occur at random, but at a definite average rate. By definition, the Poisson distribution is the probability of obtaining ν counts in any definite interval, i.e.,

$$P(\nu \text{ counts in any definite interval}) = p_\mu(\nu), \tag{3.3}$$

where the Poisson distribution, $p_\mu(\nu)$, is given by

$$p_\mu(\nu) = e^{-\mu}\frac{\mu^\nu}{\nu!}. \tag{3.4}$$

The parameter μ which characterizes the Poisson distribution $p_\mu(\nu)$ is just the average number of counts expected if the experiment is repeated many times. Parameters of Poisson statistics are summarized in Table 3.1.

For cases where the noise contributions from the airglow system and background are negligible, $\sqrt{\nu}$ gives the correct SNR since the only noise of consequence is from the photon arrival rate itself. In our particular nomenclature with S being the total photon count from the source as shown in Eq. 2.6, this translates to SNR = $\frac{S}{\sqrt{S}} = \sqrt{S}$. Alas, this simplification eludes us in reality, and we must employ the "well-known CCD equation" which has the basic form

$$SNR = \frac{S}{\sqrt{(S + B) + D + R^2}} \tag{3.5}$$

(adapted from *Howell* [1989]).

Expanding this CCD equation to provide a detailed definition of the SNR for airglow systems, we get the following (adapted from *Pallamraju* [2003] and *Baumgardner et al.* [1993]):

$$SNR = \frac{t \cdot V_{\theta,W} \cdot L_\lambda \cdot O_\lambda \cdot I_\lambda \cdot T_\lambda \cdot q \cdot be \cdot af \cdot no \cdot k \cdot A\Omega}{\sqrt{t \cdot be \cdot af \cdot no\,[q \cdot V_{\theta,W} \cdot L_\lambda \cdot O_\lambda\,(I_\lambda \cdot T_\lambda + B)\,k \cdot A\Omega + D] + af \cdot no(ro)^2]}} \tag{3.6}$$

where,

t	$[s]$	exposure time
$V_{\theta,H}$	dimensionless	elevation and height-dependent van Rhijn effect
$A_{\theta,H}$	dimensionless	elevation and height-dependent arc-length effect
L_λ	dimensionless	wavelength-dependent lens vignetting function
O_λ	dimensionless	wavelength-dependent flat-fielding function
I_λ	$[R/nm]$	wavelength-dependent signal strength
T_λ	dimensionless	wavelength-dependent filter transmission
q	$[count/ph]$	detector quantum efficiency
B	dimensionless	$bg \cdot fa$, background continuum $*$ filter area (or bandwidth where background is considered)
D	$[e^- pix^{-1} s^{-1}]$	dark noise
ro	$[e^-(RMS)]$	read out noise
be	dimensionless	number of pixels binned *before* readout
af	dimensionless	number of pixels binned *after* readout
no	dimensionless	number of co-adds
k	$[photons\ s^{-1}R^{-1}]$	$photons\ s^{-1}R^{-1}$ incident on a pixel for a given f/#
$A\Omega$	$[cm^2 sr]$	Etendue.

Eq. 3.6 lays a foundation for evaluating the quality of the signal, and provides a context for determining methods for improvement. By increasing the SNR, we enhance our data. Obviously, by extension, we can achieve this progress in performance by either increasing our signal or decreasing the noise.

Using Eq. 3.6 as a basis for identifying the errors which might afflict our systems allows us to combat potential noise sources and to highlight areas for boosting the signal.

3.2 Calibration Types

As stated earlier, our end-goal for imaging airglow emissions is to perform scientific evaluations on the dataset. To this end, our aspiration must be to obtain the best quality data with the given instrumentation and field site. Armed with the knowledge of the many factors which may potentially contaminate the data or decrease its usefulness, we can implement methods of eliminating or reducing their destructive impact. Calibration is one of the primary means to achieve this goal of quality.

The term "calibration" is a loosely-used term usually relying on context to differentiate the meaning. In terms of laboratory procedures, calibration can refer to any of the following four items [*Stimson*, 1974]:

1. to determine the position as a pointer on a scale
2. to mark the graduations on the scale as of a meter
3. to correct the indications of an instrument
4. to determine the deviation of the readings from the correct values

For our purposes in gaining highest quality image data from our airglow imager field experiments, we are concerned with the last three above. Within each

of these categories, various procedures related to specific issues for our applications apply. Sometimes these procedures are referred to – interchangeably – as corrections, characterization, normalization, or calibration. Further complicating the terminology, the broad term "calibration" can refer to any of the following specific types of calibration:

- Radiometric (or photometric) calibration
  - noise calibration (or noise removal)
  - optics spatial calibration
    - flat-fielding correction
    - vignetting correction
  - filter calibration
  - brightness[1] (or absolute brightness or quantitative or spectral) calibration
  - full system calibration (or characterization)
- Geometric (or Spatial) calibration
  - star calibration (or mapping to standard coordinates)
  - geographic mapping calibration
  - uniform spacing calibration (or unwarping)

A number of journal papers (*Oznovich et al.* [1994], *Shiokawa et al.* [2000], *Garcia et al.* [1997], *Mende et al.* [1977]) address subsets of this list, but none offers a

[1] A common semantical error is to refer to "brightness" calibration as "intensity" calibration. Brightness refers to a surface feature while intensity refers to the flux. It is the source brightness that we measure with our airglow imagers.

Table 3.2: Error–Calibration Classification Summary

Error Type	Impact	Symbol	Source	Calibration Type	Calibration Fix/ Correction
systematic/	accuracy	$V(\theta, W)$	van Rhijn effect	radiometric	assume uniform layer or offset with vignetting
		$L(\lambda)$	vignetting	radiometric	vignetting function
		$O(\lambda)$	optical path variation	radiometric	flat-fielding function
		$T(\lambda)$	filter transmission	radiometric	characterize filter
		q	CCD quantum efficiency	radiometric	brightness calibration
		$N_{(i,j)} \rightarrow N_{(x,y)}$	angular/geometric distortion	geometric	spatial calibration
		I_c	background continuum	n/a	address through background images
		ST	stars	n/a	remove via image processing
random/ indeterminate	precision	$\sqrt{I(\lambda)}$	photon noise	radiometric	increase exposure time
		DK	thermal noise	radiometric	subtract dark current
		RD	read noise	radiometric	use small number of co-adds
miscellaneous/ dynamic illegitimate	accuracy and precision		human error instrument malfunction		train operators service equipment routinely
limitations	accuracy and precision		sky transmission, clouds moonlight emission height variation vertical structures column integrated		field equipment at dry, high altitude site collect data only when sun and moon are down supplement with complementary dataset supplement with complementary dataset

comprehensive look at calibration as a whole. Table 3.2 revisits the signal contamination discussed in Section 2.3.2, providing a summary of the classification of error types, how each of these impact the data, potential sources of error, and the corresponding calibration or correction techniques to address the error. In this chapter, we touch upon each of these calibration terms, putting them in relative context while covering some topics in decided detail. To begin, we examine some radiant energy sources available for radiometric calibration.

3.3 Calibration Sources

Many of the radiometric calibration procedures require the use of a calibration source which is a standardized source of radiant energy – itself calibrated to a source traceable to the National Bureau of Standards. Several types of sources exist. The choice of which to select depends upon availability and the type of calibration to be performed. For flat-fielding, a constant (i.e., uniform) "flat" source – known as a Lambertian source – is required. A Lambertian source is a uniformly, diffusing source of which the radiance is the same in all measurable directions or isotropic, if you will. While the nearest approach to a Lambertian source is a large integrating sphere housing internal lamp(s), another recognized approximation to a Lambertian source can be provided by a portable calibrated light source. For brightness calibration, either of these sources, or a C14-activated radioactive source can be used. Note that if the source is not uniformly bright, it is not considered Lambertian, and this can introduce errors into the analysis.

3.3.0.4 C14

While historically the C14 appears to have been the most prevalent, preferred source used for brightness calibration, as well as the simplest procedurally, now the restrictions for transporting, housing, and handling the radioactive material (RAM) hinder its usage. Driven by safety concerns, following are examples of the requirements, documents, and standard information (manufacturer/ model/ radiation amount) required for receiving and using RAM:

- a copy of the manufacturer's license with the Nuclear Regulatory Commission (NRC)
- NRC Form 3 posted in the work area
- dose information from the manufacturer to show that thermoluminescent dosimeters (TLD's) do not need to be worn
- a copy of the manufacturer's As Low As Reasonably Achievable (ALARA) training
- documentation showing users have had ALARA training
- documentation showing users have had Radiation Safety Officer (RSO) training (Air Force requirement)
- sources kept in a locked cabinet when not in use.

If, however, the imager to be calibrated is located at, or can be transported to, one of the sites such as NRL or Arecibo which maintain C14 sources, this method of brightness calibration remains viable and perhaps preferred. Aside from the safety issues, the procedure is straightforward and unincumbered with operational details.

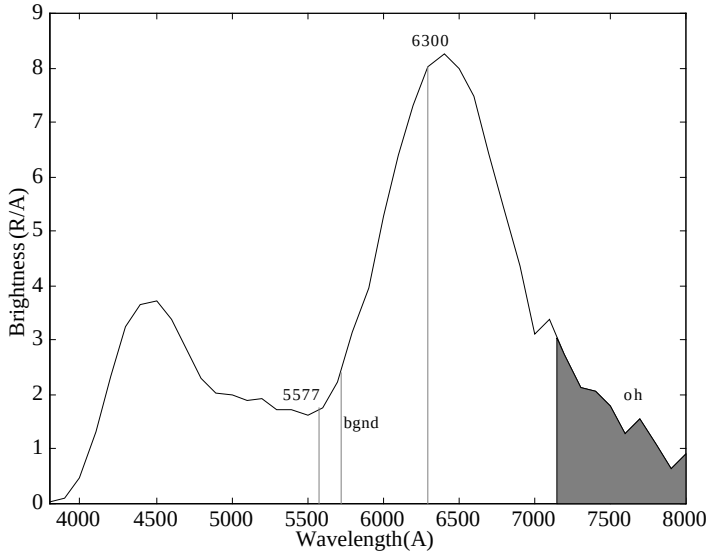

Figure 3.1: C14 calibration source intensity profile plotted as a function of wavelength in angstroms.

The C14 is actually physically three different sources: red, blue, green. The radioactive process excites a phosphor coating on each which emits photons in the respective wavelength range, generating a source profile as depicted in Figure 3.1. For brightness calibration, the sources are held adjacent to the objective lens producing an image as shown in Figure 3.2; the brightness range is controlled by varying the exposure time of the imager.

3.3.0.5 Integrating Sphere

The integrating sphere is a preferentially large (e.g., 2m diameter), "hollow" device with the interior designed and coated with barium sulfate ($BaSO_4$) to approximate a Lambertian surface [*Stimson*, 1974]. One or more incandescent or fluorescent lamps are housed inside. For flat-fielding, the imager is positioned inside the sphere as far as possible in order to flood completely the field of view.

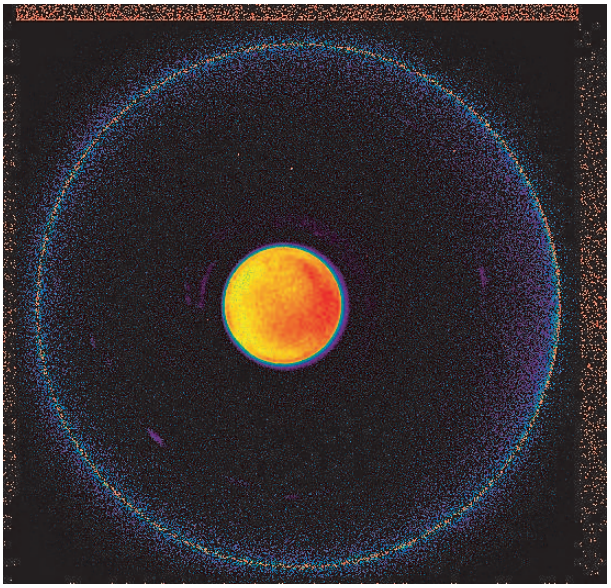

Figure 3.2: Brightness image of C14 source. (Figure courtesy of J. Baumgardner, Boston University.)

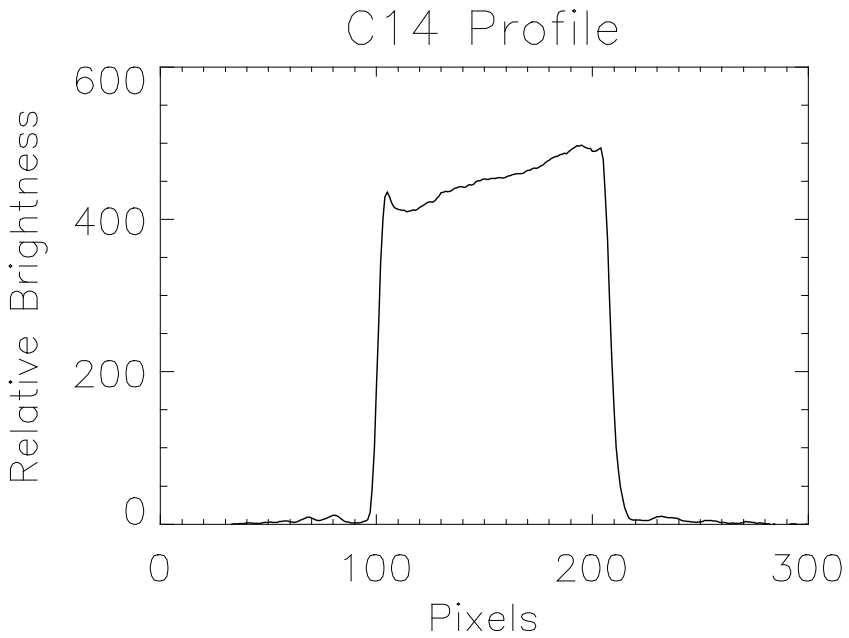

Figure 3.3: Cross-sectional profile of C14 brightness image. (Plot courtesy of J. Baumgardner, Boston University.)

With this setup, the photometric properties of the integrating sphere are altered, so this arrangement is unsuitable for brightness calibration. For brightness calibration, the imager is positioned viewing the opening of the sphere from a distance approximately one meter away. This placement is two-fold – intended both to avoid back-loading and to ensure an extended source. Back-loading occurs when brightness in the integrating sphere is increased due to contamination from light reflecting off a surface (such as the camera lens) and back into the sphere, thus corrupting the measurements. Also with the one-meter placement, the integrating sphere can be viewed as an extended source, evidenced by the opening of sphere being significantly larger than individual CCD pixels. Given that the radiance of an extended source is not affected by viewing distance, care must still be taken to include only pixels corresponding to the middle of the integrating sphere opening to avoid edge effects where the assumptions are invalid. With a close approximation to a Lambertian source, as provided by an integrating sphere without backloading, the apparent brightness is not affected by viewing angle.

The integrating sphere apparatus is not specifically designed for low light applications such as airglow imaging. As such, the light source(s) emanating from the sphere will likely saturate the airglow system without some intervening attenuation. To decrease the amount of light reaching the CCD, neutral density filter(s) can be placed in the optical path of the imager. As with all filters, neutral density filters come in different sizes, so it is important to verify that the selected filters will fit into the system to be tested. The fact that they fit in front of the re-imaging lens in one of Cornell University's imagers does not guarantee they will fit in another. Some neutral density filters, made to fit at the opening of small integrating spheres, are very small squares; while some, though circular,

will just miss aligning to fit the system.

In the visible regime, neutral density filters attenuate all wavelengths approximately equally by a given factor within the band of interest, and may be combined to create a filter with an effective density equal to the sum of the densities of the component filters. Bouger's Law indicates how the thickness of the homogenous material in a filter affects its transmission (modified from *Stimson* [1974]):

$$T_\lambda = 10^{-da_\lambda} \tag{3.7}$$

where T is the transmission and d is the path length through the homogenous material with spectral absorbtivity a. Equation(3.7) can be rewritten:

$$Density_\lambda = log_{10}\frac{1}{T_\lambda} = da_\lambda. \tag{3.8}$$

Substituting from Eq. 3.8 into Eq. 3.7, and omitting the subscript λ since neutral density filters effect all wavelengths of concern, we can write the percent of light allowed through a neutral density filter as:

$$T = 10^{-D} * 100\% \tag{3.9}$$

where, T is once again the transmission, and D is the effective density.

Three neutral density filters used in a study performed at the Naval Research Laboratory (NRL) [*Makela*, 2005 personal communication], and later obtained on loan from that facility had densities of $D = 1.8,\ 3.0,$ and 4.0. Thus, applying Eq. 3.9, the $D = 1.8,\ 3.0,$ and 4.0 filters allow 1.58%, 0.1%, and 0.01% of the incident light through, respectively. As stated above, combining the neutral density filters in series results in an effective density described by the sum of the D factors of the individual filters; so connecting the neutral density filters with densities of 1.8 and 4.0, creates a filter with an effective density of 5.8, and a transmission of 1.6×10^{-4}%.

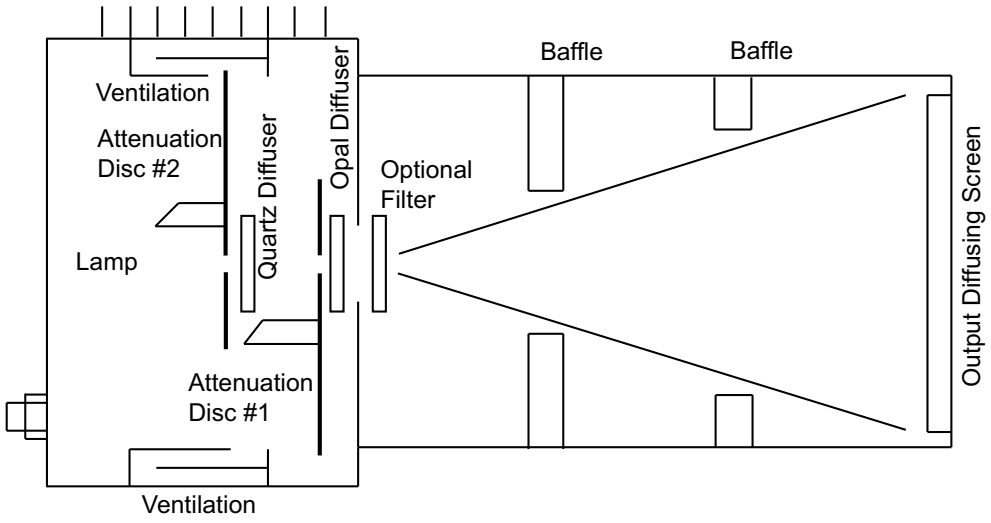

Figure 3.4: Schematic of the portable calibrated light source built by Keo Consultants and on-loan from SRI, Incorporated.

3.3.0.6 Portable Calibrated Light Source

A portable calibrated light source, obtained on-loan from Stanford Research Institute, Incorporated (SRI, Inc.), was the light source used in the calibration study detailed in this dissertation. Designed and manufactured by Keo Consultants – the company which built many of the airglow and auroral imagers in operation today, including two of the Cornell University imagers – the portable calibrated light source is a small, portable, lightweight device for calibrating low-light-level devices in field environments. The source consists of a $50 - 55$ W quartz tungsten-halogen lamp mounted in a ventilated metal box containing a system of attenuators and diffusing screens, as diagramed in Figure 3.4. The unit is $13\,\text{cm} \times 15\,\text{cm} \times 30\,\text{cm}$, with a circular output screen 10 cm in diameter. An adjustment 10-turn potentiometer is provided for trimming the lamp current during use. The regulated power supply, current sensing resistor, digital panel meter, and elapsed time meter are permanently mounted in a fairly sturdy metal instrument case, which also holds the lamp box and cable for transport. Note,

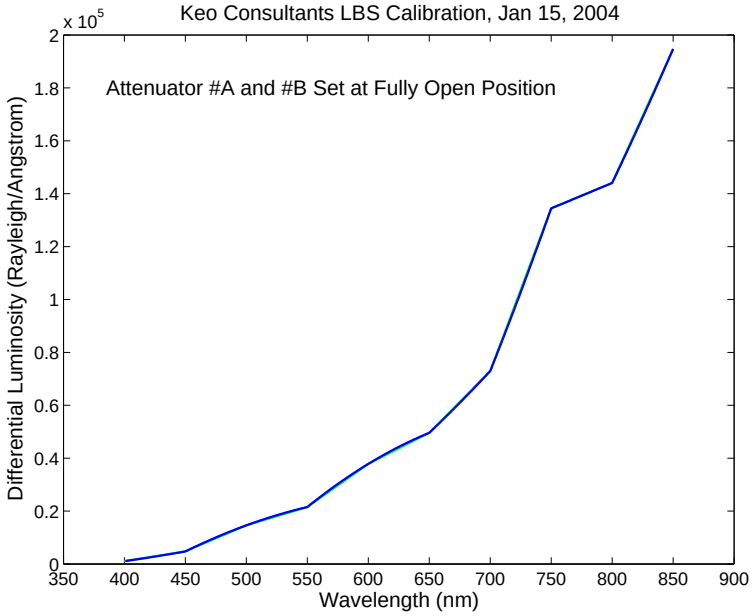

Figure 3.5: Spectral output curve for SRI's portable calibrated light source built by Keo Consultants. The spectral distribution is given in differential luminosity for the maximum brightness configuration, i.e., with both attenuator knobs set in the fully open position. (Plot data courtesy of R. Doe, SRI, Inc.)

however, experience reveals that to avoid damage, the instrument case should - further - be securely packed inside a sturdy box for any shipping or transporting of any kind other than hand-carrying.

The spectral distribution of the calibrated light source is shown in Fig 3.5. In this calibration source design, constant light output is maintained through current control; the current is monitored by ensuring the power supply maintains an accurate voltage drop across a precision resistor in series with the bulb. Constant current control is achieved by manual adjustment of the 10-turn potentiometer to maintain the reading (13.7 V shown discrepantly as 137.0 V on the LED screen) for which the bulb has been calibrated. As a precaution, an initial warmup period of approximately 5 – 15 minutes is required each time the source is started to allow the bulb, precision resistor, and power supply to come

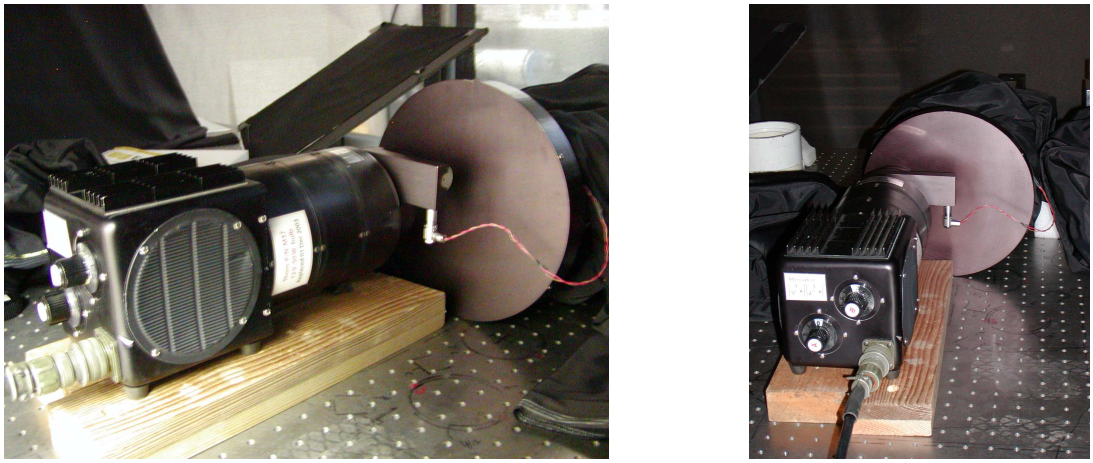

(a) (b)

Figure 3.6: CNFI and the portable calibrated light source configured for flat-fielding. Both panels (a) and (b) show that the narrow-field, objective lens of CNFI has been removed and the output diffusing screen of the light source is positioned flush to the opening of the imager housing the two plano-convex telecentric elements just prior to the filter wheel.

to stable operating conditions. During this warmup period, the light output can be expected to drop by approximately 5% if there is no voltage adjustment. To combat this drop, an initial adjustment should be made to the potentiometer; further modifications are infrequently required.

For flat-fielding, the imager – with the objective lens removed – should be placed flush to the output diffusing screen of the calibration source (as shown in Panels (a) and (b) of Figure 3.6) so as to fill fully the optical entrance of the imager. For brightness calibration, the objective (i.e., primary lens) is re-attached to the imager, as shown in Figure 3.7 for a vignetting setup. As with the integrating sphere, for brightness calibration, instruments to be calibrated should be positioned so that the distance between the light source screen and the front element of the imager (i.e., the objective lens) is greater than ten times the radius of the front element. Smaller separations can lead to back-loading as light

Figure 3.7: Vignetting data-collection setup for CASI.

reflected by the lens can illuminate the source screen significantly causing errors in calibration. This is an important point to keep in mind when fitting the imager with a PVC "collar", as shown in Panel (a) of Figure 3.8, configured to mount the light source to the system (particularly in a vertical arrangement); the collar should be designed such to maintain this distance requirement. Panel (b) of Figure 3.8 shows looking down the barrel of such a collar. The collar tube is slid over the objective lens of the imager to hold the calibration source in place. The particular collar in Figure 3.8 is shown to measure only $6\frac{5}{8}$ inches (see Panel (c) of Figure 3.8), leaving approximately 3 inches of space between the objective lens and the diffusive output screen of the source – much less than the approximately 20 inches desired to ensure back-loading is avoided. Care should also be taken to monitor the elapsed time meter provided to record lamp hours used; the manufacturer's recommendation is to recalibrate the unit every 200 hours.

Maximum output radiance of the portable calibrated light source at 550 nm is approximately $8{\times}10^{-8}$ watts cm^{-2} ster^{-1} $\mathrm{\AA}^{-1}$ (nominal), or $\sim$ 250 kR/nm. Given that the nighttime sky these airglow imagers typically observe has brightness on

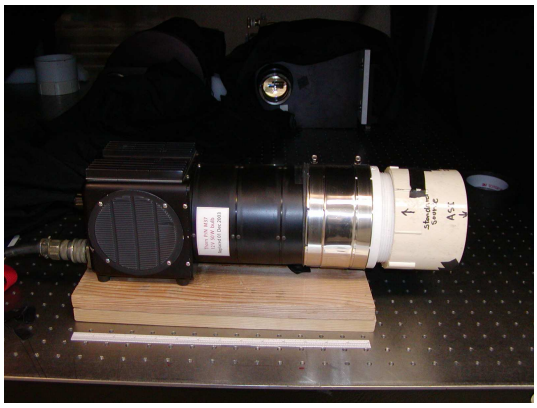

(a)

(b)

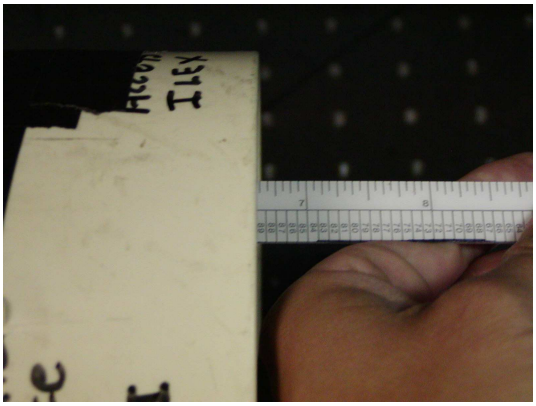

(c)

Figure 3.8: Panel (a) shows the PCLS fitted with the PVC collar designed to mount the portable calibrated light source over the objective lens of an all-sky imager. Panel (b) shows the view looking inside the PVC collar attached to the PCLS. Looking down the collar towards the light source, the camera used to snap the photo is seen reflected in the diffusive output screen. Panel (c) shows the measurement of depth of the PVC collar designed to stabilize the portable calibrated light source on an airglow imager for calibration. The distance measured is from the diffusive output screen of the light source to the edge of the collar.

the order of 100 R to 1000 R, even the light from the low-light calibration source must be further attenuated. Attenuation is achieved by means of two field stop discs. The holes in the aperture #2 (i.e., aperture A) discs are photo-fabricated so that the hole area changes by a nominal factor of 5 for each field-stop position. The disc has 3 positions (60° click stops) with an effective attenuation ratio of ~ 5 with a range of approximately 5^2. Aperture #1 (i.e., aperture B) has 12 positions (30° click stops) with one position closed, one fully open, and 10 calibrated holes giving a nominal range of $2^{10} = 1024$. The total available attenuation is $\sim 2.5 \times 10^4$. During operation knob #2 (A) should remain in the maximum light position, and knob #1 (B) used ($\times\frac{1}{2}$ per step) to adjust the light to the desired level. If knob #1 (B) does not provide sufficient attenuation, then knob #2 (A) may be used to give additional attenuation factors of 5 or 25 as needed.

3.4 Radiometric Calibration

In this section, the various radiometric calibration procedures are described. Radiometry involves evaluating radiant energy sources and sensors, as well as their performance. Radiometric calibration refers to those procedures which relate to obtaining the truest measurements, that is the most accurate and precise measurements, of the radiant energy of interest – for our purposes, the airglow emission signal. To combat the contaminates described above which generate uncertainty in our data, these radiometric calibration procedures include removing noise, normalizing the CCD characteristics to a uniform spatial response over the entire detector array, removing the effects of vignetting, determining the detector response to a standard radiance source, and characterizing the transmission response of the interference filters. Some of these procedures

are performed with every data-collection series, while others only need to be undertaken annually with the results applied to the data between performance checks. Currently, all of the airglow imagers fielded by Cornell University are telecentric systems as discussed in Section 2.2. However, since this may not always be the case, mention should be made that the overall procedures for radiometric calibration can vary slightly for collimating systems with the primary difference being requirements for filter characterization.

3.4.1 Noise Calibration

Noise, for the most part, is addressed with each data-collection sequence. Unfortunately under low light conditions, read noise, R in Eq. 3.5 or ro in Eq. 3.6, typically exceeds photon noise. Since these are the existing conditions for our nighttime airglow studies, we employ long exposure times to increase the signal strength, particularly for narrowband filters. Integration times of 90s for these filters allow for sufficient signal strength such that our resultant image is photon-limited, preferential to read-noise limited.

While increasing exposure time combats read noise, a longer integration time brings with it an increase in dark current. Using high sensitivity CCDs incorporating multi-pinned-phase (MPP), or inverted, operation helps eliminate the scourge of thermal noise, D in Eq. 3.5 or d in Eq. 3.6. Additionally, in an effort to reduce the remaining dark current, CCDs are usually cooled, typically through thermoelectric cooling. Further cooling is accomplished by combining the basic thermo-electrically cooled camera head with additional instrumentation either for air cooling, liquid cooling, or cryogenic cooling. Cornell Univer-

sity imagers all incorporate liquid cooling units (see Section 2.2.2.2), reducing the dark current by a factor of two for every 6°C the CCD is cooled. After minimizing the thermally-generated charge as much as possible through cooling the CCD, the remnant dark current is corrected for by subtracting a master dark image. Dark current can be measured with a closed-shutter exposure taken with an integration time equivalent to that used for the airglow signal image. A master dark image is generated by first averaging[2] a large set of dark images ($\sim$ 20); a large set is required so as not to increase the noise levels. As stated, these dark images which represent the residual dark current should be taken at standard operating procedure exposure times.[3] The mean dark image is then median-clipped by $3-5$ sigma (standard deviation) producing the master dark image. The median-clipped master dark image for CASI is shown in Figure 3.9; and, likewise, the median-clipped master dark image for CNFI is shown in Figure 3.10.

Another method employed to improve the SNR is binning, whereby charge from adjacent pixels on the CCD is combined during readout. While binning neighboring pixels offers the advantages of increasing SNR and readout speed while lowering storage requirements, the resulting byproduct is a decrease in spatial resolution. The tradeoffs are beneficial, however, and using 2×2 binning which is our standard operating procedure, we reduce our 1024×1024 pixel CCD resolution to 512×512 pixel images.

[2] A median average is preferred here to eliminate spurious points. However, as was the case in this calibration study, computer memory issues can manifest from loading 20+ images at once to process. If memory issues are encountered, an alternate approach is to determine the median average image one line at a time; that is, by loading only one row from each dark image at a time, median averaging that row, then going to the next row, proceeding through the matrix in a row-by-row fashion.

[3] An alternate, but less accurate, method is to generate a bias exposure dark image taken at "zero" exposure time ($\sim$ 1 s in practice), and then to extrapolate this out to the required standard operating procedure exposure time [*Baumgardner*, personal communication].

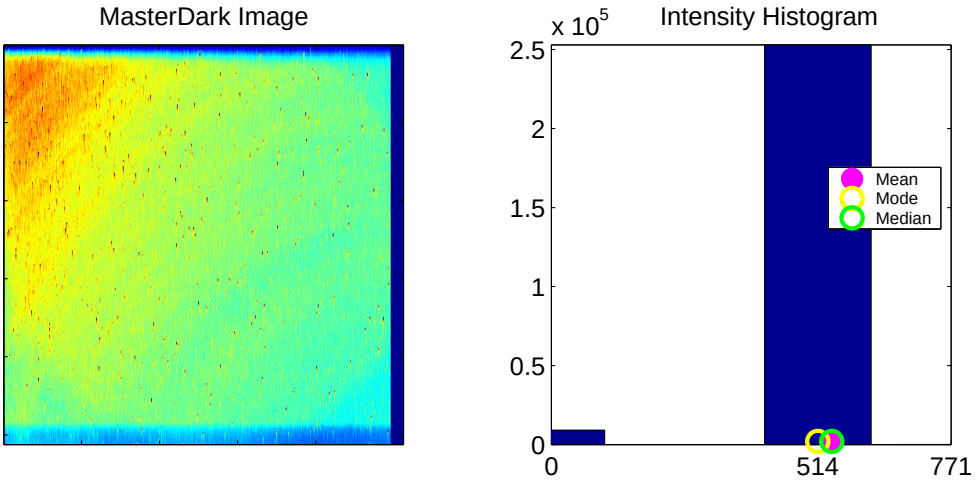

Figure 3.9: CASI MasterDark: The panel on the left shows the master dark image for CASI. The image was obtained by first averaging approximately 20 closed-shutter dark images taken with 90s exposure times, then 5σ median-clipping the resultant image. The histogram for the master dark image is shown in the panel on the right, with intensity represented on the x-axis and pixel count depicted on the y-axis.

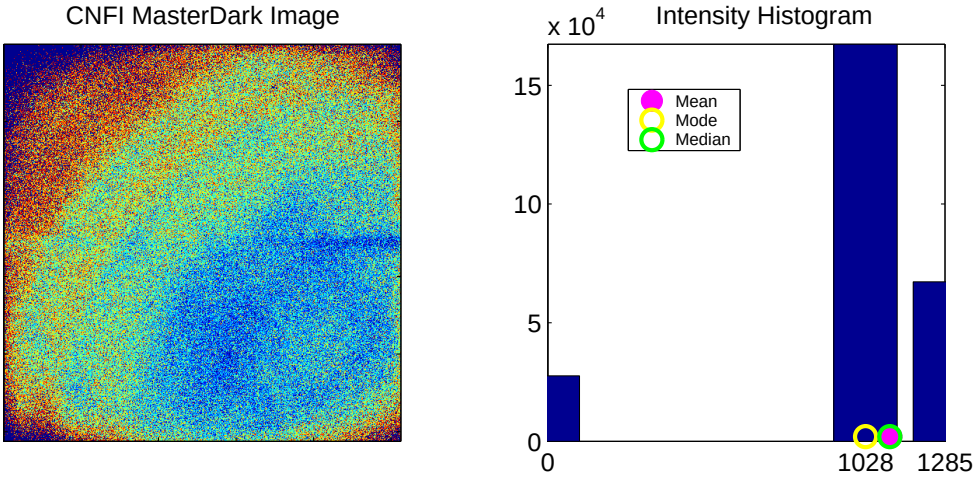

Figure 3.10: CNFI MasterDark: The panel on the left shows the master dark image for CNFI. The image was obtained by first averaging approximately 20 closed-shutter dark images taken with 90s exposure times, then 5σ median-clipping the resultant image. The histogram for the master dark image is shown in the panel on the right, with intensity represented on the x-axis and pixel count depicted on the y-axis.

3.4.2 Optics Spatial Calibration

Optics spatial calibration addresses spatial variation in an image attributable to non-uniform sensitivity from any portion of the optics train, encompassing effects due to lenses, filters, or the detector, and originating either from product irregularities or outside contaminates. The sections below for flat-fielding and vignetting will address: the motivation behind its necessity, the equipment setup required, the procedures to be followed, and the results from the most recent calibration study.

Note that, strictly speaking, vignetting is an effect separate from those accounted for in flat-fielding, and specific procedures exist for determining the vignetting correction function. However, the term "flat-fielding" is often used with the intended meaning that vignetting has been included. The savvy researcher must use context or direct questioning to determine whether vignetting has been stealthily incorporated. In truth, there can be some vignetting contributed from the optical path, but the primary source is the objective lens, particularly for fisheye lenses.

In practice, only some specific calibration procedures will allow the vignetting effect to be isolated from the flat-fielding procedure. In the cases where no distinct vignetting characterization is performed, note that it is not possible to isolate the vignetting contribution coming from the lens, or to segregate the overall vignetting effect in order to distinguish it from the other flat-fielding components. In this section on optics spatial calibration, the two effects of vignetting and flat-fielding will be treated separately with notation made on where they are naturally combined.

3.4.2.1 Flat-fielding Calibration

Flat-field calibration corrects for the spatial variation along the optical path of the imager from the point where the objective lens attaches through to the detector. This fixed, inherent, spatial pattern impressed on individual images is due to instrumental effects such as variability in the optics train or pixel grain on the CCD. While the term "flat-field calibration" can sometimes refer to the process of applying the flat-fielding correction function to a data image, it usually refers to the process of determining the flat-field response for an imager system by generating the flat-fielding function, $O(\lambda)$ in Eq. 3.1 or O_λ in Eq. 3.6. In a lab environment, determining the flat-field response requires only one bench apparatus setup, and only one intensity (or attenuation) setting, but several data-collection steps depending on the number of filters to be analyzed. Note that each interference filter has its own unique flat-field response for a given imager.

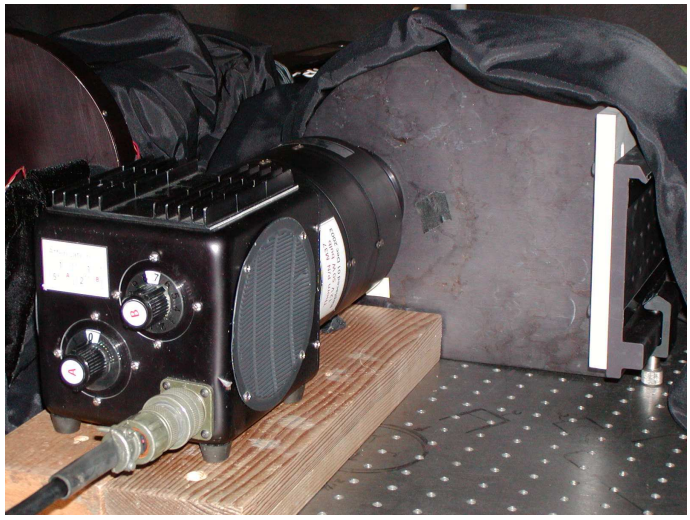

Figure 3.11: CASI and the portable calibrated light source configured for flat-fielding. The fisheye, objective lens of CASI has been removed, and the output diffusing screen of the light source is positioned flush to the opening of the imager housing the two plano-convex telecentric elements just prior to the filter wheel.

The measure of the flat-field response is determined by first taking multiple images of a known calibration source fully illuminating the field of view of the system. As noted in Section 3.3, it is a challenge to obtain a spatially and spectrally uniform flat field that fills the field of view of the instrument. For the portable calibration light source (PCLS), a low-light source, this means the output diffusing screen is positioned flush to the optical entrance of the camera with the objective lens removed, as shown for CASI in Figure 3.11. Other researchers using a diffusing light box with a collimating imager system, insert a diffuser in one location within the filter wheel in order to create a broadband flat field independent of filter characteristics [*Baumgardner*, personal communication]. For the integrating sphere source with internal lamps, full illumination means the imager is placed as far into the sphere as possible thus accounting for as much of the field of view as possible. Note that this camera placement changes the radiometric properties of the sphere, and as such is only suitable for flat-fielding evaluation; i.e., it is unsuitable for radiometric calibration. Note also that the integrating sphere will allow for the combined vignetting with flat-fielding function to be determined *using flat-fielding procedures* (as opposed to the PCLS which only permits determination of the combined function using vignetting procedures to be discussed in the next section). When the integrating sphere is used to determine the combined vignetting with flat-fielding function, the objective lens remains attached to the imager as the imager is placed as far as possible into the sphere, again affecting the radiometric properties of the source. In either of these two cases (with or without the primary lens) involving the integrating sphere, objects such as lamps or vents around the edge of the sphere may appear in the image due to the placement of the imager. These non-"flat" objects should be removed from the image, and the image smoothed.

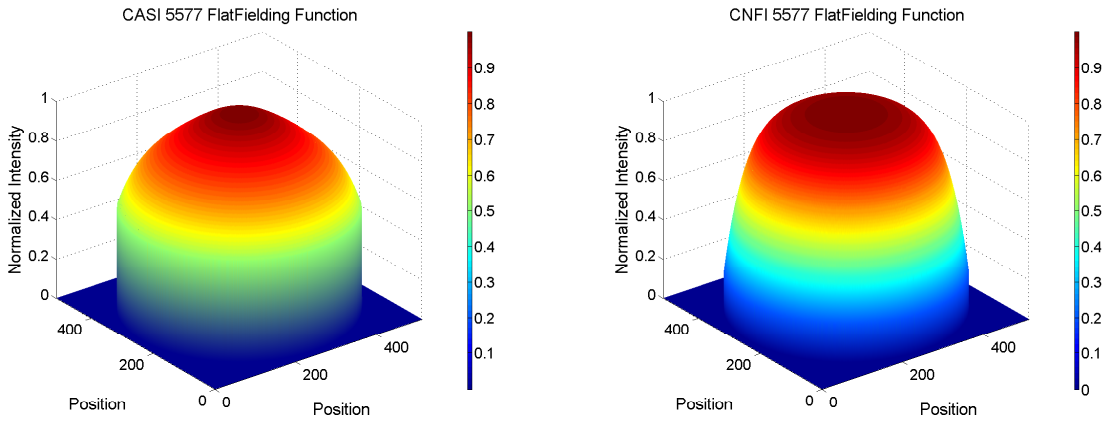

(a) CASI 5577 (b) CNFI 5577

Figure 3.12: Panels (a) and (b) show 3-D plots of the flat-fielding function for the 557.7-nm filters in CASI and CNFI, respectively.

When collecting the flat-field images using either calibration source, images should be taken for each filter at the standard operating procedure exposure time. Only one intensity setting is required. For statistical purposes, multiple images (at a minimum 3) should be taken for each configured setting and averaged. This collection of multiple images per filter, for both CASI and CNFI, is included in Appendix F. Figure F.1 shows the "raw" flat-field data taken for CASI, while Figure F.2 shows the same for CNFI, both using the portable low light source (PCLS).

Secondly, a master dark image should be generated as described in Section 3.4.1, and subtracted from the averaged, fully-illuminated images. The resultant image should be fairly uniform and will contain the flat-field response of the camera for a particular filter. Lastly, this flat-field response image must be normalized. This final normalized image will serve as the flat-fielding function for the given filter-camera combination. Three-dimensional plots of representative flat-fielding functions are displayed in Figure 3.12; plots for the remain-

ing filters are shown in Appendix F (see Figure F.3 and Figure F.4). Results of statistical analysis performed on the flat-fielding functions are also provided in Appendix F for additional detail: Two-dimensional plots of the flat-field responses for CASI are shown in the left-hand panels of Figures F.5 – F.7; those for CNFI are shown in the left-hand panels of Figures F.8 – F.9. The red circle in each of these images corresponds to the field of view of the primary lens, which although removed for this data-collection series, indicates the region to which the statistical calculations, summarized in the right-hand panels, were confined. Histograms of the flat-fielding function are presented on standardized scales in the middle panels.

When called for during calibration procedures, flat-fielding is applied to data by dividing the flat-fielding function array into an image that has had the dark current subtracted. At other times, such as in routine airglow data processing, flat-fielding is applied to data by dividing a background-subtracted image by the flat-fielding function array (i.e., the "flat-fielding image"). These two operations are approximately analogous with respect to dark current since the background image, itself, also contains the additive dark-current imprint of the system. Subtracting the background image, in essence, cancels the dark current evident in the source image, as well as removes the airglow continuum captured with the background filter. Either way – having subtracted the dark current or background first – the effect of then applying the flat-fielding function to an image is to remove the non-uniform sensitivity within the system as illustrated in Figure 3.13 for the BGND filters in CASI and CNFI. Notice the desired effects of flattening the data profile and of brightening the edges of the image. Results for some additional filters are included for reference in Appendix F (see Figure F.10 and Figure F.11).

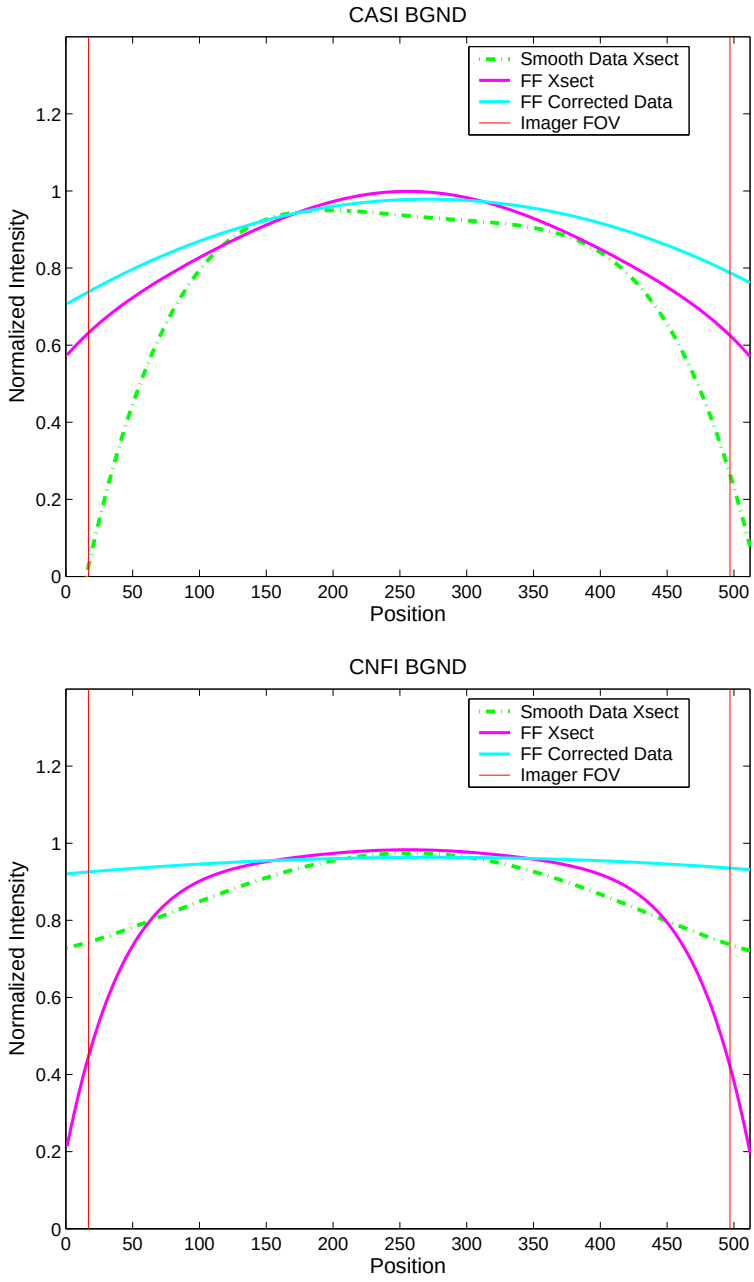

Figure 3.13: These example plots illustrate the application of the flat-fielding function for both CASI and CNFI. For both imagers, cross-sections are shown for an example BGND dataset (in green), and the same dataset corrected by the flat-fielding function for the BGND (541.0-nm) filter (in light blue). Note the attenuation evident on the sides in the original dataset has been rectified following the flat-fielding.

Worth noting again here is a point of confusion regarding the semantics of flat-fielding. In this section, we have been discussing the optical path definition of flat-fielding disregarding the objective lens, and procedures for generating this strict flat-field response. However, often the term flat-fielding is used in general to represent the combined effect of applying both flat-fielding and vignetting functions. When flat-fielding is performed in routine processing of airglow data, this combined operation is what is usually meant. As noted earlier in this section, using the integrating sphere allows for the generation of a combined function using the flat-fielding calibration procedure, with the limitation that the separate components (flat-field function and vignetting function) cannot be isolated unless additional calibration data is obtained with the primary lens removed. Vignetting calibration procedures are discussed in the next section, whereby a combined function (the practical goal) is produced, and uncoupled response functions can be obtained when combined with the flat-fielding results from this section.

3.4.2.2 Vignetting Calibration

Vignetting calibration corrects for the decrease in radiance brightness generated by the objective (i.e., primary) camera lens at the edges of the field of view. This radially symmetric effect is ubiquitous for commercial camera lenses, but is more pronounced for wide-angle lenses such as the fisheye lens. Lens vignetting, $L(\lambda)$ in Eq. 3.1 or L_λ in Eq. 3.6, is usually combined with flat-fielding, both in ascertaining its effects and in applying correction functions to image data. Depending on the calibration source used, the method for determining the lens vignetting effect may vary. Regardless of the procedure or source used,

Figure 3.14: Vignetting data-collection setup for CASI on optics bench at Maui Remote Experiment site.

note that the calibration measurements obtained represent a combined effect, coupling the vignetting response with the flat-fielding response. The approach for isolating the vignetting function is to measure the flat-fielding response and to divide it into the combined function to obtain the vignetting response. In this section, care will be taken to avoid the semantics pitfall, making a distinction in the terminology, where appropriate, by referring to the effect of only lens vignetting as the "isolated vignetting function", $L(\lambda)$, and referring to the combined effect of vignetting and flat-fielding as the "coupled vignetting function", $LO(\lambda)$. Although this coupled effect is what is often referred to in general as flat-fielding, the procedures described below are considered vignetting calibration procedures. Where no semantic distinction is made below, the vignetting reference applies to either type of response – coupled or isolated.

Determining the vignetting function requires changing the physical laboratory bench setup through multiple stages. To begin, the calibration source should be placed some distance from the camera such that the source appears as a sizeable spot on the image, but far enough away to avoid back-loading. While positioned equidistant from the camera, the source should be moved radially through small angles across the field of view of the camera from edge to edge, passing through the center of the field of view. Some recommend the small angles should allow the source to overlap in the images from successive angle positions [*Baumgardner*, personal communication]. Figure 3.14 illustrates a bench setup for vignetting data collection. Note that the multitude of black cloth has been pulled back to show the equipment arrangement for the photograph. In practice, even in a darkroom environment with lights out and computer monitors turned off, the black velvet and felt cloth, along with black cardboard, black electrical tape, and black drapes covering the entire bench are all

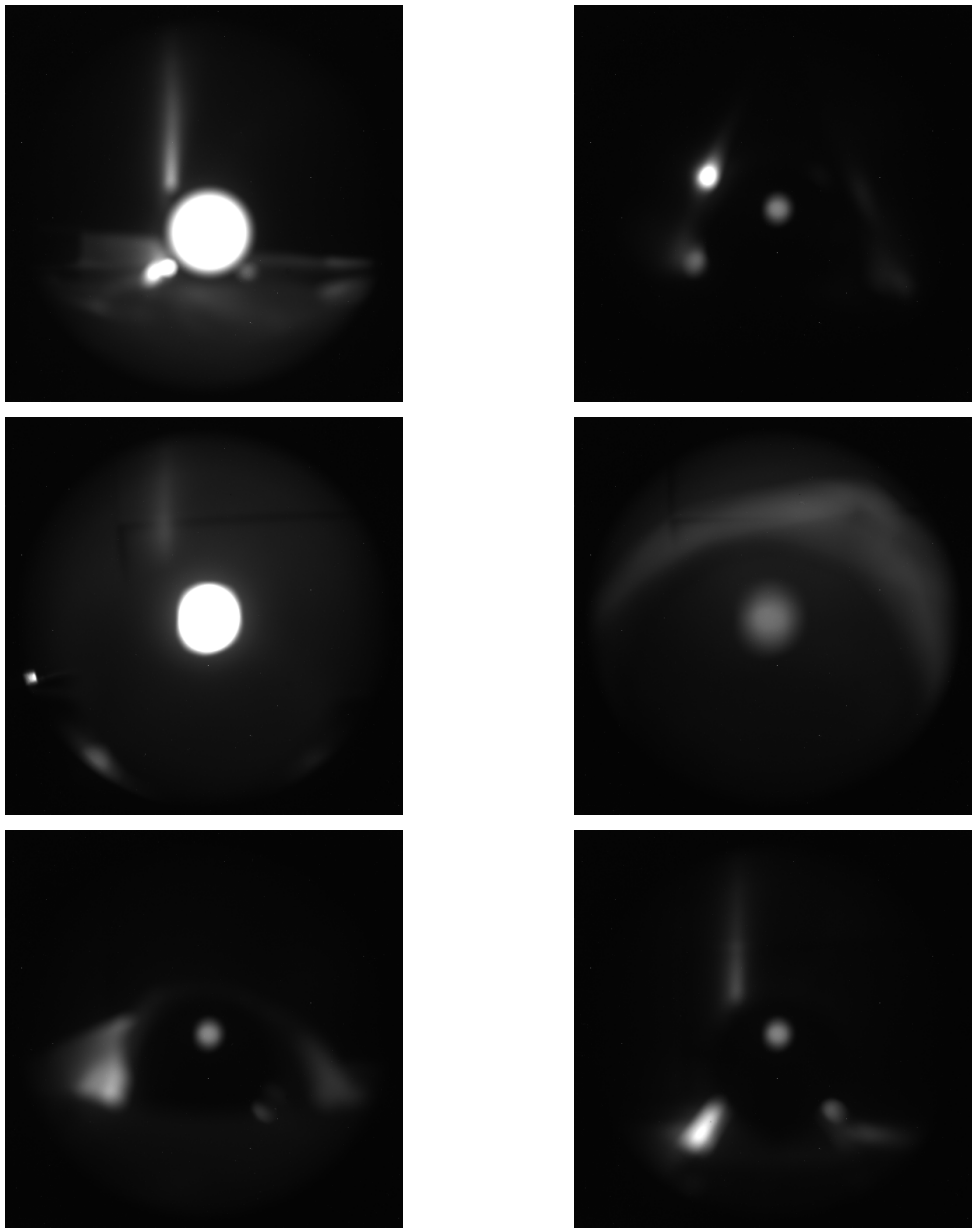

Figure 3.15: The six panels illustrate an assortment of the glaring encountered during the setup stage for vignetting calibration of CNFI. Through trial-and-error the various elements contributing to the glare were identified and eliminated prior to beginning the calibration procedure.

needed to eliminate unwanted glares. Figure 3.15 illustrates some of the glares identified and eliminated at the Maui Remote Experiment site while setting up for this vignetting calibration session.

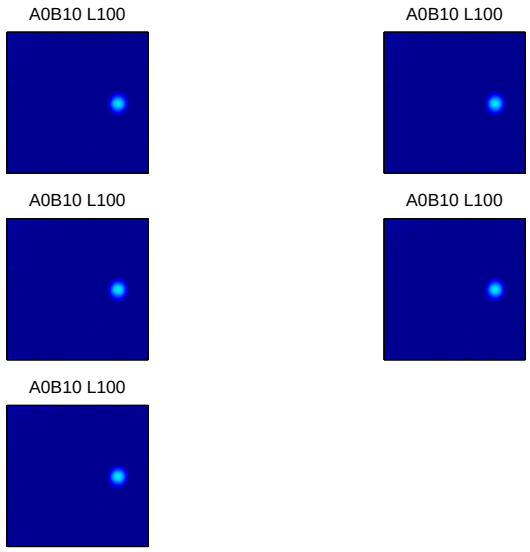

Figure 3.16: The five 90s exposure images above illustrate raw individual vignetting images taken for the 557.7-nm filter in CNFI. The above data were taken with the PCLS positioned 10° left of center in the horizontal plane. The attenuation setting for the PCLS was held constant at A=0, B=10 throughout the vignetting procedure for this imager.

In order to track the positions transitioned across the field of view in this study, a simple protractor and string arrangement was devised. As shown in Figure 3.14, the protractor was fixed in place on the optics bench and aligned with the center of the primary lens. A string attached to the calibration light source intersected the protractor at each new imaging position. At each of these positions, multiple images as shown in Figure 3.16 should be taken for each filter and averaged. The attenuation setting on the calibration source used for a particular combination of filter and imager should remain constant throughout the vignetting data-collection sequence. Upon completion of the transition of the source horizontally from left to right, data for the perpendicular axis (that

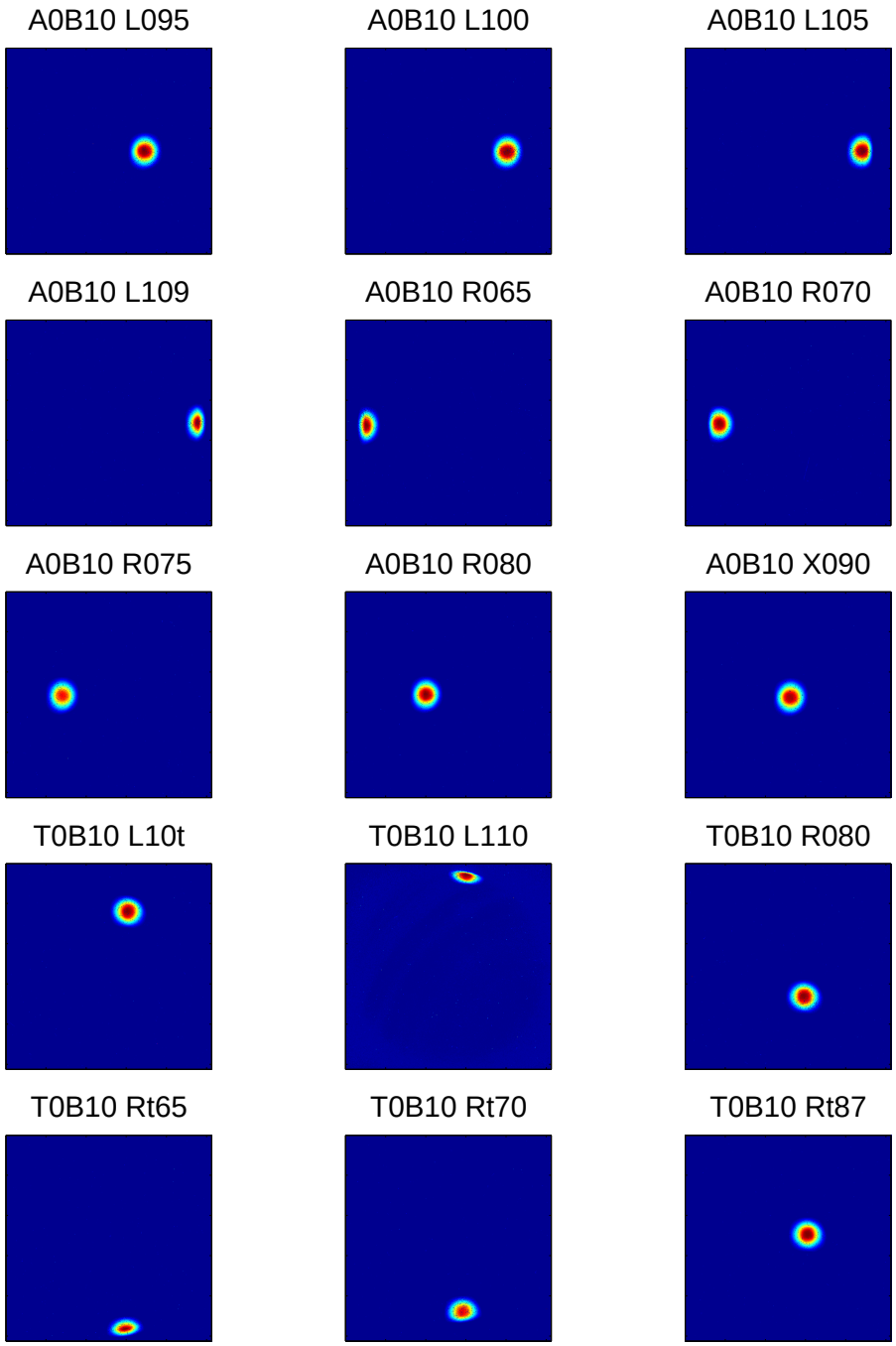

Figure 3.17: The above panels show the set of processed images for all the vignetting positions collected for the CNFI 557.7-nm filter. The image in each of the above panels is the flat-fielded, average of a sample (as shown in Figures 3.16) of images with the dark count removed. The subtitles represent the attentuation settings and rotation position.

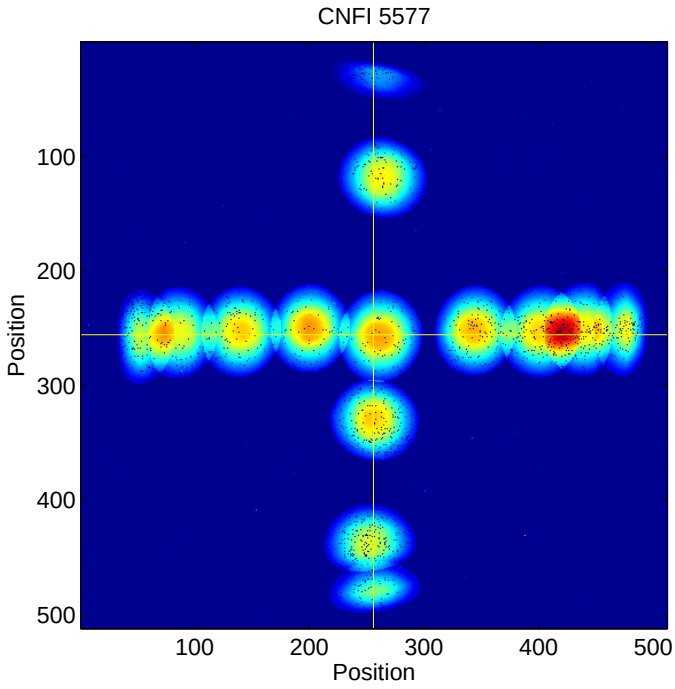

Figure 3.18: 2-D vignetting data compilation for the 557.7-nm filter in CNFI.

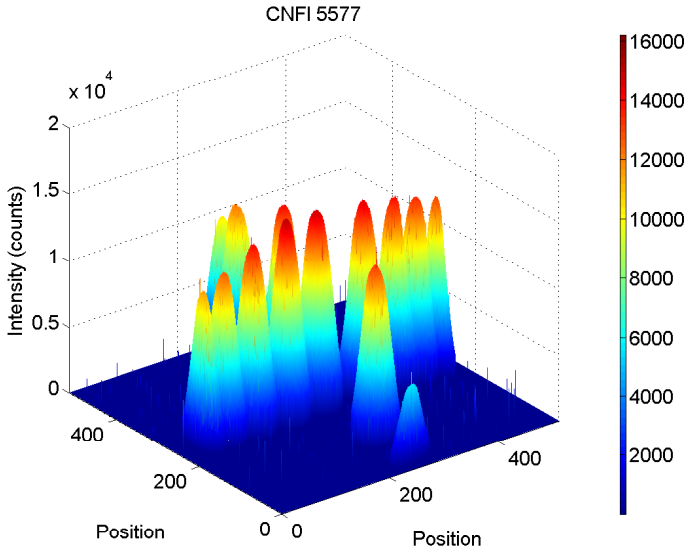

Figure 3.19: 3-D vignetting data compilation for 557.7-nm filter in CNFI.

is, the vertical up and down direction) can be obtained by rotating the camera 90° and repeating the process. This alleviates the need to develop a mechanism to position either the light source or the imager in the vertical plane. Following this series of data collection, the average image for each position should then have the master dark image subtracted. As an example, Figure 3.17 displays the average images with the master dark removed for all the vignetting positions collected for the 557.7-nm filter in CNFI.

To generate a vignetting function from this dataset series (as collectively shown in both Figure 3.18 and Figure 3.19), the final (i.e., averaged with master dark subtracted) images from all positions are used to create a two-dimensional radial profile. To begin, we must identify the peak brightness values from the light source as recorded in each of these average images corresponding to a source position. In this study, for CNFI in particular, false maximum values ("speckles") lying outside the spatial range of the light source were encountered. The scope of these false maximum values were individual pixels in varying locations within the array, perhaps due to the combination of aligned, hot pixels in the averaging process. A pre-processing procedure was performed to identify and to remove these outliers prior to determining the vignetting position peak. To highlight point-size intensity spikes, the difference between the first and second derivatives of the array was analyzed. An example of this differential for the x-direction, i.e., $\partial N/\partial x - \partial^2 N/\partial^2 x$, is shown in the left-hand panel of Figure 3.20. The maximum values of this differential array were evaluated, and those falling outside of $5\,\sigma$ from the mean were set to zero. The right-hand panel of Figure 3.20 shows the maximum values across the columns both before (indicated with the blue dot-dash line) and after (indicated in green) the speckles were removed.

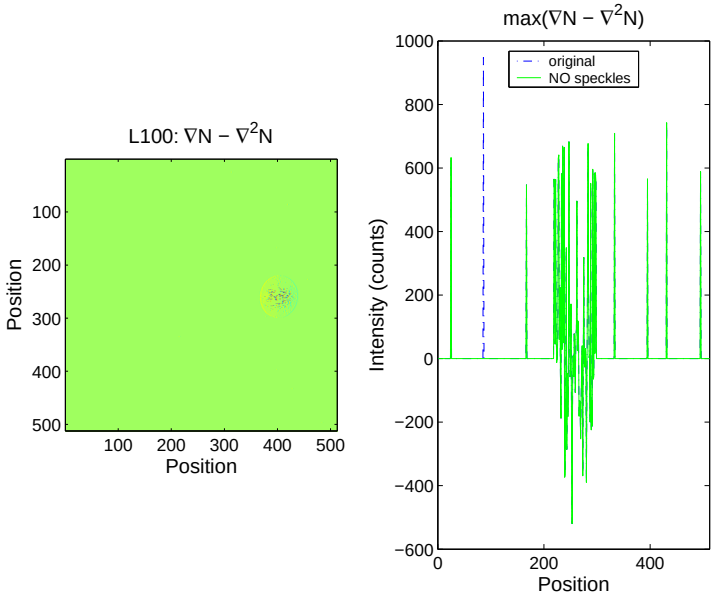

Figure 3.20: Vignetting-profile speckle removal results for the case when the light source was placed 10° left of center (right of center from the perspective of the imager) in the horizontal plane: The left-hand panel shows a plot of the gradient with respect to x of the vignetting profile for this placement with the Laplacian (also with respect to x) of the profile subtracted. The right-hand panel shows the maximum values for the rows of the image on the left. The blue dot-dashed line indicates that only one high-intensity point (speckle) was located outside the specified parameters of 5σ from the mean. The green line shows the maximum row values after the outlying point was set to zero.

Once any misleading speckles were removed, the maximum brightness values were identified for each source position as highlighted by the red overlays on the cross-sections shown in Figure 3.21. Both horizontal and vertical profiles were then compiled by combining the peaks from the corresponding directions. Once the peaks were collected, polynomial functions were fitted to these points to create smooth profiles as shown by the green curves overlaying the peaks in Figure 3.22. The next step was to generate a representative one-dimensional average radial profile by averaging the left and right halves of both the horizontal and vertical profiles. As depicted in Figure 3.23, the horizontal (blue solid line) and vertical (green dot-dash line) profiles were first averaged to generate

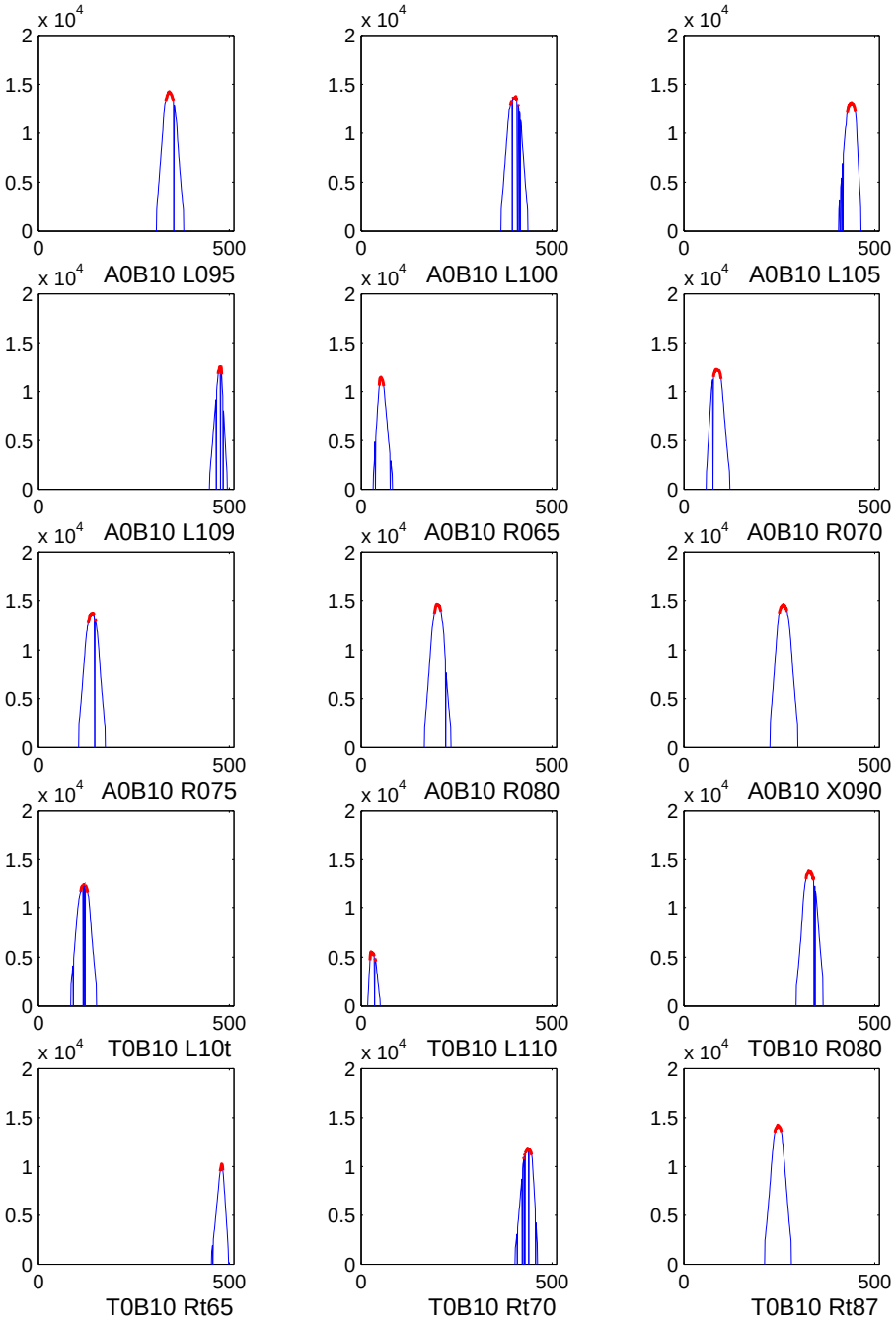

Figure 3.21: Each panel shows an individual cross-section for one of the light source placement positions evaluated in the vignetting calibration for CNFI for the 557.7-nm filter.

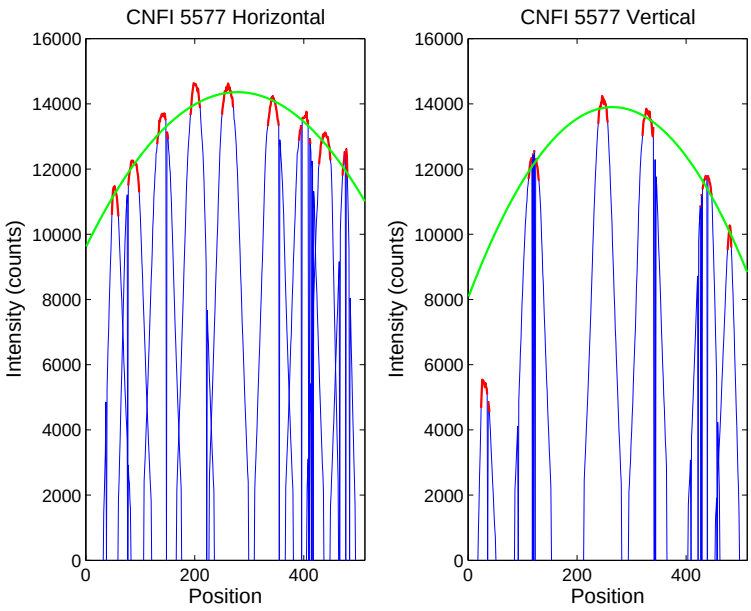

Figure 3.22: The left panel shows in blue the amalgamated plot of individual cross-sections from images of light-source positions along the horizontal axis. The peaks found for each individual position are highlighted by the red overlays. The polynomial function fit to the peaks is shown in green. The right-hand panel shows the same information plotted for the vertical axis. All the data shown is for the 557.7-nm filter in CNFI.

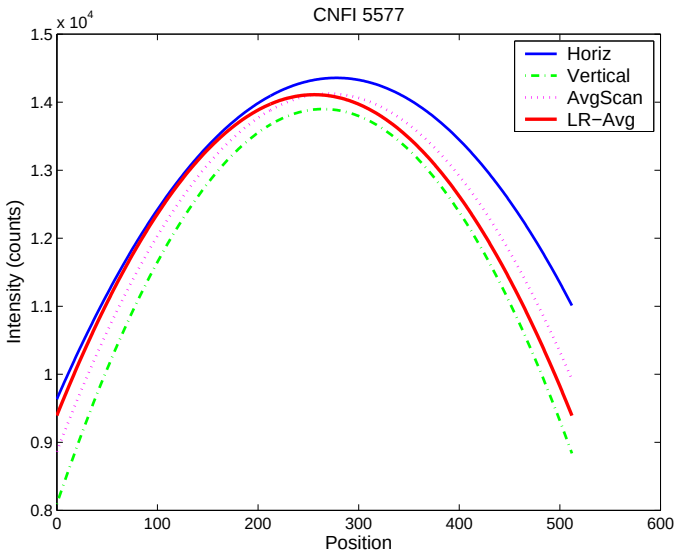

Figure 3.23: Plots of the horizontal and vertical vignetting profiles for the 557.7-nm filter in CNFI are shown, along with the average (magenta dotted line) of these two scans. Additionally, the left-right average of this average scan is shown (red solid line).

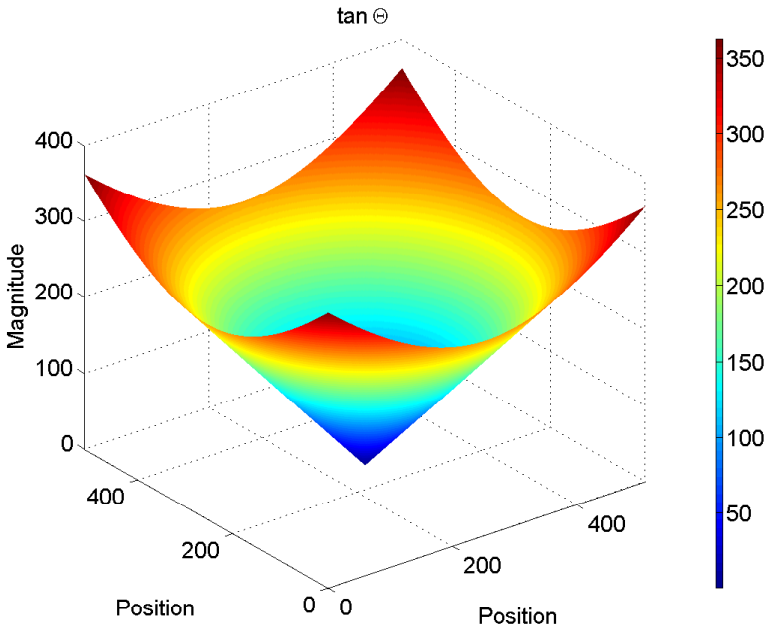

Figure 3.24: Reference array comprised of the magnitude of tangent values corresponding to the cartesian coordinates for each pixel in a 512×512 square array.

a combined profile, and then further, the left and right halves of this average scan (magenta dotted line) were averaged to generate the overall average radial profile (red solid line). Sweeping this average radial profile through 360° generates the 2-D vignetting function. As a starting point for this process, a radial reference array was generated as shown in Figure 3.24. This reference array, comprised of the tangent values corresponding to the cartesian coordinates for each pixel in the 512 × 512 CCD, allows us to identify all the points lying on a circle of given radius within the square array. With this radial reference array in place, one can march outward from the origin at the center of the array, stepping through concentric circles with ever-increasing radii. In another array initialized to zero, the pixel locations for each successive concentric circle are set to the brightness value for the corresponding radial distance in the one-dimensional radial profile. The process is chronicled in Figure 3.25. The middle panel shows examples of three of the concentric circles. The values for all points

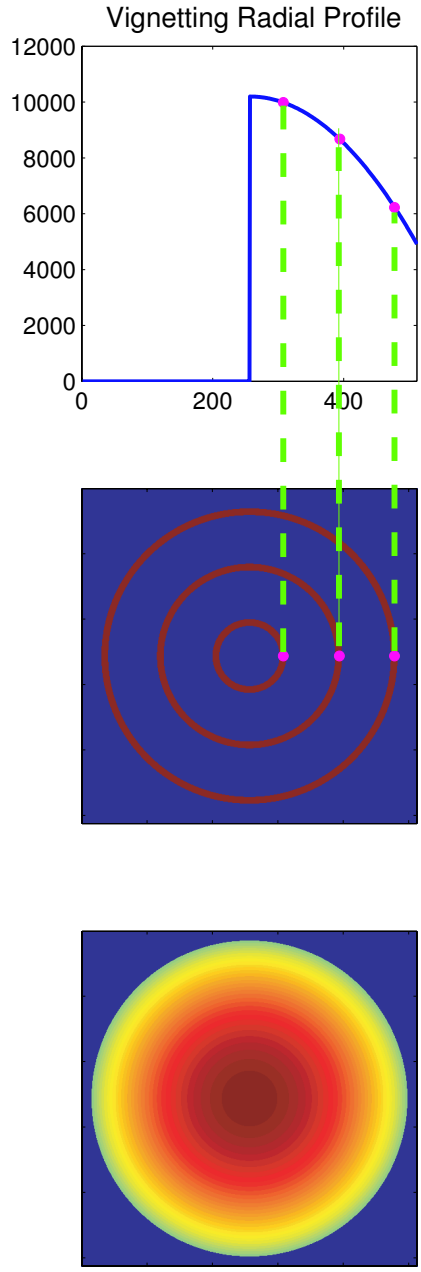

Figure 3.25: "Spinning" radial profile process: The top panel shows the radial vignetting profile for the 630.0-nm filter in CASI. All the points in each concentric circle in the middle panel are set to the corresponding value in the radial profile; three representative concentric circles are shown for illustration. The bottom panel shows the resultant 2-D contour.

in each of these circles were set to the brightness values in the corresponding radial location in the one-dimensional profile for the CASI 6300 filter, depicted in the top panel. The resultant two-dimensional coupled vignetting profile is in the bottom panel. Alternatively, three-dimensional plots provide an illustrative perspective; for the 5577 filters in CASI and CNFI, the coupled vignetting profile brightness is presented in Figure 3.26. Similar three-dimensional plots for the remaining filter-imager configurations are shown in Appendix F (see Figure F.12 and Figure F.13).

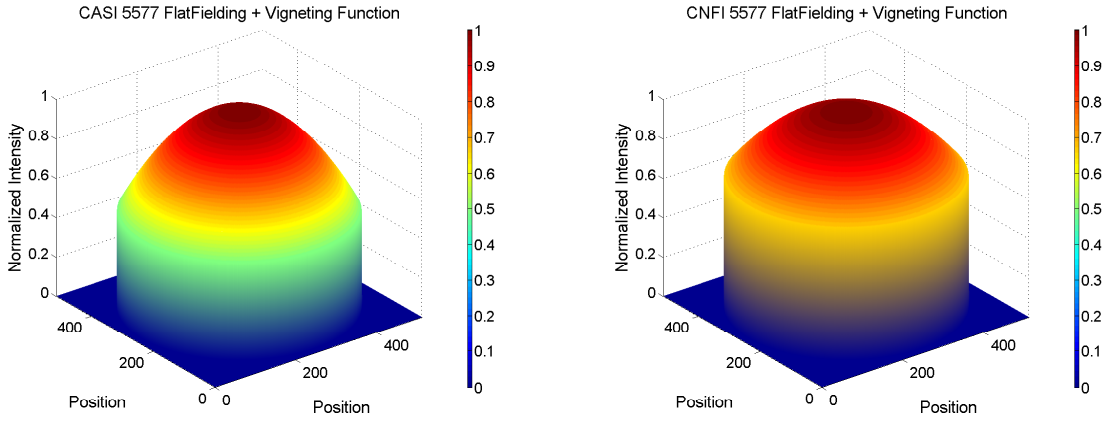

(a) CASI 5577 (b) CNFI 5577

Figure 3.26: Panels (a) and (b) show 3-D plots of the vignetting with flat-fielding functions for the 557.7-nm filters in CASI and CNFI, respectively.

Having generated the coupled vignetting function, the isolated vignetting response can now be determined as mentioned earlier in this section. Simply dividing the coupled vignetting response by the flat-field response from Section 3.4.2.1 yields the isolated vignetting function shown in Figure 3.27. This isolated vignetting function characterizes the vignetting response for the primary lens in the optical system.

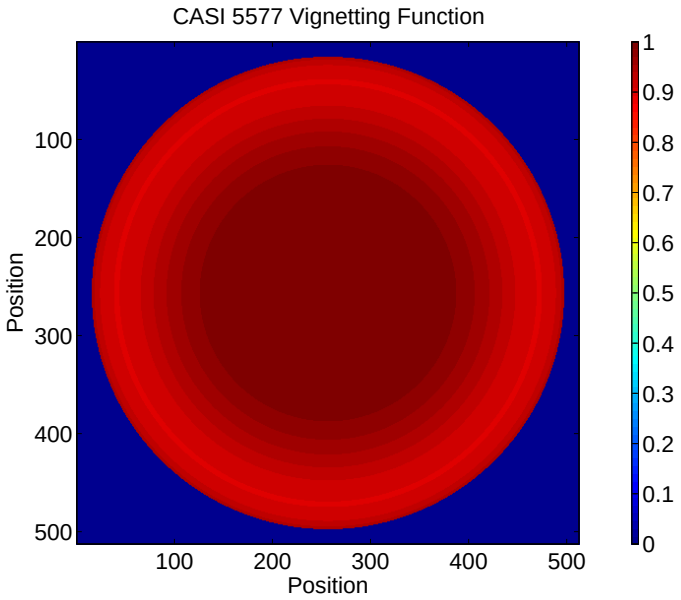

Figure 3.27: Two-dimensional plot of vignetting function for 557.7-nm filter in CASI.

Just as described for flat-fielding at the end of Section 3.4.2.1, the vignetting function is applied to data that has already had either the dark current or the background subtracted. In practice, it is usually the coupled vignetting response that is used. Otherwise, to achieve the same results, a two-stage correction would be needed, applying both the strict flat-fielding function (with objective lens removed) and the isolated vignetting function. Again similar to the flat-fielding function, the effect of applying the coupled vignetting function to an image is to remove the non-uniform sensitivity within the system achieving the desired effect of flattening the data profile. Dissimilar in this vignetting correction scheme is the greater brightening achieved at the edges of the image as illustrated in Figure 3.28. Results for some additional filters are included for reference in Appendix F (see Figure F.14 and Figure F.15).

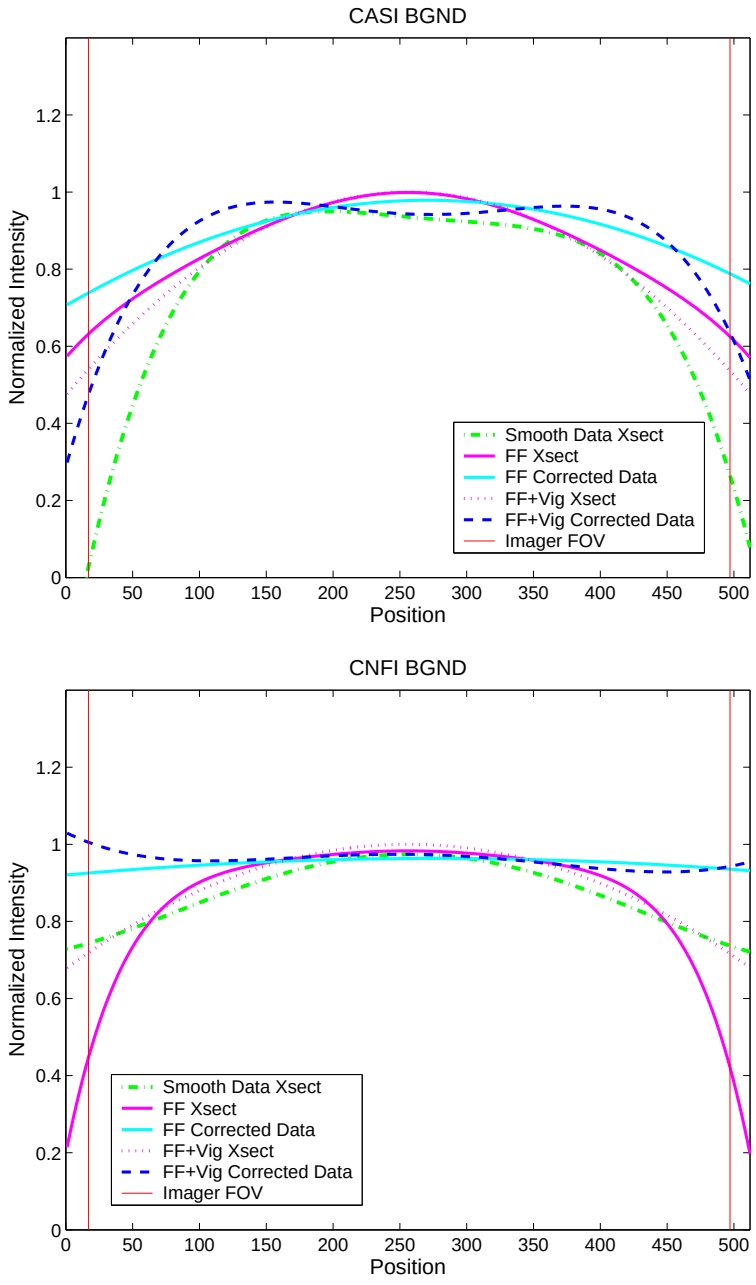

Figure 3.28: These example plots illustrate the application of the coupled vignetting with flat-fielding function for both CASI and CNFI. For both imagers, cross-sections are shown for an example BGND dataset (green dash-dot line), and the same dataset corrected by the coupled vignetting with flat-fielding function for the BGND (541.0-nm) filter (dark blue dashed line). Note the attenuation evident on the sides in the original dataset has been rectified following application of the coupled vignetting correction function (dotted magenta line). Cross-sections for the flat-fielding correction function (solid magenta line) and flat-field-corrected data (solid light blue line) are shown for comparison.

3.4.3 Filter Calibration

Filter calibration characterizes the transmission properties, $T(\lambda)$ in Eq. 3.1 or T_λ in Eq. 3.6, of the interference filters used to isolate emission bands in airglow studies. Depending on the type of imager system in which the filters are housed, and the purpose of the filter calibration, the extent of the filter characterization process varies.

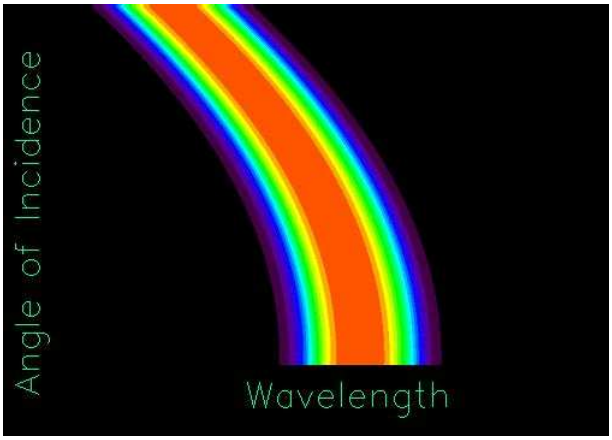

Figure 3.29: Example 2-D plot representing filter passband shift with angle of incidence (AOI) for a collimating imager system. A horizontal cut through this plot is a standard filter transmission curve at a given AOI. A vertical cut through this plot is the transmission of a filter at a specific wavelength as a function of AOI. (Plot courtesy of J. Baumgardner, Boston University.)

If the end goal is brightness calibration for a collimating system, a filter transmission array is required. To generate this array, start by building up a 2-D plot, like that in Figure 3.29, of filter shift with angle of incidence. Each horizontal cut through this 2-D plot is the standard filter transmission curve at a given angle of incidence. As illustrated in Figure 3.30, each vertical cut is the transmission of the filter at a specific wavelength as a function of incidence angle. Finally, use a vertical cut to make a radially symmetric function using the method described in Section 3.4.2.2 above for generating a λ-specific filter-induced vignetting cor-

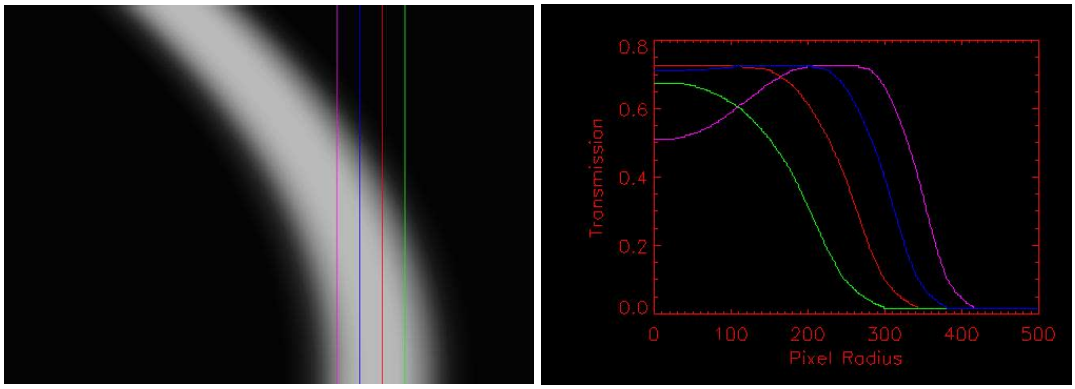

(a) (b)

Figure 3.30: Panel (a) is a 2-D plot of angle of incidence (AOI) versus wavelength, similar to Figure 3.29, showing filter passband shift with AOI. Panel (b) shows several vertical slices through the 2-D plot in panel (a) with each corresponding to a different wavelength. For a given wavelength, the corresponding vertical cut profile can be spun 360° to generate a radially symmetric filter function representing the transmission shift with AOI. (Plots courtesy of J. Baumgardner, Boston University.)

rection array.

For telecentric systems, it is sufficient to use only the standard filter transmission curves. However, as shown later in Section 3.4.4, depending on the processing scenario, it may be necessary to calculate the area under the curve over the passband of the filter.

The nine filters utilized in the two imagers (CASI and CNFI) currently fielded in Maui were calibrated on-site at the Maui Space Surveillance Site. Characterization curves were obtained by Boeing Incorporated using their in-house spectrometer. As the data was supplied in graphical form only, gaussian probability density functions were fitted to the plots to create digital vector representations required for the brightness calibration calculations. The recreated characterization curves for each of the filters are shown in Appendix F in com-

posite plots fitted to the same scale in Figure F.16 and Figure F.17. The individual profile plots showing more detail are collected in Figure F.18 and Figure F.19. Also in Appendix F, peak transmission values are recorded in Table F.1, along with the result of integrating the transmission curve over the entire passband for each filter. Filter identification information is also included in this table for reference.

3.4.4 Brightness Calibration

Brightness calibration facilitates the conversion of relative brightness measurements to absolute brightness values – that is, to standardized brightness scales or units. It allows us to determine the value of $I(\lambda)$ in Eq. 3.1 or I_λ in Eq. 3.6. With brightness calibration, data previously constrained to qualitative analysis can now be used quantitatively. In addition, the data can then be further converted to scales (specifically, rayleighs) useful for comparative analysis.

Regardless of the imager type (telecentric or collimating), the overall procedure for determining the responsivity of the system is the same for brightness calibration. The strategy for brightness calibration is to determine the conversion factor to correlate the flux received at the detector as pixel counts to the actual radiance emitted by the source. More specifically, our end goal for the conversion is finding the ratio of pixel (or photon) counts to rayleigh-seconds; the ratio, or conversion factor, is noted as G below and has units of $[counts/s/R]$. Determining and applying G include a number of steps; each step will be explained in detail following the summary below:

1. Specify G:

   Define G in equation form by representing pixel counts in terms of the source radiance, pulling wavelength-independent terms out of the integral, and designating these wavelength-independent terms outside the integral to be G.

2. Determine Actual Counts:

   Determine the counts actually received at the detector by taking a series of images at progressively longer exposure times of a source with known spectral radiances calibrated to standards traceable to the National Bureau of Standards, removing the dark count, and applying flat-fielding.

3. Determine Expected Number of Rayleighs:

   Determine the number of rayleighs expected at the detector given the characteristics of both the specific imaging system and the radiant source.

4. Calculate G:

   Calculate G by multiplying the expected number of rayleighs by the integration time, and dividing the term into the number of counts: $G = N/(< I_{R/\lambda} > \cdot t)$

5. Apply G:

   Determine a method for applying the G factor to ascertain the brightness in rayleighs given the pixel counts in an image from a realistic airglow environment.

3.4.4.1 Specify G

To define G, we need to represent pixel counts at the CCD in terms of the spectral radiance of the source. In airglow radiometry, the standard units for rep-

resenting and comparing calibration source radiances, as when comparing the absolute brightness of images, is in terms of rayleighs. Since the manufacturers of the calibrated light sources usually specify the spectral radiances as a function of wavelength in units of $[W/cm^2/sr/nm]$, we must first convert the units to $[R/nm]$. As part of this conversion, we use the energy, E, of a photon:

$$E(\lambda) = \frac{hc}{\lambda}, \tag{3.10}$$

where h is Planck's constant ($6.626 \times 10^{-34} Js$) and c is the speed of light ($3 \times 10^8 m/s$). E has units of $[J/ph]$ or, noting that $1W = 1J/s$, the units become $[W \cdot s/ph]$. We also make use of the fact that the apparent emission rate in rayleighs is $4\pi I_{R/nm}$; that is, if I is measured in units of $[10^6 ph/cm^2/s/sr]$, then $4\pi I$ is in rayleighs, and the factor $\frac{4\pi}{10^6}$ can be used to convert from $[ph/cm^2/s/sr]$ to $[R]$. Using E and this conversion factor, we can obtain the radiance, $I_{R/nm}$:

$$I_{R/nm} = \frac{4\pi}{10^6} \cdot \frac{I_{W/cm^2/sr/nm}}{E}, \tag{3.11}$$

where the units cancel as follows:

$$\frac{R}{nm} = \frac{sr}{ph/cm^2/s/R} \frac{J/s/cm^2/sr/nm}{J/ph}. \tag{3.12}$$

Note that although the original spectral radiance of the PCLS lamp filament is given in terms of $[\mu W/nm^2/sr/nm]$, the latest spectral output curve provided with the source has already been converted to units of $[R/\text{Å}]$ as indicated in Figure 3.5. Hence, we must only divide the given spectral radiance by 0.1 to convert from $[R/\text{Å}]$ to $[R/nm]$.

Now, to determine G, we use $I_{R/nm}$ as the brightness value in the formula for our airglow image model given in Eq. 3.1, along with a few other modifications

to yield Eq. 3.13 below. Note that special notation is made to indicate that $I(\lambda)$ is given in units of $[R/nm]$, and the corresponding conversion factor $(10^6/4\pi)$ is included. Also, the term $F_{ND}(\lambda)$ is included to facilitate neutral density filters, if required. The terms $V(\lambda, W)$, n_{ST}, n_{BG} and n_{RD} are omitted here; there obviously are no sky effects on the data or background sky emissions in the laboratory setting, and read noise is considered negligible in these calculations. The counts collected at the CCD can then be represented in terms of the spectral radiance of the source as [modified from *Shiokawa et al.* [2000], and corrected for the omission of the term t]:

$$\mathcal{N}^{(i,j)} = t \cdot \int \frac{10^6}{4\pi} L(\lambda)\, O(\lambda)\, I_{R/nm}(\lambda)\, A\Omega\, T(\lambda)\, F_{ND}(\lambda)\, q\, d\lambda + N_{DK} \tag{3.13}$$

where the variables with respective units and definitions are tabulated as follows:

$\mathcal{N}$	$[counts]$	image data array for emission wavelength(s)
(i, j)		indices into this data array, $\mathcal{N}$, of measured counts
t	$[s]$	exposure time
$10^6/4\pi$	$[ph/cm^2/s/sr/R]$	factor to convert from $[R]$ to $[ph/cm^2/s/sr]$
$L(\lambda)$	dimensionless	λ-dependent lens-vignetting function
$O(\lambda)$	dimensionless	λ-dependent flat-fielding function
$I_{R/nm}(\lambda)$	$[R/nm]$	λ-dependent source signal strength
$A\Omega$	$[cm^2 sr]$	system throughput (or Etendue) of the imager
T_λ	dimensionless	λ-dependent optical transmittance of the filter
$F_{ND}(\lambda)$	dimensionless	neutral density filter transmission coefficient
q	$[count/ph]$	detector quantum efficiency incorporating gain
N_{DK}	$[counts/s]$	dark current signal contribution.

Pulling the terms independent of wavelength out of the integral, we get:

$$\mathcal{N}^{(i,j)} = t \cdot \frac{10^6}{4\pi} A\Omega\, q \int L(\lambda)\, O(\lambda)\, I_{R/nm}(\lambda)\, T(\lambda)\, F_{ND}(\lambda)\, d\lambda + N_{DK} \tag{3.14}$$

such that

$$G = \frac{10^6}{4\pi} A\Omega\, q \tag{3.15}$$

and $\mathcal{N}$ can now be written as

$$\mathcal{N}^{(i,j)} = t \cdot G \int L(\lambda)\, O(\lambda)\, I_{R/nm}(\lambda)\, T(\lambda)\, F_{ND}(\lambda)\, d\lambda + N_{DK}. \tag{3.16}$$

3.4.4.2 Determine Actual Counts

Given the wavelength dependencies in Eq. 3.14, the imager is calibrated for each wavelength band studied – that is, for each filter. As such, the matrix of data collected for brightness calibration includes multiple images taken at multiple exposure times at multiple calibration source brightness settings for each of the filters. Recording images from multiple exposure times as well as from multiple brightness settings allows the linearity of the system to be analyzed. Targeting exposure times near normal field-use values, typical exposure times for calibration are 20s, 45s, 60s, and 90s. Multiple brightness settings on the calibration source are used in a trial and error attempt to produce images of typical pixel counts for each arrangement. Normal pixel counts should provide some dynamic range while avoiding saturation. For low light calibration sources (specifically, the PCLS), intensities are varied by altering the internal baffling structure using external settings knobs. For large integration spheres, the brightness can be controlled by the number of internal lamps in use. For statistical purposes, multiple images should be taken at each test arrangement. Each multiple image collection should include 3 to 8 images, plus dark current images. Again, due to the overall wavelength dependency, this assembly of data is required for each filter.

As with the procedures for flat-field calibration, one physical bench setup

suffices for brightness calibration - that is, no movement or repositioning of the calibration source or the imager is required during the calibration. However, compared to flat-field calibration, this time the objective (i.e., primary) lens remains fixed in place in the system as per normal operating procedures. The distance the light source is placed from the front element of the imager system (for our systems, the objective lens) depends upon the type of source used. Distance requirements are specified by the manufacturer to ensure that the separation is sufficient to avoid back-loading. As described in Section 3.3, "back-loading" occurs when the brightness from the source is increased by light reflecting off a surface (such as the camera lens) back into the source. This affected increase in brightness can cause errors in the calibration. Depending on the field location and environment, the imager can either be moved and stationed on an optics bench in a darkroom environment, or remain in its field-deployed configuration. The disadvantage to the latter is being able to remove all stray light from entering the system, and being able to position the calibration source in a suitable, specified position relative to the imager. The obvious advantage of the lab arrangement is the ability to control the environment with respect to unwanted light sources and equipment position. As calibration can be a lengthy process, the comfort of the researcher might warrant one arrangement over the other as well.

To determine the actual number of counts for brightness calibration, a mean value is calculated for a defined region in the center of the average, flat-fielded brightness image with the dark count removed. Figure 3.31 illustrates the region of interest for this calibration study as denoted by the green box.

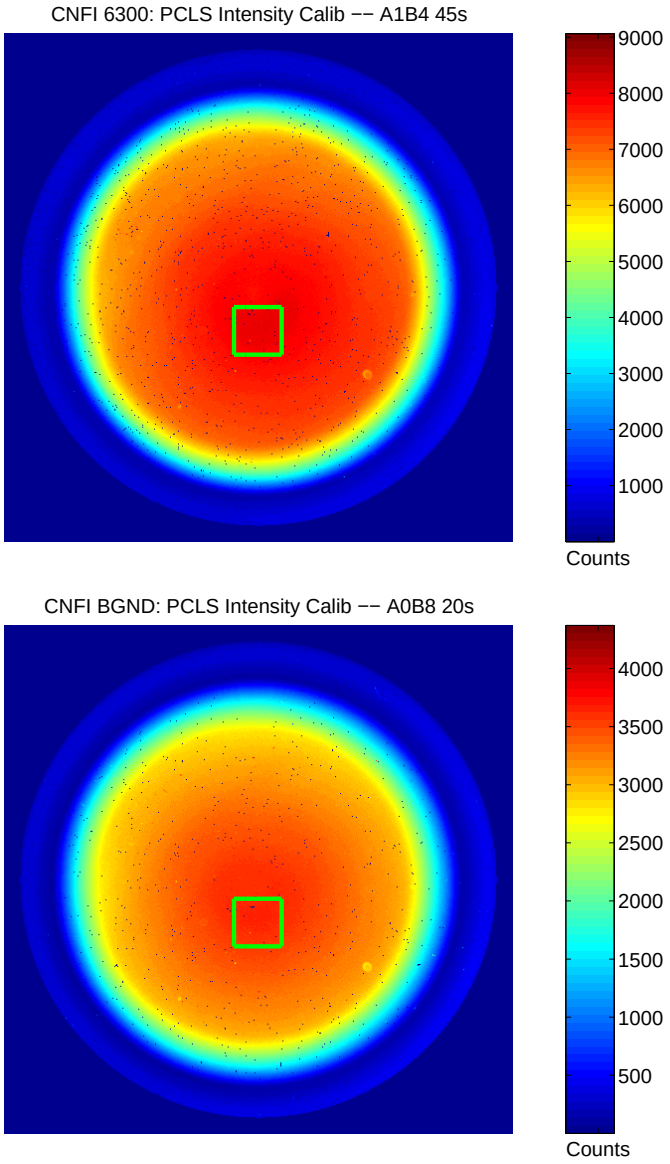

Figure 3.31: Example calibration brightness images for CNFI are shown. The top and bottom panels show example average brightness images taken for the 630.0-nm and background filters, respectively. The 6300 image is a 45s exposure taken with a brightness setting of A1B4 on the PCLS. The BGND image is a 20s exposure taken with a brightness setting of A0B8 on the PCLS. The green box in each image denotes the area used in the calibration calculation. The box is shifted down from center due to a slight misalignment between the PCLS and the imager.

3.4.4.3 Determine Expected Number of Rayleighs

To compare to the actual counts obtained at the CCD, we now determine the number of rayleighs expected at the detector given the characteristics of both the specific imaging system and the radiant source. Recall that the "actual counts" refers to those photon counts attributable to the radiant source, itself, so contributions to the measured count resulting from dark current and optical path variability were removed. Modifying Eq. 3.14 to reflect this processing applied to the measured counts, and noting that no neutral density filters were used in this study, we get:

$$\frac{(\mathcal{N}^{(i,j)} - N_{DK})}{L(\lambda)\, O(\lambda)} = t \cdot G \int I_{R/nm}(\lambda)\, T(\lambda)\, d\lambda. \tag{3.17}$$

The left side of the equation has units of [*counts*]. On the right-hand side of the equation, t has units of [s]; G has units of [$counts/s/R$]; and the integral has units of [R]. Hence, determining this integral is our goal in this section. The integral represents the rayleighs expected at the CCD, and can be written, in general, as:

$$I_{CCD} = \int I_{R/nm}(\lambda)\, T(\lambda)\, F_{ND}(\lambda)\, d\lambda. \tag{3.18}$$

If required, neutral density filters can be included as shown in Eq. 3.18. The combined effective neutral density filter transmission coefficient can be determined as discussed in Section 3.3, based on the formula in Eq. 3.9. The F_{ND} factor was not required in this study using the PCLS.

Our starting point for determining the value of $I_{R/nm}(\lambda)$ in the above equation is the spectral radiance curve for the source. As stated earlier in this section, the latest spectral radiance curve for the PCLS is given in units of [R/Å], so the reported values were divided by 0.1 to convert to units of [R/nm]. This calibrated output profile for the source is based on having the attenuation knobs

for the unit set in the full-open position. Each of the settings for knobs A and B employed in this study reduced the transmitted radiance of the source and must be factored in here to reflect the true radiance projected. It is important to note again here, for this particular calibration source, the full-open position is expected to be engaged with knob A = 2 and knob B = 11. However, it is imperative to verify this fact since any unintended adjustment to the alignment of the knobs will impact the entire calibration results as the formula for the attenuation factor is directly based on these full-open position values. For this study, the full-open positions were verified to be, surprisingly, knob A = 2 and knob B = 10. Also, on a semantics note, it is important to clarify that the formula for the "attenuation" factor for the PCLS, in fact, calculates the percent transmission. It does *NOT* give percent attenuation, and as such, does *NOT* require an additional subtraction from one to result in the percent transmission (transmission = 1 - attenuation).

The attenuation factor (×100), or percent transmission, for the PCLS is defined as:

$$\%\,\text{Transmission} = \frac{1}{5^{FOA-A}} \times \frac{1}{2^{FOB-B}} \times 100 \tag{3.19}$$

where, FOA and FOB refer to the full-open positions for knobs A and B, respectively; and A and B refer to the knob settings for the configuration being analyzed. The percent transmission calculated from this attenuation factor equation is then multiplied by the spectral radiance curve to give the true radiance projected from the source. This product is finally piecewise integrated with the appropriate filter transmission curve from Section 3.4.3 – taking care to align the wavelength ranges – to give the expected number of rayleighs at the CCD.

3.4.4.4 Calculate G

Putting it all together for brightness calibration, G is calculated by multiplying the expected number of rayleighs by the integration time, and dividing the product into the number of counts:

$$G = \frac{N}{< I_{R/\lambda} > \cdot t} \tag{3.20}$$

where, G in $[counts/s/R]$ is the brightness calibration factor, N in $[counts]$ is the actual number of counts received at the CCD due to the source, $< I_{R/\lambda} >$ in $[R]$ is the expected number of rayleighs at the CCD, and t in $[s]$ is the exposure time.

Plotting the brightness calibration results illustrates the linearity of the imager systems. $R \cdot s$ plotted against *counts* gives a straight line for which G represents the slope. Comprehensive results are plotted in Appendix F in Figures F.20 and F.21 for each filter–imager combination, all calibrated with the PCLS, in this study. The associated statistical uncertainty for each point is shown by the error bars. Another representation of the results is plotted in Figures F.22 and F.23, indicating the exposure time for each point on the plots. Examples of these two plot variations are shown here in Figure 3.32 for the BGND filters in both CASI and CNFI. All of the calculated G factors and the associated errors with respect to the linear fits are tabulated in Table F.2 in Appendix F, along with the results from past brightness calibration studies performed on the Cornell All-sky Roving Imager (CARI) [*Garcia*, 1999; *Makela*, 2005 personal communication]. The G factor results for CASI are surprisingly low, but the same method was employed as that used for CNFI and that data came out right on par with the integrating sphere results. It is worth noting that CASI is a much older imager, and perhaps this fact impacted the results.

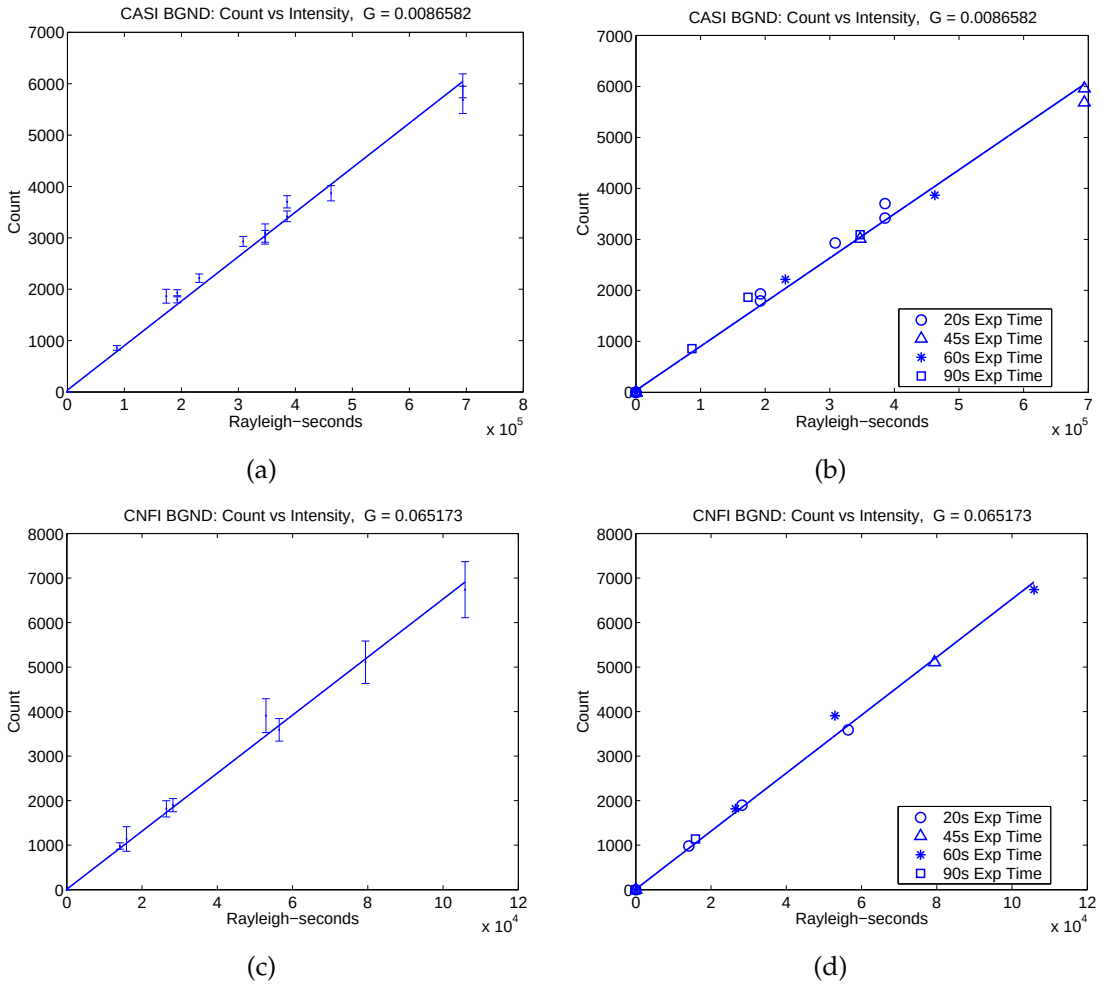

Figure 3.32: Count versus brightness plots for the BGND filters in CASI and CNFI; two representations are shown for each imager. For all the plots, data from at least three images taken for a particular PCLS intensity setting and exposure time are used for each point. In each case, the least squares best fit line is plotted, corresponding to the *G* factor noted in each title. For panels (a) and (c), the error bar shown with each point is derived from the associated set of images for that point. Panels (b) and (d) highlight the exposure times for each point. Exposure times are noted in the legends, and are indicated by the plot-point style.

3.4.4.5 Apply G

Having determined the G factors, the final step towards obtaining properly calibrated images is the correct application of these factors in order to ascertain the brightness in rayleighs given the pixel counts in an image from a realistic airglow environment. In general, the goal is to invert Eq. 3.16, solving now for $I(\lambda)$ after subtraction of the dark count and application of the flat field. The integration over wavelength in the equation complicates this basic task. The key to evaluating $I(\lambda)$ accurately is modelling a representative airglow emission. Three airglow emission models are considered: (1) an emission line characterized by a delta function; (2) a continuum emission characterized by a constant brightness over wavelength; and (3) a delta-function emission line superposed on a constant emission. The method to select depends upon the processing status of the image data to be analyzed. While the first case, as presented in *Garcia* [1999], is the usual approach adopted, this model is valid only if the background has already been subtracted from the emission wavelength-of-interest data. The third case is the most realistic overall representation of the three, albeit not entirely correct, and is best suited for images with minimal preprocessing, that is, flat-fielded images with the dark count subtracted, but the background emission still superposed. Both this third model and the first model fall short in that the delta-function only approximates the emission line which actually has a gaussian shape characterized by parameters such as temperature. Without knowing the specific shape of the gaussian curve, the delta-function provides a suitable approximation. The three cases are examined below.

Case 1: Delta-function emission line. Assuming we have a delta-function emission line radiating at wavelength λ_0, Eq. 3.16 simplifies to (after removal

of dark count and application of flat-fielding):

$$\mathcal{N}_{\lambda_0} = t \cdot G_{\lambda_0} I(\lambda_0) T(\lambda_0). \tag{3.21}$$

Inverting this, we get:

$$I(\lambda_0) = \frac{\mathcal{N}_{\lambda_0}}{t \cdot G_{\lambda_0} T(\lambda_0)}. \tag{3.22}$$

Notice that the filter transmission is only required at the emission wavelength of interest. These percent transmission values are provided in the fourth column of Table F.1 from Section 3.4.3 for the filters calibrated both in this study using the PCLS and the prior study using an integrating sphere. Note that, as mentioned in Chapter 2, although the specified filter wavelengths are in most instances not necessarily the central wavelengths (CWL) of the filters, we use the percent transmission values for the central wavelengths in our calculations. The blue-shift inherent in filter performance has been designed into the filter manufacturing specifications such that the apparent red-shifted offset of the CWL, in practice, results in the wavelength with the largest offset due to the maximum image-forming cone angle aligning with our emission line of interest.

Case 2: Constant brightness continuum emission. Now assuming instead that our emission is a constant over the passband of the filter, then only the brightness term $I(\lambda)$ can be pulled out of the integral, after removal of dark count and application of flat-fielding, and Eq. 3.16 reduces to:

$$\mathcal{N}_{continuum} = t \cdot G_{continuum} I_{continuum} \int T(\lambda)\, d\lambda. \tag{3.23}$$

Inverting this, we get:

$$I_{continuum} = \frac{\mathcal{N}_{continuum}}{t \cdot G_{continuum} \int T(\lambda)\, d\lambda}. \tag{3.24}$$

In this case, to solve for brightness, the filter transmission curve must be integrated over the entire passband. These values are provided in the last column

of Table F.1 from Section 3.4.3 for the filters calibrated both in this study using the PCLS, as well as for the prior study using an integrating sphere.

Case 3: Delta-function line superposed on a continuum emission. Finally, in our third case, we analyze the real-life situation whereby emission lines are, in fact, superposed on a background emission – hence, the inclusion of background filters in the system design in the first place. The assumption is that the brightness of the background emission measured at 541.0 nm is representative of the continuum found at other emission wavelengths. Given our assumption of superposition, we can evaluate the brightness term in Eq. 3.16 piecewise for both the line (at λ_0) and continuum contributions. Eq. 3.16 becomes:

$$\mathcal{N}_{\lambda_0} = t \cdot G_{\lambda_0} \int (I_{continuum} + I(\lambda_0))\, T(\lambda)\, d\lambda. \tag{3.25}$$

Breaking the integral into the sum of two integrals, we get:

$$\mathcal{N}_{\lambda_0} = t \cdot G_{\lambda_0} \left[\int I_{continuum}\, T(\lambda)\, d\lambda + \int I(\lambda_0)\, T(\lambda)\, d\lambda \right]. \tag{3.26}$$

$I_{continuum}$ can be solved for using the background filter (541.0 nm) and the technique from case#2 above. This constant numerical value for $I_{continuum}$ can now be pulled out of the integral so that the first integral term on the right-hand side of Eq. 3.26 becomes:

$$\mathcal{N}_{continuum,\lambda_0} = t \cdot G_{\lambda_0} I_{continuum} \int T(\lambda)\, d\lambda, \tag{3.27}$$

and Eq. 3.26 can be re-written as:

$$\mathcal{N}_{\lambda_0} = \mathcal{N}_{continuum,\lambda_0} + t \cdot G_{\lambda_0} \int I(\lambda_0)\, T(\lambda)\, d\lambda. \tag{3.28}$$

Using the integrated filter transmission from the last column of Table F.1 for the emission of interest, a value can be determined for $\mathcal{N}_{continuum,\lambda_0}$. Finally, using this

value for $\mathcal{N}_{continuum,\lambda_0}$ and the technique from case#1 above, the second term on the right-hand side of Eq. 3.26 can be solved for $I(\lambda_0)$ from the formula:

$$I(\lambda_0) = \frac{\mathcal{N}_{\lambda_0} - \mathcal{N}_{continuum,\lambda_0}}{t \cdot G_{\lambda_0} T(\lambda_0)} \tag{3.29}$$

or, alternatively:

$$I(\lambda_0) = \frac{\mathcal{N}_{\lambda_0}}{t \cdot G_{\lambda_0} T(\lambda_0)} - \frac{I_{continuum} \int T(\lambda)\, d\lambda}{T(\lambda_0)}. \tag{3.30}$$

Using Eq. 3.30 above is the more accurate, preferred method to evaluate the brightness in Rayleighs of airglow data for which the background emission has not been or cannot be removed.

3.4.5 Full Calibration

Full calibration or characterization of the system refers to the amalgamation of the various radiometric calibration procedures. The steps for full system characterization are best described in terms of how these radiometric procedures are applied to calibrating images. As noted the steps vary slightly for telecentric and collimating systems, including one pointed difference in the need for telecentric system procedures to account for filter transmission non-uniformities.

For telecentric systems, overall radiometric calibration includes:

1. Generate master dark image and subtract from all images
2. Normalize line-emission and background images with respective filter-specific "coupled" vignetting function (also referred to as flat-fielding the image)

3. Subtract average normalized off-band background image (order can be interchanged with item 4, if the appropriate linearity factor is selected)
4. Use appropriate linearity factors to get rayleighs.

For collimating systems, the procedures for overall radiometric calibration are:

1. Generate master dark image and subtract from all images
2. Normalize images with broad-band vignetting function
3. Use appropriate linearity factors to get rayleighs
4. Subtract off-band background image (which may need to be scaled to account for different continuum brightness and filter areas)
5. Correct final image with filter transmission array

This summary for collimating systems is used by researchers at Boston University [*Baumgardner*, 2005].

3.5 Geometric Calibration

Spatial variation discussed earlier in this chapter, in Section 3.4.2 on optics spatial calibration, referred to non-uniformities found within the optical path of the imager system, itself. In this section, the spatial variation addressed results from external influences based on the geometry of the field environment, as well as from the interface between this environment and the airglow system imposed by the primary lens. The hemispherical nature of the objective (i.e., primary) lens introduces unavoidable distortions in the recorded planar image data, $\mathcal{N}^{(i,j)}$

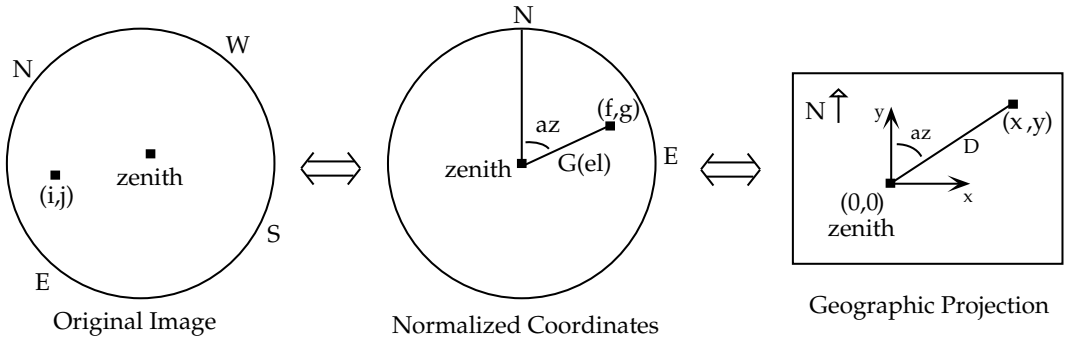

Figure 3.33: Schematic of image point mapping indicating transformation from original airglow image to normalized coordinates to the geographic projection.

in Eq. 3.1. Random placement or necessitated positioning of the systems in the field environment further impacts the recorded images by masking the physical context. Geometric calibration establishes the physical orientation of the fielded equipment and removes lens-induced distortions, thereby permitting a thorough assessment of the collected data.

3.5.1 Star Calibration

To correct for spatial variation arising from physical external factors, raw images are first aligned through a transformation to standard coordinates using spatial calibration based on known star positions. Described by *Hapgood and Taylor* [1982] for narrow-angle optics, and generalized to the all-sky format by *Lanchester* [1985], the standard coordinate system is a linear transformation of the original image coordinates scaled so that 0° elevation at the horizon corresponds to a circle of unit radius. Zenith angle (i.e., elevation) varies linearly with distance from the image center. From the standard coordinates, we further refine the mapping by rotating the image so that north lies at the top, and flipping it so that east lies to the right. The standard coordinates re-oriented via

compass direction are defined as the normalized coordinates.

Combining the above procedures, all-sky images are converted from the original image coordinate system defined in terms of (i,j) to the standard coordinate system defined in terms of (f,g) through a linear transformation which incorporates four operations: translation, scaling, rotation, and lateral flipping. The combined linear transformation can be represented as:

$$\begin{bmatrix} f \\ g \end{bmatrix} = \begin{bmatrix} a_0 & a_1 & a_2 \\ b_0 & b_1 & b_2 \end{bmatrix} \cdot \begin{bmatrix} 1 \\ i \\ j \end{bmatrix} \tag{3.31}$$

where the a's and b's are the spatial calibration coefficients. The method for determining these coefficients involves four steps. First a set of observed star positions are identified in the original image. In practice, bright stars towards the interior region of the image are selected. Second, for each star identified, its elevation and azimuth are computed from its right ascension and declination based on the time and date of the image, along with the latitude and longitude of the imager site. Third, the azimuth and elevation calculated for each star are converted to standard coordinates using

$$\begin{bmatrix} f \\ g \end{bmatrix} = \left(1 - \frac{\theta}{\pi/2}\right) \begin{bmatrix} \sin(az) \\ \cos(az) \end{bmatrix}. \tag{3.32}$$

Finally, fourth, now knowing both the measured original image coordinates (i,j) and derived normalized coordinates (f,g) for a set of stars, the spatial calibration coefficients are determined by performing a least squares fit between the two datasets as shown:

$$\begin{bmatrix} a_0 & b_0 \\ a_1 & b_1 \\ a_2 & b_2 \end{bmatrix} = \begin{bmatrix} \mathbf{1}^T\mathbf{1} & \mathbf{1}^T\boldsymbol{i} & \mathbf{1}^T\boldsymbol{j} \\ \mathbf{1}^T\boldsymbol{i} & \boldsymbol{i}^T\boldsymbol{i} & \boldsymbol{i}^T\boldsymbol{j} \\ \mathbf{1}^T\boldsymbol{j} & \boldsymbol{i}^T\boldsymbol{j} & \boldsymbol{j}^T\boldsymbol{j} \end{bmatrix}^{-1} \begin{bmatrix} \mathbf{1}^T \\ \boldsymbol{i}^T \\ \boldsymbol{j}^T \end{bmatrix} \begin{bmatrix} \boldsymbol{f} & \boldsymbol{g} \end{bmatrix} \tag{3.33}$$

where $\boldsymbol{i}$ and $\boldsymbol{j}$ are column vectors containing the observed star locations (i, j) in the original image, $\boldsymbol{f}$ and $\boldsymbol{g}$ are column vectors with the normalized coordinates derived for each star, and $\mathbf{1}$ is a column vector containing all 1's with the same length as the other vectors. A star calibration routine was developed for the Cornell University imagers and incorporated into a software analysis package by a former graduate student [*Garcia*, 1999].

3.5.2 Geographic Mapping Calibration

We determine physical coordinates in terms of azimuth and elevation via a polar transformation of the normalized coordinates. True geographic coordinates, discussed next, address the geographic distortion inherent with wide-angle imaging.

3.5.3 Uniform Spacing Calibration

Uniform sampling is a critical prerequisite for the standard spectral analysis techniques employed today in processing image data. As stated, however, wide-angle lenses, such as hemispherical all-sky lenses, introduce distortions by projecting the curved surface of the field of view of the sky onto the planar CCD. These distortions are most evident at low elevations where large-scale linear wave patterns appear curved and compressed. To alleviate this inherent distortion, images are converted from polar azimuth-elevation coordinates to cartesian geographic coordinates, resulting in a projection of the curved surface onto a 2-D, uniformly-spaced grid at the height of the specific airglow layer. This

projection, termed *unwarping*, while a crucial solution, can, itself, introduce uncertainty by generating errors: the regularly sampled points in the geographic coordinate system need not map directly to pixels in the image coordinate system, thus requiring interpolation to fill the gaps. Regardless, unwarping is a widely-accepted practice, as the advantage created by the uniform-sampling field is generally deemed well worth the trade-off of introducing interpolation errors. The unwarping routine is given full coverage in *Garcia et al.* [1997].

CHAPTER 4

THEORY

While in Chapter 2 we described *where* and *how* we observe phenomena of interest, we now investigate *what* it is that we actually observe. In this chapter, we explain the origin of the airglow which our instruments capture in digital representations. The airglow electromagnetic light waves provide a means to visualize atmospheric waves and bores. To date, all existing theories on mesospheric bore development cite gravity waves as a necessary source. Given this, it is advantageous to review gravity wave theory as a preface to understanding bore generation. The three sections in this chapter provide the foundations in theory for airglow, waves, and bores, respectively.

4.1 Airglow

Airglow is the faint light in the upper atmosphere that we target at night with our apply-named "airglow" imagers. Unequivocally known as "nightglow", *airglow* is the terminology more commonly used, even though some airglow – "dayglow" – does, in fact, exist during daylight hours, as observed by interferometers. The dominant light in the night sky shines – rather obviously – from the moon reflecting sunlight, from the stars, and also from the scattering of surface lights. The Sun and stars generate light at a continuum of frequencies governed by the Planck distribution; as such, they can be described approximately as high-temperature, black-body sources. In opposition to this continuum, the faint airglow emissions at discrete frequencies are readily discerned as series of band emissions or line emissions with sharp peaks in intensity, as summarized in Fig. 4.1. The full airglow spectrum from 300.0 nm to 1000.0 nm, as rendered

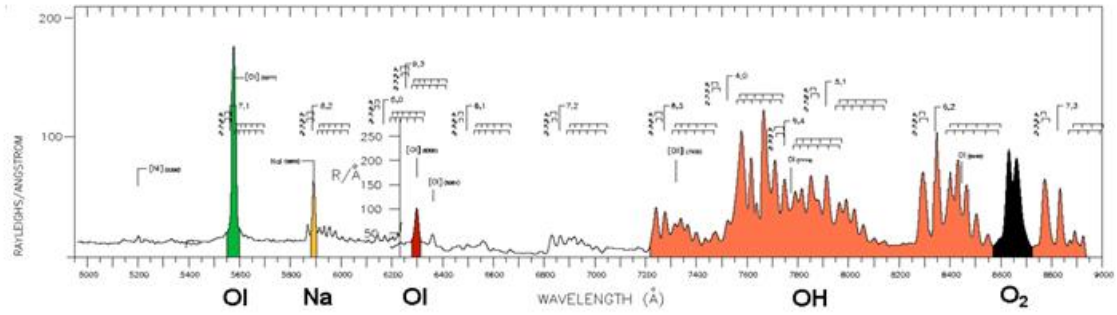

Figure 4.1: Spectrum of airglow emissions from 500.0 nm to 900.0 nm. Line emissions are indicated for OI (greenline), Na (sodium), OI (more specifically [OI_{21}] or redline), and O2. The band emission for OH is also highlighted. (Formulated from *Broadfoot and Kendall* [1968], courtesy of M.J. Taylor, Utah State University.)

by *Broadfoot and Kendall* [1968], is detailed in Figures 4.2–4.4.

The production of airglow photons can result from any of a number of chemical reactions in the upper atmosphere. The wavelength and associated energy of the emitted photons depend on the reactants and physics involved, thus allowing us to discern the specific reactions responsible for the observed photons. The chemical reactions producing the airglow photons require energy, and that energy originates from the Sun. That is, we define *airglow* as the optical emissions driven by excited atmospheric species whose original source of energy arises from solar radiation. Given that sunlight, which bathes the entire planet, is its original source, airglow is not restricted to any particular regions of Earth's atmosphere, and as such, can be found at all latitudes. This ubiquitous nature of airglow contrasts the more familiar aurora, which is usually restricted to high latitudes, and is caused by impact excitation from energetic particles streaming along the Earth's magnetic field lines.

Radiation from the Sun bombards the Earth during the day. This energetic radiation, comprised of extreme ultraviolet (EUV) and ultraviolet (UV) radia-

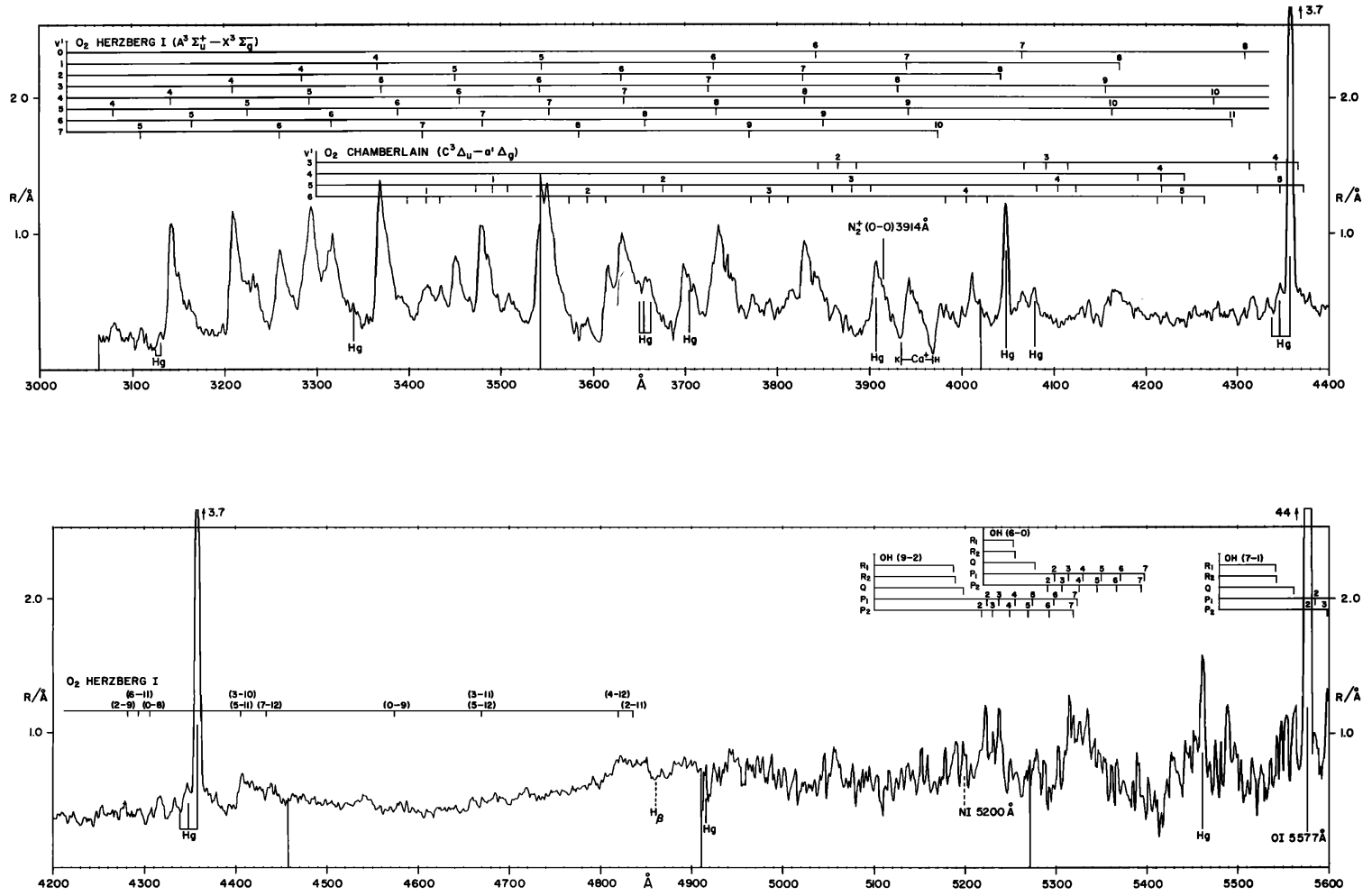

Figure 4.2: Detailed spectrum of airglow emissions from 300.0 nm to 560.0 nm. (From *Broadfoot and Kendall* [1968].)

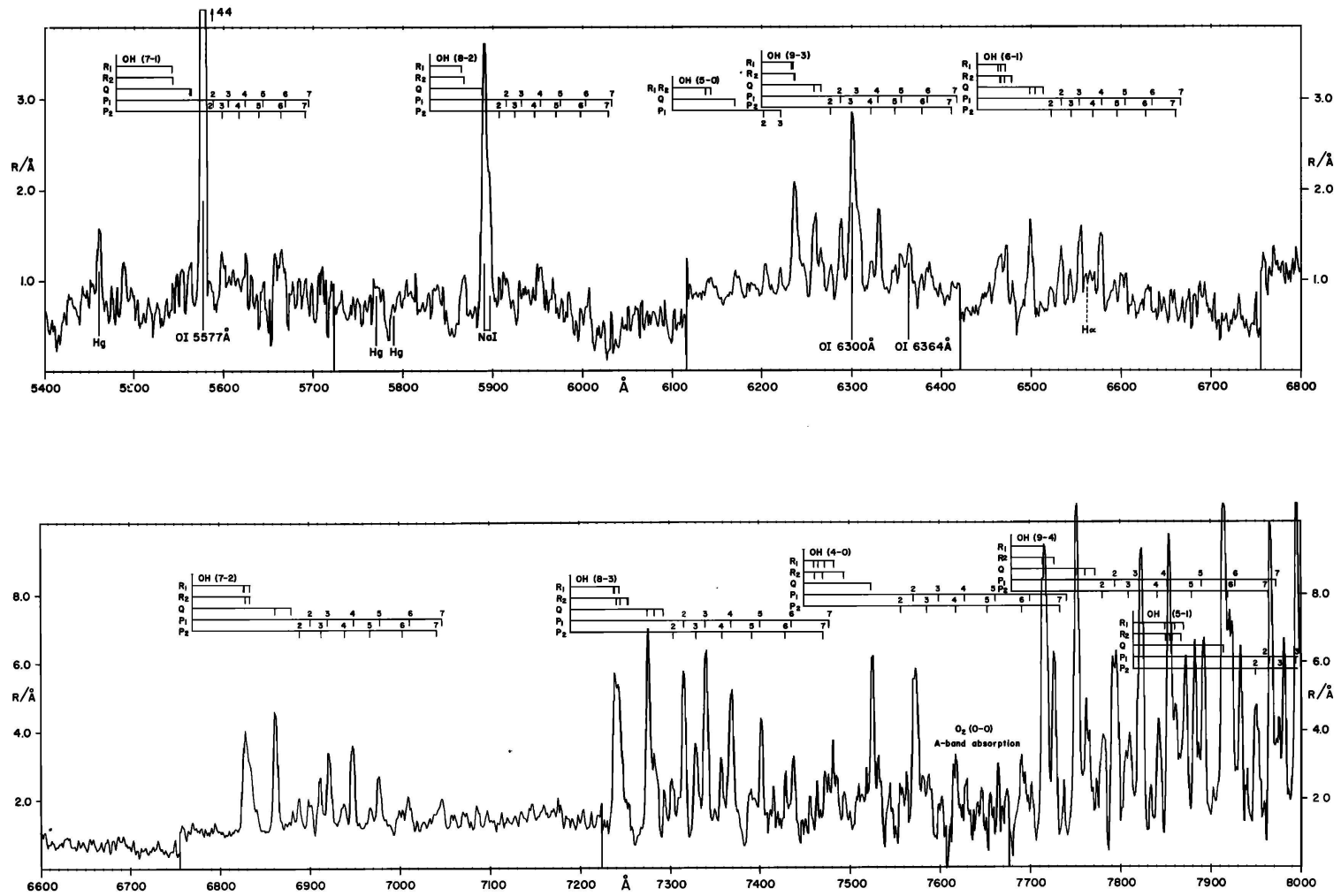

Figure 4.3: Detailed spectrum of airglow emissions from 540.0 nm to 800.0 nm. (From *Broadfoot and Kendall* [1968].)

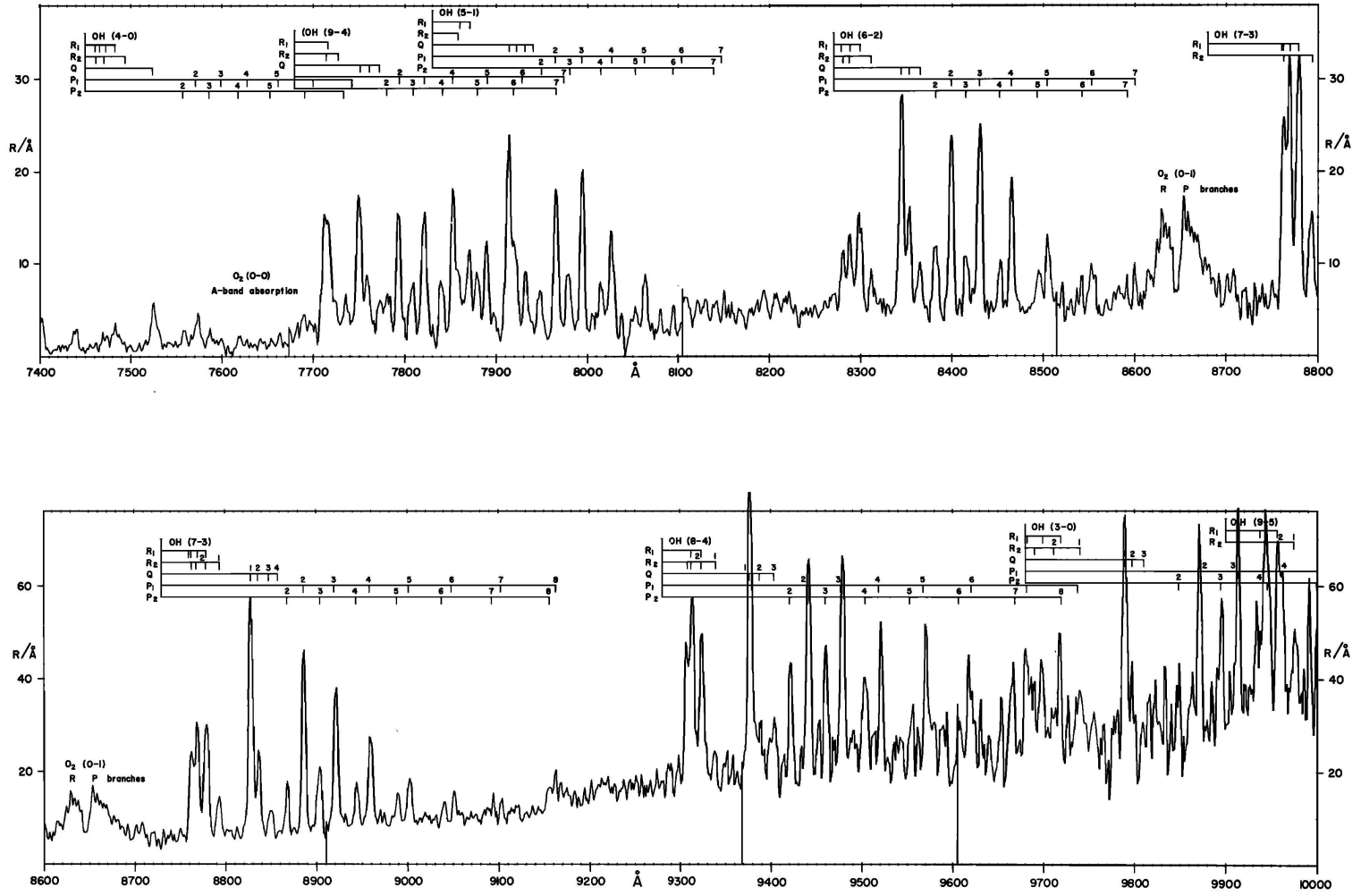

Figure 4.4: Detailed spectrum of airglow emissions from 740.0 nm to 1000.0 nm. (From *Broadfoot and Kendall* [1968].)

tion, is absorbed into the upper atmosphere through the dissociation of molecular oxygen (O_2), producing atomic oxygen (O). In this manner, the solar energy has been converted to chemical energy in the form of atomic oxygen, which is then able to initiate additional chemical reactions. After sunset, O recombination dominates production through various exothermic chemical channels, given that O serves as a reservoir of chemical energy. As a result, the newly-formed, but short-lived, molecule is usually formed in an excited state, which, in turn, gives up its excess energy. To represent this overall process, whereby absorption of a photon of photochemically active radiation leads to electronic excitation, we can write symbolically:

$$AB + h\nu \rightarrow AB^*, \tag{4.1}$$

where, for generality, AB is a molecular species composed of unlike atoms. These excited atmospheric species (AB^*) drop to a lower level of excitation by any of several possible pathways [*Wayne*, 1991]:

1. Dissociation: $AB^* \rightarrow A + B^*$;
2. Ionization: $AB^* \rightarrow AB^+ + e$;
3. Luminescence: $AB^* \rightarrow AB + h\nu$;
4. Intramolecular energy transfer: $AB^* \rightarrow AB^§$;
5. Intermolecular energy transfer: $AB^* + CD \rightarrow AB + CD^*$;
6. Quenching: $AB^* + M \rightarrow AB + M$;
7. Reaction: $AB^* + EF \rightarrow$ chemically different species

While process #1 accounts for the atomic oxygen, for our purposes we are most interested in processes #3 and #6. Collisional de-excitation, known as *quenching*,

shown in path 6 above, is when energy is given up to a major gas molecule (N_2 or O_2). For many airglow emitters significant in the atmosphere, quenching is the most important of the above processes [*Wayne*, 1991]. It is a special case of intermolecular energy transfer, one where electronic excitation is degraded to vibrational, rotational, or translational modes. The luminescence path, shown in item 3, involves the spontaneous emission of a photon, that is, radiation of excess energy away in the form of light, such as airglow. Depending on whether the excited states are purely electronic with higher energy levels (consisting of like atoms, e.g., O_2) or rotational-vibrational states with comparatively lower energy levels (consisting of unlike atoms, e.g., OH), the light emitted during the relaxation to the lower energy level will be of higher frequency for the former, and likewise, lower frequency for the latter. This accounts for the wide spectrum of airglow, whereby some emissions lie in the UV range, some in the visible range, and others, like the emission spectrum of OH molecules, lie in the near infrared region of the electromagnetic spectrum. In each of these cases, airglow light is generated at discrete frequencies when the excited states decay back towards the ground state.

Due to its discrete-frequency nature, we are able to isolate the airglow in the night sky using a filtered-imager scheme, as described in Section 2.2. While nightglow can be observed in some cases using space-borne satellites as long as the wavelengths of interest are not overwhelmed by reflected sunlight, ground-based airglow imagers outfitted with specifically designed filters are more commonly employed. With these highly sensitive airglow imagers, we observe the faint flux of photons at a given wavelength along a given look direction. Quantitatively, this chemiluminescent light is measured in units of Rayleighs, defined as 10^6 photons/cm^2/s. As noted in Section 2.3.1, the Rayleigh was introduced

for its convenient relationship with the volume emission rate, $\mathcal{F}_\lambda$, introduced in relation to the surface brightness, I_λ, in Eq. 2.2. In terms of the chemical reactions producing a specific airglow emission line, we can describe $\mathcal{F}_\lambda$, the volume emission rate $[ph/cm^3/s]$ from an excited species by the rate law:

$$\mathcal{F}_\lambda = k_r[A^*], \tag{4.2}$$

where k_r is the reaction rate coefficient, and $[A^*]$ is the concentration of the excited chemical species, A, i.e., the number density of A^*.

In general for chemical kinetics, that is, the study of chemical reactions, a basic two-body, or bimolecular, reaction can be represented by the following stoichiometric equation:

$$aA + bB = cC + dD, \tag{4.3}$$

where A and B denote the reactants, C and D represent the product molecules, and a, b, c, and d indicate the number of molecules of the various species involved in the reaction [*Schunk and Nagy*, 2000]. While a general expression for the reaction rate of such a chemical process can be determined using kinetic collision theory, the details of this approach are beyond the scope of this dissertation. For the purposes of this section where we examine the chemical kinetics of airglow emissions, it is sufficient to realize that the reaction rate is a function of the concentration of the reactant species, that is, it is proportional to the densities of the reactants, and for the bimolecular reaction between species A and B given in Eq. 4.3, it can be written as:

$$\mathcal{F}_\lambda = k_{AB}[A]^i[B]^j, \tag{4.4}$$

where k_{AB} is the reaction rate constant and i and j are the orders of the reaction with respect to constituents A and B, respectively [*Schunk and Nagy*, 2000].

In a thorough analysis, the various time constants associated with the different processes involved, including both chemical and transport aspects, must be analyzed to determine which control the overall effects, and which might be neglected. Once this has been evaluated, the relevant continuity equations are determined. For example, in the case of a first order spontaneous de-excitation process given by:

$$A^* \rightarrow A + h\nu, \qquad k_r \tag{4.5}$$

the relevant continuity equation can be represented as follows:

$$\frac{d[A^*]}{dt} = -k_r[A^*]. \tag{4.6}$$

While, inevitably, radiative decay competes with the production of excited species, quenching has been shown as the predominate additional loss mechanism in the cycle. Given this, the generalized excitation–de-excitation mechanism can be described as follows [*Wayne*, 1991]:

$$\text{Source} \rightarrow A^* \qquad \text{Excitation; Rate} = P \tag{4.7}$$

$$A^* \rightarrow A + h\nu \qquad \text{Emission;} \quad \text{Rate} = k_r[A^*] \tag{4.8}$$

$$A^* + M \rightarrow A + M \qquad \text{Quenching; Rate} = k_q[A^*][M]. \tag{4.9}$$

In the case of both steady-state conditions (that is, when $P = nL$) and negligible transport effects, the continuity equation simplifies to a balance between production and loss. Solving this continuity equation for the number density of the excited species reveals the desired volume emission rate. A generic representation of the emission rate for an excited species, A^*, can be provided by the following modified equation based on *Wayne* [1991] and *Schunk and Nagy* [2000]:

$$k_r[A^*] = \frac{k_r \sum_P P[A^*]}{\left(\sum_\lambda k_r[A^*]\right) + \left(\sum_q k_q[M]\right)}, \tag{4.10}$$

where $P[A^*]$ represents the various production rates of $[A^*]$ by the different source mechanisms, the k_q's are the quenching rate coefficients, and the summations are over all production, quenching, and radiative de-excitation processes.

The rate at which spontaneous de-excitation occurs, k_r, – often designated by $\mathcal{A}$ and generally referred to as the Einstein A factor or *Einstein coefficient* – is equivalent to the transition probability and is related to the radiative lifetime, τ, by [*Wayne*, 1991]:

$$\tau = \frac{ln2}{k_r}. \tag{4.11}$$

Combining Eq. 4.2, with our representation of the surface brightness from Eq. 2.2, we can show the relationship between the surface brightness (in Rayleighs) and the concentration of excited species, to be:

$$I_\lambda = 10^{-6} \int_0^\infty \mathcal{F}_\lambda(z)dz = 10^{-6} \int_0^\infty k_r[A^*]dz \tag{4.12}$$

As this equation shows, changes in the environment causing variations in the density or temperature-dependent reaction rate, such as atmospheric wave disturbances passing through the airglow layer, are reflected as perturbations in the surface brightness. These intensity variations can be isolated as shown in Section 2.3.4, to allow us to study the natural dynamic disturbances.

The five-position filter wheels included in the Cornell airglow imagers each house four line (or band) emission filters and one background filter, as described in Section 2.2.1.3. Typically, as seen in Chapter 3, the four emission filters include: 557.7 nm, 630.0 nm, 777.4 nm, and either 589.0 nm or OH (a broad-band filter). Descriptions of the chemical processes involved in the production of most of these airglow emissions have been previously summarized in the dissertations of former Cornell graduate students [*Garcia*, 1999; *Makela*, 2003]. As such, the reader is referred to these documents for summaries of the relevant

chemistry associated with the 630.0-nm, 777.4-nm, and OH emissions. Since the MLT (mesosphere and lower thermosphere) data discussed in this dissertation concentrates on greenline (557.7-nm) and sodium (589.0-nm) emissions, the chemical kinetics of only these two airglow processes will be discussed here.

4.1.1 Greenline Chemical Kinetics

One of the first airglow lines to be discovered, the greenline emission inarguably receives more attention by experimenters than most any other airglow emission due to several fortuitous facts: first, it is the brightest emission line in the visible spectrum; second, it is a line rather than a band; and, lastly, the region it exists within provides an optimal combination of favorable instrument sensitivity and small atmospheric extinction [*Rees*, 1989]. In actuality, the greenline emission originates from two distinct layers: the F-region at about 250-300 km, and the MLT region at about 95-100 km. Important to this study, the latter is the bright 557.7-nm MLT emission line arising from the ($^1D_2$ – $^1S_0$) forbidden transition in the ground configuration of atomic oxygen. This line originates from reactions involving neutrals – the predominate species type in the MLT region which houses the maximum concentration of atomic oxygen. Additionally at MLT altitudes, the density is low enough to mitigate quenching from functioning as the dominant process. The relatively feeble F-region 557.7-nm line arises from the dissociative recombination of O_2^+, given by

$$O_2^+ + e \rightarrow O + O(^1S_0), \tag{4.13}$$

and accompanies the 630.0-nm emission ion chemistry which occurs at higher altitudes where the atmosphere has an imbedded plasma. Given this dual source, some care must be taken when interpreting the 557.7-nm data.

Having been, as stated above, one of the first airglow emission lines discovered, it has been known as far back as 1923 [*Babcock*, 1923; *Bates*, 1981] that the greenline emission is due to the (electric quadrupole) transition:

$$O(^1S_0) \rightarrow O(^1D_2) + h\nu\ (\lambda = 557.7\ \text{nm}) \qquad k_g \tag{4.14}$$

(which accounts for the weak F-region greenline). Interesting and important to note is that although the 630.0-nm emission arises from the $^1D_2$ state, and hence one might expect a cascading 630.0-nm emission to follow the 557.7-nm emission even in the mesosphere, this is not the case due to the long lifetime (110 s) of the $^1D_2$ state [*Rishbeth and Garriot*, 1969]. At the height of the MLT 557.7-nm emission, collisions are so frequent as to deactivate the $^1D_2$ state well before a red photon can be emitted.

The source of the excited $^1S_0$ in the MLT is now generally accepted to be a two-step Barth process, rather than the Chapman process [*Bates*, 1981; *Torr*, 1985]. The first of these two steps is a three-body association:

$$O + O + M \rightarrow O_2^* + M, \qquad \gamma_1 \tag{4.15}$$

followed by the excitation transfer process for the production of $^1S_0$:

$$O_2^* + O \rightarrow O_2 + O(^1S_0). \qquad \beta_1 \tag{4.16}$$

This two-step process requires a collision with a third-body M, which is reasoned to be molecular, and considered most probably to be N_2 [*Torr*, 1985]. The rate coefficients are given by γ_1 and β_1, respectively. We allow for the loss of O_2^* by competing processes either in the form of deactivation, i.e., quenching:

$$O_2^* + M \rightarrow O_2 + M, \qquad \beta_2 \tag{4.17}$$

or by direct emission. In the *Bates* [1981] paper, where the development of the theory of the 557.7-nm emission from the upper atmosphere is reviewed, an

Table 4.1: Chemical kinetic parameters employed in the O(^{1}S) nightglow model. The reactions are in accordance with the two-step Barth process [*Bates*, 1981; *Torr*, 1985],and the rate coefficients used to determine I_{5577} are given by *Torr* [1985]; *Torr et al.* [1985].

Eq.#	Reaction	Coefficient
4.15	$O + O + M \rightarrow O_2^* + M$	$\gamma_1 = 4.7 \times 10^{-33} \exp(300/T)$ cm^3 s^{-1}
4.16	$O_2^* + O \rightarrow O_2 + O(^1S_0)$	$\beta_1 = 3 \times 10^{-13}$ cm^3 s^{-1} note([1])
4.17	$O_2^* + M \rightarrow O_2 + M$	$\beta_2 = 2.8 \times 10^{-13}$ cm^3 s^{-1} note([2])
4.14	$O(^1S_0) \rightarrow O(^1D_2) + h\nu$	$k_g = 1.06$ cm^3 s^{-1}

[1]The value is uncertain. The uncertainty involves the efficiency for the production of $O_2(A'^3\Delta_u)$ by reaction (4.15), and $O(^1S)$ by reaction (4.16); γ_1 is the total rate coefficient for production of all intermediate states, and β_1 includes the combined efficiencies.
[2]Here O_2^* is $O_2(A'^3\Delta_u)$ (Spacelab 1 data suggest this to be O_2^*).

intermediate reaction is given as:

$$O_2^* \rightarrow O_2 + h\nu; \qquad k_1 \tag{4.18}$$

however *Rees* [1989], also purporting the Barth mechanism, follows Eq. 4.16 with the forbidden transition given in Eq. 4.14 to describe the direct emission process. It appears that while *Rees* [1989] neglects to discuss the loss mechanisms for the excited O_2 molecules, *Bates* [1981] merely fails to provide thorough closure of the complete process by omitting Eq. 4.14; however, inclusion by *Bates* [1981] of the excited molecular oxygen loss mechanisms allows us to investigate further and to evaluate the airglow emission rate.

Following the procedure given in *Bates* [1981], we can find the rate of $O(^1S_0)$ formation by equating terms for production and loss of O_2^* from Eq.s 4.15–4.18 to get:

$$\gamma_1 [O]^2 [M] = \beta_1 [O_2^*] [O] + \beta_2 [O_2^*] [M] + k_1 [O_2^*] . \tag{4.19}$$

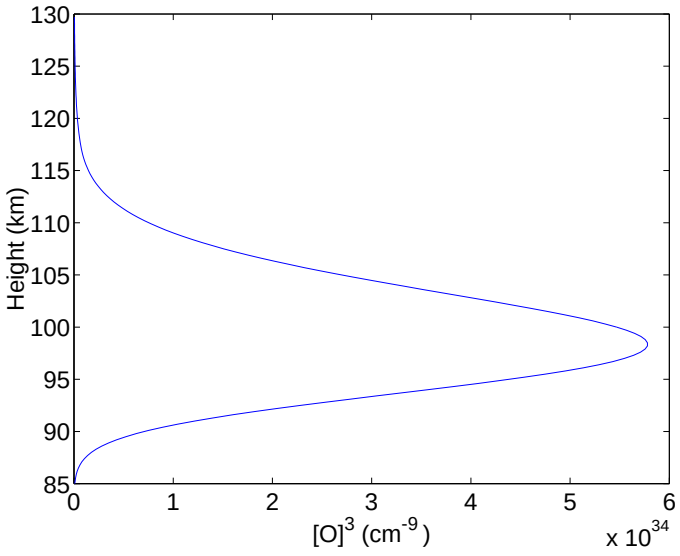

Figure 4.5: Atomic oxygen profile as generated by the MSIS-86 model for the geographic latitude and longitude of Arecibo, Puerto Rico. (Plot courtesy of F.J. Garcia, Cornell University.)

Rearranging terms and solving for $\left[O_2^*\right]$, we find that:

$$[O_2^*] = \frac{\gamma_1 [O]^2 [M]}{\beta_1 [O] + \beta_2 [M] + k_1}, \tag{4.20}$$

and using this to evaluate the rate of production of $O(^1S_0)$ shown in Eq. 4.16 we have:

$$[O_2^*] [O] \beta_1 = \frac{\gamma_1 \beta_1 [O]^3 [M]}{\beta_1 [O] + \beta_2 [M] + k_1}. \tag{4.21}$$

Now solving for the total emission rate of the 557.7-nm airglow line in terms of the various species concentrations and reaction rates, we assume the only loss of $^1S_0$ is from emission and combine the above results with Eq. 4.12 to get:

$$I_{5577} = 10^{-6} k_g \frac{\gamma_1 \beta_1 [O]^3 [M]}{\beta_1 [O] + \beta_2 [M] + k_1}. \tag{4.22}$$

Assuming that the gas density is high enough to ensure $\beta_2 [M] \gg \beta_1 [O] + k_1$ as in *Bates* [1981], we can simplify Eq. 4.22 to:

$$I_{5577} = 10^{-6} k_g \frac{\gamma_1 \beta_1}{\beta_2} [O]^3, \tag{4.23}$$

in $[ph/cm^3/s]$, showing that the emission rate is proportional to the cube of the concentration of atomic oxygen. The rate coefficients, and their associated references, are listed in Table 4.1 for each of the reactions involved in determining I_{5577}. *Garcia* [1999] generated a plot of this function (Eq. 4.23), as shown in Figure 4.5, using data from the MSIS-86 model to illustrate that the bulk of the concentration of atomic oxygen lies between 95 km and 100 km, thus explaining the origin of the emission as a layer. This analysis supports the findings of the layer-height evaluation study performed during the ALOHA-93 campaign when two all-sky imagers were used to triangulate the height of the 557.7-nm emission structures. The ALOHA-93 triangulation study found the height to be 95 ± 2 km [*Taylor et al.*, 1995b]. For the study in this dissertation, we use the value cited in *Torr* [1985] whereby the MLT greenline emission layer is reported to be located at 97 ± 2 km.

4.1.2 Sodium Chemical Kinetics

Sodium emissions are attributed to the unresolved Na doublet, Na-D, at 589.0 nm and 589.6 nm according to *Torr* [1985] and *Rees* [1989], and at the midpoint 589.3 nm as reported by *Molina* [1983], and cited by *Nappo* [2002]. The sodium, indeed, metallic ions in general, originate from meteor ablation in the upper atmosphere, and are lost through downward transport. For sodium, the peak emission layer has been identified through rocket-borne photometer measurements to be located in the range 88-95 km according to *Torr* [1985], and in the slightly wider range of 83-95 km according to *Rees* [1989]. For our studies, we typically consider the sodium airglow emission layer to reside at approximately 90 km altitude.

The sodium emission is due to the transition:

$$Na(^2\mathrm{P}) \rightarrow Na(^2\mathrm{S}) + h\nu \ (\lambda = 589.0 \text{ nm}). \qquad k_s \tag{4.24}$$

Observational and theoretical evidence both convincingly favor an oxidation-reduction cycle as the source of the excited sodium state [*Rees*, 1989]. The mechanisms proposed first by *Chapman* [1939], and later in the meteor context by *Chapman* [1956] and *Baggaley* [1977a, 1981], are:

$$Na + O_3 \rightarrow NaO + O_2, \qquad \beta_1 \tag{4.25}$$

$$NaO + O \rightarrow Na^* + O_2, \qquad \beta_2 \tag{4.26}$$

and finally:

$$Na^* \rightarrow Na + h\nu, \qquad k_1 \tag{4.27}$$

where, as before, "Na^*" indicates the excited state, and the rate coefficients are given by β_1, β_2, and k_1, respectively. More specifically, we must write:

$$Na + O_3 \rightarrow NaO + O_2, \qquad \beta_1 \tag{4.28}$$

$$NaO + O \rightarrow Na(^2\mathrm{P},^2\mathrm{S}) + O_2, \qquad \beta_2 \tag{4.29}$$

and finally:

$$Na(^2\mathrm{P}) \rightarrow Na(^2\mathrm{S}) + h\nu. \qquad k_1 \tag{4.30}$$

The photon emission rate can be determined by the same means employed for finding the greenline emission rate. That is, we can find the rate of $Na(^2\mathrm{P})$ formation by equating terms for production and loss of NaO to get:

$$\beta_1 [Na][O_3] = \beta_2 [NaO][O]. \tag{4.31}$$

Rearranging terms and solving for $[NaO]$, we find that:

$$[NaO] = \frac{\beta_1 [Na][O_3]}{\beta_2 [O]}, \tag{4.32}$$

and using this to evaluate the rate of production of NaO we find ourselves back to Eq: 4.31 with:

$$[NaO]\,[O]\,\beta_2 = \beta_1\,[Na]\,[O_3]\,. \tag{4.33}$$

Now solving for the total emission rate of the sodium airglow line in terms of the various species concentrations and reaction rates, we assume the only loss of ^{2}P is from emission and combine the above results with Eq. 4.12 to get:

$$I_{5893} = 10^{-6} k_1 \;\; f_{2P}\,\beta_1\,[Na]\,[O_3]\,, \tag{4.34}$$

in $[ph/cm^3/s]$, where f_{2P} is the fraction of Na atoms produced in the excited ^{2}P state in Eq. 4.29.

4.2 Waves

Waves are universal events with a fixed place in the common vernacular. Everyone – children, cooks, Valley girls, surfing dudes, boaters, meteorologists, DJs, animal behaviorists, football fans, physicists, etc. – is familiar with the concept of a wave. Water waves are particularly observable. Perhaps less recognizable to the public are common properties shared by waves such as frequency, wavelength, and propagation speed. The fact that tsunami waves are faster than a commercial jet was a surprise to most people following the December 2004 Indian Ocean earthquake. Less well-known to the general populace are the myriad variety of waves which exist and the mathematical analysis techniques used to evaluate them. Some commonly known waves result from electromagnetic processes governed by electrodynamic properties described by Maxwell's equations. Other waves result from fluid motion governed by the properties of fluid dynamics as described by the equations of motion. While airglow is a

type of electromagnetic (wave) radiation, for our study, the airglow itself is but a means to an end. Observing perturbations in airglow brightness allows researchers to discern waves in the Earth's atmosphere – a specific compressible, rotating, spherical-shell fluid permeated by both density and temperature gradients [*Beer*, 1974]. We are concerned here with atmospheric waves, and more specifically, with upper atmospheric phenomena, including a particular type of internal wave motion in a fluid – gravity waves. First, however, we provide some general contextual background for waves.

4.2.1 Fundamentals

4.2.1.1 Properties

Some commonalities exist among all waves. First, waves have the ability to transport energy and momentum; that is, energy and momentum are propagated from one point to another by means of a passing wave. Energy and momentum are distributed more rapidly with the contribution of waves than if left to the mean flow alone [*Nappo*, 2002]. Wave transport resulting in energy and momentum deposition is a key component to the dynamics of the mesospheric region. It is this transference of energy and momentum by waves which break (as on a beach) that communicates the influence of one region to another [*Salby*, 1996]. Second, wave disturbances of low amplitude (non-breaking waves) travel through a medium without imparting any permanent displacement to the medium as a whole.

4.2.1.2 Linear Theory

We can describe wave-imposed transient effects on the medium, and hence analyze the wave motion, by applying linear theory through the perturbation method of analysis. In this common theoretical methodology, the wave is considered to be a *small* (first-order) perturbation on a stationary (or steady, slowly changing) background. Waves result from the harmonic oscillations displacing fluid particles, such that the apparent motion of the wave is the result of phase differences between the oscillations of adjacent particles [*Nappo*, 2002]. Given this, small-amplitude waves can be decomposed into Fourier components. The simplification of linear theory allows these individual wave components with unique characteristics (amplitude, frequency, wavelength) to be superimposed without interacting; that is, the wave disturbances are regarded as sufficiently weak such that their products can be considered negligible in the governing equations. If, however, the wave amplitude grows, rather than attenuates, as it progresses, then non-linear effects become important and linear theory is no longer valid. The linearization process, when applicable, eliminates wave-wave interactions and the resulting transfers of energy. The topic of linear theory will be revisited in Section 4.2.3.6 where the equations describing wave motion are discussed.

4.2.1.3 Classes

Waves can be categorized in broad terms according to various features, including: the direction the wave propagates relative to the displacement of the medium, the physical scope of the wave, the medium in which the wave resides, and the restoring force driving the wave. While these properties apply

to waves in general, here we briefly discuss each of these categories for fluid motion waves.

Waves can be divided into classes – *longitudinal* and *transverse* – according to their propagation and displacement properties. For electromagnetic (EM) waves, these terms refer to the direction of the propagation constant $\vec{\mathbf{k}}$ relative to the oscillating electric field $\vec{\mathbf{E}}$; for longitudinal EM waves, $\vec{\mathbf{k}} \parallel \vec{\mathbf{E}}$, while for transverse EM waves, $\vec{\mathbf{k}} \perp \vec{\mathbf{E}}$ [*Chen*, 1984; *Schunk and Nagy*, 2000]. For waves in a fluid, "longitudinal" refers to waves in which the displacements are in the same direction as the propagation. "Transverse" waves in fluids are further distinguished as "vertical transverse" or "horizontal transverse" waves depending upon the direction of the fluid displacement relative to the wave propagation direction [*Beer*, 1974].

Waves can also vary in dimension. A classic example of three-dimensional waves are surface ring waves. These form after a disturbance such a stone being tossed into a pond or a sugar cube being dropped into a cup of tea. By contrast two-dimensional waves, called *plane waves*, appear as wave trains, or a series of repeating motions changing only with height and the direction parallel to the propagation direction; examples include waves breaking at the beach and gravity waves.

A variety of fluid environments exist on the Earth, including oceans, rivers, lakes, atmospheric regions, surface boundaries, and laboratory setups. Some waves exist at the surface boundaries between these regions; for example shallow water waves which exist on the surface of water with air above. These waves are called *external* waves as the sharp interface between water and air is displaced. Two restoring forces act on the displaced water – gravity is the down-

Table 4.2: Principal Atmospheric Waves

Wave	Period	Restoring Force	Application
Acoustic	< 270 sec	Compressibility	Speech
Gravity	270 sec – 3 hrs	Buoyancy	Upper Atmosphere
Tides	$24/m$ hrs ($m = 1, 2, ...$)	Buoyancy/Rotational	Geomagnetic variations Upper Atmosphere
Rossby	> 12 hrs	Rotational	Meteorology

ward restoring force and water pressure is the upward force. Wholly within a medium such as water or the atmosphere, no sharp interfaces exist. Waves which develop in a stably stratified region with no sharp fluid interfaces are termed *internal* waves. For internal waves in the ocean, the change of salinity causes the density of sea water to vary with depth. This density gradient is crucial for internal waves to exist.

For the medium of interest to this study, waves are excited when air is disturbed from equilibrium. These disturbances can be mechanical, such as when air is displaced over elevated terrain, or thermal, when air is heated by convection. When positive restoring forces which oppose these disturbances from equilibrium are present, then local oscillations in field properties are supported and wave motion develops [*Salby*, 1996]. The key features of Earth's atmosphere supporting wave activity are that it is compressible, rotating, and spherical, and it contains both density and temperature gradients. Each of these features provides a restoring force supporting a different kind of wave, as summarized in Table 4.2. Only acoustic waves would exist if the atmosphere was a homogeneous stationary fluid with no external forces. The balance between compressibility and inertia drives acoustic waves. However, external forces acting on the

Earth, such as gravitational, magnetic, and Coriolis forces, allow for a more prolific assortment of waves. The Earth's gravity creates a distinct density gradient with altitude, endowing the Earth's atmosphere with a stabilizing restoring force provided by buoyancy. Gravity waves occur when the dominant restoring force is fluid buoyancy. When buoyancy and compressibility forces are comparable, acoustic gravity waves arise. Rossby or planetary waves are large scale waves which result from the Coriolis effect, which is the influence of the curvature of the Earth and its rotation. Atmospheric tides are waves driven by buoyancy and rotation with periods that are sub-multiples of the solar day.

4.2.2 Mechanics

In this section, we define many of the basic parameters needed to describe wave properties. We use the Cartesian coordinate system (x, y, z) with x and y in the horizontal plane and z in the vertical plane. We define x to be the zonal (eastward) component, y to be the meridional (northward) component, and z to be the upward component, as depicted in Figure 4.6. The coordinates have unit vector $(\hat{x}, \hat{y}, \hat{z})$. We define horizontal wave motion to be along the x-axis.

4.2.2.1 Wave Parameters

Wavelength, λ, is defined as the distance between successive crests, that is, one full period of a wave. The *wave number*, a fundamental property of a wave, is denoted generally by, k:

$$k = \frac{2\pi}{\lambda}. \tag{4.35}$$

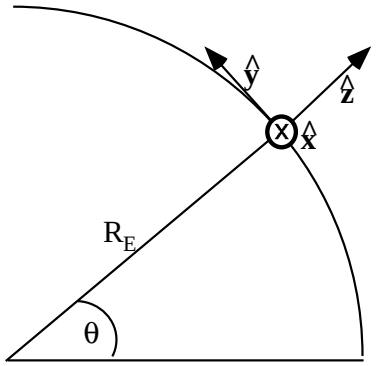

Figure 4.6: Definition of the cartesian coordinate system used in our analysis. x is defined as eastward, y northward, and z upward. The latitude is θ. R_E is the radius of the Earth.

In 3-D nomenclature, the wave numbers in the x-, y-, and z-directions, are labelled k, l, and m, respectively, as shown:

$$k = \frac{2\pi}{\lambda_x},\ l = \frac{2\pi}{\lambda_y},\ m = \frac{2\pi}{\lambda_z}, \tag{4.36}$$

where λ_x, λ_y, and λ_z are the wavelengths in the x-, y-, and z-directions. The *wave vector*, $\vec{\mathbf{k}}$, defines the direction of propagation for a wave, and is given by:

$$\vec{\mathbf{k}} = k\hat{x} + l\hat{y} + m\hat{z}. \tag{4.37}$$

In the Lagrangian reference frame, the *wave period*, τ, is the time required for a fluid particle to make one oscillation; whereas from the Eulerian perspective, the wave period is the time required for successive wave fronts to pass a stationary observer. The *wave frequency* is given by:

$$\omega = \frac{2\pi}{\tau}. \tag{4.38}$$

4.2.2.2 Phase Speed

Propagating waves, as with any wave, are characterized by their amplitude and phase; however, with motion, phase now depends not only on time, but also on

space variables as well. Given a one-dimensional wave represented by:

$$f(x,t) = A\cos(kx - \omega t), \tag{4.39}$$

where A is the amplitude, k is the wave number, and ω is the frequency, let us define the phase, ϕ, to be:

$$\phi = kx - \omega t. \tag{4.40}$$

Now, expanding this to two dimensions, we describe an arbitrary wave moving in the x-z plane (so as to incorporate a vertical component) as:

$$f(x,z,t) = \Re A e^{i\phi} = A\cos(kx + mz - \omega t), \tag{4.41}$$

where we have included the representation in exponential notation for completeness. The real part is included to indicate only physically meaningful results are considered. From the 2-D case, we note that lines of constant phase determine the spatial orientation of the wave fronts. The family of *wave fronts* is specified by:

$$\phi(x,z) = kx + mz = \text{constant}. \tag{4.42}$$

The *phase speed* (also called *phase velocity*), v_p, is the speed at which a point of constant phase moves in the direction of propagation, and is defined as:

$$\mathrm{v}_p \equiv \frac{\omega}{|\vec{\mathbf{k}}|}. \tag{4.43}$$

This can easily be shown in general for our 2-D case by first borrowing upon polar coordinates to represent the phase, also known as the *phase angle*, as:

$$\phi \;=\; \vec{\mathbf{k}}\cdot\vec{\mathbf{r}} - \omega t \;=\; kx + mz - \omega t, \tag{4.44}$$

where $\vec{\mathbf{r}}$ is the radius vector defined by:

$$\vec{\mathbf{r}} = x\hat{x} + z\hat{z}, \tag{4.45}$$

and the phase is represented by the positive angle between this radius vector and the horizontal axis, corresponding to $\phi = 0$, of a polar coordinate diagram. Now if the phase is to remain constant following the motion, then the Lagrangian derivative must be zero, such that:

$$\left.\frac{D\phi}{Dt}\right|_{\phi} = \frac{D}{Dt}(\vec{\mathbf{k}} \cdot \vec{\mathbf{r}} - \omega t) = \vec{\mathbf{k}} \cdot \frac{D\vec{\mathbf{r}}}{Dt} - \omega = 0, \tag{4.46}$$

and, consequently,

$$\frac{D\vec{\mathbf{r}}}{Dt} = \mathrm{v}_p = \frac{\omega}{|\vec{\mathbf{k}}|} = \frac{\omega}{\sqrt{k^2 + m^2}}\,. \tag{4.47}$$

In general, Eq. 4.47 is true. However, to be thorough for our atmospheric application, we should mention that for internal gravity waves (with perturbation characteristics defined in Eq. 4.183 as discussed at the end of Section 4.2.3.6), we must include the effects of gravity in our analysis which, for horizontally propagating waves (i.e., k and ω real), manifests in a complex value for our vertical wave number, m. As a result, our Eq. 4.41 should be modified to

$$f(x,z,t) = e^{z/2H}\Re A e^{i\phi} = \exp(z/2H)\Re A \exp\, i(kx + mz - \omega t), \tag{4.48}$$

in order to include the $\exp(z/2H)$ term which describes the upward amplification of internal gravity waves – a property which necessarily both offsets the stratification of atmospheric mass and makes energy densities invariant with height [*Salby*, 1996]. The impact on the phase velocity is that we pick up an extra $1/(4H^2)$ term under the square root sign in the denominator:

$$\frac{D\vec{\mathbf{r}}}{Dt} = \mathrm{v}_p = \frac{\omega}{|\vec{\mathbf{k}}|} = \frac{\omega}{\sqrt{k^2 + m^2 + \frac{1}{4H^2}}}\,. \tag{4.49}$$

Distinguishing from the theoretical discussions, however, it is important to note that the phase speed we actually **measure** in our intensity images when we

observe wave activity is:

$$v_p = \frac{\sigma}{|\vec{\mathbf{k}}|}, \tag{4.50}$$

where σ is the *observed frequency*; whereas ω (from Eq.s 4.38 and 4.43) is the *instrinsic frequency* - that relative to the medium - given by:

$$\omega = \sigma - \left(\vec{\mathbf{k}} \cdot \overline{\vec{\mathbf{u}}}\right) \tag{4.51}$$

where $\vec{\mathbf{k}}$ is the zonal wave number and $\overline{\vec{\mathbf{u}}}$ is the average velocity of the background wind. The term $\vec{\mathbf{k}} \cdot \overline{\vec{\mathbf{u}}}$ represents a Doppler shift of the intrinsic frequency by background motion. A component propagating opposite to $\overline{\vec{\mathbf{u}}}$ is Doppler-shifted to higher frequency: $\omega > \sigma$, whereas one propagating in the same direction as $\overline{\vec{\mathbf{u}}}$ is Doppler-shifted to lower intrinsic frequency: $\omega < \sigma$ [*Salby*, 1996]. For our present study, we unfortunately do not have supporting equipment to provide the background wind speed, and so we have conducted analysis using the observed speeds only. To hold with convention, we continue to use ω to represent frequency in this theoretical development, keeping in mind that when discussing actual data, distinctions are required.

4.2.2.3 Group Velocity

As noted in Section 4.2.1.2, waves result from the harmonic oscillations displacing fluid particles and can be decomposed into Fourier components. Wave disturbances originating from a source, then, result in energy being distributed over a wavenumber spectrum of waves, i.e., *wavelets*, which together comprise a *wave packet* (bundle or group) modulated by an envelope manifesting the larger, overall wave and confining its associated energy. Each wavelet moves at a particular phase speed, $v_p(k)$, determined by its wavenumber, k, as defined in Section 4.2.2.2. The wave components, or wavelets, with larger wavelengths have

greater phase speeds, yet the overall wave activity and energy transport moves with the envelope – irrespective of these individual phase speeds.

To analyze the energy transport of the group, the common approach is to consider the simple case of a wave packet composed of only two wavelets, both travelling in the x-direction [*Holton*, 1979; *Salby*, 1996; *Nappo*, 2002]. We let the waves have equal amplitudes, a, but slightly different frequencies, i.e., $\omega \pm \delta\omega$, and wavenumbers, i.e., $k \pm \delta k$. The superposition of these waves is given by:

$$\psi = a\,cos[(k + \delta k)x - (\omega + \delta\omega)t] + a\,cos[(k - \delta k)x - (\omega - \delta\omega)t], \tag{4.52}$$

which, with some trigonometry, reduces to:

$$\psi = 2a\,cos(\delta kx - \delta\omega t)cos(kx - \omega t). \tag{4.53}$$

Equation 4.53 shows that the two wavelets combine to form an amplitude-modulated carrier given by $cos(kx - \omega t)$, modulated by an envelope given by $2a\,cos(\delta kx - \delta\omega t)$.

Group velocity defines the speed of the envelope, that is, the speed at which the wave energy propagates, and following from Equation 4.53, is given by:

$$\mathrm{v}_g = \frac{\delta\omega}{\delta k}. \tag{4.54}$$

In the limit as $\delta k \to 0$, Equation 4.54 becomes

$$\mathrm{v}_g \equiv \frac{\partial\omega}{\partial k}, \tag{4.55}$$

representing the general form for group velocity. More specifically for a 2-D case, the x and z components of the group velocity are defined separately by:

$$\mathrm{v}_{g_x} = u_g = \frac{\partial\omega}{\partial k}, \tag{4.56}$$

and

$$v_{g_z} = w_g = \frac{\partial \omega}{\partial m}, \tag{4.57}$$

with group velocity in the $x - z$ plane denoted by

$$\vec{\mathbf{v}}_g = \left(\frac{\partial \omega}{\partial k}, \frac{\partial \omega}{\partial m} \right). \tag{4.58}$$

Again distinguishing between observed and intrinsic frequency, the experimental form of Equation 4.58 in terms of observed frequency, σ is given by:

$$\vec{\mathbf{v}}_g = \left(\frac{\partial \sigma}{\partial k}, \frac{\partial \sigma}{\partial m} \right). \tag{4.59}$$

Likewise, the experimental form in terms of intrinsic frequency, ω, is given by:

$$\vec{\mathbf{v}}_g = \left(\frac{\partial \omega}{\partial k} + \overline{u}, \frac{\partial \omega}{\partial m} \right). \tag{4.60}$$

4.2.2.4 Wave Dispersion

As noted in Section 4.2.2.2, phase speed is a function of both wave frequency and wavenumber, i.e., $v_p = \omega/k = \lambda_x/\tau$. Thus for a given wave period, τ, long waves travel faster than short waves, leading to *wave dispersion*. That is, given phase speeds dependent on k, the various sinusoidal components of a disturbance originating at a given location will, at some later time, be found in different places; i.e., they are dispersed [*Holton*, 1979]. Such waves are called *dispersive*, and the relation between phase speed and wavenumber is called the *dispersion relation*.

Some wave types have phase speeds independent of wavenumber; acoustic waves are an example. For nondispersive waves such as these, a spatially localized disturbance comprised of Fourier wave components will preserve its

shape in space while propagating at the phase speed. In contrast, for dispersive waves, with the waves making up the disturbance travelling at different speeds, the shape of the wave group will NOT remain constant as the group propagates. Individual wave components may even move through the group as the packet propagates. In fact, over time, these disturbances, in general, tend to broaden. More specifically, the energy of the group will become concentrated in certain regions, since the individual Fourier components of the group may either reinforce or cancel each other, depending on the relative phases of the components [*Holton*, 1979].

4.2.3 Dynamics

In this section, we investigate the dynamics of gravity waves – the theorized precursors to bore formation. The term "gravity wave" suggests that gravity somehow supports this wave type, when, in fact, *buoyancy* which arises from gravity is the restoring force acting on a fluid parcel displaced from equilibrium. Our goal in describing gravity wave motion is to define the associated dispersion relation. Before this development, some concepts related to dry atmospheric thermodynamics are introduced first in order to describe the properties of the atmospheric environment necessary for gravity wave propagation. We also introduce frames of reference and the fundamental equations.

4.2.3.1 Atmospheric Properties

Equation of State The thermodynamic state of the atmosphere is determined by the values of pressure, p, temperature, T, and density (or specific volume), ρ

(or α), at any given point. These variables are related to each other for dry air by the *equation of state* for an ideal gas by:

$$p\,\alpha = RT \quad \text{or} \quad p = \rho RT, \tag{4.61}$$

where R is the gas constant for dry air ($R = 287\ J/kg/K$).

Hydrostatic Approximation Vertical motions of the atmosphere tend to be small except in localized small-scale regions of isolated convection, for example, thermal plumes, cumulus clouds, squall lines, tornados, hurricanes, etc. Aside from these exceptional cases, an excellent approximation exists for the vertical condition of the atmosphere. In the absence of atmospheric motions, the force of gravity must exactly balance the vertical component of the pressure gradient force; that is, there is a balance between the upward-directed pressure force and the weight of the atmosphere. This can be shown by considering an elemental volume of atmosphere with unit cross-section, height δz, and density ρ. The weight of the volume is given by $\rho g \delta z$ directed downward. The net pressure force, δp, acting on the volume is the difference between the forces acting on the top and bottom of the volume. This balance between pressure and gravity is given by:

$$\delta p = -\rho g\, \delta z. \tag{4.62}$$

In the limit $\delta z \to 0$, Eq. 4.62 becomes:

$$\frac{\partial p}{\partial z} = -\rho g, \tag{4.63}$$

which is the *hydrostatic equation* describing the condition of *hydrostatic equilibrium*.

Scale Height Substituting the equation of state for an ideal gas (Eq. 4.61) into the hydrostatic equation (Eq. 4.63), leads to:

$$\frac{1}{\rho}\frac{\partial p}{\partial z} + \frac{1}{T}\frac{\partial T}{\partial z} = -\frac{g}{RT}, \tag{4.64}$$

where R is the universal gas constant for dry air, and T is the temperature. Replacing the atmospheric temperature, T, by the average temperature, $<T>$, and integrating over z, we get:

$$\rho(z) = \rho(0)\, e^{-gz/R<T>}, \tag{4.65}$$

where $\rho(0)$ is the density at the ground surface. Letting $\rho_0 = \rho(0)$, and defining the isothermal *scale height*, H, of the atmosphere to be $H = R <T> /g$, gives:

$$\rho(z) = \rho_0\, e^{-z/H}. \tag{4.66}$$

Thus, Eq. 4.66 shows that the pressure decreases exponentially with height by a factor of e^{-1} per scale height.

Adiabatic Process An *adiabatic process* in a system is a reversible process in which no heat is exchanged with the surroundings.

Potential Temperature The *potential temperature*, θ, is defined as the temperature that a dry air parcel would have if it were expanded or compressed adiabatically from its existing pressure, p, and temperature, T, to a standard pressure, p_0, usually taken to be 1000 *mb*. We can determine an expression for the potential temperature by starting with the first law of thermodynamics for an adiabatic process. Given an adiabatic process with no loss or gain of heat within the system, the first law of thermodynamics can be set to zero, such that:

$$dq = c_p\, dT - \alpha\, dp = 0, \tag{4.67}$$

where c_p is the specific heat capacity at constant pressure, and $\alpha = 1/\rho = RT/p$ is the specific volume. Substituting the definition of specific volume, $\alpha = RT/p$ into Eq. 4.67, we arrive at:

$$\frac{c_p}{R}\frac{dT}{T} = \frac{dp}{p}. \tag{4.68}$$

Integrating this expression from a state at pressure p_0 where the temperature is θ to a state at pressure p where the temperature is T, gives:

$$\frac{c_p}{R}\ln\left(\frac{T}{\theta}\right) = \ln\left(\frac{p}{p_0}\right). \tag{4.69}$$

Taking the antilogarithm of Eq. 4.69, we obtain the potential temperature:

$$\theta = T\left(\frac{p_0}{p}\right)^{R/c_p}, \tag{4.70}$$

where $p_0 = 1000\ mb$, and $R/c_p = 0.286$.

Adiabatic Lapse Rate We start again with the first law of thermodynamics for an adiabatic process, given in Eq. 4.67. Substituting the hydrostatic equation (Eq. 4.63) into Eq. 4.67, leads to:

$$c_p\,dT + g\,dz = 0. \tag{4.71}$$

The *adiabatic lapse rate*, Γ_d, that is, the rate of decrease with respect to height, is defined as:

$$\Gamma_d \equiv -\frac{dT}{dz} = \frac{g}{c_p} \approx 0.0098\ K/m \tag{4.72}$$

[*Nappo*, 2002], using the nomenclature, Γ_d of [*Holton*, 1979; *Salby*, 1996].

The development given in *Holton* [1979] conveys additional insight. In this case, the relationship is obtained by taking the logarithm of the expression for potential temperature given in Eq. 4.70, and differentiating with respect to

height. Using the hydrostatic equation (Eq. 4.63) and the ideal gas law (Eq. 4.61) to simplify the result gives:

$$\frac{T}{\theta}\frac{\partial\theta}{\partial z} = \frac{\partial T}{\partial z} + \frac{g}{c_p}. \tag{4.73}$$

This expression shows that the adiabatic lapse rate given in Eq. 4.72 is valid for an atmosphere in which the potential temperature is constant with respect to height.

Static Stability If potential temperature is a function of height whereby it increases with altitude, an air parcel which undergoes an adiabatic displacement from its equilibrium level will be positively (negatively) buoyant when it is displaced vertically downward (upward), thus tending to return to its equilibrium level. Such an atmosphere is said to be statically stable or *stably stratified* [*Holton*, 1979]. Criteria for conditions of static stability are provided in Section 4.2.3.3.

4.2.3.2 Buoyant Force

Adiabatic oscillations of a fluid parcel about its equilibrium level in a stably stratified atmosphere are referred to as *buoyancy oscillations* [*Holton*, 1979]. We derive the characteristic frequency of such oscillations following the development presented in *Nappo* [2002] which corresponds closely to *Holton* [1979].

Beginning with an atmosphere at rest, we consider an air parcel of mass m_p in equilibrium with its environment at height z_e. The air parcel is then displaced adiabatically a small distance δz from z_e without disturbing its environment, that is, we assume the parcel does not mix with its surroundings during this

displacement. The buoyant force, $\vec{F}_b$, acting on the fluid parcel is:

$$\vec{F}_b = -g(m_p - m_a)\hat{z}, \tag{4.74}$$

where m_a is the mass of the air displaced by the fluid parcel, and g is the acceleration (positive upward) due to gravity. Considering the environment to be in hydrostatic balance, such that Eq. 4.63 applies (here, in the form $-\frac{m_p}{\rho_p}\frac{\partial p_p}{\partial z} = m_a g$), and using the second law of motion ($F = ma$), Eq. 4.74 becomes:

$$m_p \frac{d^2(\delta z)}{dt^2} = -g(m_p - m_a) = m_p\left(-g - \frac{1}{\rho_p}\frac{\partial p_p}{\partial z}\right), \tag{4.75}$$

where ρ_p and p_p are the density and pressure of the parcel, respectively. The mass of each air parcel is given by:

$$m_p = \rho_p v_p, \tag{4.76}$$

where v_p is the volume of the air parcel, and as stated above, ρ_p is its density. Satisfying the condition that the environment remain undisturbed, we assume that the volumes of the air parcel and the displaced air are equal, and that the pressure of the air parcel is always equal to the environmental pressure. Given these conditions, and using both Eq. 4.76 and the ideal gas law from Eq. 4.61, the vertical acceleration of the parcel can be written as:

$$\frac{d^2(\delta z)}{dt^2} = -g\frac{\rho_p - \rho_a}{\rho_a} = -g\frac{T_a - T_p}{T_a}, \tag{4.77}$$

where ρ_a is the environmental air density and T_a and T_p are the environmental and parcel temperatures, respectively. To proceed in our analysis considering only small vertical displacements, we first must expand both T_a and T_p to the first order:

$$T_a(z_e + \delta z) = T_0 + \left.\frac{\partial T_a}{\partial z}\right|_{z_e} \delta z + ... \tag{4.78}$$

$$T_p(z_e + \delta z) = T_0 + \left.\frac{\partial T_p}{\partial z}\right|_{z_e} \delta z + ..., \tag{4.79}$$

where T_0 is the temperature at equilibrium height z_e. Noting that the change of environmental temperature due to the vertical displacement is small, i.e.,

$$T_0 \gg \frac{\partial T_a}{\partial z}\delta z, \tag{4.80}$$

we can represent T_a for small displacements by its first order component. So, using this fact along with Eqs. 4.78 and 4.79, we can rewrite Eq. 4.77 as:

$$\frac{d^2(\delta z)}{dt^2} = -\frac{g}{T_a}\left(\frac{\partial T_a}{\partial z} - \frac{\partial T_p}{\partial z}\right)\delta z. \tag{4.81}$$

Recognizing the second term in the parenthesis above as the adiabatic lapse rate from Eq. 4.72, and setting $\partial T_a/\partial z = \Gamma$ (= γ_a in *Nappo* [2002]) to define the *atmospheric temperature gradient*, we now modify Eq. 4.81 to get:

$$\frac{d^2(\delta z)}{dt^2} = -\frac{g}{T_a}\left(\Gamma_d - \Gamma\right)\delta z. \tag{4.82}$$

Taking the logarithmic derivative of the potential temperature, given in Eq. 4.70, and using the ideal gas law from Eq. 4.61, we can generate the following expression:

$$\frac{1}{\theta}\frac{\partial \theta}{\partial z} = \frac{1}{T_a}\left(\frac{\partial T_a}{\partial z} + \frac{g}{c_p}\right) = \frac{\Gamma_d - \Gamma}{T_a}. \tag{4.83}$$

Substituting from Eq. 4.83 into Eq. 4.82, we finally arrive at the result:

$$\frac{d^2(\delta z)}{dt^2} = -\frac{g}{\theta}\frac{\partial \theta}{\partial z}\delta z, \tag{4.84}$$

or

$$\frac{d^2(\delta z)}{dt^2} = -N^2\delta z, \tag{4.85}$$

where

$$N^2 = \frac{g}{\theta}\frac{\partial \theta}{\partial z} \tag{4.86}$$

is a measure of the static stability of the environment, given that it is proportional to the restoring force of buoyancy as shown by

$$N^2 = -\frac{f_b}{\delta z} \tag{4.87}$$

[*Salby*, 1996]. Note that N^2 can be expressed in a number of other forms developed by *Holton* [1979], *Salby* [1996], and *Beer* [1974], including:

$$N^2 \;=\; g\frac{d\ln\theta}{dz} \;=\; \frac{g}{T}(\Gamma_d - \Gamma) \;=\; g\left[\frac{d(\ln\rho)}{dz} + \frac{g}{c^2}\right]. \tag{4.88}$$

Conditions of stability are discussed below in Section 4.2.3.3. Taking the square root of Eq. 4.86, gives

$$N = \sqrt{\frac{g}{\theta}\frac{\partial\theta}{\partial z}}, \tag{4.89}$$

which is known as the *Brunt-Väisäillä Frequency*, and represents the maximum frequency for vertically propagating gravity waves.

The fact that the Brunt-Väisäillä frequency represents an upper bound for the frequency of vertically propagating gravity waves can be verified by examining a more realistic case of parcel displacement. The above derivation was based on a buoyant force restricted to purely vertical displacements. These occur for waves only when the wave train is moving horizontally, such as surface waves. Gravity waves, however, typically propagate at an angle to the vertical, and as such, off-angle fluid parcel displacements should be evaluated. Once again we follow the development espoused by *Nappo* [2002] in our examination, this time considering a displacement δs of a fluid parcel from its equilibrium position on a surface inclined from horizontal by angle β. Air parcels displaced by a gravity wave oscillate along streamlines perpendicular to the propagation path of the wave; here, the inclined surface will represent the streamline. So now, the buoyant force acting on the displaced particle is:

$$\vec{F}_s = m_p\frac{d^2(\delta s)}{dt^2} = -g\,\sin\beta\,(m_p - m_a), \tag{4.90}$$

where $-g\,\sin\beta$ is the component of gravity along s. Eq. 4.77 can now be written as:

$$\frac{d^2(\delta s)}{dt^2} = -g\,\sin\beta\,\frac{T_a - T_p}{T_a}. \tag{4.91}$$

Expanding T_a and T_p in the Taylor series in the s-direction, and using these in Eq. 4.91 gives:

$$\frac{d^2(\delta s)}{dt^2} = -\frac{g\ \sin\beta}{T_a}\left(\frac{\partial T_a}{\partial s} - \frac{\partial T_p}{\partial s}\right)\delta s. \tag{4.92}$$

Since the air parcel will warm or cool at the adiabatic lapse rate projected onto the streamline, Eq. 4.92 can be written as:

$$\frac{d^2(\delta s)}{dt^2} = -\frac{g\ \sin\beta}{T_a}\left(\frac{\partial T_a}{\partial s} - \frac{g\ \sin\beta}{c_p}\right)\delta s. \tag{4.93}$$

Taking the derivative of the potential temperature (Eq. 4.70) in the s-direction and once again using the hydrostatic equation (Eq. 4.63) and the equation of state (Eq. 4.61), we get:

$$\frac{1}{\theta}\frac{\partial \theta}{\partial s} = \frac{1}{T_a}\left(\frac{\partial T_a}{\partial s} + \frac{g\ \sin\beta}{c_p}\right). \tag{4.94}$$

However, since $\partial T_a/\partial s = (\partial T_a/\partial z)\sin\beta$, Eq. 4.94 becomes:

$$\frac{1}{\theta}\frac{\partial \theta}{\partial s} = \frac{1}{T_a}\left(\frac{\partial T_a}{\partial z} + \frac{g}{c_p}\right)\sin\beta = \frac{1}{\theta}\frac{\partial \theta}{\partial z}\ \sin\beta. \tag{4.95}$$

Finally, substituting the last term from Eq. 4.95 into Eq. 4.93 gives:

$$\frac{d^2(\delta s)}{dt^2} = -\frac{g}{\theta}\frac{\partial \theta}{\partial z}\ \sin^2\beta\,\delta s, \tag{4.96}$$

and the motion of the parcel along the s-direction is:

$$\delta s(t) = Ae^{iN't} + Be^{-iN't}, \tag{4.97}$$

where

$$N' = \left[\frac{g}{\theta}\frac{\partial \theta}{\partial z}\ \sin^2\beta\right]^{1/2} = N\ \sin\beta, \tag{4.98}$$

revealing that the range of buoyancy frequencies extends from 0 to N depending on the angle, β, of propagation relative to the horizontal plane [*Nappo*, 2002].

4.2.3.3 Stability Analysis

If no initially infinitesimal wavelike disturbance grows exponentially, then a medium is said to have conditions for "stability". In this section, we look both at some different types of stability associated with gravity waves, and at the means for assessing the stability of the environment.

Static Stability Eqs. 4.82, 4.84, and 4.85 are all examples of the equation for simple harmonic motion in the vertical direction. If $N^2 > 0$, then Eq. 4.85 has solutions of the form:

$$\delta z(t) = Ae^{iNt} + Be^{-iNt}, \tag{4.99}$$

such that an air parcel displaced vertically and released will repeatedly exchange kinetic and potential energy as it oscillates about its equilibrium height, z_e, at a frequency given by N (introduced in Eq. 4.89):

$$N = \sqrt{\frac{g}{\theta}\frac{\partial\theta}{\partial z}}. \tag{4.100}$$

These oscillations become smaller and more rapid the stronger the stability is. By limiting vertical motion, positive stability also imposes constraints on horizontal motion [*Salby*, 1996].

For $N^2 = 0$, the environment is considered statically neutral as the restoring force vanishes, that is, no accelerating force exists and the parcel remains in neutral equilibrium at its new level *Holton* [1979]. *Salby* [1996] goes on to explain that in this event, the solution grows linearly with time, corresponding to a displaced parcel moving inertially with no conversion between potential and kinetic energy, such that small disturbances remain bounded, but ultimately involve into finite displacements of air.

For the case of $N^2 < 0$, a layer of negative stability evolves from the thermal properties of the atmosphere leading to a situation of *convective instability*. If $N^2 < 0$, then N is imaginary, and the solution to Eq.4.85 becomes:

$$\delta z(t) = Ae^{-N_i t} + Be^{N_i t}, \tag{4.101}$$

where $N = iN_i$. The second term in the solution represents unbounded growth, and is the driving force behind the evolution towards fully developed convection, in which nonlinear effects limit subsequent amplification by modifying the stratification of the layer [*Salby*, 1996].

Summarizing, the stability criteria for dry air are as follows:

$N^2 > 0$	$d\theta/dz > 0$	statically stable
$N^2 = 0$	$d\theta/dz = 0$	statically neutral
$N^2 < 0$	$d\theta/dz < 0$	statically unstable.

Dynamic Stability A fundamental parameter in turbulence theory is the *Richardson number*, designated as

$$R_i = \frac{N^2}{(\partial u/\partial z)^2}, \tag{4.102}$$

where N^2 is the Brunt-Väisäillä frequency squared, and $\partial u/\partial z$ is the zonal wind shear. According to *Gossard and Hooke* [1975] and *Salby* [1996], Eq. 4.102 is known as the "gradient Richardson number", distinguishing it from the "flux Richardson number" which will not be discussed here; as such, all references to the Richardson number will indicate the expression in Eq. 4.102. The Richardson number reflects the *dynamic stability* of the mean flow. It provides a criterion for the onset of turbulence by providing a measure of the stabilizing influence of

gravity, modified by temperature gradients, in comparison with the destabilizing effects of wind shears [*Beer*, 1974]; or in other words, it represents the ratio of turbulence produced by buoyancy to turbulence produced by velocity shear.

For $N^2 > 0$, R_i is positive and buoyancy stabilizes the motion as disturbances having vertical motion are damped out IF the destabilizing influence of the shear in the denominator is sufficiently small; that is, if

$$R_i \geq \frac{1}{4}. \tag{4.103}$$

In this case, the flow is stable, such that if disturbed by a small vertical displacement, it will return to its initial configuration or harmonically oscillate about that state [*Nappo*, 2002]. Conversely,

$$R_i \leq \frac{1}{4}, \tag{4.104}$$

is a necessary, but not sufficient, condition to deem the flow to be *dynamically unstable*. This situation corresponds to shear production of turbulent kinetic energy exceeding buoyancy damping by a factor of 4, such that small disturbances amplify to fully developed turbulence [*Salby*, 1996]. In summary, the stability criteria given by the Richardson number are as follows:

$$\begin{aligned} & R_i > 0.25 && \text{dynamically stable} \\ 0.25 \geq\ & R_i \geq 0 && \text{dynamically unstable} \\ & R_i < 0 && \text{convectively unstable.} \end{aligned}$$

4.2.3.4 Frames of Reference

The governing equations that express the Laws of Conservation are the starting point for determining the dispersion relation, and can be derived for neutral

fluids from two different frames of reference: Eularian or Lagrangian. In the *Lagrangian* reference frame, fluid observations are made in a coordinate system moving along with the flow. The Lagrangian frame is considered particularly useful for derivations. Most atmospheric observations, however, are made from the *Eularian* frame of reference in which the coordinate system is fixed relative to the Earth. The Eularian frame, considered more convenient for solving most problems, is the reference frame used here to derive the dispersion equation. These two reference frames are connected by a relationship between the rate of change of a field variable following the motion and its rate of change at a fixed point. The first derivative is called the total, material, substantial, or Lagrangian derivative, and is denoted by D/Dt or d/dt. The latter is called the local or Eularian derivative, and is merely a partial derivative with respect to time, denoted by $\partial/\partial t$.

To transform to the Eularian description, the Lagrangian derivative must be expressed in terms of field properties. Following *Salby* [1996], we consider the field variable $\psi = \psi(x, y, z, t)$, and express the incremental change of property ψ by the total differential

$$\begin{aligned} d\psi &= \frac{\partial \psi}{\partial t}\,dt + \frac{\partial \psi}{\partial x}\,dx + \frac{\partial \psi}{\partial y}\,dy + \frac{\partial \psi}{\partial z}\,dz \\ &= \frac{\partial \psi}{\partial t}\,dt + \nabla\psi \cdot d\boldsymbol{x}, \end{aligned} \tag{4.105}$$

where $d\boldsymbol{x} = (dx, dy, dz)$. Now, differentiating Eq. 4.105 with respect to time gives the time rate of change of ψ moving along with a material element:

$$\begin{aligned} \frac{d\psi}{dt} &= \frac{\partial \psi}{\partial t}\frac{dt}{dt} + \frac{\partial \psi}{\partial x}\frac{dx}{dt} + \frac{\partial \psi}{\partial y}\frac{dy}{dt} + \frac{\partial \psi}{\partial z}\frac{dz}{dt} \\ &= \frac{\partial \psi}{\partial t} + u\frac{\partial \psi}{\partial x} + v\frac{\partial \psi}{\partial y} + w\frac{\partial \psi}{\partial z} \\ \frac{D\psi}{Dt} &= \frac{\partial \psi}{\partial t} + \boldsymbol{U} \cdot \nabla\psi \end{aligned} \tag{4.106}$$

which defines the Lagrangian derivative of the field variable $\psi(\boldsymbol{x}, t)$. Note that $\boldsymbol{U} = \hat{i}u + \hat{j}v + \hat{k}w$ is the velocity vector, and that the nomenclature for the material derivative has been switched to D/Dt which is used in the subsequent analysis. Eq. 4.106 reveals that the material derivative includes two contributions. The first term, $\partial\psi/\partial t$, is the Eularian or local derivative, representing the rate of change of the material property ψ introduced by temporal changes in the field variable at the position $\boldsymbol{x}$ where the material element is located. The second contribution, $\boldsymbol{U}\cdot\nabla\psi$, is the *advective contribution* or *advection*, representing the change of the material property ψ due to motion of the material element to positions of different field values; that is, the rate that ψ changes for the material element is given by its velocity in the direction of the gradient of ψ times that gradient. Finally, rearranging terms in Eq. 4.106, we can write the form for the Eulerian derivative we will be using as

$$\frac{\partial\psi}{\partial t} = \frac{D\psi}{Dt} - \boldsymbol{U}\cdot\nabla\psi, \tag{4.107}$$

which states that the local rate of change of ψ equals the rate of change of ψ following the motion plus the advective rate of change of ψ.

4.2.3.5 The Fundamental Equations

The starting point for deriving the gravity wave dispersion relation begins with the determination of a set of fundamental equations. Moreover, these in turn, can be derived through two approaches. For a neutral fluid, these basic equations can be derived directly from first principles starting with the Laws of Conservation; that is, atmospheric motions are governed by three fundamental physical principles: conservation of mass, conservation of momentum, and conservation of energy. Another approach highlighting the relevance to the iono-

spheric environment, is to develop a set of transport equations which describe the spatial and temporal evolution of physically significant velocity moments. The flow of fluids, including those found in the upper atmosphere comprised of both plasma and neutral atmospheric flows, can be represented by these transport equations. Transport equations, in turn, can be derived from the Boltzmann equation which for the case when collisions are important describes the *distribution* of particles, rather than the motion of individual particles. In general due to complexity, evaluations are limited to low-order velocity moments of the species distributions. *Schunk and Nagy* [2000] describe a closed system of transport equations at the 13-moment level of approximation. Typically, a perturbation scheme is employed and numerous assumptions are asserted before the transport equations are applied, and in our case of gravity waves in the mesospheric region, additional assumptions and application of a linearization process are in order to bring the problem down to a much more manageable set of governing equations, and finally, to the relevant dispersion equation.

As an example of the starting-point complexity for the transport equation approach, we cite the general equation of motion given for a plasma by *Gossard and Hooke* [1975]:

$$\overbrace{\rho\left(\frac{D\mathbf{U}}{Dt}\right)}^{1} - \overbrace{\mathbf{J}\times\mathbf{B}}^{2} + \overbrace{\nabla p}^{3} + \overbrace{\rho\mathbf{g}}^{4} + \overbrace{\rho\nu(\mathbf{U}-v_n)}^{5} + \overbrace{2\rho\boldsymbol{\Omega}\times\mathbf{v}}^{6} + \overbrace{\rho(\boldsymbol{\Omega}\times(\boldsymbol{\Omega}\times\mathbf{r}))}^{7} - \overbrace{\mathbf{F}}^{8} = 0, \tag{4.108}$$

where the various terms in Eq. 4.108 are noted in Table 4.3, and where the following definitions apply:

$$\mathbf{U} = \frac{m_i n_i v_i + m_e n_e v_e}{m_i n_i + m_e n_e}, \tag{4.109}$$

$$\mathbf{J} = (e/c)(Z n_i v_i - n_e v_e), \tag{4.110}$$

Table 4.3: Description of terms included in the general equation of motion for a plasma given in Eq. 4.108.

#	Term	Force
1:	$\rho\left(\frac{D\mathbf{U}}{Dt}\right)$	inertial
2:	$\mathbf{J}\times\mathbf{B}$	electromagnetic
3:	∇p	pressure
4:	$\rho\mathbf{g}$	gravitational
5:	$\rho\nu(\mathbf{U}-v_n)$	collisional
6:	$2\rho\mathbf{\Omega}\times\mathbf{v}$	Coriolis
7:	$\rho(\mathbf{\Omega}\times(\mathbf{\Omega}\times\mathbf{r}))$	centrifugal
8:	$\mathbf{F}$	frictional

and,

$$\nu = \frac{m_i n_i \nu_i + m_e n_e \nu_e}{m_i n_i + m_e n_e} \simeq \nu_i + \frac{m_e}{m_i}\frac{n_e}{n_i}\nu_e \simeq \nu_i. \tag{4.111}$$

Further, in the above equations, only one species is considered; m_i and m_e are the masses of the ions and electrons; v_i and v_e are their respective velocities, and n_i and n_e are the number of particles. Z is the number of charges per ion, and e/c is the charge of an electron. Continuing, we define ρ as the mass density in $[kg/m^3]$; $\mathbf{U}$ is the fluid velocity vector in $[m/s]$; $\mathbf{\Omega}$ is the Earth's angular frequency of rotation in $[s^{-1}]$; $\mathbf{r}$ is the radius of the Earth in $[m]$; $p = \rho RT$ is the pressure in $[N/m^2]$; $\mathbf{g}$ is the gravitational acceleration in $[m/s^2]$; and $\mathbf{F}$ is the frictional force.

As stated earlier, a perturbation scheme is employed to refine the system of 13-moment transport equations down, resulting in one means to derive the Euler and Navier-Stokes equations of hydrodynamics. For convenience in the derivations, as in the example of Eq. 4.108, only a single-component neutral gas is considered; appropriately, this corresponds to the classical case in which the hydrodynamic equations apply. In the perturbation scheme applied to at-

tain both of these classical systems of equations, the collision frequency is assumed to be sufficiently large that the neutral velocity distribution is very nearly Maxwellian. In this collision-dominated limit for deriving the Euler equations, the stress tensor and heat flow vectors are small compared to the density, velocity, and temperature components, all of order one. To lowest order in the perturbation scheme, stress and heat flow effects are neglected, and the 13-moment equations of continuity, momentum, and energy result in the Euler equations. *Schunk and Nagy* [2000] note that the Euler hydrodynamic equations pertain to the case when the neutral velocity distribution is a drifting Maxwellian. To the next order in the perturbation scheme, the stress tensor and heat flow equations are used to express the stress tensor and heat flow vectors in terms of density, velocity, and temperature. Order one terms are again retained, this time reducing the transport equations into the Navier-Stokes system of equations consisting of the continuity, momentum, and energy equations coupled with the collision-dominated expressions for the stress tensor and the heat flow vector. For our purposes, the complete Euler equations listed below, modified from *Nappo* [2002], represent the starting-point neutral atmosphere – a rotating, frictionless environment – for our quest to describe gravity waves. Additional assumptions to follow will provide us further reduction of the system of Euler equations, representing in order below: the conservation of momentum, the conservation of mass, and the conservation of thermal energy.

$$\rho \frac{D\mathbf{U}}{Dt} = -\nabla p + 2\rho\boldsymbol{\Omega} \times \mathbf{U} + \rho(\boldsymbol{\Omega} \times (\boldsymbol{\Omega} \times \mathbf{r})) + \rho\mathbf{g} \tag{4.112}$$

$$\frac{D\rho}{Dt} + \rho\nabla \cdot \mathbf{U} = 0 \tag{4.113}$$

$$\frac{Dp}{Dt} - C_s^2 \frac{D\rho}{Dt} = 0, \tag{4.114}$$

where ρ is the neutral density in $[kg/m^3]$; $\mathbf{U}$ is the neutral fluid velocity vector in $[m/s]$; $\boldsymbol{\Omega}$ is the Earth's angular frequency of rotation in $[s^{-1}]$; $\mathbf{r}$ is the radius of

the Earth in $[m]$; p is the pressure in $[N/m^2]$; $\mathbf{g}$ is the gravitational acceleration in $[m/s^2]$; $C_s^2 = (c_p/c_v)(p/\rho)$ is the speed of sound in $[m/s]$ where c_p is the specific heat capacity at constant pressure and c_v is the specific heat capacity for dry air at constant volume.

The centrifugal force, given by $\mathbf{\Omega} \times (\mathbf{\Omega} \times \mathbf{r})$ in Eq. 4.112, tends to counteract the gravitational force with respect to latitude; as such, its effects can be incorporated into that of the effective gravity [*Gossard and Hooke*, 1975; *Kelley*, 1989]. Given this, we often see the Euler equations in a rotating frame depicted merely as:

$$\rho \frac{D\mathbf{U}}{Dt} = -\nabla p + 2\rho\mathbf{\Omega} \times \mathbf{U} + \rho\mathbf{g} \tag{4.115}$$

$$\frac{D\rho}{Dt} + \rho\nabla \cdot \mathbf{U} = 0 \tag{4.116}$$

$$\frac{Dp}{Dt} - C_s^2 \frac{D\rho}{Dt} = 0. \tag{4.117}$$

Here we have used the velocity divergence form of the continuity equation in Eq. 4.116; and we have represented the conservation of energy in Eq. 4.117 in terms of pressure and density variations. This collection of equations will be used for a good portion of our analysis to come. Alternately, we can depict the continuity equation in terms of mass divergence by applying both the vector identity

$$\nabla \cdot (\rho\mathbf{U}) = \rho\nabla \cdot \mathbf{U} + \mathbf{U} \cdot \nabla\rho, \tag{4.118}$$

and the relationship between the Lagrangian and Eulerian derivatives given in both Eq. 4.106 and Eq. 4.107. According to *Beer* [1974], we can also express the energy equation using the temperature, T, as the dependent variable, where

$$\frac{DT}{Dt} + (\gamma - 1)T\nabla \cdot \mathbf{U} = 0 \tag{4.119}$$

leads to Eq. 4.122 below. Incorporating these changes, we can then represent an

alternate form of the system of equations as:

$$\rho\frac{D\mathbf{U}}{Dt} + 2\boldsymbol{\Omega}\times\rho\mathbf{U} + \nabla p = -\rho\mathbf{g} \tag{4.120}$$

$$\frac{\partial\rho}{\partial t} + \nabla\cdot(\rho\mathbf{U}) = 0 \tag{4.121}$$

$$c_p\frac{DT}{Dt} - \frac{RT}{p}\frac{Dp}{Dt} = 0. \tag{4.122}$$

We will use Eq.s 4.120–4.122 to begin our analysis of internal gravity waves in the next section.

4.2.3.6 The Dispersion Equation

In this section, we investigate the dispersive relationship between the phase speeds and wavenumbers for internal gravity waves by deriving the appropriate dispersion equations. Our approach will be as follows: First, we revisit the concept of linear theory by defining the methodology used to linearize the fundamental equations. We then introduce the dispersive effects of internal gravity waves through some basic sea water wave examples, first in 3-dimensions then in 2-dimensions. Next, we introduce our atmospheric, internal-gravity-wave example of interest: acoustic gravity waves. We pause for a discussion of the Boussinesq approximation before continuing with the development of the acoustic gravity wave 2-D dispersion relation. Finally, we end the section by considering a more general 3-D case with increased complexity which, further, allows us to investigate the resulting vertical propagation characteristics of internal gravity waves. (Note: The materials on the sea water, internal-gravity-wave introduction and the more complex general case are both taken from ECE 585 class notes provided courtesy of Prof. Charles Seyler. Some minor changes were made to allow for consistency of notation and formatting.)

Linearization Methodology As introduced in the section on linear theory (Section 4.2.1.2), the next step towards developing the dispersion equation is to linearize the fundamental equations (Eq.s 4.115-4.117 and/or Eq.s 4.120-4.122), by rewriting each of the parameters in terms of the sum of a steady, horizontally-uniform background value, $q_0(z)$, and a first-order perturbation, $q_1(x, y, z, t)$, according to the form:

$$q(x, y, z, t) = q_0(z) + q_1(x, y, z, t), \tag{4.123}$$

followed by *Nappo* [2002], *Schunk and Nagy* [2000], *Beer* [1974], and *Gossard and Hooke* [1975]. Alternatively, *Kelley* [1989] designates the perturbed state as δq, while *Holton* [1979] and *Salby* [1996] use q'. The perturbation method is a well-known approach for solving non-linear ordinary differential equations, as well as the non-linear partial differential equations of hydrodynamics. While the higher-order terms no doubt add to the description of the physical phenomena, linearizing the basic equations to obtain first-order solutions provides a mathematically tractable method.

Internal Gravity Waves: Sea Water Waves Gravity waves are often introduced in the context of shallow water waves. In that case the downward restoring force is gravity acting on the water displaced above the equilibrium level. The upward restoring force is water pressure. Such waves are external waves in that the the sharp interface between water and air is displaced. There is no sharp interface in the atmosphere, but there is stable stratification in which level surfaces of constant density achieve an equilibrium such that the normal vectors of the level surface are parallel to g. If the surface is perturbed from equilibrium, then the forces of gravity and pressure restore equilibrium just as in water waves. Gravity waves in a stably stratified medium which do not have

a sharp fluid interface are called internal gravity waves. The equations which describe internal gravity waves are more complicated than the equations which describe large-scale motion of the atmosphere because a number of the assumptions which apply to large-scale motion do not apply to gravity waves. We can simplify using some additional assumptions appropriate for gravity waves:

1. Use β - plane with $\beta = 0$, i.e. $f \approx f_0$.
2. $\partial/\partial t \sim N \gg \Omega$
3. Also, given that the wavelengths of gravity waves are smaller than planetary radii, we can utilize the Cartesian coordinate system represented by (x, y, z) corresponding to the meteorological convention of (eastward, northward, vertically upward) as introduced in Section 4.2.2.

Applying these, we have:

$$\frac{Du}{Dt} - fv + \frac{1}{\rho_0}\frac{\partial p_1}{\partial x} = 0 \tag{4.124}$$

$$\frac{Dv}{Dt} + fu + \frac{1}{\rho_0}\frac{\partial p_1}{\partial y} = 0 \tag{4.125}$$

$$\frac{Dw}{Dt} + \frac{1}{\rho_0}\frac{\partial p_1}{\partial z} = -g\frac{\rho_1}{\rho_0} \tag{4.126}$$

$$\frac{\partial \rho_1}{\partial t} + \nabla \cdot (\rho_0 \mathbf{U}) = 0 \tag{4.127}$$

$$\frac{DT_1}{Dt} - \frac{1}{\rho_0 c_p}\frac{Dp_1}{Dt} + \frac{T_0 N^2}{g} w = 0 \tag{4.128}$$

We now linearize Eq.s 4.124–4.128 assuming that the flow is small so that $\partial/\partial t \gg \mathbf{U} \cdot \nabla$. The equation of state when linearized gives $\frac{\rho_1}{\rho_0} = \frac{p_1}{p_0} - \frac{T_1}{T_0}$. We then obtain:

$$\frac{\partial u}{\partial t} - fv + \frac{1}{\rho_0}\frac{\partial p_1}{\partial x} = 0 \tag{4.129}$$

$$\frac{\partial v}{\partial t} + fu + \frac{1}{\rho_0}\frac{\partial p_1}{\partial y} = 0 \tag{4.130}$$

$$\frac{\partial w}{\partial t} + \frac{1}{\rho_0}\frac{\partial p_1}{\partial z} = g\left(\frac{T_1}{T_0} - \frac{p_1}{p_0}\right) \tag{4.131}$$

$$\frac{1}{p_0}\frac{\partial p_1}{\partial t} - \frac{1}{T_0}\frac{\partial T_1}{\partial t} + \frac{\partial u}{\partial x} + \frac{\partial v}{\partial y} + \frac{1}{\rho_0}\frac{\partial}{\partial z}(\rho_0 w) = 0 \tag{4.132}$$

$$\frac{1}{T_0}\frac{\partial T_1}{\partial t} - \frac{R}{pc_p}\frac{\partial p_1}{\partial t} + \frac{N^2}{g}w = 0 \tag{4.133}$$

Eq.s 4.129–4.133 are the linearized equations describing internal gravity waves including Coriolis effects. Let's take simple cases before considering the most general case. Consider sea water waves due to a slight stabilizing salinity gradient. For such internal gravity waves assume,

1. $\rho_0 = \rho_0 + \frac{d\rho_0}{dz} z$, Second term $\sim 10^{-3}$ of first.
2. $\frac{D\rho}{Dt} = 0 \Rightarrow \nabla \cdot \mathbf{v} = 0$, i.e. water is incompressible at normal pressures
3. $\frac{D\rho}{Dt} = 0 \Rightarrow \frac{\rho_1}{\partial t} + w\frac{d\rho_0}{dz} = 0$
4. $N^2 \equiv -\frac{g}{\rho_0}\frac{d\rho_0}{dz}$

Then we have,

$$\frac{\partial u}{\partial t} - fv + \frac{1}{\rho_0}\frac{\partial p_1}{\partial x} = 0 \tag{4.134}$$

$$\frac{\partial v}{\partial t} + fu + \frac{1}{\rho_0}\frac{\partial p_1}{\partial y} = 0 \tag{4.135}$$

$$\frac{\partial w}{\partial t} + \frac{1}{\rho_0}\frac{\partial p_1}{\partial z} = -g\frac{\rho_1}{\rho_0} \tag{4.136}$$

$$\frac{\partial \rho_1}{\partial t} - \frac{\rho_0 N^2}{g}w = 0 \tag{4.137}$$

$$\frac{\partial u}{\partial x} + \frac{\partial v}{\partial y} + \frac{\partial w}{\partial z} = 0 \tag{4.138}$$

Eq.s 4.134–4.138 can also be applied to wind flow over mountains as long as height variations are small compared to a scale height.

Consider the simplest possible internal gravity wave problem. To start, assume a non-rotating reference frame such that the Coriolis force term can now be neglected. This assumption can be justified given that the wave periods of gravity waves are typically much smaller than planetary rotation periods. This is the same justification that allowed us to formulate our problem in a Cartesian coordinate system. Further now, owing to the neglect of both viscosity and the Coriolis effects, we note that the horizontal directions are not coupled; however, since gravity waves are transverse resulting in motion perpendicular to the wave vector, $\mathbf{k}$, two dimensions are required to represent their propagation. One convention is to describe the motion of gravity waves in the $x - z$ plane, such that $\mathbf{U} = (u, 0, w)$, allowing us to represent the momentum equation as two separate equations. Summarizing our assumptions:

1. No compressibility effects $\Rightarrow$ for oceanography, Eq.s 4.134–4.138 can be used
2. $\partial/\partial t \gg f$. Neglect Coriolis force.
3. $\partial/\partial y = 0$. Wave is in $x - z$ plane.

Taking a time derivative of Eq. 4.136 and substituting Eq. 4.137, we get:

$$\frac{\partial^2 w}{\partial t^2} + \frac{1}{\rho_0}\frac{\partial}{\partial z}\frac{\partial}{\partial t}p_1 = -N^2 w \tag{4.139}$$

$$\frac{\partial u}{\partial t} + \frac{1}{\rho_0}\frac{\partial p_1}{\partial x} = 0 \tag{4.140}$$

$$\frac{\partial u}{\partial x} + \frac{\partial w}{\partial z} = 0. \tag{4.141}$$

Combining the above to get a single PDE for w, we find:

$$\frac{\partial^2}{\partial t^2}\left(\frac{\partial^2 w}{\partial x^2} + \frac{\partial^2 w}{\partial z^2}\right) + N^2\frac{\partial^2 w}{\partial x^2} = 0. \tag{4.142}$$

We assume a plane-wave solution of the form $\exp[i(kx + mz - \omega t)]$, and find the dispersion relation:

$$\frac{\omega^2}{N^2} = \frac{k^2}{k^2 + m^2}. \tag{4.143}$$

Comments:

1. N^2 is the maximum frequency, which is achieved for $k^2 \gg m^2$.
2. If θ is the tilt angle of the phase fronts, then $\omega = N \sin\theta$.
3. Continuity equation $\Rightarrow \mathbf{k} \cdot \mathbf{U} = 0$ which means the waves are transverse.
4. The buoyancy equation (Eq. 4.137) $\Rightarrow \rho_1$ follows w.
5. Hydrostatic balance $\Rightarrow$ p_1 lags ρ_1 by 90^o.
6. The energy flux for gravity waves in general is:

$$\mathbf{F}_E = \underbrace{\frac{1}{2}\overline{\rho_0 \mathbf{U} v^2}}_{\text{kinetic energy flux}} + \underbrace{\overline{\rho_0 \mathbf{U} e}}_{\text{internal energy flux}} + \underbrace{\overline{\mathbf{U} p_1}}_{\text{pressure work flux}} \tag{4.144}$$

For incompressible waves, the internal energy flux is zero and the kinetic energy flux is small if the wave amplitude is sufficiently small. We now evaluate the energy flux in this case, using

$$-i\omega u + \frac{ik}{\rho_0} p_1 = 0, \tag{4.145}$$

and

$$iku + imw = 0. \tag{4.146}$$

Thus,

$$\overline{p_1 u} = \overline{\rho_0 \frac{\omega}{k} u^2} = \frac{1}{2} \rho_0 u_0^2 \frac{\omega}{k}, \tag{4.147}$$

and

$$\overline{p_1 w} = \overline{\rho_0 \frac{\omega}{k} u \left(-\frac{k}{m}\right) u} = -\frac{1}{2} \rho_0 u_0^2 \frac{\omega}{m}, \tag{4.148}$$

so that,

$$\mathbf{F}_E = (\overline{up_1}, \overline{wp_1}) = \frac{1}{2}\rho_0 u_0^2 \left(\frac{\omega}{k}, -\frac{\omega}{m}\right) \tag{4.149}$$

Note: $\mathbf{k} \cdot \mathbf{F}_E = 0$.

Internal Gravity Waves: Acoustic Gravity Wave Introduction Returning to our analysis based on Eq.s 4.115–4.117, we can represent the basic Euler equations in a non-rotating reference frame as:

$$\rho \frac{D\mathbf{U}}{Dt} = -\nabla p + \rho \mathbf{g} \tag{4.150}$$

$$\frac{D\rho}{Dt} + \rho \nabla \cdot \mathbf{U} = 0 \tag{4.151}$$

$$\frac{Dp}{Dt} - C_s^2 \frac{D\rho}{Dt} = 0. \tag{4.152}$$

Incorporating our further simplifying assumptions for internal gravity waves, we now write the Euler equations which represent a neutral, flat, irrotational, inviscid atmosphere supporting two-dimensional propagation in the $x-z$ plane as:

$$\frac{Du}{Dt} = -\frac{1}{\rho}\frac{\partial p}{\partial x} \tag{4.153}$$

$$\frac{Dw}{Dt} = -\frac{1}{\rho}\frac{\partial p}{\partial z} - g \tag{4.154}$$

$$\frac{1}{\rho}\frac{D\rho}{Dt} + \frac{\partial u}{\partial x} + \frac{\partial w}{\partial z} = 0 \tag{4.155}$$

$$\frac{Dp}{Dt} - C_s^2 \frac{D\rho}{Dt} = 0. \tag{4.156}$$

Note that the gravity term in Eq. 4.154 is now negative, indicating that the vector direction is vertically downward.

For our investigation of gravity wave properties, the initial atmosphere is usually assumed to be isothermal (T_0 =constant); stationary, i.e., windless ($\mathbf{U}_0 = 0$); horizontally stratified; and in hydrostatic equilibrium ($\nabla p_0 = \rho_0 \mathbf{g}$ in

vector notation, or following Eq. 4.63, $\partial p_0/\partial z = -\rho_0 g$). The initial hydrostatic equilibrium of the atmosphere can also be expressed by the balance equation:

$$\frac{1}{n_0}\frac{\partial n_0}{\partial z} = -\frac{1}{H_0}, \tag{4.157}$$

where $p_0 = n_0 k_B T_0$, and $H_0 = k_B T_0/mg$ is the atmospheric scale height from Eq. 4.66 given $R = k_B/m$. Eq. 4.157 indicates that this initial atmospheric state varies only with z, and in an exponential manner [*Kelley*, 1989; *Schunk and Nagy*, 2000]:

$$p_0, \rho_0 \propto e^{-z/H_0}. \tag{4.158}$$

At this stage in the derivation, the various textbooks proceed with two different approaches. In the atmospheres described above, acoustic waves exist along with our targeted gravity waves given the assumptions made thus far to reduce the scope of the basic equations. One approach is to continue in this manner, analyzing *acoustic-gravity waves* (AGW), which involve both buoyancy and compression. [Note: To clarify the nomenclature, in some texts, such as *Schunk and Nagy* [2000], "AGW" refers to *atmospheric gravity waves*. Semantically, the meanings are the same as both terms refer to the category of waves including both acoustic waves and gravity waves.] The second approach is to pause at this point and make additional assumptions to eliminate acoustic waves from the mix. This can be achieved through the Boussinesq approximation discussed below.

Boussinesq Approximation The *Boussinesq approximation* enables us to treat a fluid as incompressible. In this approximation, density is treated as a constant everywhere except where it is coupled with gravity in the buoyancy term of the vertical momentum equation, i.e., of the vertical components of Eq. 4.150. The

fluctuating changes in density due to local pressure are assumed to be small perturbations of the constant basic state density field, and as such, are considered negligible. Given this, i.e., that the vertical variation of the basic state density is neglected except where coupled with gravity, the Boussinesq approximation is valid only for motions in which the vertical scale is less than the atmospheric scale height [*Holton*, 1979]. Applying the Boussinesq approximation can be advantageous in numerical modelling. By eliminating the acoustical waves requiring finer resolution time constants to describe the flow, the Boussinesq approximation allows the use of larger time constants which reduces the simulation run time.

Acoustic Gravity Wave 2-D Dispersion Continuing the derivation of the dispersion equation for AGWs, we substitute the perturbation quantities into Eq.s 4.153-4.156, and retain only those terms that are linear in the perturbations. The first-order perturbed equations of motion, continuity and state are then found to be:

$$\rho_0 \frac{\partial u_1}{\partial t} + \frac{\partial p_1}{\partial x} = 0 \tag{4.159}$$

$$\rho_0 \frac{\partial w_1}{\partial t} + \frac{\partial p_1}{\partial z} + g\rho_1 = 0 \tag{4.160}$$

$$\frac{\partial \rho_1}{\partial t} + w_1 \frac{\partial \rho_0}{\partial z} + \rho_0 \left(\frac{\partial u_1}{\partial x} + \frac{\partial w_1}{\partial z} \right) = 0 \tag{4.161}$$

$$\frac{\partial p_1}{\partial t} + w_1 \frac{\partial p_0}{\partial z} - C_s^2 \left(\frac{\partial \rho_1}{\partial t} + w_1 \frac{\partial \rho_0}{\partial z} \right) = 0, \tag{4.162}$$

where the subscript "0" refers to the background state, and the subscript "1" refers to the perturbed state. For convenience, it is customary at this point to express the equations in terms of the perturbation ratios ρ_1/ρ_0 and p_1/p_0 instead of ρ_1 and p_1. Additionally, using Eq. 4.158, we can rewrite terms containing

elements of $\nabla\rho_0$ and ∇p_0 in terms of the atmospheric scale height, H_0, such that:

$$\mathbf{U_1} \cdot \nabla\rho_0 = w_1 \frac{\partial \rho_0}{\partial z} = -\frac{\rho_0}{H_0} w_1 \tag{4.163}$$

$$\mathbf{U_1} \cdot \nabla p_0 = w_1 \frac{\partial p_0}{\partial z} = -\frac{p_0}{H_0} w_1, \tag{4.164}$$

where w_1 is the vertical component of the perturbed velocity. Following the method of *Schunk and Nagy* [2000], and noting that Eq.s 4.159 and 4.160 contain the x and z components of ∇p_1 which can be expanded as:

$$\nabla p_1 = \nabla\left(p_0 \frac{p_1}{p_0}\right) = p_0 \nabla\left(\frac{p_1}{p_0}\right) + \frac{p_1}{p_0}\nabla p_0, \tag{4.165}$$

Eq.s 4.159-4.162 now become:

$$\frac{\partial u_1}{\partial t} + \frac{p_0}{\rho_0}\frac{\partial}{\partial x}\left(\frac{p_1}{p_0}\right) = 0 \tag{4.166}$$

$$\frac{\partial w_1}{\partial t} + \frac{1}{\rho_0}\frac{p_1}{p_0}\frac{\partial p_0}{\partial z} + g\frac{\rho_1}{\rho_0} = 0 \tag{4.167}$$

$$\frac{\partial}{\partial t}\frac{\rho_1}{\rho_0} - \frac{w_1}{H_0} + \left(\frac{\partial u_1}{\partial x} + \frac{\partial w_1}{\partial z}\right) = 0 \tag{4.168}$$

$$\frac{\partial}{\partial t}\frac{p_1}{p_0} - \frac{w_1}{H_0} + \frac{\gamma}{\rho_0}\left(\frac{\partial \rho_1}{\partial t} + w_1\frac{\partial \rho_0}{\partial z}\right) = 0, \tag{4.169}$$

where $\gamma = 5/3$, the ratio of specific heats at constant pressure and constant volume, is substituted into Eq. 4.169 based on the relation:

$$C_s^2 = \gamma p_0/\rho_0 = \gamma g H_0 = \gamma RT. \tag{4.170}$$

We assume that the atmospheric perturbations can be described by plane waves, such that:

$$\left(\frac{\rho_1}{\rho_0}\right), \left(\frac{p_1}{p_0}\right), \mathbf{U_1} \propto e^{i(\mathbf{k}\cdot\mathbf{r}-\omega t)} = \exp\, i(k_x x + k_z z - \omega t) = \exp\, i(kx + mz - \omega t), \tag{4.171}$$

where $\mathbf{k}$ is the wave vector and ω is the wave frequency. To isolate the perturbed quantities in the governing equations given in Eq.s 4.166-4.169, we make use of

the sinusoidal relationships outlined in Eq. 4.171 to obtain the space and time derivatives of the plane waves to get:

$$-i\omega u_1 + \frac{p_0}{\rho_0} ik_x \left(\frac{p_1}{p_0}\right) = 0 \tag{4.172}$$

$$-i\omega w_1 + \frac{1}{\rho_0}\frac{p_1}{p_0}\frac{\partial p_0}{\partial z} + g\frac{\rho_1}{\rho_0} = 0 \tag{4.173}$$

$$-i\omega\frac{\rho_1}{\rho_0} - \frac{w_1}{H_0} + ik_x u_1 + ik_z w_1 = 0 \tag{4.174}$$

$$-i\omega\frac{p_1}{p_0} - \frac{w_1}{H_0} + \frac{\gamma}{\rho_0}\left(\frac{\partial \rho_1}{\partial t} + w_1\frac{\partial \rho_0}{\partial z}\right) = 0, \tag{4.175}$$

To accommodate our next step, we can rewrite some terms using the chain rule and the relation expressed earlier in Eq. 4.170. Consider, for example, modifying the coefficient of $\frac{p_1}{p_0}$ in the second term in Eq. 4.173:

$$\frac{1}{\rho_0}\frac{\partial p_0}{\partial z} = \frac{1}{\rho_0}\left[\frac{\partial p_0}{\partial z} + p_0\left(\frac{\partial}{\partial z}\right)\right] = \frac{1}{\rho_0}\left(-\frac{p_0}{H_0}\right) + ik_z\frac{p_0}{\rho_0} = \frac{p_0}{\rho_0}\left(ik_z - \frac{1}{H_0}\right) = \frac{C_s^2}{\gamma}\left(ik_z - \frac{1}{H_0}\right). \tag{4.176}$$

We can now express the four linear equations for the four unknown perturbations in matrix form:

$$\begin{bmatrix} 0 & ik_x\frac{C_s^2}{\gamma} & -i\omega & 0 \\ g & \left(ik_z - \frac{1}{H_0}\right)\frac{C_s^2}{\gamma} & 0 & -i\omega \\ -i\omega & 0 & ik_x & \left(ik_z - \frac{1}{H_0}\right) \\ 0 & -i\omega & i\gamma k_x & \left(i\gamma k_z - \frac{1}{H_0}\right) \end{bmatrix} \cdot \begin{bmatrix} \frac{\rho_1}{\rho_0} \\ \frac{p_1}{p_0} \\ u_1 \\ w_1 \end{bmatrix} = 0, \tag{4.177}$$

where the columns of the 4×4 matrix correspond to the coefficients of the perturbation variables, and the rows correspond to the x-momentum, z-momentum, continuity, and energy (or adiabatic state) equations, respectively.

Solving using matrix techniques for linear equations, a non-trivial solution to Eq. 4.177 is obtained only when the determinant of the coefficient matrix vanishes, i.e. when the determinant is set to zero. The expansion of the determinant

leads to the dispersion equation relating $\mathbf{k}$ and ω for AGWs:

$$\omega^4 - \omega^2 C_s^2(k_x^2 + k_z^2) + (\gamma - 1)g^2 k_x^2 - i\gamma g\omega^2 k_z = 0. \tag{4.178}$$

As is universally addressed at this juncture [*Hines*, 1960; *Beer*, 1974; *Kelley*, 1989; *Schunk and Nagy*, 2000], further analysis is required to investigate the various wave modes imbedded in this dispersion relation (Eq. 4.178). For the simplest case, if we let $g = 0$, we isolate the acoustic mode, and arrive at the dispersion relation for acoustic waves:

$$\omega^2 = C_s^2(k_x^2 + k_z^2) = C_s^2\mathbf{k}^2. \tag{4.179}$$

For sound waves, the fact that both ω and $\mathbf{k}$ are real translates to their propagating without attenuation or growth. Further, they also avoid dispersion since $\omega/k = d\omega/dk = \pm C_s$ = constant; the ± signs correspond to sound waves propagating in opposite directions [*Schunk and Nagy*, 2000].

Now, when we include gravity ($g \neq 0$), k_x, k_z, and ω cannot all be real. For horizontally propagating waves, k_x and ω must be real; hence, we must necessarily assume k_z is complex, such that $k_z = k_{zR} + ik_{zI}$, where k_{zR} and k_{zI} are the real and imaginary parts, respectively. Incorporating this complex k_z into Eq. 4.178, we get:

$$\omega^4 - \omega^2 C_s^2(k_x^2 + k_{zR}^2 - k_{zI}^2) + \gamma g k_{zI}\omega^2 + (\gamma - 1)g^2 k_x^2 - i\omega^2 k_{zR}(\gamma g + 2C_s^2 K_{zI}) = 0. \tag{4.180}$$

Assessing the imaginary part of Eq. 4.180 (5$^{\text{th}}$ term on the left-hand side of the equation), we find that if the frequency, ω, is not zero, either:

$$k_{zR} = 0, \tag{4.181}$$

whereby the vertical wavenumber is purely imaginary, or

$$k_{zI} = -\frac{\gamma g}{2C_s^2} = -\frac{1}{2H_0}. \tag{4.182}$$

The option presented in Eq. 4.181 results in waves with no vertical phase variations, only exponential amplification or decay with height. This is characteristic of surface waves and evanescent waves [*Beer*, 1974]. For our purposes, we are interested in the second alternative, presented in Eq. 4.182. Incorporating the complex k_z into the expression for the velocity perturbation from Eq. 4.171, we get:

$$\mathbf{U_1} \propto e^{z/2H_0} e^{i(k_x x + k_{zR} z - \omega t)} = \exp(z/2H_0) \exp i(k_x x + k_{zR} z - \omega t), \tag{4.183}$$

representing the propagation characteristics of *internal gravity waves* (IGW). An important property of IGWs is that the wave perturbation energy, $\frac{1}{2}\rho_0 U_{1z}^2$, remains constant because the density, ρ_0, varies as e^{-z/H_0} (from Eq. 4.158), while, as we just concluded, the vertical velocity component, U_{1z}, varies as $e^{z/2H_0}$ (from Eq. 4.183). As a result, a unique feature of IGWs is that the wave amplitude grows as the wave propagates towards higher amplitudes as illustrated in the schematic in Figure 4.7 [*Hines*, 1960, 1974].

Internal Gravity Waves: General Case - 3-D Dispersion Relation At the beginning of this section (Section 4.2.3.6), we introduced internal gravity waves in the context of sea water waves with a slight stabilizing salinity gradient and neglected the Coriolis force. In this segment, we consider the more general case, including the Coriolis force and more general stratification variables p_0, T_0, ρ_0 which are functions of z. Recall the linearized equations, Eq.s 4.129–4.133, from above, remembering that we have assumed $f \approx f_0 =$ constant. Assume an $e^{-i\omega t}$ dependence but retain spatial derivatives; then, Eq. 4.129 and Eq. 4.130 give u and v in terms of p_1:

$$-i\omega u - fv = -\frac{1}{\rho_0}\frac{\partial p_1}{\partial x} \tag{4.184}$$

$$-i\omega v + fu = -\frac{1}{\rho_0}\frac{\partial p_1}{\partial y} \tag{4.185}$$

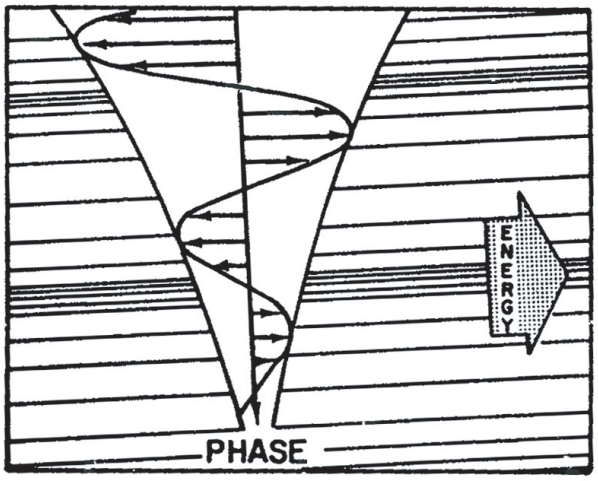

Figure 4.7: Schematic diagram illustrating the propagation characteristics of a large-scale gravity wave, and the associated variations in velocity and density. The small horizontal arrows show the neutral velocity variation with height, highlighting the growth in the wave amplitude with increased altitude. The nearly horizontal lines representing the phase fronts show the density variation. The long downward arrow indicates the direction of the phase velocity, while the wide, obliquely-upward arrow indicates the direction of the group velocity and associated energy flow. (From *Hines* [1960, 1974].)

which can be solved to yield:

$$u = \frac{i\omega\frac{\partial p_1}{\partial x} - f\frac{\partial p_1}{\partial y}}{\rho_0(f^2 - \omega^2)} \tag{4.186}$$

$$v = \frac{i\omega\frac{\partial p_1}{\partial y} + f\frac{\partial p_1}{\partial x}}{\rho_0(f^2 - \omega^2)}. \tag{4.187}$$

Eq.s 4.131 and 4.133 give a relation between p_1 and w:

$$\rho_0\frac{\partial^2 w}{\partial t^2} + \frac{\partial}{\partial z}\frac{\partial}{\partial t}p_1 = \rho_0 g\left(\frac{R}{pc_p}p_1 - \frac{N^2}{g}w\right) - \frac{\rho_0 g}{p_0}\frac{\partial p_1}{\partial t}, \tag{4.188}$$

therefore:

$$\left(N^2 - \omega^2\right)w = \frac{i\omega}{\rho_0}\left[\frac{\partial}{\partial z} + \frac{g\rho_0}{p_0}\left(1 - \frac{R}{c_p}\right)\right]p_1. \tag{4.189}$$

Eq.s 4.132 and 4.131 give a relation between u, v, w, p_1:

$$-i\omega\left(1 - \frac{R}{c_p}\right)\frac{p_1}{p_0} + \frac{\partial u}{\partial x} + \frac{\partial v}{\partial y} + \frac{1}{\rho_0}\frac{\partial}{\partial z}(\rho_0 w) + \frac{N^2}{g}w = 0. \tag{4.190}$$

Substitute the expressions for the velocities into this equation (Eq. 4.190) to obtain:

$$-i\omega\left(N^2-\omega^2\right)\left(1-\frac{R}{c_p}\right)\frac{p_1}{p_0}+\left(N^2-\omega^2\right)\frac{\partial}{\partial x}\left[\frac{i\omega\frac{\partial p_1}{\partial x}-f\frac{\partial p_1}{\partial y}}{\rho_0(f^2-\omega^2)}\right]$$
$$+\left(N^2-\omega^2\right)\frac{\partial}{\partial y}\left[\frac{i\omega\frac{\partial p_1}{\partial y}+f\frac{\partial p_1}{\partial x}}{\rho_0(f^2-\omega^2)}\right]+i\omega\left(N^2-\omega^2\right)\frac{1}{\rho_0}\frac{\partial}{\partial z}\left[\frac{\frac{\partial p_1}{\partial z}+\frac{\rho_0 g}{p_0}\left(1-\frac{R}{c_p}\right)p_1}{N^2-\omega^2}\right]$$
$$+\frac{i\omega N^2}{\rho_0 g}\left[\frac{\partial p_1}{\partial z}+\frac{\rho_0 g}{p_0}\left(1-\frac{R}{c_p}\right)p_1\right]=0 \tag{4.191}$$

Note that the first and the last terms in the above expression cancel. We can simplify further by assuming f is constant (f - plane). Also note that $1-R/c_p = c_v/c_p = 1/\gamma$. Some algebra leads to:

$$\omega^2\frac{\rho_0}{\gamma p_0}p_1+\frac{N^2-\omega^2}{f^2-\omega^2}\left(\frac{\partial^2 p_1}{\partial x^2}+\frac{\partial^2 p_1}{\partial z^2}\right)+\left(N^2-\omega^2\right)\frac{\partial}{\partial z}\left(\frac{\frac{\partial p_1}{\partial z}+\frac{\rho_0 g}{\gamma p_0}p_1}{N^2-\omega^2}\right)+\frac{N^2}{g}\frac{\partial p_1}{\partial z}=0. \tag{4.192}$$

At this point the vertical structure is still arbitrary. Now specialize to T_0 = constant. In this case, we have the following simplifications:

$$\frac{\rho_0}{\gamma p_0}=\frac{1}{\gamma R T_0}=\frac{1}{c_s^2}=\frac{1}{\gamma H g} \tag{4.193}$$

$$N^2=\frac{g}{T_0}\frac{g}{c_p}=\frac{R}{c_p}\frac{g}{H}=\frac{\gamma-1}{\gamma}\frac{g}{H} \tag{4.194}$$

which lead to the following simplification of terms appearing in the previous equation (Eq. 4.192):

$$\frac{\partial^2 p_1}{\partial z^2}+\frac{1}{\gamma H}\frac{\partial p_1}{\partial z}+\frac{\gamma-1}{\gamma H}\frac{\partial p_1}{\partial z}=\frac{\partial^2 p_1}{\partial z^2}+\frac{1}{H}\frac{\partial p_1}{\partial z}=e^{-z/2H}\frac{\partial^2}{\partial z^2}\left(e^{z/2H}p_1\right)-\frac{1}{4H^2}p_1 \tag{4.195}$$

Using the above result and letting $\Psi = e^{z/2H}p_1$, the final equation is:

$$\left(\frac{N^2-\omega^2}{f^2-\omega^2}\right)\left(\frac{\partial^2\Psi}{\partial x^2}+\frac{\partial^2\Psi}{\partial y^2}\right)+\frac{\partial^2\Psi}{\partial z^2}+\left(\frac{\omega^2}{c_s^2}-\frac{1}{4H^2}\right)\Psi=0 \tag{4.196}$$

or using subscript notation for partial derivatives

$$\left(\frac{N^2-\omega^2}{f^2-\omega^2}\right)\left(\Psi_{xx}+\Psi_{yy}\right)+\Psi_{zz}+\left(\frac{\omega^2}{c_s^2}-\frac{1}{4H^2}\right)\Psi=0. \tag{4.197}$$

Eq. 4.196 is a differential eigenvalue problem in which the frequency ω is determined by the condition that solutions to Eq. 4.196 exist with appropriate boundary conditions. However since the coefficients of Eq. 4.196 are constant, we can consider plane waves even though the atmospheric pressure and density vary with height. Since plane waves exist in the variable Ψ, this means that p_1 is decreasing with altitude. However, the relative pressure perturbation $p_1/p_0 \sim \exp(z/2H)$ increases with altitude. At some point the linear approximation will break down, and when that happens, the waves will break and create turbulence.

Assuming solutions of the form $\exp[i(kx + \ell y + mz)]$ we obtain the dispersion relation:

$$\frac{\omega^2}{c_s^2} - \left(\frac{N^2 - \omega^2}{f^2 - \omega^2}\right)\left(k^2 + \ell^2\right) - m^2 - \frac{1}{4H^2} = 0. \tag{4.198}$$

Note that Eq. 4.198 is a quadratic equation in ω^2 and is easily solved as such, but it is more informative to examine the two limiting cases:

1. $\omega^2 >> N^2,\ f^2 \quad \Rightarrow \quad \frac{\omega^2}{c_s^2} = k^2 + \ell^2 + m^2 + \frac{1}{4H^2}$ Acoustic waves
2. $\omega^2 >> f^2$ and $\frac{\omega^2}{c_s^2} << k^2 + \ell^2 + m^2 + \frac{1}{4H^2} \quad \Rightarrow$

$$\frac{\omega^2}{N^2} = \frac{k^2 + \ell^2}{k^2 + \ell^2 + m^2 + \frac{1}{4H^2}} \tag{4.199}$$

Eq. 4.199 is the dispersion relation for internal gravity waves. The main differences between this result and the result (given in Eq. 4.143) for incompressible waves from the segment on sea water waves are the altitude profile and the appearance of the scale height in the dispersion relation. The scale height term has a significant effect on the vertical propagation characteristics.

Internal Gravity Waves: Vertical Propagation Characteristics Going back to the full dispersion relation (Eq. 4.198) and solving for the vertical wavenumber, m^2, in terms of ω^2 and the horizontal wavenumbers, we find:

$$m^2 = \frac{\omega^2}{c_s^2} + \frac{N^2 - \omega^2}{\omega^2 - f^2}(k^2 + \ell^2) - \frac{1}{4H^2}. \tag{4.200}$$

Now we ask the question, when is $m^2 < 0$? That is, what are the conditions for vertical propagation? When $m^2 < 0$, the wave does not propagate vertically but is evanescent. So setting $m^2 = 0$ and solving for the magnitude squared of the perpendicular wave number, $k^2 + \ell^2$, we have:

$$k^2 + \ell^2 = \left(\frac{1}{4H^2} - \frac{\omega^2}{c_s^2}\right)\frac{\omega^2 - f^2}{N^2 - \omega^2}. \tag{4.201}$$

Eq. 4.201 gives the bounding curves for vertical propagation. We can deduce their shape by considering the following limits:

a) $k^2 + \ell^2 \longrightarrow \frac{\omega^2}{c_s^2}$ as $\omega^2 \to \infty$

b) $k^2 + \ell^2 \longrightarrow 0$ as $\omega^2 \to \frac{c_s^2}{4H^2}$

c) $k^2 + \ell^2 \longrightarrow \infty$ as $\omega^2 \to N^2$

d) $k^2 + \ell^2 \longrightarrow \frac{\omega^2}{N^2}\frac{1}{4H^2}$ for $f^2 << \omega^2 << N^2$

e) $k^2 + \ell^2 \longrightarrow 0$ for $\omega^2 \to f^2$

f) m^2 changes sign across $\omega = f$.

From these limits, we deduce the diagram in Figure 4.8, where $k_\perp \equiv \sqrt{k^2 + l^2}$:

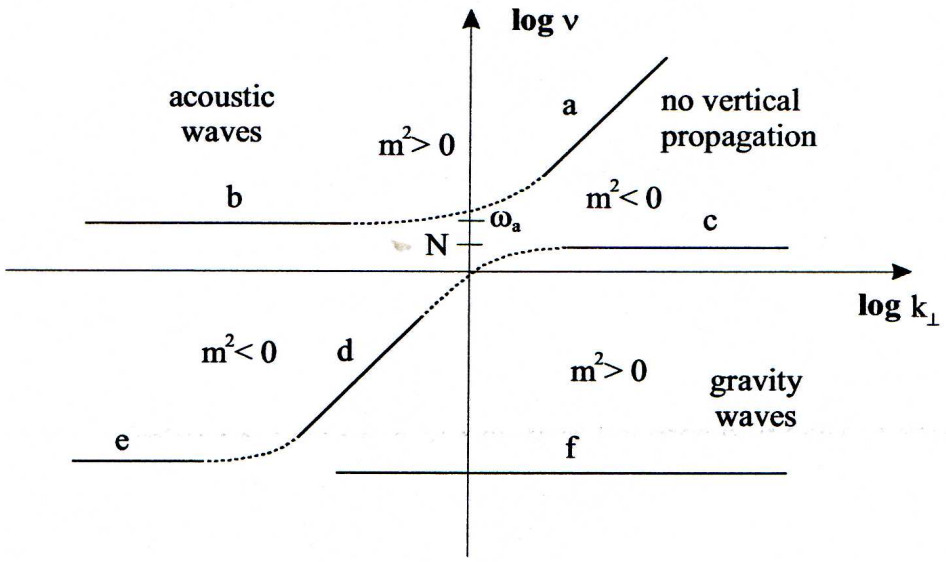

Figure 4.8: Diagram of the bounding curves for the vertical propagation of internal gravity waves. (Plot courtesy of C.E. Seyler, Cornell University.)

There are two special frequencies:

$$\omega_a^2 = \frac{c_s^2}{4H^2} = \frac{\gamma RT}{4H^2} = \frac{\gamma gH}{4H^2} = \frac{\gamma g}{4H} \tag{4.202}$$

is the acoustic frequency, and

$$N_{iso}^2 = \frac{g}{T}\left(\frac{dT}{dz} + \frac{g}{c_p}\right) = \frac{g^2}{c_p T} = \frac{Rg}{c_p H} = \frac{\gamma - 1}{\gamma}\frac{g}{H} \tag{4.203}$$

is the isothermal bouyancy frequency. There are also special values of the horizontal wave number found by equating expressions for the limits of ω^2 and finding the intersection, as follows:

$$\omega^2 = c_s^2(k^2 + \ell^2) = \frac{c_s^2}{4H^2} \qquad \Rightarrow \qquad \sqrt{k^2 + \ell^2} = \frac{1}{2H}. \tag{4.204}$$

The special values fix the entire diagram of bounding curves for the vertical propagation of internal gravity waves.

4.3 Bores

A *tidal bore*, or hydraulic jump, in an open channel is an abrupt change in the depth of the channel fluid in response to a transition from supercritical (where the flow velocity exceeds the long-wave speed) to subcritical flow; at critical flow, the flow velocity equals the long-wave speed. These bores are analogous to the shock that forms in a gas in the transition from supersonic to subsonic flow. Tidal bores, illustrated in Figure 4.9, have been well studied. *Lighthill* [1979] provided a good description of open-channel bore theory. The literature also reveals a second class of bores - the stratified, or internal, bore - occurring in stably stratified fluids. *Dewan and Picard* [1998] cited examples (e.g., see *Smith* [1988]) of bores in the troposphere to show that internal atmospheric bores can and do occur. While examples of stratified bores have been documented in the troposphere and oceans, none were ascribed to the mesosphere until *Dewan and Picard* [1998] advanced their analytic theory attributing sharp airglow fronts with trailing oscillations to "*mesospheric bores*". The inspiration for their hypothesis is shown in Figure 1.1 which juxtaposes an aerial view of a tidal, river bore with an image of a mesospheric sharp front.

Both channel and internal bores can appear either with or without trailing waves in the wake of their leading edge. Bores with trailing waves are termed *undular*; those lacking trailing oscillations are *turbulent* or foaming bores [*Lighthill*, 1979]. The latter are very difficult to distinguish from another type of mesospheric phenomenon called wall waves.

The "channels" in the atmospheric bore cases are hypothesized to be layers of stable air surrounded immediately above and below by less stable layers. *De-*

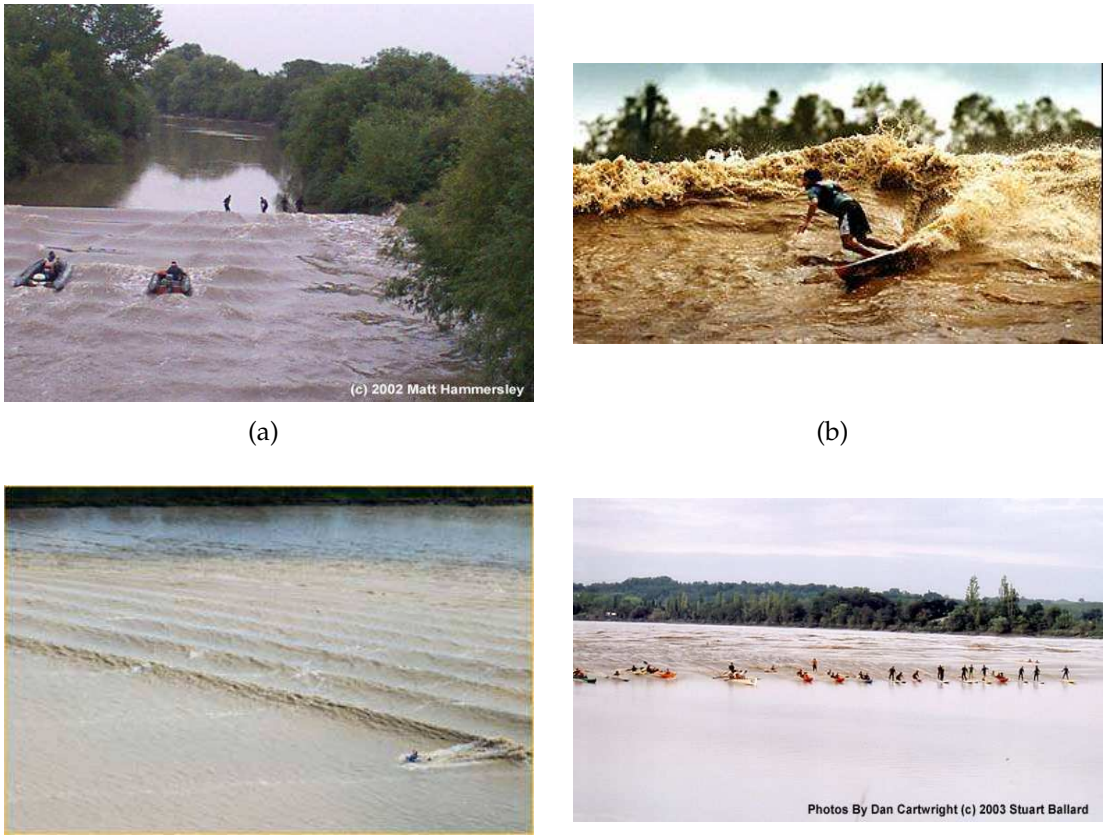

(a) (b)

(c) (d)

Figure 4.9: Panels (a) and (d) show the Severn Bore on the River Severn in Great Britain. Panels (b) and (c) show the "Pororoca" bore on the Amazon River in Brazil, South America. (All photographs are posts to Boreriders.com, a website maintained by a group of European river-bore surfers.)

wan and Picard [2001] proposed that layers of temperature inversion, also called *mesospheric inversion layers* (MILs), provide an analogous situation. In explaining the first documented mesospheric bore observed during the ALOHA-93 campaign, they suggested that a horizontal waveguiding channel existed between two airglow layers, at approximately 90–94 km, in which a bore propagated. As the bore passed overhead, it produced symmetric oscillations about the center of the channel. The upper layer (OI 557.7 nm) was vertically displaced upward, making it cooler, less dense, and presumably less bright. The lower layer (OH)

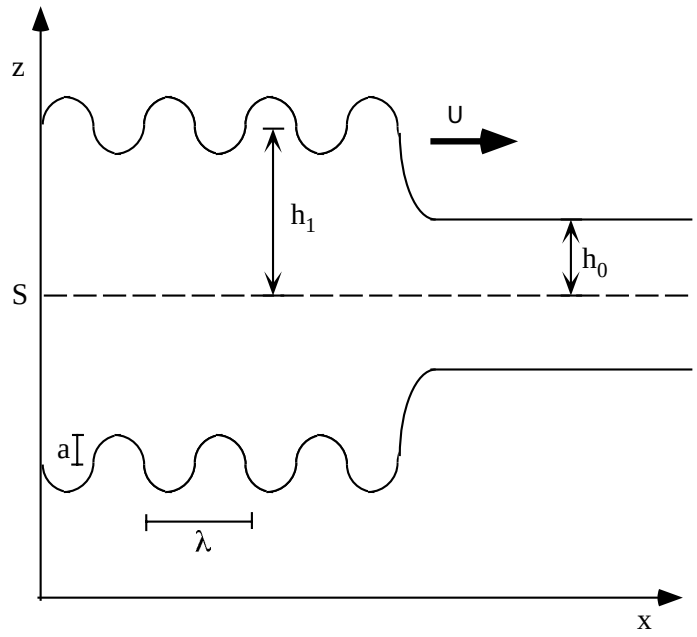

Figure 4.10: Illustration of a symmetrical undular bore with symmetry plane S, where the displacement is zero in analogy with the rigid bottom in channel bores. In this schematic, the z axis is altitude and the x axis is horizontal distance. h_0 is the undisturbed height of the fluid; $h_1 - h_0$ is the height of the bore; U is the bore velocity; λ is the wavelength of the trailing oscillations; and a is the bore amplitude. (From *Dewan and Picard* [1998].)

was displaced symmetrically downward, making it warmer, more dense, and brighter. In Figure 4.10 a schematic of the symmetric bore theory illustrates this vertical displacement.

Motivated further by open-channel bore theory, as well as by inversion layer formation theory [*Huang et al.*, 1998, 2002], *Dewan and Picard* [2001] extended their original work to include a possible mechanism for mesospheric bore generation. They showed that when the horizontal phase velocity of a gravity wave and the total background wind (including the mean wind plus the tidal component) are equal (i.e., at a critical layer), the resulting interaction between the wind and wave, combined with nonlinear effects, accelerates the fluid and acts as a piston, driving bore formation. *Dewan and Picard* [2001] proposed that

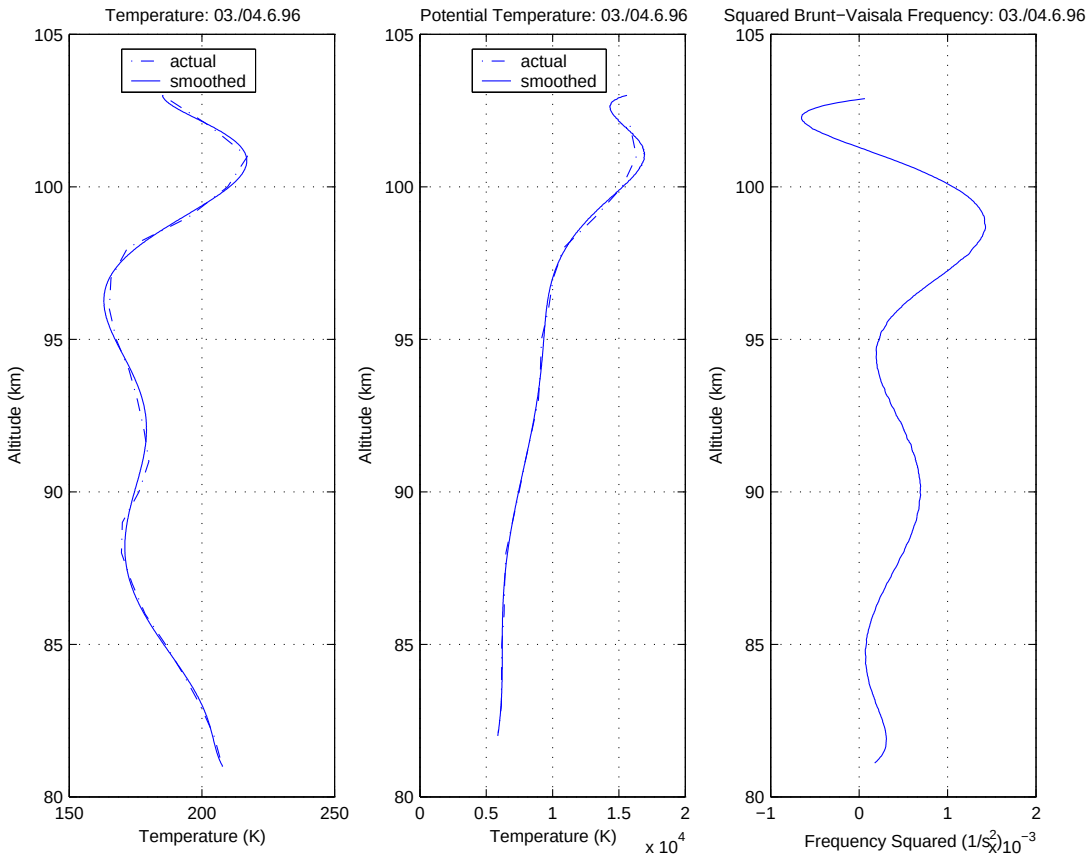

Figure 4.11: Temperature and potential temperature profiles with corresponding Brunt-Väisälä frequency for a ship-borne lidar measurement taken at 15°S 29°W on 3-4 June 1996. Analysis is based on data published by *von Zahn et al.* [1996] and the CIRA-86 atmospheric model.

mesospheric bores could be formed by the same mechanism initially responsible for producing the inversion layer itself, serving as a waveguide for the bore. Our analysis, following below, of a published example of such an inversion layer [*von Zahn et al.*, 1996] concurs with *Dewan and Picard* [1998] that bore propagation could, indeed, be supported in this region.

To demonstrate the feasibility that the MILs could provide a suitable propagation duct for the bores, we examined representative buoyancy frequencies from our region of interest, that is, near the mesopause region. We used lidar temperature profiles published by *von Zahn et al.* [1996] and the CIRA-86 at-

mospheric pressure model to generate potential temperature profiles for mesospheric altitudes. A sample temperature profile is shown in the left-hand side of Figure 4.11 with the corresponding potential temperature and squared buoyancy frequency (i.e., squared Brunt-Väisälä frequency, N^2) plotted in the next two panels, respectively. Internal waves only propagate if their frequency is less than the squared Brunt-Väisälä frequency. Thus, when N^2 is small on the bottomside of the inversion layer, waves are evanescent. From this exercise, we show that variation in N^2 is sufficient to allow for bore propagation. Note in this dataset at about 102 km, N^2 goes negative indicating the notion of static instability. If these negative values for N^2 are true and not an artifact of the smoothing techniques, we would expect to see observational evidence such as mixing.

Examples of mesospheric inversion layers are actually quite common, for example *Meriwether and Mlynczak* [1995]; *Meriwether et al.* [1998b, a]; *Meriwether and Gardner* [2000]. *Huang et al.* [1998] proposed a theory for the creation of inversion layers involving the flux divergence of gravity wave momentum near the associated critical levels, that is, where the horizontal phase velocity of the gravity wave equals the mean wind velocity. Given the presence of an inversion layer as well as the presence of gravity waves, *Dewan and Picard* [2001] were able to describe a mechanism for bore formation in this region. Gravity waves created by thunderstorms in the troposphere [*Taylor and Hapgood*, 1994] can propagate to the mesosphere and may be a potential source for MILs. Gravity waves from these same thunderstorms as well as other possible sources may also, in turn, create the piston-like effect on an MIL, leading to the formation of a bore [*Dewan and Picard*, 2001]. Figure 4.12 shows a strong thunderstorm developing in the northeast just prior to the bore event that occurred on 6 January 1998 (event (f) from Chapter 5). The bore did, indeed, advance from the northeast propa-

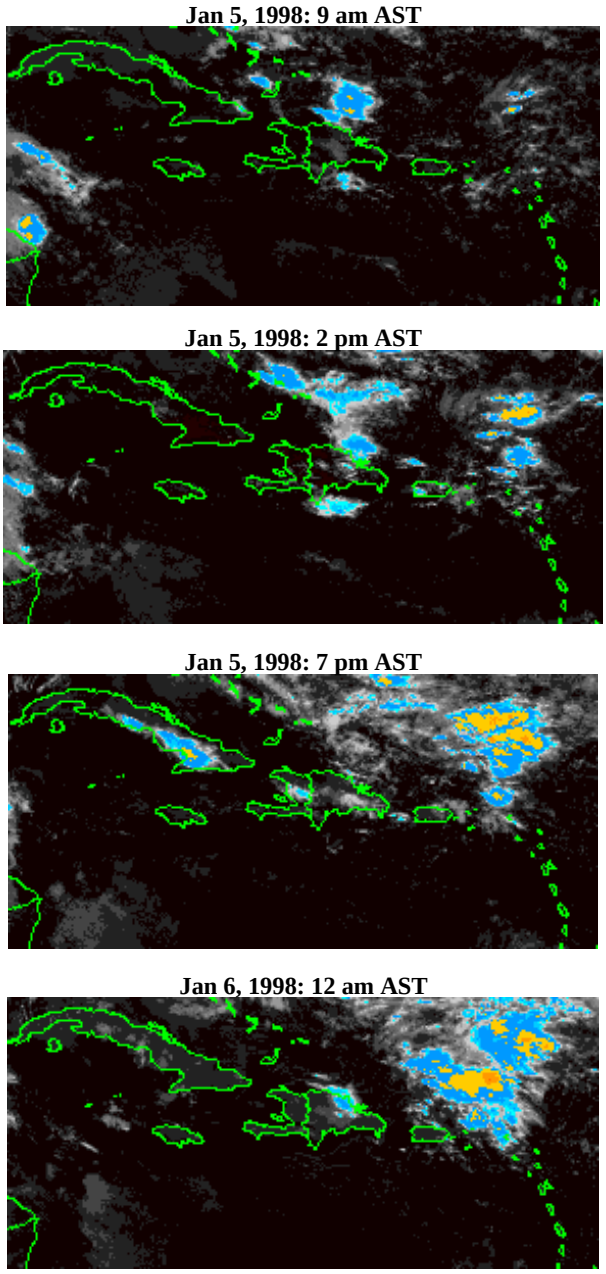

Figure 4.12: A series of infrared satellite images taken of the Caribbean region during 5 January 1998. They show a strong storm developing to the northeast of Puerto Rico, which may be the source of the sharp front seen in the airglow emissions for 6 January 1998.

gating orthogonally to the tropospheric front, with the small-scale wavefronts of the bore aligned parallel to the thunderstorm. Corresponding low-pressure systems were also documented for both the ALOHA-93 and the naked-eye bore events [*Swenson et al.*, 1998; *Smith et al.*, 2003].

A quantitative model for mesospheric bore theory, illustrated in Figure 4.10 above, was developed by *Dewan and Picard* [1998] using a very simplified density profile depicted in panel (a) of Figure 4.13. The profile consists of three discrete layers decreasing in density with altitude. Panels (b) and (c) of Figure 4.13 show the corresponding potential temperature and buoyancy frequency atmospheric profiles, respectively. The low and high density regions are assumed to be semi-infinite in altitude, while the intermediate region is limited to an undisturbed width of $2h_0$. Any oscillation on the ρ_{23} surface will be mirrored in the ρ_{21} surface about the plane of symmetry S, where there is no vertical motion. Thus, S acts as if it were the rigid bottom of an open-channel bore. This gives rise to the situation illustrated in Figure 4.10.

A summary of the basic equations of the analytic bore theory postulated by *Dewan and Picard* [1998] follows. They state that the equations governing open-channel bores will hold for this basic model if the acceleration due to gravity, g, is replaced by the buoyant acceleration g', defined as:

$$g' = g\frac{\Delta\phi}{\bar{\phi}} \tag{4.205}$$

where ϕ is the potential temperature. The equation for the bore velocity, U, is then:

$$U^2 = \frac{1}{2}g'(h_0 + h_1)\frac{h_1}{h_0}, \tag{4.206}$$

where h_0 is the undisturbed height of the fluid, h_1 is the perturbed height of the fluid as a result of the bore, and g' is the buoyant acceleration given in Eq. 4.205.

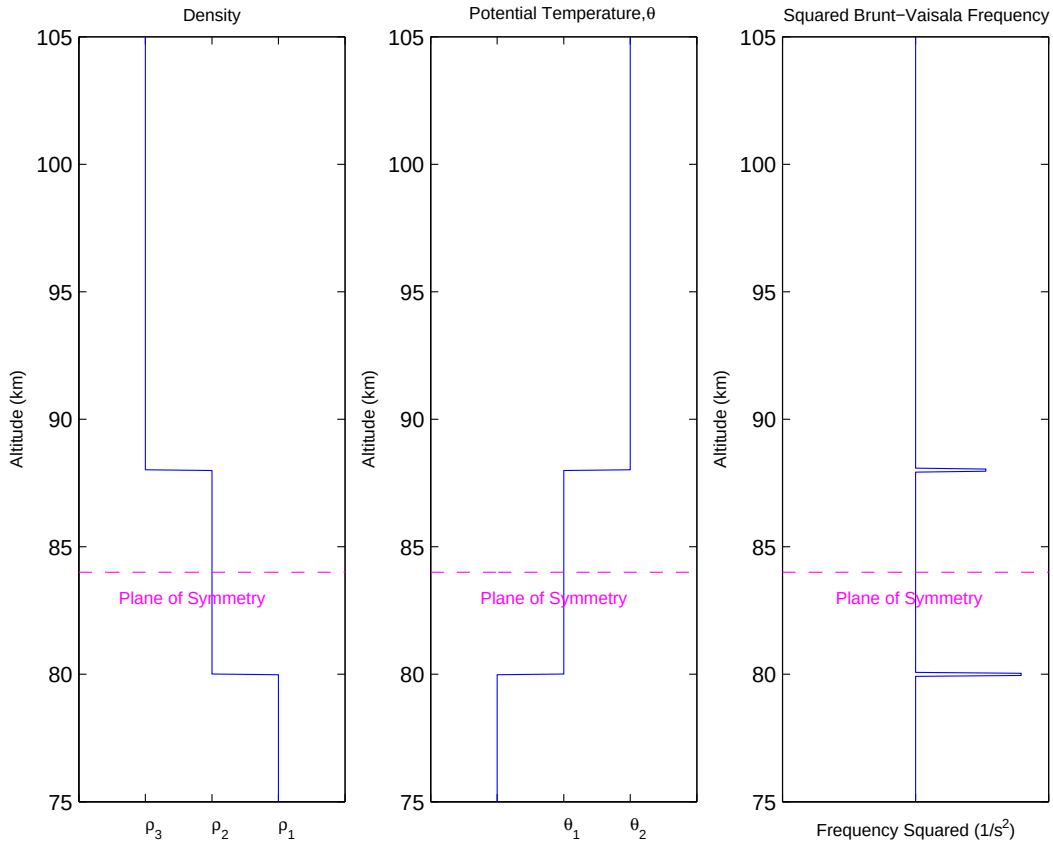

Figure 4.13: The highly idealized density profile used by *Dewan and Picard* [1998]. The corresponding potential temperature and buoyancy frequency profiles are shown in the second and third panels.

Lighthill [1979] used laboratory experiments to show that, for an undular bore, the bore strength, β, defined as the normalized bore amplitude, is bounded above:

$$\beta \equiv \frac{h_1 - h_0}{h_0} \leq 0.3 \ \text{(approx.)} \tag{4.207}$$

When this upper bound for the bore strength is exceeded, turbulent bores with no trailing waves result. For weak bores, where $\beta \ll 1$, the waves behind the discontinuity are sinusoidal, as seen predominantly in the mesospheric bore data. The wavelength of the waves behind the bore is given by:

$$\lambda = \frac{2\pi h_1}{3}\sqrt{\frac{2h_0}{h_1 - h_0}} \tag{4.208}$$

The amplitude, a, of the displacement about the perturbed height, h_1, for the waves behind the bore can be approximated by:

$$a = \frac{1}{\sqrt{3}} \frac{h_1}{h_0} (h_1 - h_0) \tag{4.209}$$

Dewan and Picard [1998] use expressions for the rate of energy dissipation, D, and for the amount of energy per wave crest, E, to come up with an expression for the rate of wave crest generation, W, given by:

$$W = \frac{D}{E} = \frac{U(h_1 - h_0)^3}{2a^2 \lambda h_1} \tag{4.210}$$

Using this equation for W, counting the number of wave crests (C) behind the bore, and knowing the velocity of the bore (U), one can use the following equation

$$\chi = U \frac{C}{W} \tag{4.211}$$

to estimate the distance to the point where the bore originated.

CHAPTER 5

OBSERVATIONS AND CLASSES OF BORE PHENOMENA

5.1 Background

Since the first spectacular gravity wave events observed a decade ago during the Airborne Lidar and Observations of Hawaiian Airglow ALOHA-93) campaign, additional examples of sharp airglow fronts have been observed by imaging systems at a variety of locales. The scientific community's intrigue in sharp airglow fronts began with that ALOHA-93 campaign, when remarkable mesospheric phenomena were captured in airglow images for the first time and later were described by *Swenson et al.* [1998] (9 October 1993) and *Taylor et al.* [1995a] (10 October 1993). Coining the term "mesospheric bore" to describe the second of these events, *Dewan and Picard* [1998] drew from its resemblance to tidal bores in river channels and proposed a basic mathematical model, described in Section 4.3, for an atmospheric bore at mesospheric altitudes.

Many, but not all, of the new events were characterized by small-scale waves tracking behind the sharp onset of a large-scale front. As in ALOHA-93, our observations were made over multiple airglow layers and most show the same anti-correlated intensity pattern between upper and lower altitudes. Given this, most of the bore observations confirm the validity of the original symmetric bore theory model, however, two new events appear to conflict with it. Most of the previously documented mesospheric bores displayed either a complemen-

*Original source: Loughmiller, P.J., M.C. Kelley, E.M. Dewan, F.J. Garcia, J.J. Makela, and S.M. Smith, Sharp mesospheric fronts: Observations and classes of bore phenomena, *Journal of Geophysical Research*, accepted 2007. Some notational changes have been made for consistency with the remainder of the dissertation.

tary effect, with lower airglow layers appearing to brighten behind the leading edge of the front while corresponding upper layers appeared to darken, or a complete lack of complementarity with regard to the variation in radiance. The new conflicting observations demonstrate an "inverse" complementarity, that is, the lower layers appear to be pushed up (becoming darker) while the corresponding upper layers are pushed down (becoming brighter), which appears to be inconsistent with current bore models. In the next chapter, we extend the basic model, proposing an explanation for these confounding observations.

This chapter is organized as follows. In Section 5.2 we briefly describe the basic instrumentation and processing methods used to obtain the airglow images. The bore observations, originating from a variety of locations, are recounted in Section 5.3. Parameters of each event are summarized in Section 5.3.1. We present a classification system for mesospheric bore observations in Section 5.3.2, based on the variability of the intensity in these observations. In Section 5.4, we analyze the bore observations and compare them to the basic, analytical bore model. We conclude in Section 5.5 with a discussion and summary.

5.2 Instrumentation

New airglow images were taken by the *C*ornell *A*ll-sky *R*oving *I*mager (CARI) and the *C*ornell *A*ll-*S*ky *I*mager (CASI). These self-contained, monochromatic imaging systems are detailed in Chapter 2. A summary is given here to provide a brief equipment description in proximity to the data presentation, and to maintain consistency with the journal submission.

CARI is a portable, relocatable system, while CASI, originally on long-term loan from Los Alamos National Laboratory, is housed at the Maui Space Surveillance Complex on top of the Haleakala volcano on Maui, HI, as part of the continuation of the Maui-MALT (*M*esosphere *a*nd *L*ower *T*hermosphere) campaign. The hardware configuration for both systems is comprised of a scientific-grade, charge-coupled device (CCD) fronted by fast (f/4) telecentric optics, a five-position filter wheel, and an all-sky (wide-angle (180°) fisheye) optics lens. An electronics unit controls each camera, and a liquid circulation unit removes heat from the thermo-electrically cooled CCD chip. To minimize noise, each CCD is cooled to approximately −40°C and pixels are binned on-chip by a factor of 2, producing 512×512 images from the 1024×1024 CCD. In both setups, the entire system runs on a PC and is controlled by a Windows-based program that was developed at Cornell University by graduate students.

Since chemiluminescent reactions emit radiation of specific wavelengths and these correlate fairly well to specific altitudes, we choose various narrow-band filters to isolate each wavelength, and hence, its corresponding altitude for study. To inspect mesospheric altitudes, several filters were employed to isolate a range of airglow emissions. Hydroxyl emissions at 87 km are captured by the near infrared broadband OH filter using integration times of 8 s. A 589.3-nm wavelength narrow-band filter captures sodium (Na) emissions peaking at 90 km; a 557.7-nm narrow-band filter captures greenline (OI) emissions at 96 km. Exposure times for both narrow-band filters are 90 s. Before examining the airglow emissions as tracers of mesospheric dynamics, the images underwent the following processing:

- spatial calibration to stars
- removal of stars from images
- correction for vignetting by the optical system
- correction for van Rhijn effect, i.e., line-of-sight brightening near the horizon
- unwarping, i.e., geographic projection and interpolation

More details concerning this data analysis procedure were published by *Taylor and Garcia* [1995].

The Cornell airglow imaging systems are representative of the systems used by Utah State University, the University of Illinois, and Boston University. Details on these systems can be found in the literature (e.g., *Taylor et al.* [1995a], *Swenson et al.* [1998], *Smith et al.* [2003]).

5.3 Sharp Front Observations

Until very recently, only a handful of mesospheric bore observations were known about. Now, a number of bore and bore-like observations have been published in the literature [*Taylor et al.*, 1995a; *Swenson et al.*, 1998; *Dewan et al.*, 2001; *Medeiros et al.*, 2001; *Batista et al.*, 2002; *Smith et al.*, 2003; *Loughmiller et al.*, 2004; *Brown et al.*, 2004; *She et al.*, 2004; *Medeiros et al.*, 2005; *Fechine et al.*, 2005; *Nielsen et al.*, 2006]. A classification system is introduced below, based on both the previously published bore events [*Taylor et al.*, 1995a; *Dewan et al.*, 2001; *Batista et al.*, 2002; *Smith et al.*, 2003; *Loughmiller et al.*, 2004; *She et al.*, 2004;

Medeiros et al., 2005; *Fechine et al.*, 2005; *Nielsen et al.*, 2006], and the recent inverted examples [*Dewan et al.*, 2001; *Loughmiller et al.*, 2004; *Medeiros et al.*, 2005]. General descriptions are given for new bore events, as well two previously-published events [*Taylor et al.*, 1995a; *Smith et al.*, 2003], in Subsections 5.3.0.7–5.3.0.14, with a summary tabulated in Section 5.3.1.

5.3.0.7 First Observation: 10 October 1993 - Maui, HI [Event (a)]

A new and interesting mesospheric phenomenon was detected over Haleakala, HI on 10 October 1993 [*Taylor et al.*, 1995c]. A summary of the event is shown in Figure 5.1. The feature was first detected coming in from the northwest at 23:30 LT. By 00:30 LT the principal features of this event were apparent. A sharp front approached from the northwest which, in the OI (557.7 nm) emission (96 km), created a sharp decline in the airglow intensity. In contrast, a sharp increase in the intensity occurred in the OH emission (87 km). In both emissions, a series of waves followed in the wake of the front. The trailing waves appear to be locked in phase, travelling at the same speed as the leading front. The two emission intensities were 180° out of phase. The wave-like bands extended from horizon to horizon and were parallel to the sharp front. By 01:30 LT the feature had progressed well to the southeast, and the only hints of its passage were the associated waves behind it, which filled half of the sky. As many as 10 crests can be identified in the keograms presented in Figure 5.2.

We label this type of event as "standard". By this we mean it exhibits the classic features first addressed by *Dewan and Picard* [1998] in their basic bore theory. These key features which *collectively* describe a "standard" event include:

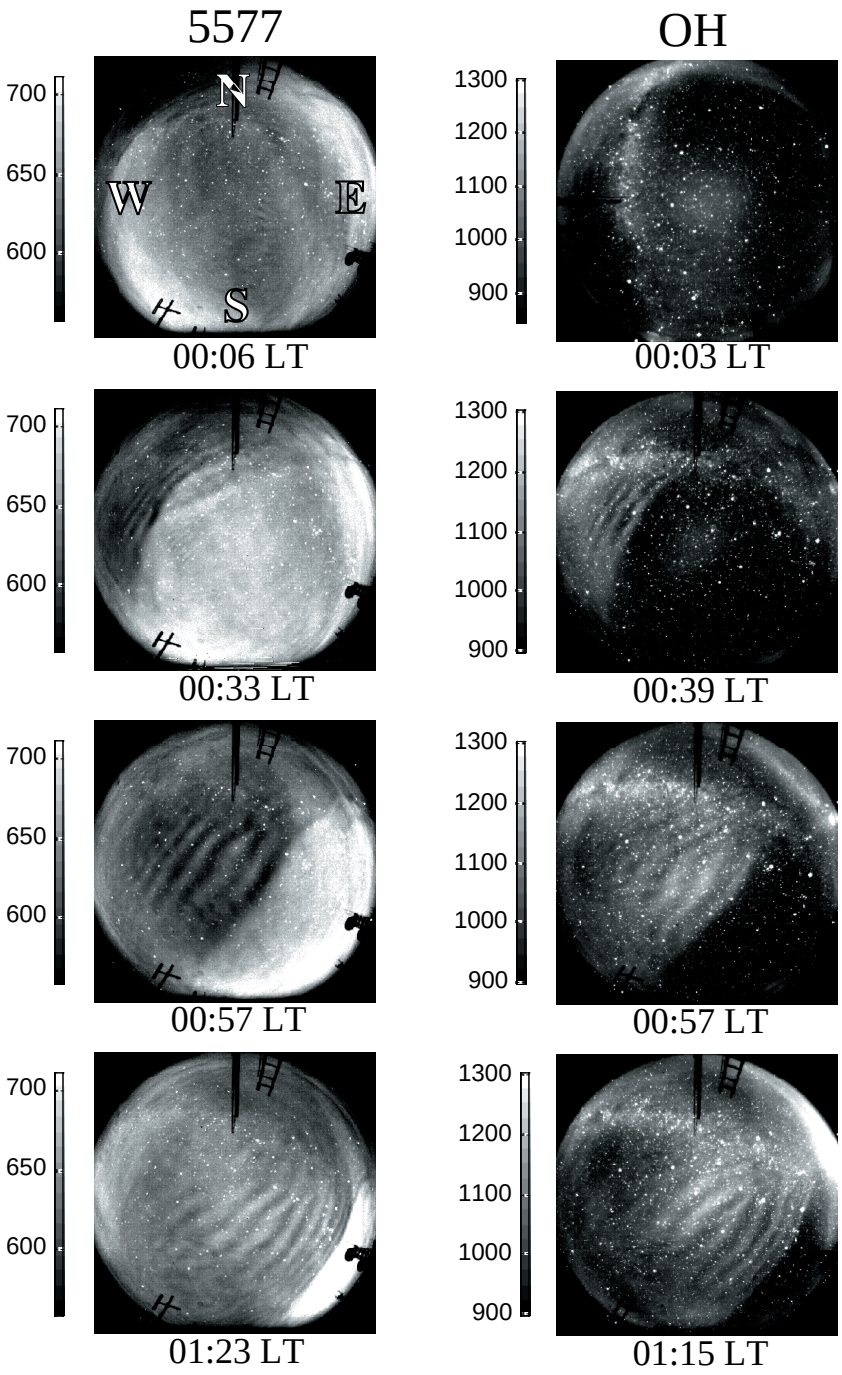

Figure 5.1: A series of 557.7-nm (OI) and OH emission images taken with the Utah State University imager on 10 October 1993 in Hawaii. The images show a front approaching from the northwest. Note the complementary intensity relationship between the two emissions. (Figure courtesy of M.J. Taylor, Utah State University.)

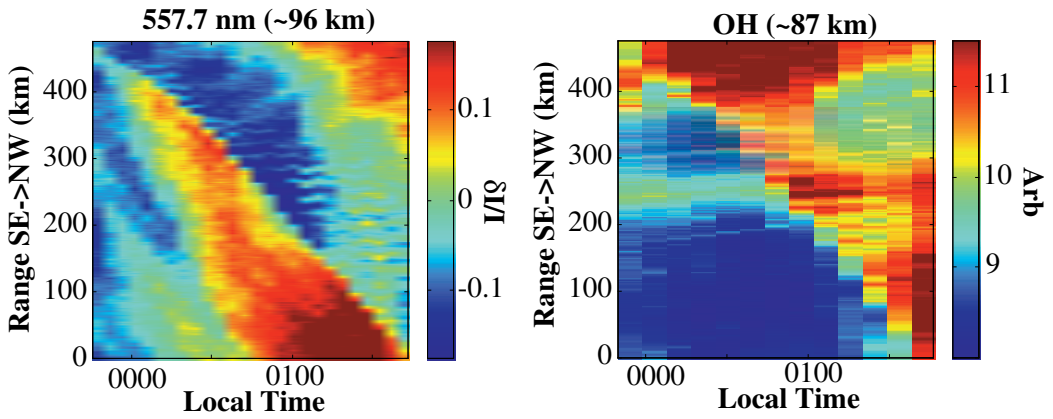

Figure 5.2: Intensity over time for a scan line across the ALOHA-93 front for both the 557.7-nm (OI) and the OH emissions.

1. a sharp front with trailing waves following behind its leading edge;
2. trailing waves which appear to be locked in step with the leading edge;
3. the addition of trailing waves, added behind the front as the event continues;
4. anti-correlated airglow emissions between different altitudes, that is, upper atmospheric layer emissions are 180° out of phase with emissions from lower layers;
5. a specific radiance complementarity characterized in lower airglow emission layers by a front with a bright leading edge and intensity enhancement which moves into a darker region; in upper airglow emission layers, the front is characterized by a dark leading edge and an intensity depletion which progresses into a brighter region.

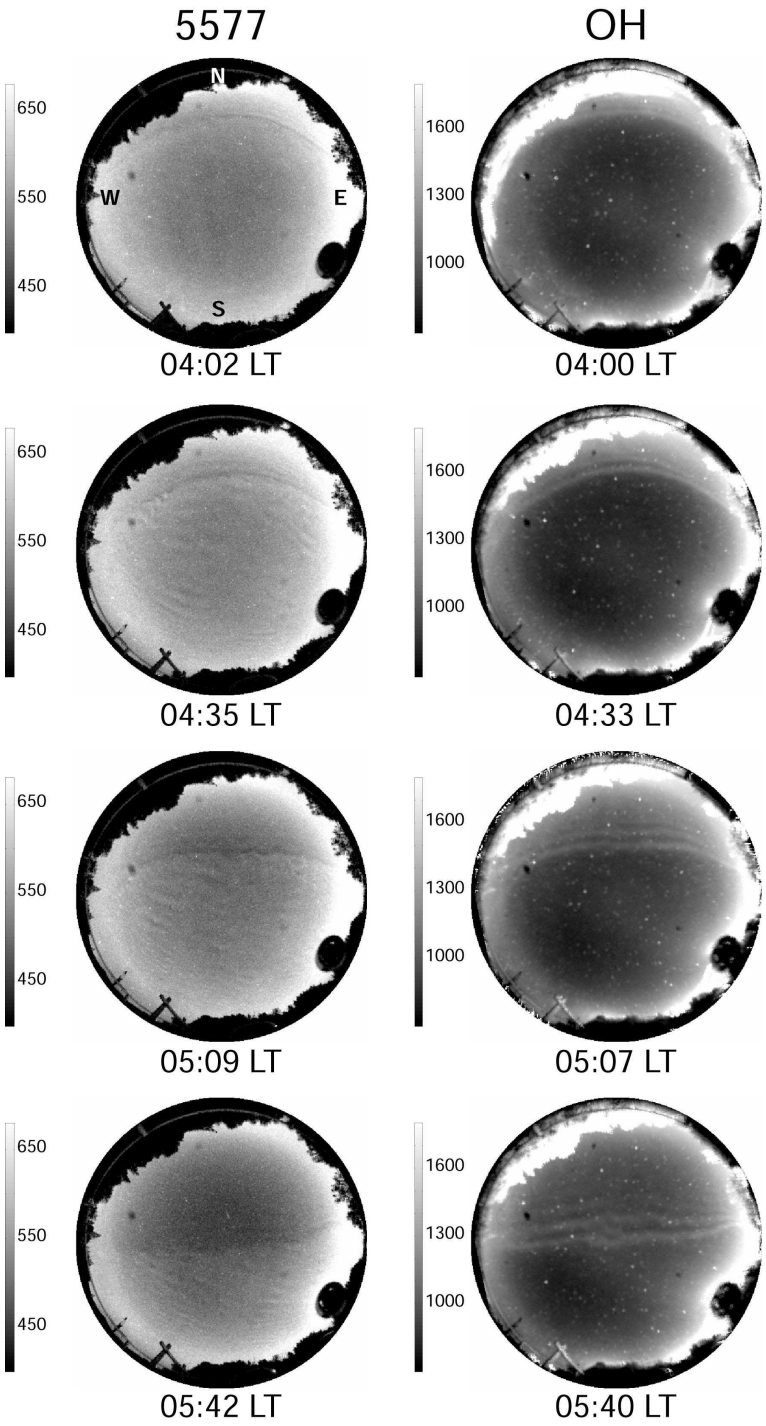

Figure 5.3: A series of 557.7-nm (OI) and OH emission images taken with the Cornell All-sky Roving Imager (CARI) on 6 January 1997 at Arecibo, PR. The images show a front approaching from the north. Note the complementary intensity relationship between the two emissions.

5.3.0.8 Standard event: 6 January 1997 - Puerto Rico [Event (b)]

A very similar event was observed with CARI on its first full night of operation, 6 January 1997. During that night, no visible structure was detected until 03:16 LT, when a front became visible in the north. Figure 5.3 shows four pairs of OH and OI (557.7 nm) images in time sequence summarizing the event. By 05:20 LT, the front was overhead in Puerto Rico. A pair of geographically projected images from both the OI (557.7 nm) and OH emissions near zenith is shown in Figure 5.4.

In the OH emission, an area of intensity enhancement propagated southward along with a corresponding depletion in the OI (557.7 nm) emission. The waves following the front are clearly evident in the OH emission, but are not as obvious in this geographic projection of the OI (557.7 nm) image, most likely due to the low signal level in the dark region. Curiously, even stronger waves are seen in both figures to the southeast of the front and approaching it, indicating that these waves were independent and unrelated to the front. The odd passing wave such as seen in this event has been used to argue that trailing undulations are an artifact and that bores are just wall waves with "coincidental" gravity waves. Subsequent data sets reveal additional occurrences of independent wave trains either crossing paths with or following in succession behind the original bore event; these multiple bore occurrences will be addressed in a later paper. The waves behind the front in the OI (557.7 nm) layer progressed along with the front and were 180° out of phase with the OH waves, as was the case with the ALOHA-93 event. One significant difference between the two events was the phase speed. The Arecibo event took almost three hours to traverse half the sky (at which point the sun rose, ending that data collection ses-

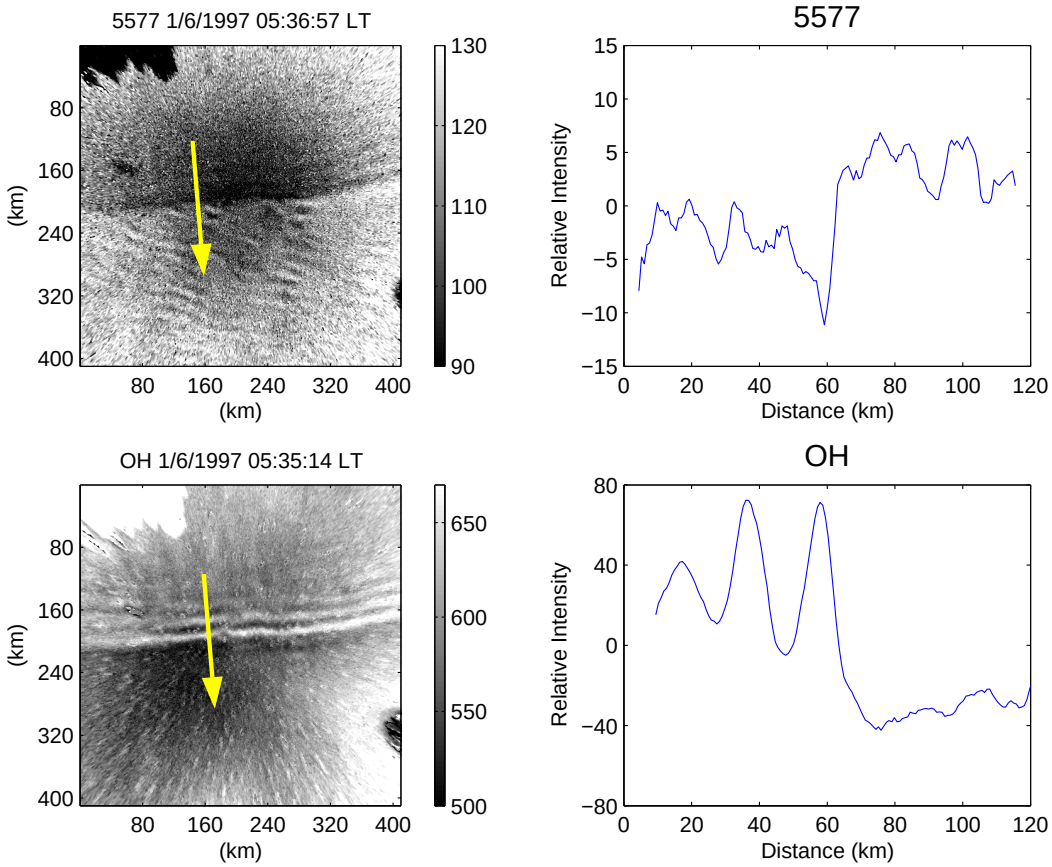

Figure 5.4: The left panels show two images taken on 6 January 1997 depicting a sharp front. The top image is of the 557.7-nm (OI) emission, and the bottom is of the OH emission. The arrows indicate the direction the front is propagating. The right panels show the relative intensity values across the scan lines (again indicated by the arrows) shown in the images. Zero kilometers on the scan-line plots corresponds with the base of the arrow.

sion), whereas the ALOHA-93 event took only a little over an hour to cross the entire sky. From basic bore theory, we would predict that a narrower propagation duct existed in this event than in the ALOHA-93 event, but vertical profile data are unavailable for verification.

Figure 5.5 shows the intensity for a scan line perpendicular to the front using two different display schemes. Discerned best in the keograms, the dark wall in the OI (557.7 nm) emission seems to deepen with time, whereas the wall

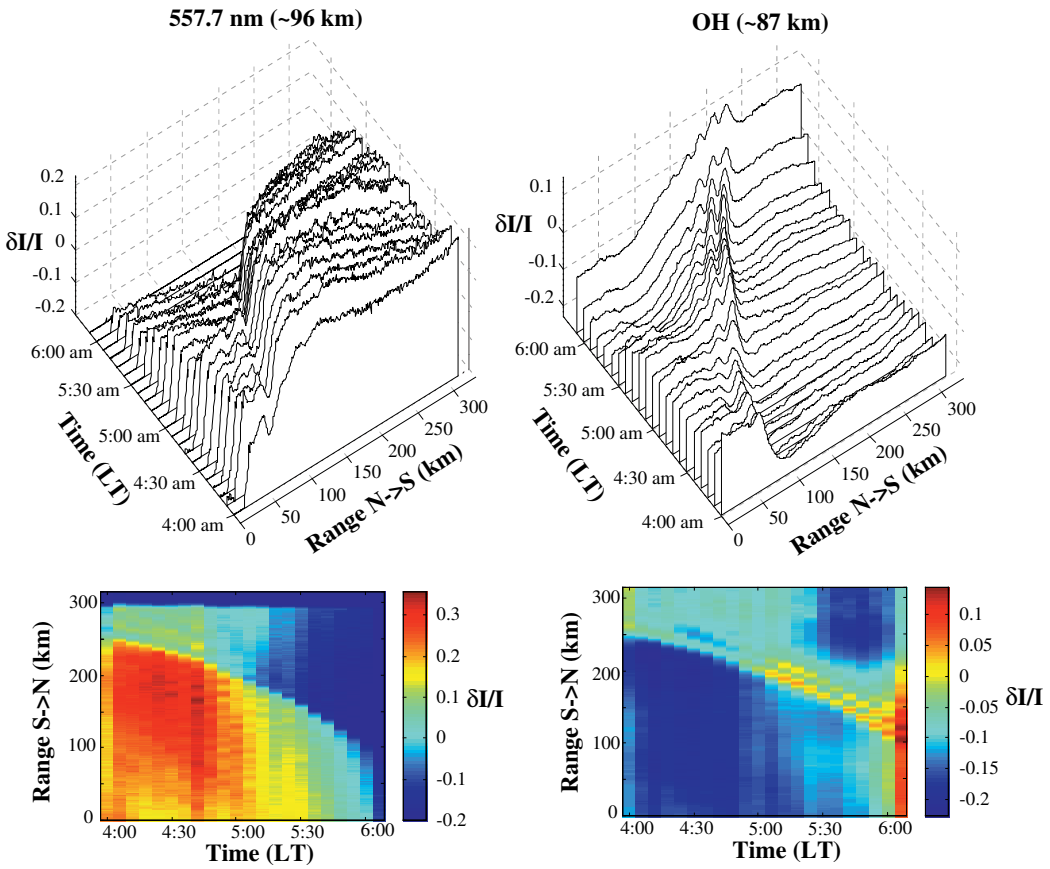

Figure 5.5: Intensity over time for a scan line across the 6 January 1997 data set from Arecibo, PR, for the 557.7-nm (OI) and OH emissions.

of light in OH decreases in relative intensity. Evident in the waterfall plots in Figure 5.5, the OI (557.7 nm) layer shows evidence of waves following the front early in the event, whereas the OH layer shows them stronger late in the event. The number of cycles visible in the OH waves increases with time at the rate predicted by *Dewan and Picard* [1998], that is, roughly two to three crests per hour. In the 04:00 LT image, only one crest is obvious. This increases to three by 05:00 LT and five by 06:00 LT. The generation of additional waves with time seems incontrovertible evidence that mesospheric bores can occur. At the same time, the relative size of the intensity jump across the front becomes smaller suggesting the bore is dissipating. The wave cycles become invisible at late

times in the OI (557.7 nm) emission as the signal itself disappears.

The complementary relationship between the two emissions is very similar to that seen in the 10 October 1993 ALOHA-93 event. This particular complementarity is an indication of something splitting the two layers, causing the upper OI (557.7 nm) emission layer to rise, cool, and darken while simultaneously causing the lower OH layer to fall, heat up, and brighten, as postulated by *Dewan and Picard* [1998].

5.3.0.9 Standard event: 30 December 2002 - Maui, HI [Event (k)]

With airglow imagers once again positioned in Maui, this time for the Maui-MALT campaign, we have captured more examples of mesospheric bores over the Pacific. The night of 30 December 2002 was filled with a variety of wave structures from the time CASI began capturing images at 19:18 LT until the camera shut off at 05:00 LT. Throughout the night, the imager captured a series of bore events, as well as both small-scale and large-scale wave structures. The phenomenon of a series of bores occurring in succession on the same night, as well as these other wave dynamics will be addressed in a later paper. In this paper, we present from this night a representative standard bore which came into view at about 00:30 LT. Figure 5.6 shows four pairs of Na and OI (557.7 nm) images similar both to the OH and OI (557.7 nm) images in Figure 5.3 depicting the 6 January 1997 event in Puerto Rico, as well as in Figure 5.1 from the ALOHA-93 campaign described in Section 5.3.0.7. Note that CASI does not incorporate an OH filter into the image sequencing; our lower mesospheric emissions for the Maui-MALT campaign are from the Na layer at 90 km.

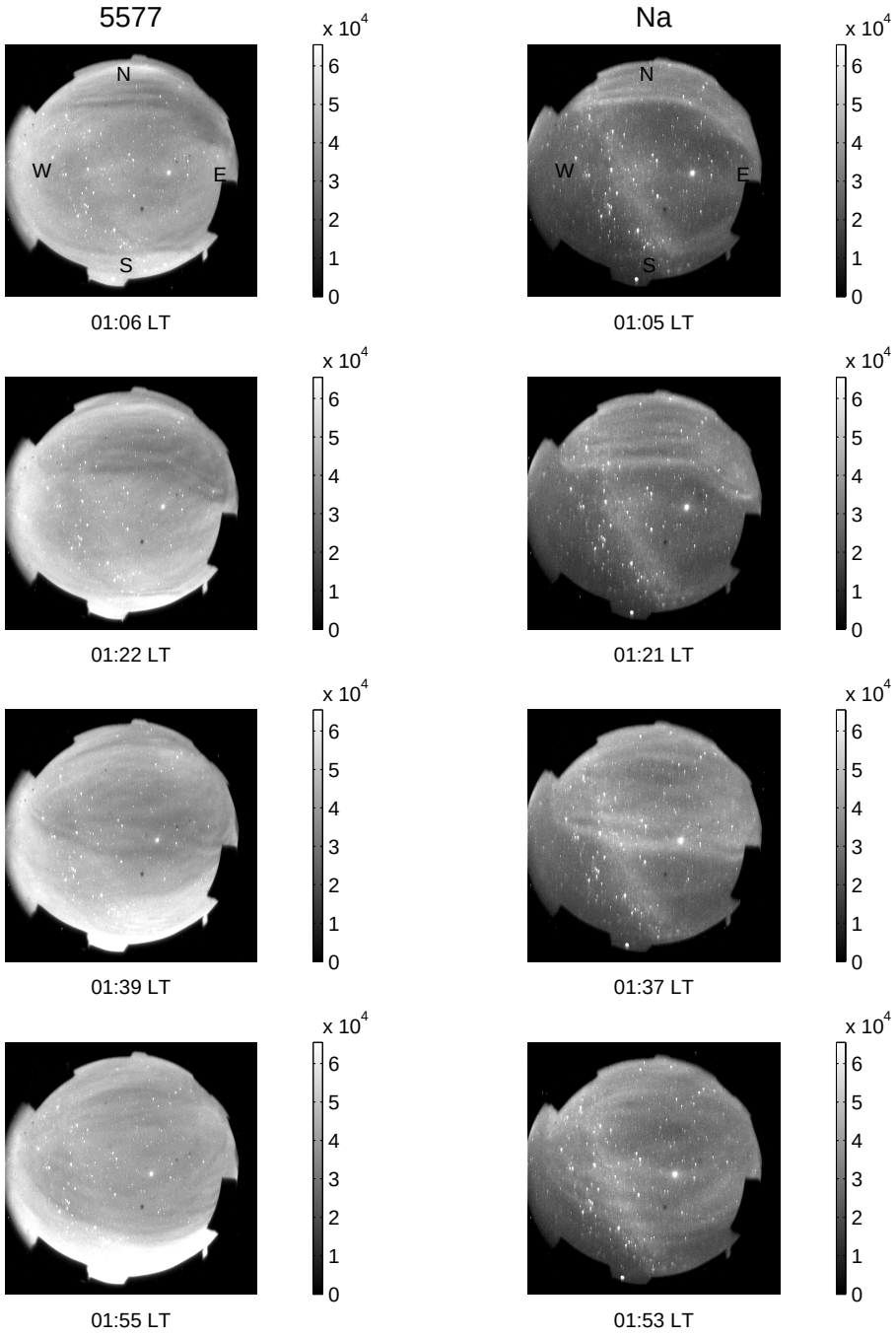

Figure 5.6: A series of 557.7-nm (OI) and Na emission images taken with the Cornell All-Sky Imager (CASI) on 30 December 2002 at Maui, HI. The images show a front approaching from the north. As in Figure 5.3, note the complementary intensity relationship between the two emissions.

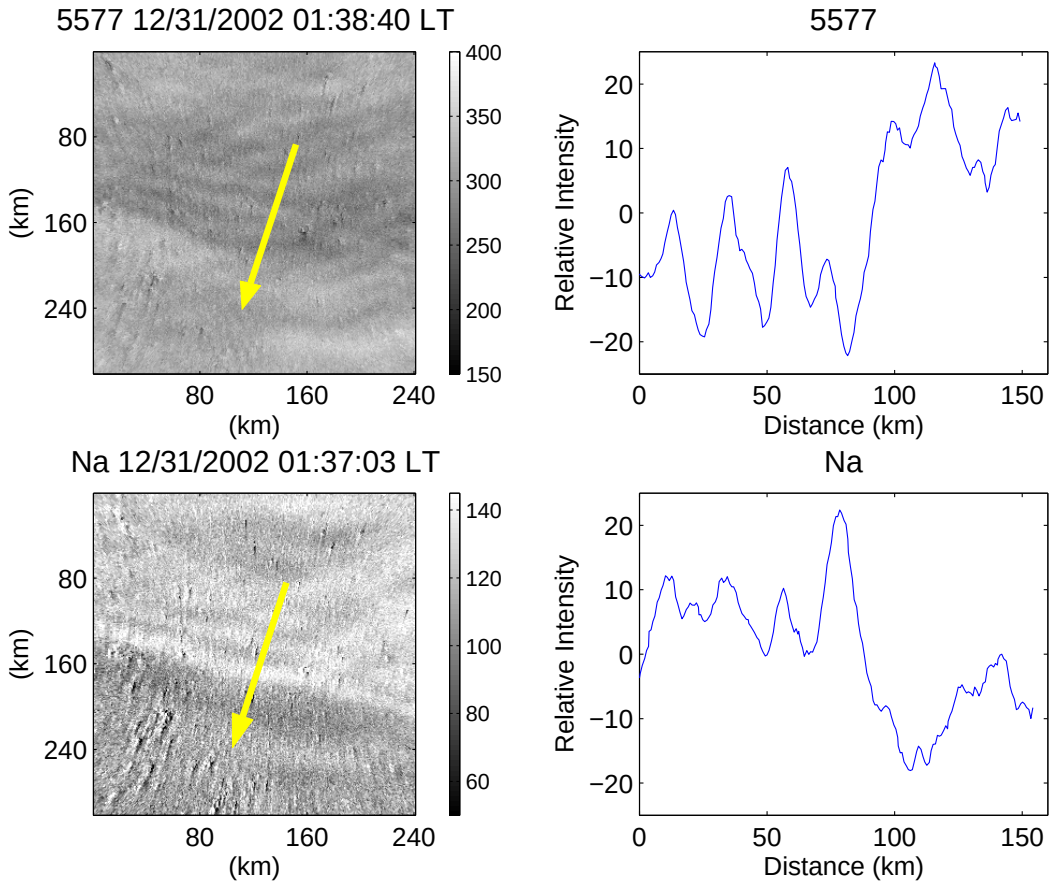

Figure 5.7: The left panels show two images taken on 30 December 2002 depicting a sharp front. The top image is of the 557.7-nm (OI) emission, and the bottom is of the Na emission. The arrows indicate the direction the front is propagating. The right panels show the relative intensity values across the scan lines (again indicated by the arrows) shown in the images. Zero kilometers on the scan-line plots corresponds with the base of the arrow.

Emerging from the horizon to the north, the front propagated to the south-southwest, and by 01:30 LT was overhead in Maui. A pair of geographically projected images from both the OI (557.7 nm) and Na emissions near zenith is shown in Figure 5.7. In the Na emission, an area of intensity enhancement propagated southward along with a corresponding depletion in the OI (557.7 nm) emission. More apparent in this event than in the 6 January 1997 event, in both emission layers there exists a sharp intensity depletion/enhancement

just prior to the leading edge of the bore. In the Na emission, this can be seen as a strong depletion area immediately in advance of the intensity enhancement brought by the bore. In contrast in the OI (557.7 nm) emission, a further increase in the background intensity develops ahead of the leading dark edge of the bore.

In our early images of this bore, as it first emerged into the field of view of CASI, the waves behind the front in the OI (557.7 nm) layer appear to progress along with the front and are 180° out of phase with the Na waves, as predicted by *Dewan and Picard* [1998] and as was the case with the corresponding layers in the ALOHA-93 event. Just before the leading edge of the bore reaches zenith, however, there already appears to be a lateral mismatch between the trailing waves in the two layers. While the leading two wave crests associated with the bore remain aligned with each other across the layers and 180° out of phase, the third and fourth peaks in the Na emission appear merged together. This lack of distinction could be due to the influence of an obliquely propagating wave structure (perhaps a crossing bore) shown in the geographically projected images of Figure 5.7 to be propagating south-southeast with a convex leading edge.

The phase speed of this Maui-MALT event falls between the ALOHA-93 event and the 6 January 1997 Puerto Rico event. While the Arecibo event took almost three hours to traverse half the sky and the ALOHA-93 event raced from horizon to horizon in only a little over an hour, the Maui-MALT event traversed the entire sky in almost two hours.

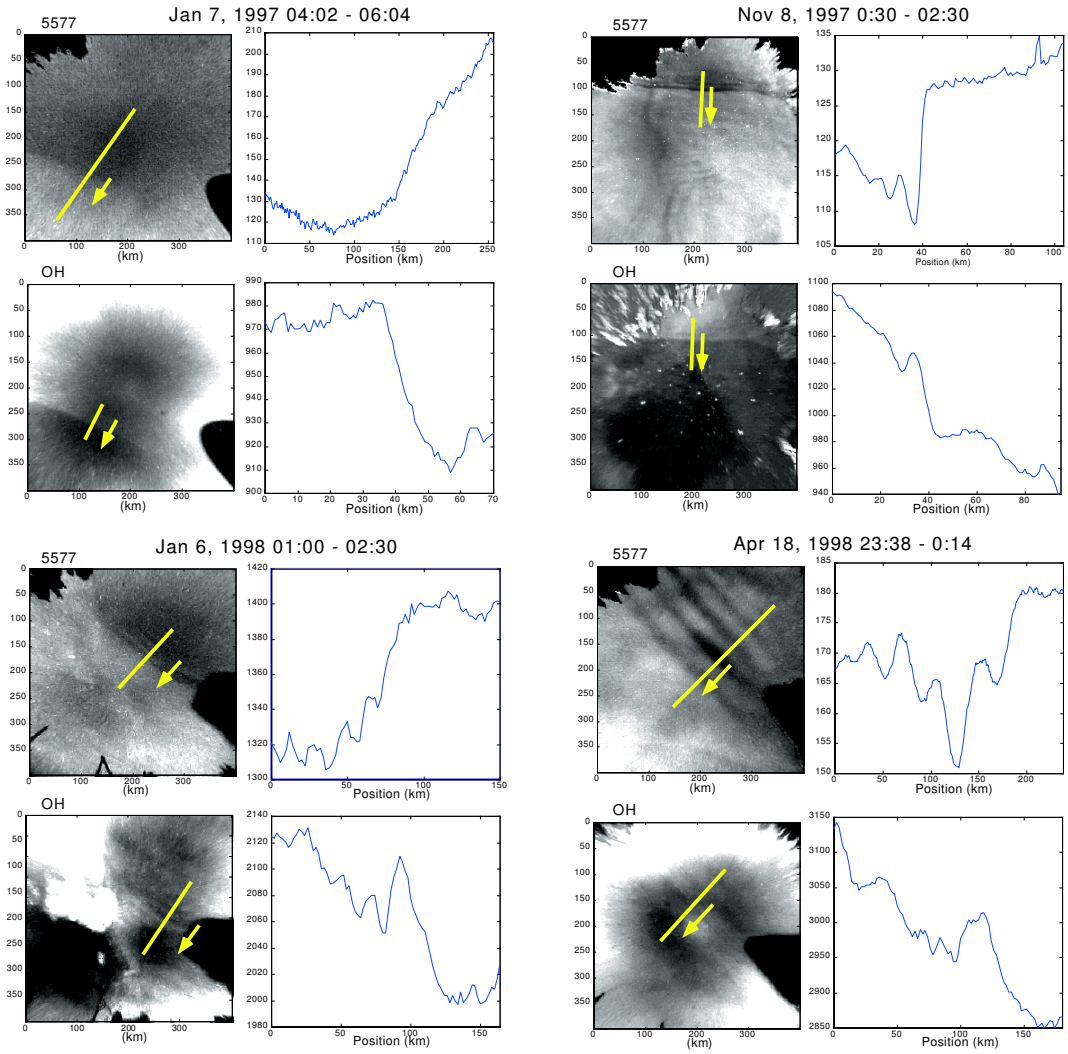

Figure 5.8: Possible turbulent bore on 7 January 1997 and other sharp fronts, all observed by the CARI in Puerto Rico. The LT time range indicates the overall duration for each event; however, only one representative time slice is shown for each event. The arrows indicate the direction each front is propagating; zero kilometers on the scan-line plots corresponds with the direction of the base of the arrow.

5.3.0.10 Possible Turbulent Bore: 7 Jan. 1997 - Puerto Rico [Event (c)]

Several additional observations of sharp fronts over Puerto Rico were documented with CARI. Selected images from the events are shown in Figure 5.8. While three of the four events (8 November 1997, 6 January 1998, and 18 April 1998) are clearly examples of standard events similar to the ALOHA-93 undular bore, the 7 January 1997 event with no trailing small-scale oscillations was atypical. The front came in from the northeast at around 04:00 LT, but was only barely detectable. It seemed to grow in strength as it crossed the field of view, and by 05:15 LT the front was clearly evident, but still had no ripples associated with it. Turbulent bores (i.e., non-undular bores) in open channels lack trailing ripples. A clear example of such a turbulent bore is shown as shown in panel (a) of Figure 5.9; in contrast, the photograph in panel (b) of Figure 5.9 depicts an undular bore in the same river [*Lighthill*, 1979]. Note that the OI (557.7 nm) intensity scan line for the 7 January 1997 event in Figure 5.8 has the same characteristic foaming appearance in the wake of the leading edge of this mesospheric bore as does the turbulent open-channel bore. Given that this holds for all time sequences for this event, we are inclined to label it a turbulent bore.

Note that power spectra plots of average intensity scan lines taken in front of, at the leading edge of, and behind the front are inconclusive as a means to support the turbulent bore claim. In theory we would expect the tell-tale 5/3 power spectra plot – indicative of turbulent regions – for calculations performed for data at the leading edge of and behind a turbulent bore, while expecting non-turbulent spectra in front of the purported turbulent bore, as well as for a representative undular bore (e.g., the 8 November 1997 dataset). Unfortunately, plots shown in Figure 5.10 do not unequivocally represent the theorized scheme.

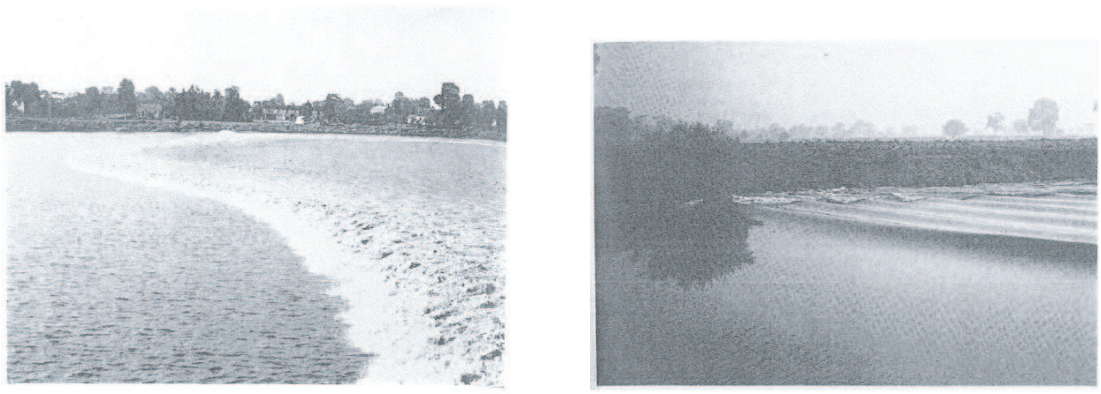

(a) (b)

Figure 5.9: Open-channel bores on the river Severn: (a) turbulent and (b) undular. (From *Lighthill* [1979].)

5.3.0.11 Inverse Bore: 6 March 1997 - Puerto Rico [Event (d)]

On 6 March 1997, a new type of event was detected over Puerto Rico, as shown in Figure 5.11. The image shown is for the OH emission. Although seemingly similar to the other fronts, this event differs in two key features:

- First, the intensity *depletion* was advancing with the front in the OH emission, that is, the *lower* airglow layer. On this night the 557.7-nm filter was underexposed; although the OI images appear noisy, by averaging over intensity scan lines perpendicular to the front, the signal-to-noise ratio may be increased. Figure 5.12 compares the scans across near-concurrent times for both emissions. There does appear to be an inverse front in the OI (557.7 nm) emission layer, manifested by an intensity enhancement advancing in this upper layer.
- Secondly, note the horizontal offset of about 8 km in the location of the jump between the two emissions as seen in Figure 5.12. It is fairly consistent for the other time-sequence images in the event as well. The leading

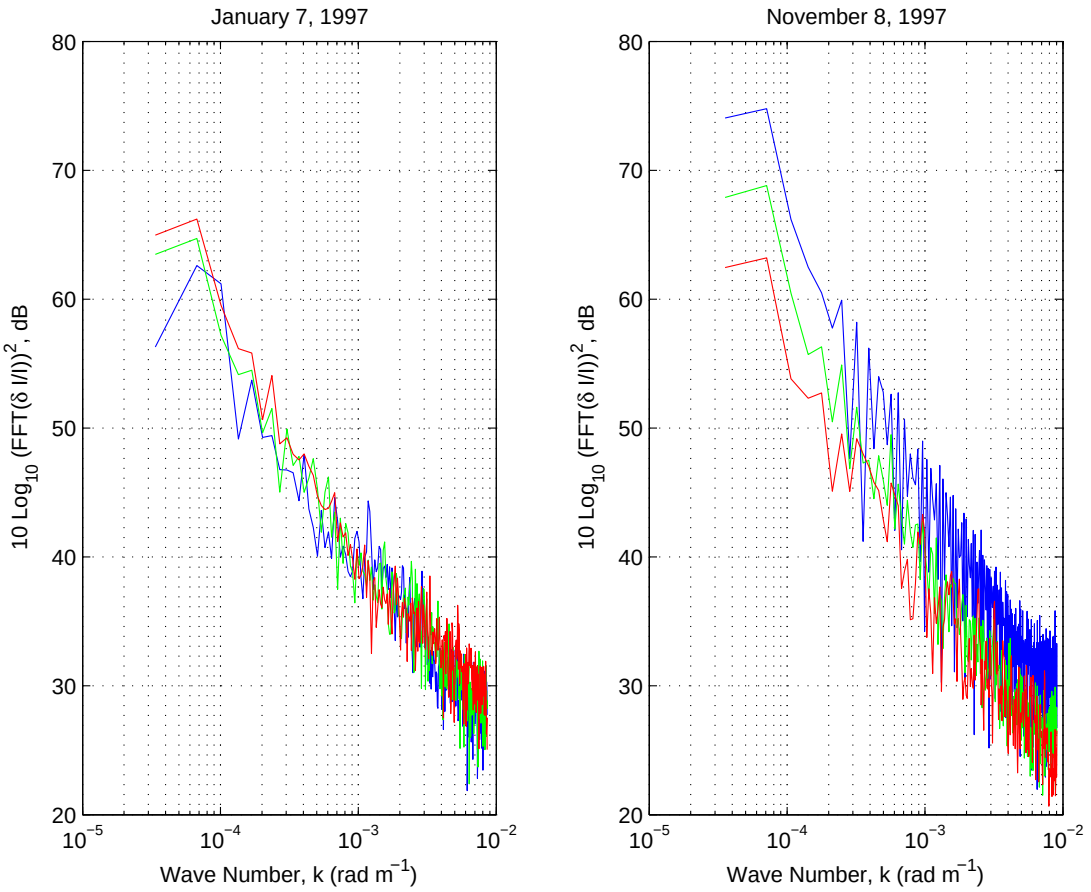

Figure 5.10: Intensity power spectra evaluating the possible turbulent bore case. Each plot line represents the power spectrum of an averaged set of scan lines taken parallel to the phase fronts either in advance of the bore (blue), immediately behind the bore (green), or far inside the bore (red). Data is shown both for the suspected turbulent bore case on 7 January 1997, and for a known undular bore case on 8 November 1997, for comparison.

edge of the bore in the upper emission layer, showing the intensity increase, trails the corresponding edge of the front in the lower layer, showing an intensity decrease.

Without the OI (557.7 nm) emission data, it would be tempting to conclude that some phenomenon developed below the OH layer, causing an upward vertical displacement. Taking the OI (557.7 nm) data into account, however, poses a serious problem for the original mesospheric bore theory which postulates

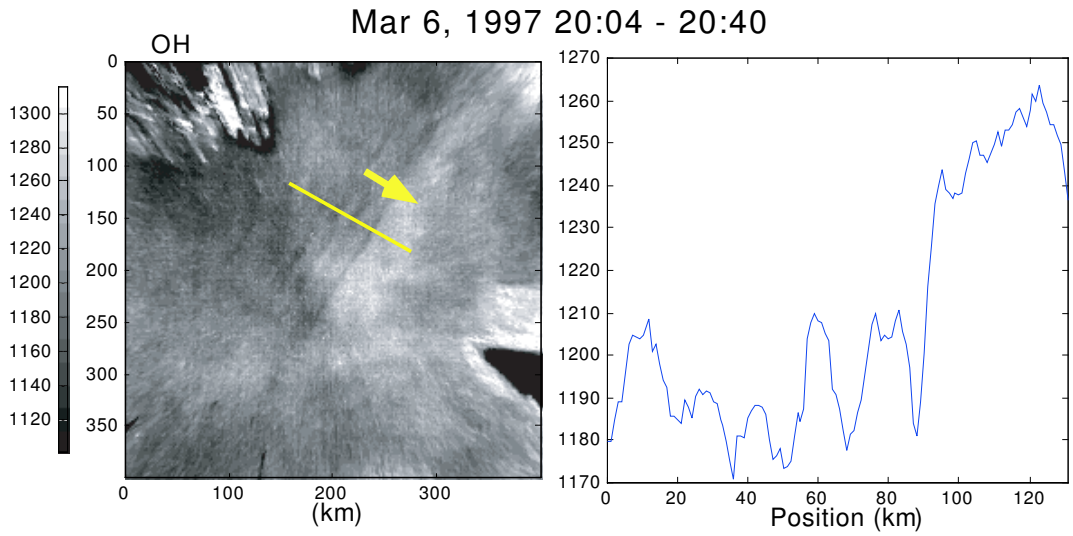

Figure 5.11: Apparent sharp front event on 6 March 1997. The image and intensity scan line shown are for the OH emission. The arrow indicates the direction of propagation of the front; zero kilometers on the scan-line plot in the right-hand panel corresponds with the direction of the base of the arrow. In this lower airglow layer from this inverse bore event, bands of intensity depletion are propagating into a brighter airglow region.

a mesospheric bore, in essence, splitting two atmospheric layers and driving them apart. As formulated, the original theory fails to explain how the two layers could be drawn closer together, as detected in this event, rather than being pushed apart, as is the case in the standard bore event. The event must be considered ambiguous.

5.3.0.12 Inverse Bore: 24 December 2000 - Peru [Event (i)]

In 2000, CARI was transported to Colan-Piura, Peru, for a campaign. A bore event was recorded on 24 December 2000. Again, images were collected at OI (557.7 nm) and OH emission layers. The bore was already in the field of view when the camera began operating at 19:54 LT. The front advanced from the southeast towards the northwest, with intensity bands stretching from hori-

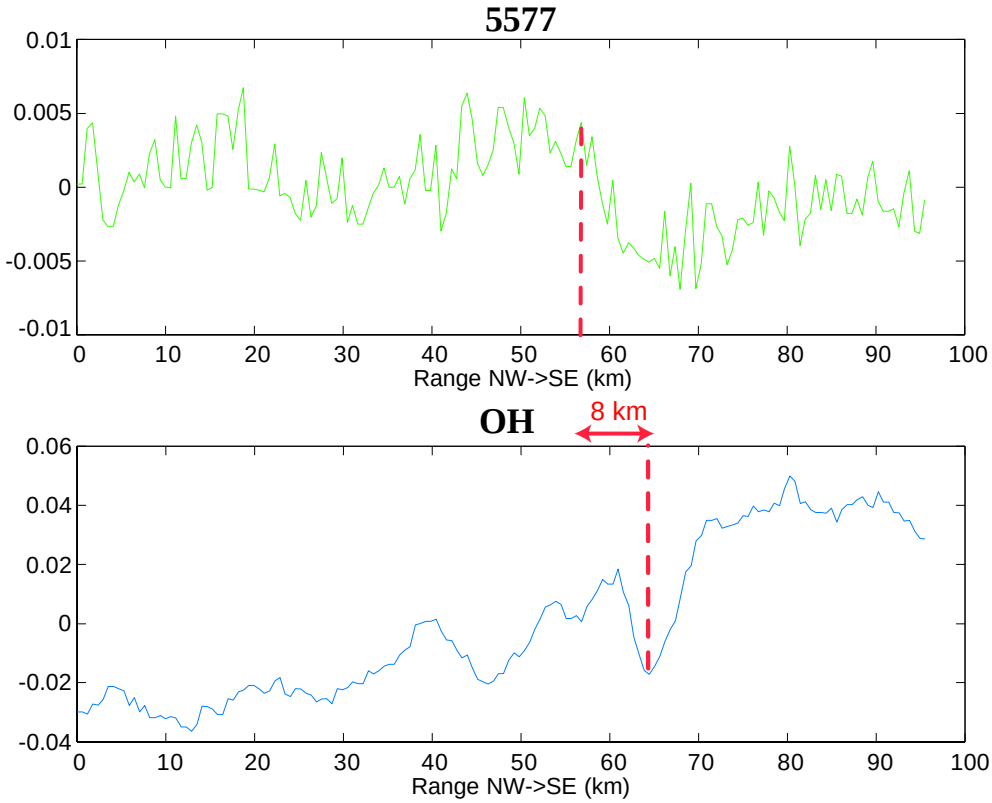

Figure 5.12: Scan lines of relative intensity versus position taken normal to wavefronts across OH and 557.7-nm (OI) emission images for the 6 March 1997 inverse bore.

zon to horizon. By 21:00 LT, the trailing oscillations had moved beyond the field of view. As in the 6 March 1997 event described above, a depletion, albeit a weak signal, was seen in the lower emission layer as the already low OH airglow intensity level decreased even further behind the front. Given this weak airglow signal from the layer to begin, the low contrast created as the depletion further diminished the signal (i.e., intensity level) is difficult to distinguish in a still frame. This time, however, the 557.7-nm filter was properly exposed by the camera. In the resulting images, the OI (557.7 nm) upper layer does appear to be pushed downward to create the increased light intensity in response to the front. Indeed, the inverse relationship held.

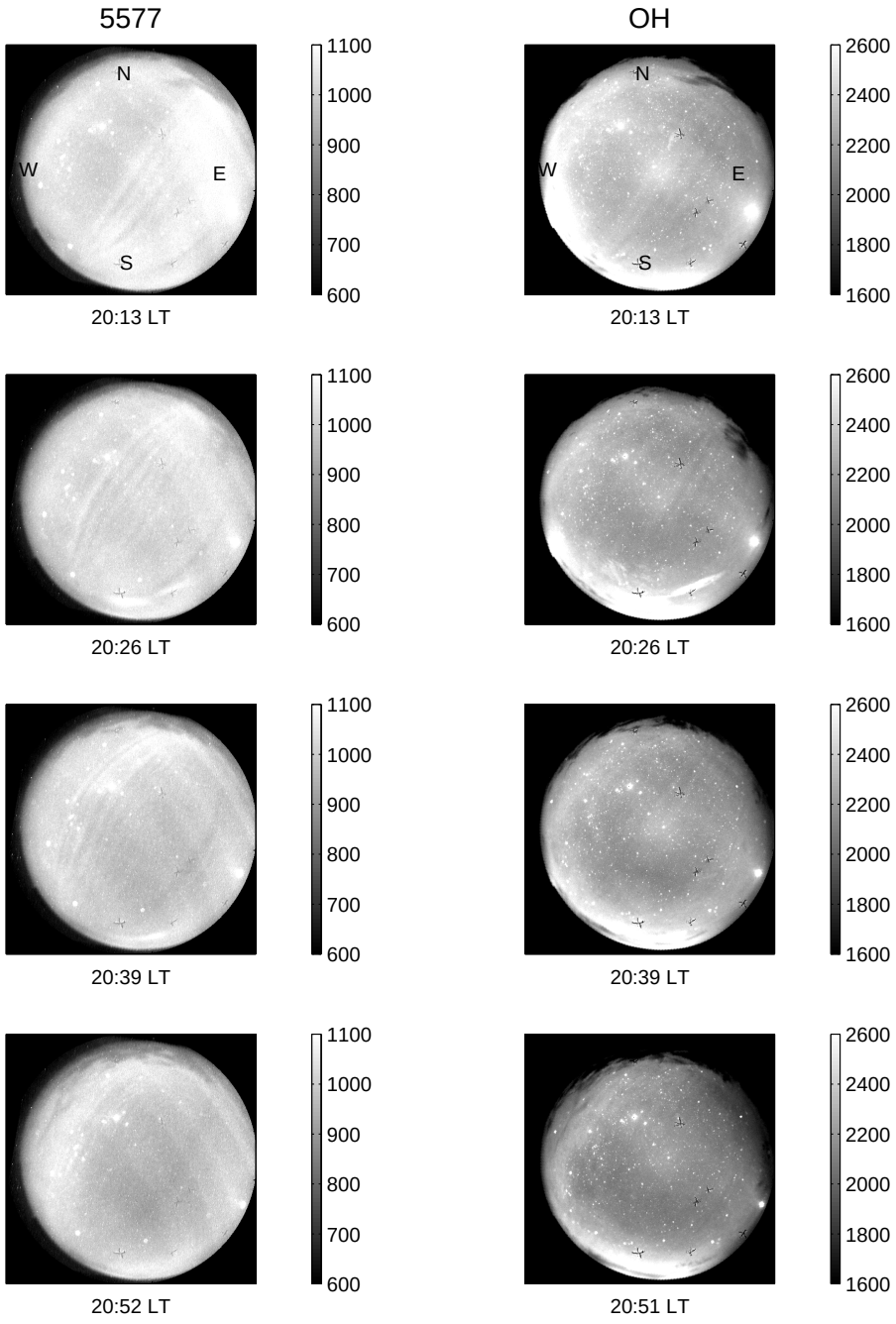

Figure 5.13: A series of 557.7-nm (OI) and OH emission images taken with CARI on 24 December 2000 in Colan-Piura, Peru. The images show a front approaching from the southeast. Note the *inverse* complementary relationship between the two emissions, i.e., note that bright bands are advancing in the 557.7-nm (OI) emission images, and corresponding dark bands are advancing in the OH emission images.

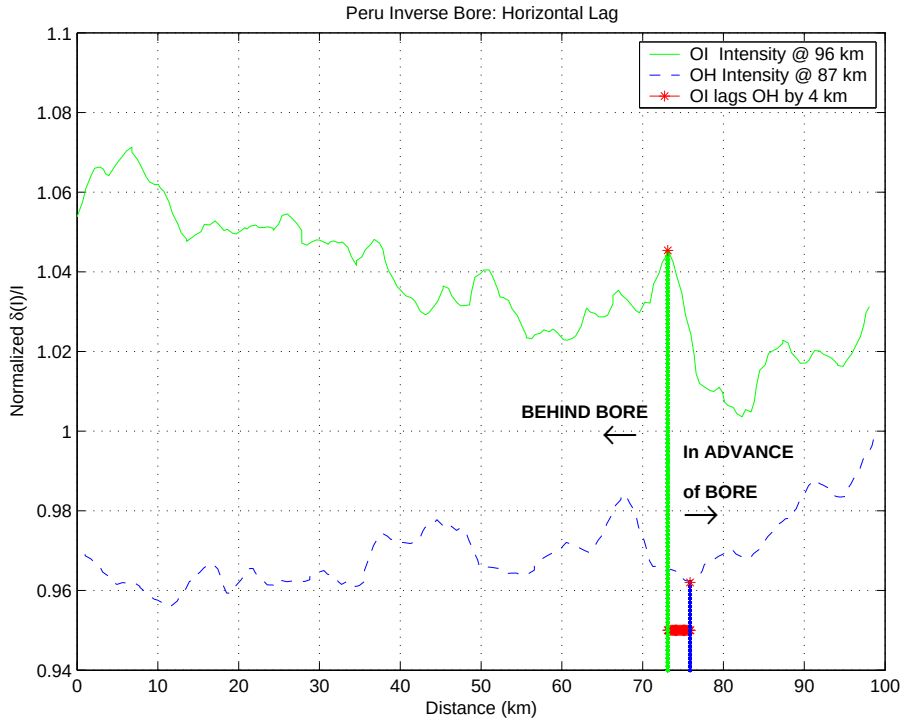

Figure 5.14: Intensity scan lines of 557.7-nm (OI) and OH emission images taken with CARI on 24 December 2000 in Colan-Piura, Peru. Both time slices were taken at 20:19 LT. The data are shifted to correct for the minor time difference between when the images were exposed. To accomodate both scan lines on the same graph, the two data sets were normalized in intensity. The plots show a decrease in intensity at the leading edge of the OH emission layer, and a corresponding increase in intensity advancing in the OI (557.7 nm) layer. The leading edge of the upper airglow layer lags the corresponding leading edge of the lower layer by approximately 4 km.

Similar again to the March event in Puerto Rico, we saw a horizontal lag between the onset of the bore in the two layers. Again this time, the leading edge of the bore in the upper emission layer trailed the corresponding edge of the front in the lower layer. In this event, this lateral offset was only about 4 km. Figure 5.14 illustrates the horizontal shift between the emission intensity drop in the lower layer and the emission intensity jump in the layer above.

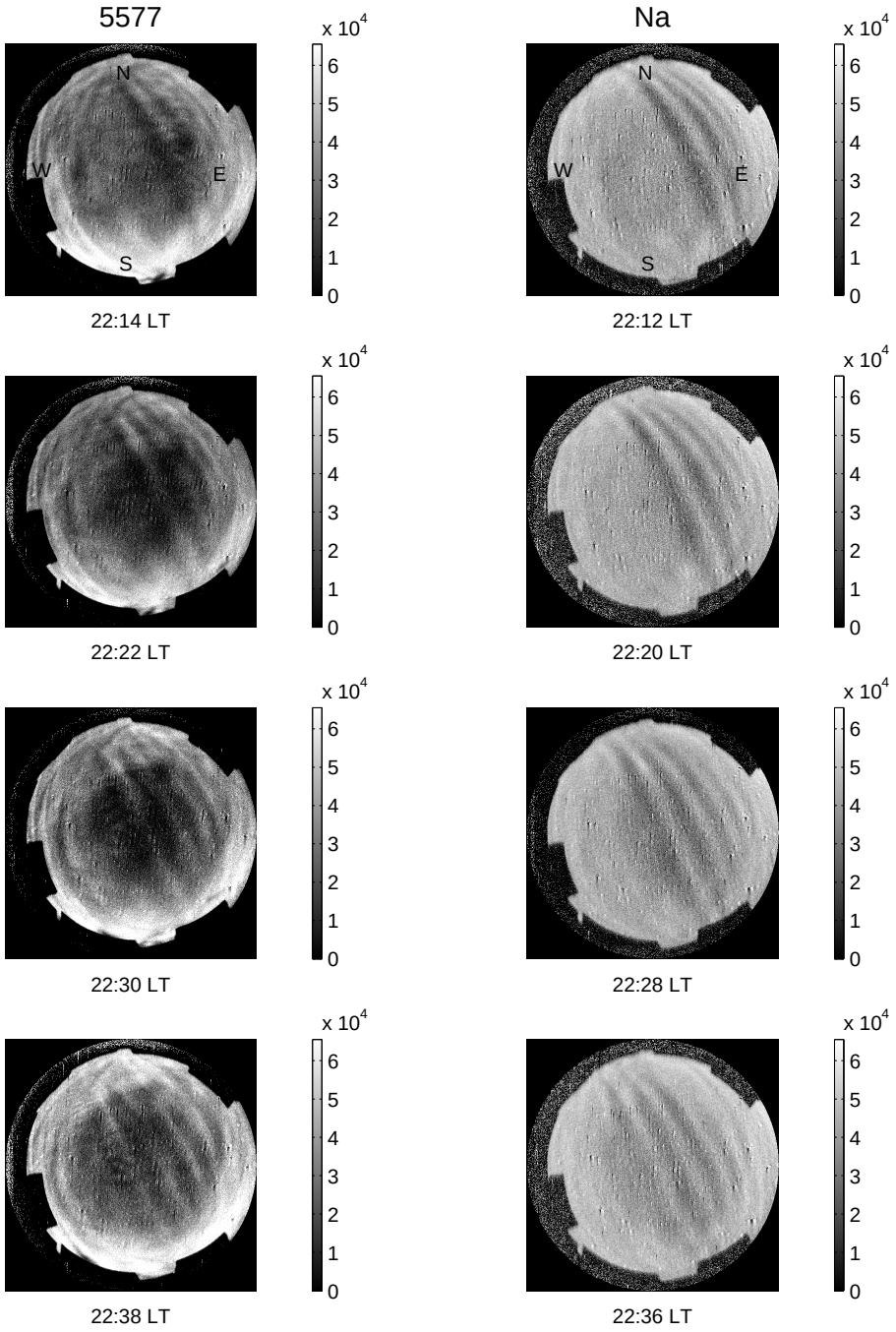

Figure 5.15: A series of 557.7-nm (OI) and Na emission images taken with CASI on 3 April 2002 in Maui, HI. These flat-fielded images, with stars removed, show a front approaching from the northeast. Note the *inverse* complementary relationship between the two emissions, i.e., note that bright bands are advancing in the 557.7-nm (OI) emission images, and corresponding dark bands are advancing in the Na emission images.

5.3.0.13 Inverse Bore??: 3 April 2002 - Maui, HI [Event (j)]

In the spring of 2002, another supposed inverse bore event was captured – this time by CASI in the first full year of the Maui-MALT campaign. As with the other Maui-MALT event, images were collected at both OI (557.7 nm) and Na airglow emission layers. On 3 April 2002, an abundance of wave activity, both small and large scale, was already in progress when the imager turned on at 19:58 LT. At 21:30 LT the predominant feature in the field of view was a sharp front approaching from the northeast. The event is summarized in the time sequence images depicted in Figure 5.15. Seeming to exhibit the "inverse" bore properties, the front appeared as horizon-to-horizon bright bands in the OI (557.7 nm) emission layer, propagating into a dark airglow region. By visual inspection, the complementary situation appears evident in the lower altitude Na layer where dark bands propagate into a bright region. The signal intensity is weaker again in the lower airglow layer, but this time the signal is visually distinguishable. By 22:54 LT this undular bore with its trailing waves almost completely filled the field of view of the camera before moving out of view to the southwest.

Also interesting in this event are packets of small-scale waves appearing orthogonal to the front, primarily at its leading edge. These packets are more apparent in the OI (557.7 nm) layer, appearing as dim, dark bands. They remain primarily at the leading edge and propagate to the northwest as the bore-like front progresses to the southwest.

As with the two inverse events, we again saw a horizontal lag between the onset of the front in the two layers. And again, the leading edge of the front in the upper emission layer trailed the corresponding edge of the front in the lower

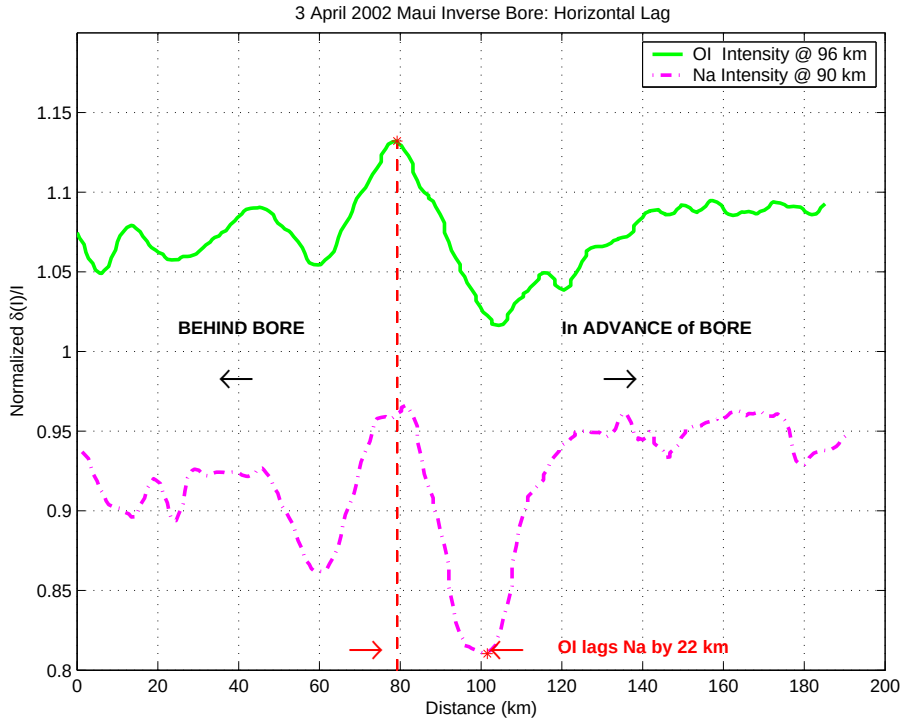

Figure 5.16: Intensity scan lines of OI (557.7 nm) and Na emission images taken with CASI on 3 April 2002 in Maui, HI. Both time slices were taken at approximately 22:20 LT, about 1.5 minutes apart. The data are shifted to correct for this minor time difference between when the images were exposed. To accomodate both scan lines on the same graph, the two data sets were normalized in intensity. The plots show a decrease in intensity at the leading edge of the Na emission layer, and a corresponding increase in intensity advancing in the OI (557.7 nm) layer. The leading edge of the upper airglow layer lags the corresponding leading edge of the lower layer by approximately 22 km (a value less than two vertical wavelengths).

layer. Designed to illustrate the horizontal shift between the emission intensity drop in the lower layer and the emission intensity jump in the layer above, Figure 5.16 instead throws doubt on the interpretation of this event. As indicated in Figure 5.16, the lateral offset calculated for this event was 22 km. However, this offset value is half the horizontal wavelength for this event, which could indicate that the intensity variations for the upper and lower airglow emission layers are actually in phase. In addition, a bore should bring either an intensity enhancement or depletion in its wake. Although this effect is suggested by

Figure 5.17: A photograph taken with a normal digital camera of the bands visible with the naked-eye on 14 November 1999 from McDonald Observatory (MDO), TX, during the reported bore event. (Photograph courtesy of S.M. Smith, Boston University.)

visual inspection of the time sequence images, the scan-line verification does not support this claim. Intensity levels in advance and behind the supposed bore remain fairly constant. Given this additional information, the inverse bore classification for this event does not hold up. The event is interesting, none-the-less, but is most likely an evanescent wave or a standard bore with the guiding structure located above both airglow layers.

5.3.0.14 Standard Bore: 14 November 1999 - McDonald Observatory, Texas [Event (h)]

Smith et al. [2003] report the observation of a bore event that occurred over western Texas on 14 November 1999. Unlike the Hawaiian ALOHA-93 event, this particular event was visible unaided to observers on the ground, demonstrating its unusually strong intensity and resulting in its alias as the "naked-eye"

bore. Figure 5.17 is a normal digital photograph taken by researchers of the event that night.

Like the ALOHA-93 event, this observation was captured at multiple airglow emission layers. Three emission layers were documented for the naked-eye event: OH at 87 km; Na at 90 km; and OI (557.7 nm) at 96 km. Images captured from the upper two layers show a region of darkness, in-phase between the two layers, propagating into a lighter region, which indicates that a bore is propagating below both of these layers. The lowest airglow layer imaged, the OH layer, varied 180° out of phase with both the Na and OI (557.7 nm) layers, indicating that the bore propagated at an altitude above this emission layer. Figure 5.18 shows the OI (557.7 nm) and Na emissions for this night.

Although evident in some other bore events, clearly discernable in this event is the fact that the leading edge of the front is *not* always the highest, relative amplitude peak as the basic bore theory predicts. In fact in this event, the small-scale trailing waves appear superimposed on a much larger underlying low-frequency wave. Beginning at 10:45 UT, the OI (557.7 nm) data in Figure 5.19 show that the subsequent peaks meet and surpass the leading edge in intensity depletion. However, the owners of this dataset regard the seemingly underlying low-frequency wave as a separate, unrelated event; more discussion is slated to understand their analysis used to ascertain this disassociation between the wave and the bore.

As described by *Smith et al.* [2003], a feature of particular interest visible in this bore event is that the spacing between successive waves increases with time. This phenomenon, discussed further in the next chapter (see Section 6.3), is evident in Figure 6.4 which shows an OI (557.7 nm) intensity scan line per-

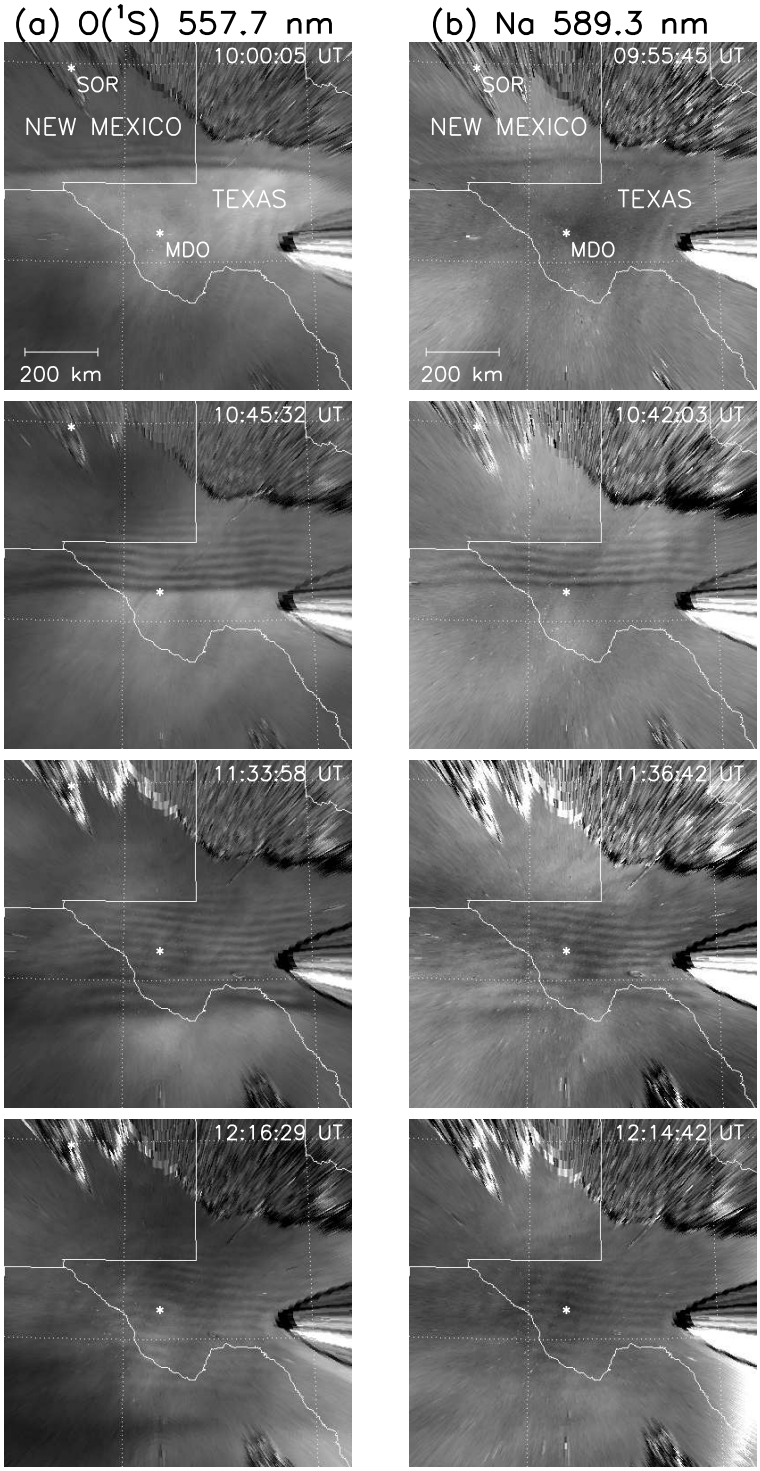

Figure 5.18: A series of unwarped 557.7-nm (OI) and 589.3-nm (Na) emission images taken with the Boston University imager on 14 November 1999 from McDonald Observatory (MDO), TX. The images show a front approaching from the north. (Figure 4 from *Smith et al.* [2003].)

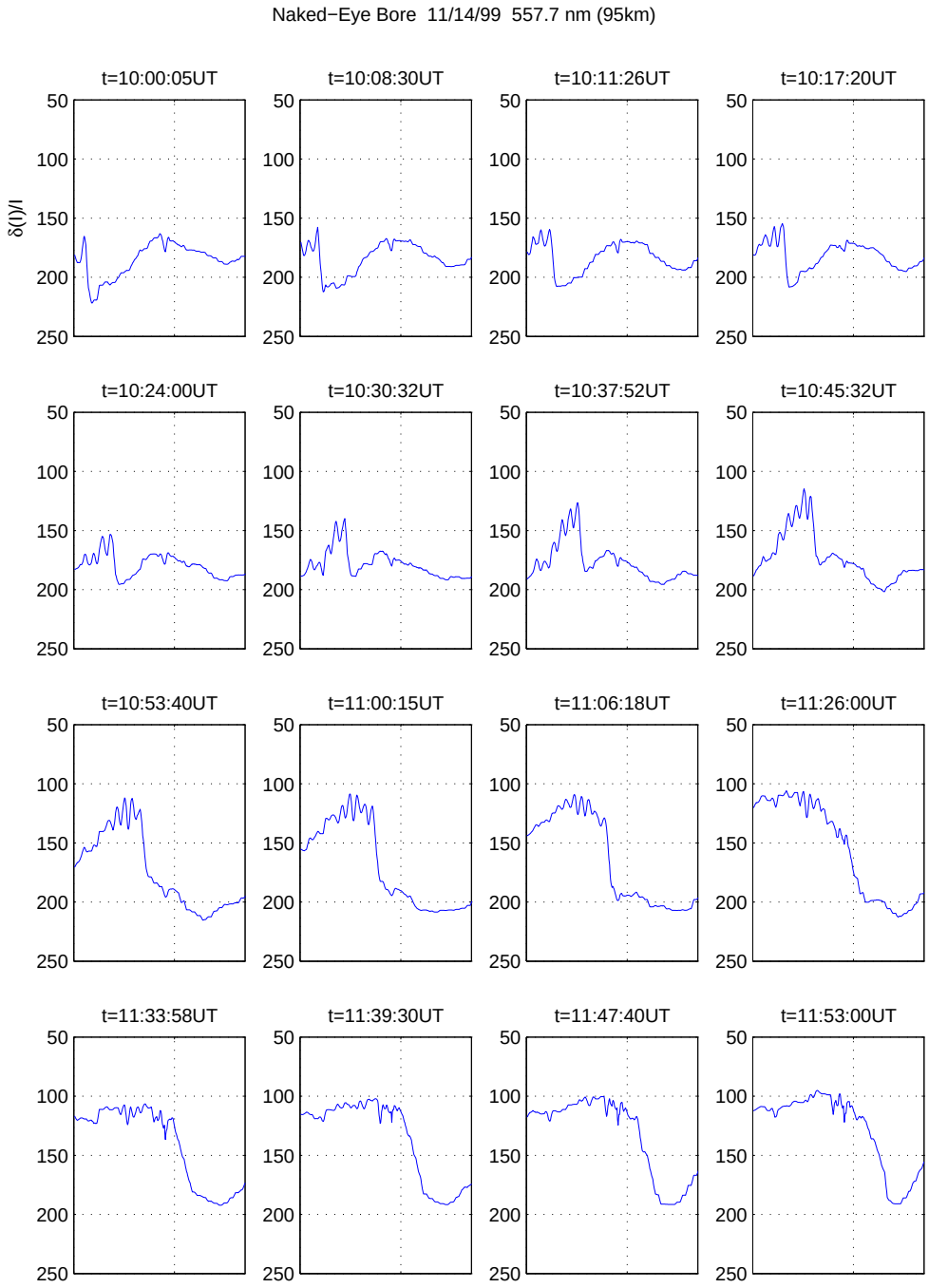

Figure 5.19: A time series of intensity scan lines for the naked-eye bore observed on 14 November 1999 by the Boston University imager from McDonald Observatory (MDO) in TX. Taken parallel to the direction the bore is propagating, these scan lines show the effect of the persistent low frequency wave. Note that intensity decreases moving up the y-axis. By 10:53:40 UT, the leading edge of the front is no longer the lowest intensity peak, i.e., the highest peak in this representation. (Adapted from *Smith et al.* [2003].)

pendicular to the wavefront for each of three airglow images taken at different times during this event. The leading wavefronts travelled faster than the trailing wavefronts, with the individual wavefronts maintaining constant velocities. These data contrast to the ALOHA-93 event, in which successive waves appear locked in step with the leading edge of the bore.

5.3.1 Summary of Observations

Table 5.1 summarizes the parameters of the bore events described in this paper. The site and source are indicated for each bore occurrence, with a legend for these codes provided in Table 5.2. Also tabulated in Table 5.1 are the dates and local times each event occurred. Key measured horizontal wave parameters are listed, including the direction of propagation, Az, given as an azimuthal heading in degrees; the horizontal phase velocity, U, in meters per second; and the period, τ, in minutes of trailing undulation in the Earth-fixed frame. The last three columns in the table are emission layers with entries indicating the intensity change brought about by the passage of the bore. "L→D" indicates a region of brighter airglow intensity propagating into a region of darker intensity; "D→L" represents a region of darkness moving into a bright airglow region.

Panel (a) of Figure 5.20 maps the location of each bore included in this chapter and identifies the class, direction of propagation, and relative velocity of each. This representation combined with the dates of occurrence from Table 5.1 indicates that these bores are equatorward-propagating events occurring in northern hemispheric winter. However, this seasonal variation and geo-

Table 5.1: Horizontal wave parameters measured for the various observed bore events. Az is the azimuthal direction of bore propagation; U is the horizontal phase velocity; τ is the period; OH, Na, and OI are emission layers with entries indicating the intensity change brought about by the passage of the bore.

Event	Site[1]	Source[1]	Date	Time(LT)	Az	U(m/s)	λ(km)	τ(min)	OH	Na	OI
(a)	HI	USU	10/9/93	23:30–01:30	135°	75	20	4.4	L→D[2]	L→D	D→L[3]
(b)	PR	CARI	1/6/97	03:16–06:00	172°	30	19	10.6	L→D		D→L
(c)	PR	CARI	1/7/97	04:02–06:00	-154°	38	20	8.8	L→D		D→L
(d)	PR	CARI	3/6/97	20:04–20:40	123°	39	11	4.7	D→L		noisy
(e)	PR	CARI	11/8/97	0:30–02:30	-174°	24	7	4.9	L→D		D→L
(f)	PR	CARI	1/6/98	01:00–02:30	-141°	32	11	5.7	L→D		D→L
(g)	PR	CARI	4/18/98	23:38–0:15	-135°	94	40	7.1	L→D		D→L
(h)	TX	BU	11/14/99	04:56–07:35	180°	60	30.2	8.4	L→D	D→L	D→L
(i)	PE	CARI	12/24/00	23:38–0:15	-60°	64	17	4.4	D→L		L→D
(j)	HI	CASI	04/03/02	21:34–0:10	-105°	42	40	15.9		D→L	L→D
(k)	HI	CASI	12/30/02	25:46–2:35	190°	51	25	8.2		L→D	D→L

[1]Refer to Table 4.2 for legends.

[2]Indicates a region of bright airglow intensity moving into a dark region.

[3]Indicates a region of darkness moving into a bright airglow region.

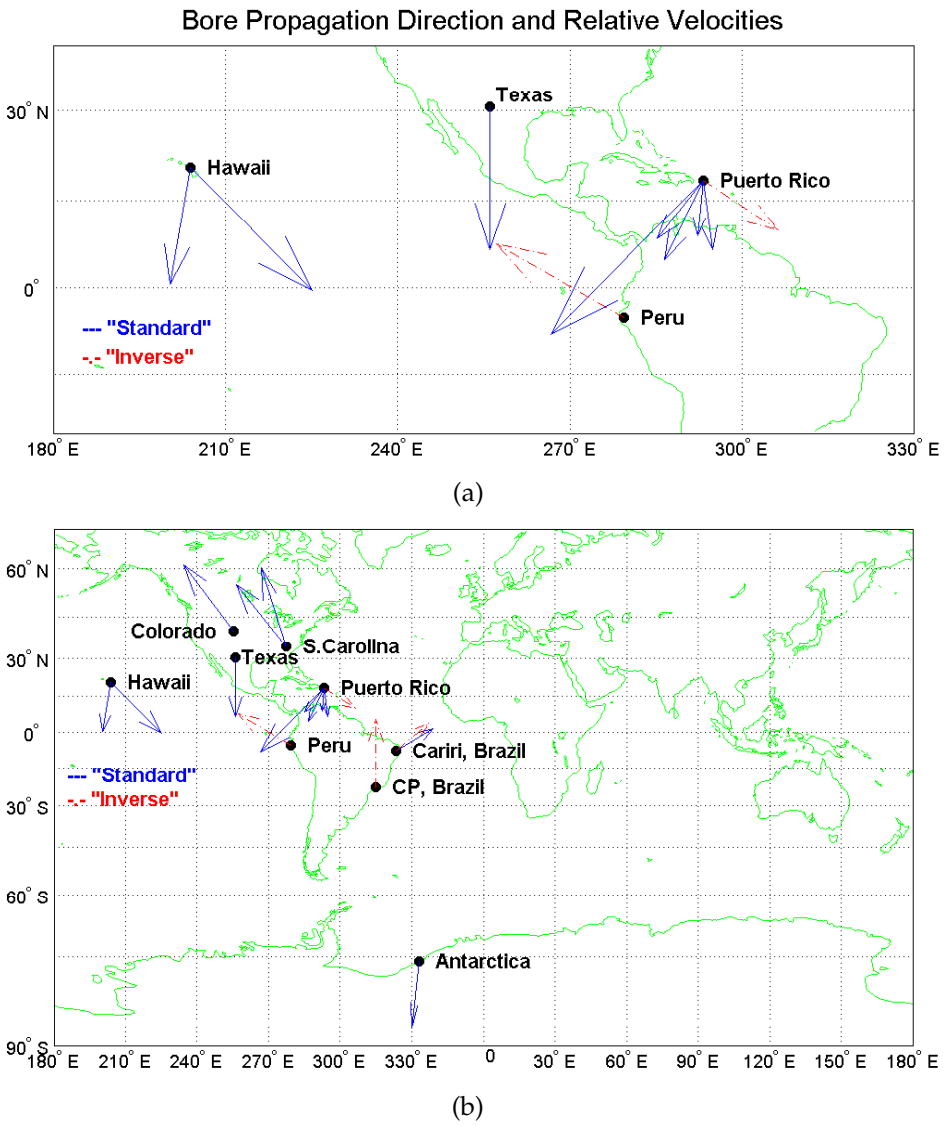

Figure 5.20: Map of bore locations with direction of propagation of the fronts and relative velocity indicated. Classification types are also indicated: "standard" bores with solid blue arrows, and "inverse" bores with dashed red arrows. Panel (a) shows the bore events discussed in this chapter; panel (b) expands the map view to include other bore-type events published in the literature to-date.

Table 5.2: Legend – Bore sites and sources.

Code	Site	Lat	Lon
HI	Haleakala, Maui, HI	20.7° N	203.8° E
PR	Arecibo, Puerto Rico	18.5° N	293.3° E
TX	McDonald Observatory, Fort Davis, TX	30.6° N	256.1° E
PE	Colan-Piura, Peru	-5.2° S	279.4° E

Code	Source	Contact
USU	Utah State University	M.J. Taylor
CARI	Cornell University	P.J. Loughmiller
BU	Boston University	S.M. Smith
CASI	Cornell University	P.J. Loughmiller

graphical dependency is refuted by our more recent data sets, as well as by the events reported by *She et al.* [2004], *Brown et al.* [2004], and *Nielsen et al.* [2006]. Panel (b) of Figure 5.20, an expanded map view including other bore and bore-like events reported in the literature, illustrates that while most of the reported events are equatorward, this propagation dependency is refuted. (Note that two representative arrows are included for the 64 events reported in *Fechine et al.* [2005] and further discussed in *Medeiros et al.* [2005].)

5.3.2 Bore Observation Classification System

The mesospheric undular bores imaged over the last decade fall into two basic types, categorized by how the upper and lower airglow emission layers oscillate with respect to each other. With this scheme, note that observing a minimum of two emission heights for an event is necessary in order to distinguish the relationship between upper and lower emission layers, and hence, to determine

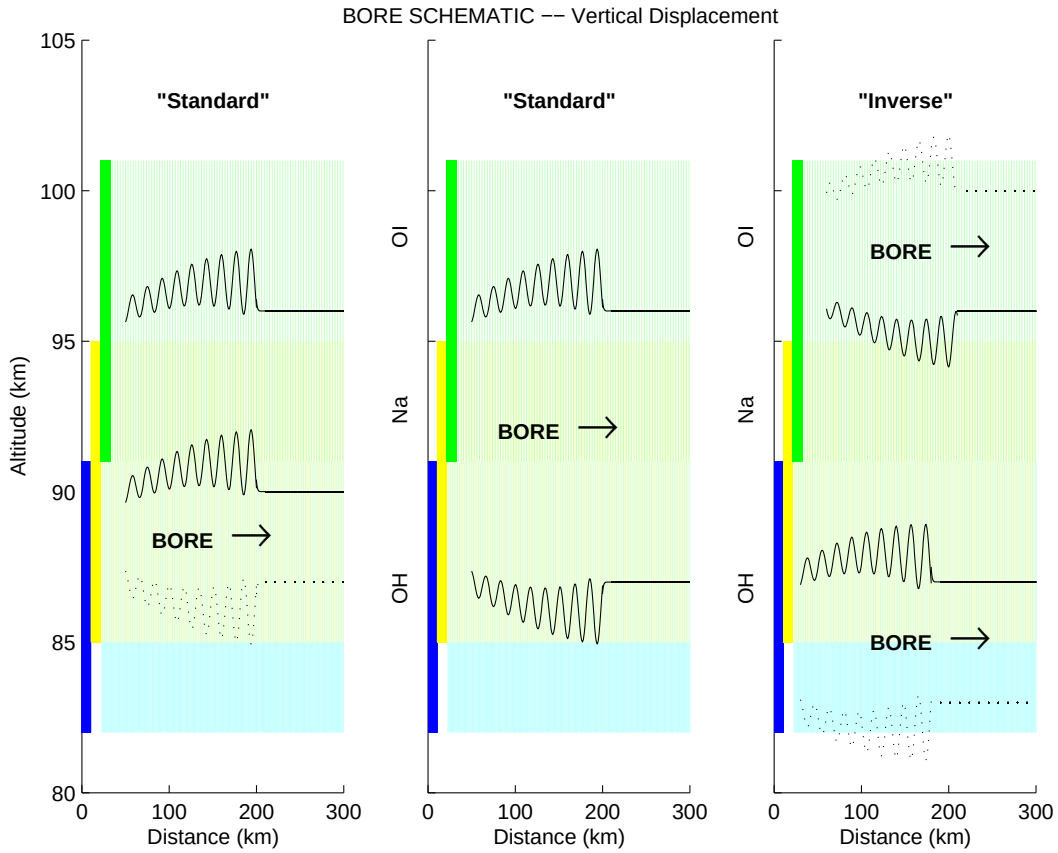

Figure 5.21: Schematic depicting basic mesospheric undular bore classifications. Solid lines indicate the vertical displacement (*not* airglow intensity) of observed airglow emission layers. Dashed lines indicate either the assumed vertical displacement of emission layers *not* observed, or regions outside airglow emission layers. Airglow emission layers are indicated schematically for reference by colored bars with OH in blue centered at 87 km, Na in yellow centered at 90 km, and OI (557.7 nm) in green centered at 96 km. Note that the emission layers as indicated are highly schematic. The locations and directions of propagation for the bores are noted for each panel. Two variations for the standard bore are shown. The left panel represents the case where images were taken only at airglow emission layers above the bore; in this case, the image data would appear to be correlated in intensity variation. The middle panel represents the case captured most often to date, in which data is collected both above and below the bore and the images show a complementary relation with regard to intensity. The right panel depicts the case recognized by the inverse complementarity between upper and lower airglow layers.

the bore observation type. We have denoted these types as *standard* and *inverse*.

Figure 5.21 illustrates the basic types of undular bore observations depicted thus far in the mesosphere. Two variations are shown for the standard bore, with the difference depending on which airglow layers are observed and in which region the bore is propagating. The "standard" category is consistent with events such as that captured during ALOHA-93 (10 October 1993) in which the upper and lower layers oscillate 180° vertically out of phase, with the bore seeming to drive the layers apart. In this mode, the upper layer rises when the lower layer descends, and vice versa. We see this effect in airglow images as dark bands (representing cooler temperatures and decreased density) in upper layers corresponding with bright bands (representing warmer temperatures and increased density) in lower layers. Note that if observations are made only above the region where the bore is propagating, as in the first of the three schematics in Figure 5.21, the emission images from these airglow layers will be correlated in intensity; the same is true if observations are made only below the bore. The second category is "inverse" and describes the inverse complementarity situation. Inverse bore features were seen in the 24 December 2000 Peru event, as well as in the 6 March 1997 Puerto Rico event. In these cases, the upper and lower emission layers appeared to be drawn together as the intensity increased in upper layers while simultaneously decreasing below.

5.4 Comparison to Basic Bore Theory

For the sharp frontal events included in this chapter, Table 5.3 lists both the predicted parametric values derived from the symmetric mesospheric bore theory

Table 5.3: Measured and derived parameters for the observed bore events. The first third of the table contains measured values for the observable parameters in the image data. Measurements of the wave crest generation rate, W, and the number of crests observed, C, are included here, along with values for λ and U, repeated from Table 5.1 above. The middle and right-hand sections of the below table contain values derived from the basic bore theory. a is the amplitude of the waves trailing the bore; W is the rate of wave crest generation; χ is the distance of the bore from its source. Derived values are based on assuming $0.1 \leq \beta \leq 0.3$, i.e., that the data are characterized as undular bores ranging in strength from weak undular bores ($\beta = 0.1$, where $h_1 = 1.1h_0$) to the upper limit for undular bores ($\beta = 0.3$, where $h_1 = 1.3h_0$). λ, U, h_1, h_0, and a are defined in Appendix A, and illustrated in Figure 4.10.

	Measured				Derived $\beta = 0.1$					Derived $\beta = 0.3$				
Event	**W** **(hr^{-1})**	C (crests)	λ (km)	U (m/s)	h_1 (km)	h_0 (km)	a (km)	**W** **(hr^{-1})**	χ (km)	h_1 (km)	h_0 (km)	a (km)	**W** **(hr^{-1})**	χ (km)
(a)	**n/a**	10	20	75	2.1	1.9	0.1	**1.5**	1775	3.7	2.8	0.6	**2.8**	976
(b)	**0.6**	5	29	31	3.1	2.1	0.2	**0.4**	1291	5.4	4.1	0.9	**0.8**	710
(c)	**—**	3	20	38	2.1	1.9	0.1	**0.8**	532	3.7	2.8	0.6	**1.4**	293
(d)	**2.2**	6	19	64	2.0	1.8	0.1	**1.4**	996	3.5	2.7	0.6	**2.5**	548
(e)	**1.0**	5	16	28	1.7	1.5	0.1	**0.7**	688	2.9	2.2	0.5	**1.3**	378
(f)	**1.3**	7	15	46	1.6	1.5	0.1	**1.2**	932	2.8	2.1	0.5	**2.3**	513
(g)	**n/a**	5	40	94	4.3	3.9	0.2	**0.9**	1775	7.4	5.7	1.3	**1.7**	976
(h)	**1.5**	17	30	60	3.2	2.9	0.2	**0.8**	4556	5.6	4.3	1.0	**1.5**	2507
(i)	**2.1**	8	18	66	2.0	1.8	0.1	**1.4**	1310	3.4	2.6	0.6	**2.6**	721
(j)	**1.0**	7	21	53	2.2	2.0	0.1	**1.0**	1298	3.9	3.0	0.7	**1.9**	714

presented in Section 4.3 and the measured observables from the image data. Given the predominantly sinusoidal appearance of the bores in the present airglow dataset, indicative of weak undular bores, we assume for these events bore strengths (denoted by β) representing undular bores tending toward weak undular bores; that is, we base our calculations on the assumption $0.1 \leq \beta \leq 0.3$.

For each beta defining this range (i.e., $\beta = 0.1$ and $\beta = 0.3$), Eq. 4.207 is used to obtain a relationship between h_0 and h_1. This resulting relationship is then substituted, along with the observed wavelength (λ), into Eq. 4.208 to obtain a value for h_1, with h_0 immediately determinable from Eq. 4.207. These values for the perturbed and unperturbed heights of the fluid are next combined with measured values for the number of wave crests counted behind the bore (C), the wavelength of the waves behind the bore (λ), and the bore velocity (U) to derive values for a, W, and χ using Eqs. 4.209-4.211 as detailed in Section 4.3.

While the derived values of Table 5.3 appear to conform reasonably to the expectations of the basic bore theory of *Dewan and Picard* [1998], in order to assert that agreement does – in fact – exist, we must close the loop where possible between observations and theory. To this end, we compare measured and derived values for W, the rate of wave crest generation. Given that our dataset for these new events is restricted to imager observations only, the scope of theoretical predictions which can be verified using measurements is limited to W. Using Eq. 4.210, theoretical value ranges for wave crest generation rates were calculated based on measured wave parameters (λ and U) combined with estimated values for h_0, h_1, and a, derived from assuming β values for undular bores. Measuring the values for the rates at which waves were observed to be added to the tail end of the bores proved to be non-trivial in most cases as

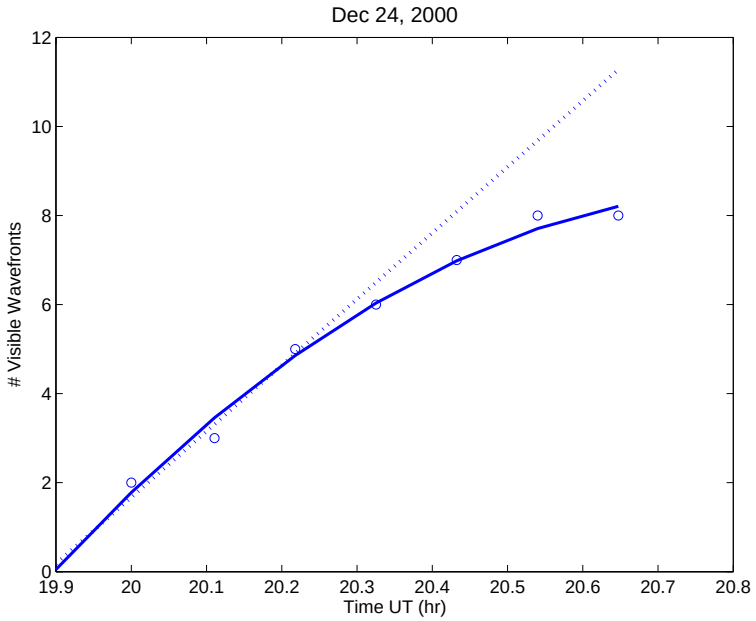

Figure 5.22: Time history of the number of visible wavefronts for the night of 24 December 2000. The dotted line is the projected number of visible wavefronts over the observation period assuming a constant wave train moving at the average phase velocity of the observed wavefronts. The solid curve is the best fit to the observed number of visible wavefronts.

forewarned in *She et al.* [2004], where it is noted that the rate of wave crest generation is a "parameter that may in principle be checked by observation, though it may be difficult in practice." Some difficulties arise merely in identifying very clear undulations over time. Coupling this with the fact that most of the events enter the field of view of the imager from over the horizon adds to the challenge. To combat this uncertainty, we employ a method like that used by *Smith et al.* [2003] in which we compare the observed time history of the number of visible wavefronts behind the bore (shown in Figure 5.22) to an estimated linear time history (represented by the dotted line in Figure 5.22) based on the assumption that all wavefronts move at the same speed. The difference between these time histories over the discernable course of the event provides a measured estimate of the waves added by the disturbance. Through this analysis,

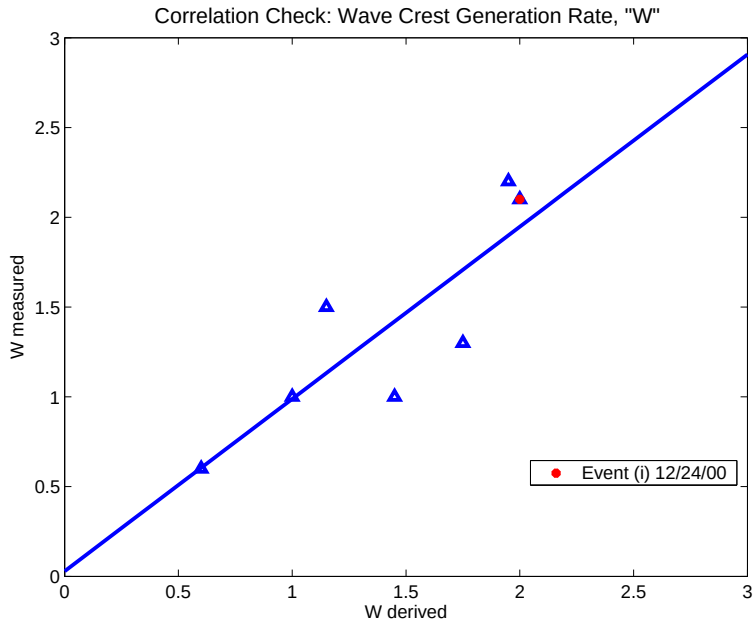

Figure 5.23: Scatter plot of measured versus average derived values for crest generation rates for the bore events tabulated in Table 5.3. Event(i), the 24 December 2000 event in Peru, is indicated by the red asterisk. The solid blue line shows a positive linear correlation between the measured values of the observations with the average of the range of derived values predicted for each event by basic bore theory.

we find good agreement between the observed wave generation rate (in column 2 of Table 5.3) and the associated theoretical predictions defined by the ranges specified by columns 9 and 14 of Table 5.3.

To test the suggested correlation between the observed wave generation rates and the value ranges predicted by theory, we produced a scatter plot of measured crest rates versus the average of the range of derived crest rate values for each of the events tabulated in Table 5.3. This analysis, shown in Fig. 5.23, reveals a linear relationship supporting a correlative connection between the measured and derived values.

Although the parameters tabulated in Table 5.3 support that sharp fronts observed thus far appear parametrically consistent with basic mesospheric bore

theory, a self-consistency check is not possible without supporting instrumentation. In addition, the "inverse" events do not support the symmetry underlying the basic model.

5.5 Conclusion

In this chapter, we presented new bore observations and revisited previously documented events [*Taylor et al.*, 1995c; *Smith et al.*, 2003]. While we showed that these fronts were parametrically consistent with the basic mesospheric bore theory, of particular interest were the new observations which appeared to confound the symmetry underlying the existing analytic model. In the next chapter, we extended the basic symmetric bore theory of *Dewan and Picard* [2001], proposing the possibility of multiple bores to explain the inverse intensity relationship exhibited by some of the new bore events. The calculations in the paper by *Seyler* [2005] offer an alternate theory against which to compare the data.

A mesospheric bore classification scheme was presented, based on the described observations, both new and old. While the case for the proposed turbulent bore is qualitative at best, many wall events exist in the scientific community's collective database and could be further analyzed for comparison. We also conclude that wall waves and turbulent bores are difficult to distinguish, and that researchers should keep an open mind about events without trailing waves.

Many more examples of all of the bore types included in this paper are being obtained during an ongoing campaign in progress at the top of the Haleakala volcano in Maui, HI. This campaign, the Maui-MALT initiative, is jointly spon-

sored by the National Science Foundation (NSF) and the Air Force Office of Scientific Research (AFOSR) to promote upper atmospheric studies of the mesosphere and lower thermosphere (MALT). Participating entities include Cornell University, the University of Illinois, Utah State University, Pennsylvania State University, and the Aerospace Corporation. This ever-growing database of bores includes features not seen in the bores presented here, and will be studied in a later paper.

CHAPTER 6

INVERSE BORE THEORY

In the previous chapter, we describe a number of bore events and compare them to the existing model, noting that some of the new observations exhibit an unexpected "inverse" intensity relationship only recently seen between airglow layers [*Dewan et al.*, 2001; *Loughmiller et al.*, 2004; *Medeiros et al.*, 2005; *Loughmiller et al.*, accepted 2007]. The possibility of two coexisting bores is proposed in this chapter to explain both the inverse phenomenon and the accompanying horizontal phase shift between the emission layers. We also compare the data to the theory proposed by *Seyler* [2005], which extends the symmetric bore theory and offers additional insights to explain the data.

6.1 Background

As reported in Chapter 5, two of the new sharp mesospheric fronts appear to conflict with the original symmetric bore theory model. These events displayed neither the usual complementary effect, with lower airglow layers appearing to brighten behind the leading edge of the front while corresponding upper layers appeared to darken, nor a complete lack of complementarity with regard to the variation in radiance. Rather, these conflicting observations first published in *Dewan et al.* [2001] and *Loughmiller et al.* [2004], and similar to the events described by *Medeiros et al.* [2005], demonstrate an "inverse" complementarity. In these examples which appear to be inconsistent with current bore models, the

*Original source: Loughmiller, P.J., M.C. Kelley, E.M. Dewan, F.J. Garcia, J.J. Makela, and S.M. Smith, Sharp mesospheric fronts: Inverse bore theory, *Journal of Geophysical Research*, in review. Some notational changes have been made for consistency with the remainder of the dissertation.

lower layers appear to be pushed up (becoming darker) while the corresponding upper layers are pushed down (becoming brighter). Initially confounding the theory, analysis of these observations has now been used to extend the theory further. We will show that the inverse relationship could be caused by the existence of two bores occurring simultaneously, one above the other. This extension of the original theory also accounts for the apparent horizontal phase shifts between layers in the new observations.

While some predictions of the original symmetric bore model cannot be validated as yet due to a lack of simultaneous vertical profile data, other observational aspects remain unexplained by the model itself. *Seyler* [2005] has developed the analytical bore model presented by *Dewan and Picard* [1998] further, including the development and analysis of two-dimensional numerical simulations. These simulations might offer an alternative explanation for the inverted contrast patterns. Seyler's analysis also sheds light on some features not addressed to date by modelling of undular mesospheric bores.

The chapter is organized as follows. We propose the dual (multiple) bore theory, in Section 6.2, to account for the new bore observations with inverted intensity patterns. In Section 6.3, characteristics of the new bore observations are compared to the predictions of the nonlinear theory developed by *Seyler* [2005]. We conclude in Section 6.4 with a discussion and summary.

6.2 Extension of Basic Bore Theory - Inverse Bore Theory

Two events that remain unexplained by the original mesospheric bore theory occurred on 6 March 1997, and on 24 December 2000, and were observed from

Puerto Rico, and from Colan-Piura, Peru, respectively. In each of these cases, a complementary effect between lower and upper airglow layers did, indeed, occur, but was opposite (or inverse) from previously reported observations. In these three cases, the lower emission layer (OH or Na) demonstrated an area of airglow depletion entering a higher intensity region, while the upper OI (557.7 nm) emission layer revealed an airglow enhancement entering a dark region. A hypothesis proposed by a co-worker (EMD) is that two bores – rather than one – were responsible for creating this effect: one bore existing above the upper layer (OI 557.7 nm) and one below the lower layer (OH or Na), in essence sandwiching the two airglow layers. The effect of the two bores would be displacement of the upper airglow layer downward and simultaneous displacement of the lower airglow layer upward. Phase shifts, such as the 8 km lateral offset between airglow layers in the 6 March 1997 event and the 4 km lateral offset in the 24 December 2000 event, can be accounted for by postulating that the two bores were not created simultaneously and, hence, not directly aligned vertically.

As *Dewan and Picard* [1998] explained, bore existence requires first that an inversion layer exist to function as a mesospheric bore duct. Given the presence of a temperature inversion layer, also called a mesospheric inversion layer (MIL), they describe the mechanism to form a bore inside this inversion layer region [*Dewan and Picard*, 2001]. As with the initial inversion layer development, the bore formation mechanism requires interaction between a gravity wave and critical level, but also depends upon the nonlinear dependence of wave velocity on amplitude.

For the case of dual bores stacked one above the other, conditions must first exist whereby *two* inversions can be created, one above the other. According to

the theory of *Huang et al.* [1998], this scenario requires two stacked critical layers, which is possible if a source of gravity waves exists in the troposphere (e.g., fronts or thunderstorms) such that the horizontal phase velocity of a set of these waves was equal to the mean wind velocity at two different altitudes. To create two inversion layers, the gravity waves must pass through the lower critical layer in order to create the higher altitude inversion. Gravity waves are usually highly attenuated as they pass through a critical layer, where the wave energy easily couples to the mean flow, resulting in wave damping [*Booker and Bretherton*, 1967]. However, a critical layer becomes transparent to gravity waves when the Richardson number is less than a quarter ($R_i < \frac{1}{4}$). This happens during the time that the lower inversion forms (see *Huang et al.* [1998]). Then subsequent gravity waves passing through the critical layer will have their momentum flux reduced by a factor of $\exp(-2\pi\mu)$, where μ is defined by $\mu \equiv (R_i - \frac{1}{4})^{\frac{1}{2}}$ [*Gossard and Hooke*, 1975].

Experimental observations indicate periods of time when $R_i < \frac{1}{4}$ inside an MIL [*Huang et al.*, 1998, 2002]. Thus, an advancing gravity wave sourced from below will create a lower MIL, which then becomes unstable ($R_i < \frac{1}{4}$), allowing waves to pass through and to proceed up to the second critical layer, thereby creating a second inversion layer. Data from *Dao et al.* [1995] in the left-hand panel of Figure 6.1 demonstrate that double MILs have, indeed, been observed. The corresponding Brunt-Väisälä profile, plotted in the right-hand panel of Figure 6.1, illustrates the existence of propagation ducts coincident with the multiple MILs. In this interpretation of these data, atmospheric tides controlled the locations of the MILs. Following this example, we assume atmospheric tides affect the formation of dual inversions and hence, impact dual bore formation. To estimate the *horizontal* separation between bore fronts at different altitudes,

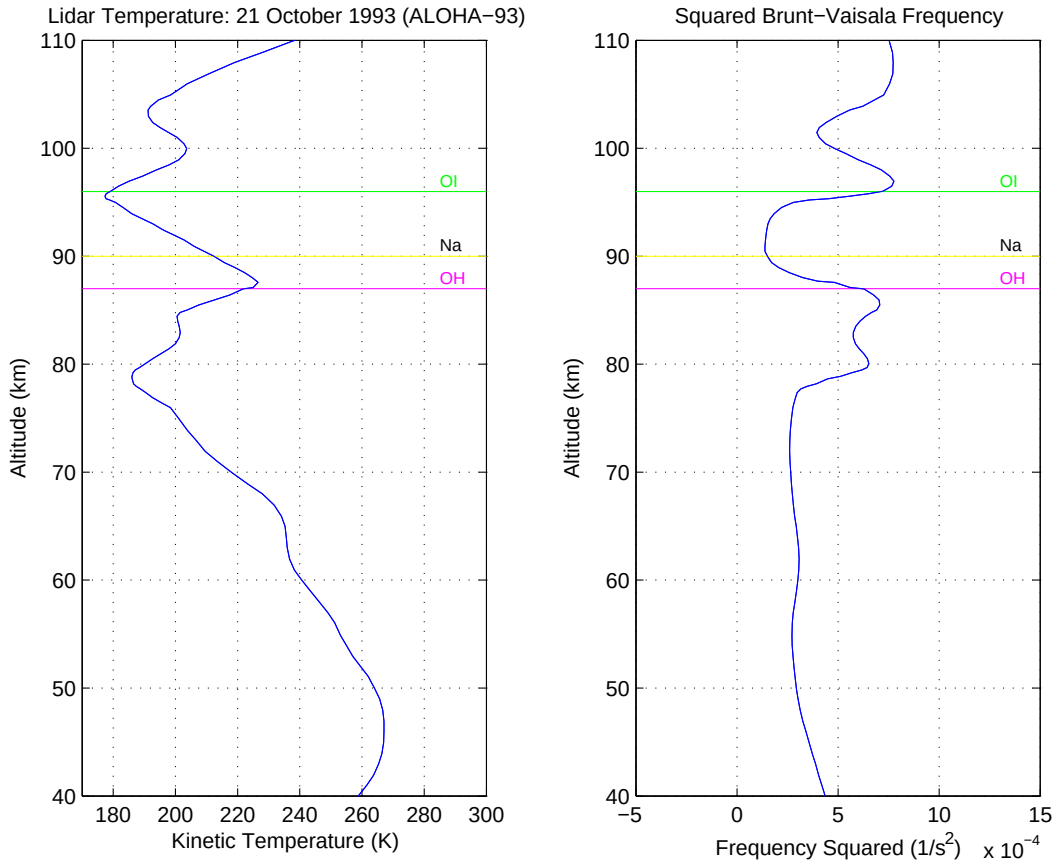

Figure 6.1: Buoyancy frequency atmospheric profile over Maui, HI, on 21 October 1993. Lidar data (adapted from *Dao* [1995]) taken during the ALOHA-93 campaign is shown in the left panel with the corresponding squared Brunt-Väisälä profile plotted in the panel to the right. Two large ducting regions are evident near 85 km and 100 km, coincident with the MILs in the temperature profile. N^2 varies by a factor of 4-5 in the ducting regions. Airglow emission heights are indicated in both panels for reference.

we consider the proposed location of the two inversions used in the dual-bore model, as shown in Figure 6.2. Note that the 20-km spacing corresponds to the tidal vertical wavelength. The airglow layers, OH at 87 km and OI (557.7 nm) at 96 km, are located *between* the inversions at 80 km and 100 km.

Having provided for the stacked MILs, now in considering dual bore formation we once again encounter the problem of gravity waves passing through the lower critical layer and propagating to the upper critical layer. In the case of

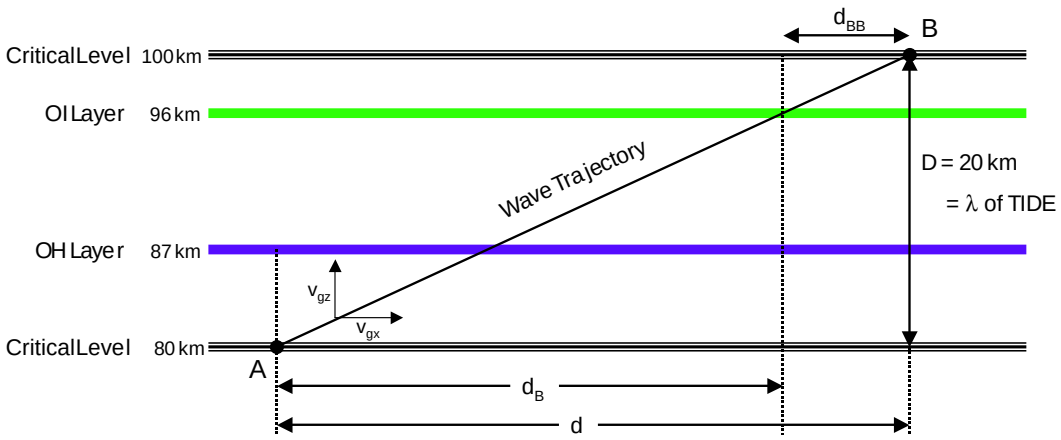

D = distance between critical levels

d_B = $v_B t$, distance traveled by lower bore horizontally during time t, the time for the wave to travel from A to B.

d_{BB} = $d - d_B = t(v_{gx} - U)$ = upper bore lead.

Figure 6.2: Dual bore schematic depicting two airglow layers (OH at 87 km and OI (557.7 nm) at 96 km) situated between two critical layers at 80 km and 100 km. The distance between the two critical layers (~20 km) corresponds to the vertical wavelength of a tide. In this diagram, a gravity wave with vertical group velocity v_{gz}, and horizontal group velocity v_{gx} propagates from point A to point B, interacting with the two critical layers to form bores at both of these layers.

inversion creation, neither time nor the ability to propagate upwards through critical layers was an inhibiting factor. Sufficient time was available for a wave-induced change in R_i, decreasing stability in the lower critical layer rendering the region "transparent" to the waves. Now, for bore formation, we are tasked with generating concurrent bores with comparable amplitudes at the two MILs without the benefit of a "transparent" lower region. The gravity wave momentum flux divergence impinging on the lower MIL is now driving the "piston" to create the lower bore, but enough flux must still penetrate through the lower MIL to form a comparable upper bore. This scenario is plausible provided that the gravity wave source has gravity waves with sufficiently large vertical wavelengths with smaller amplitudes to enable them to penetrate to higher altitudes before saturating or dissipating [*Vadas and Fritts*, 2004; *Vadas*, 2006]. The 20 km

separation between the two critical layers includes about 3.3 scale heights, assuming a scale height of approximately 6 km. Given these conditions, the exponential decrease in density between the two critical levels is approximately 28, and thus the waves would grow by a factor of 28 as they ascend. To generate comparable bores, we require the momentum flux density at the two layers to be equal. For this reason, even if only $\frac{1}{28}^{th}$ of the flux were to penetrate through the lower layer, the acceleration in the upper layer to produce that bore would be the same as for the lower layer. Hence, even this small fraction of wave energy traversing upward is sufficient to create dual bores of comparable amplitude.

We now calculate the vertical and horizontal components of the group velocities of the gravity waves in order to compare the times and relative locations of the bore origins. With these starting points, we can estimate the relative displacements of the resulting bores and compare them to the observed lateral offset values. The horizontal group velocity is given by

$$v_{g_x} = \frac{\partial \omega}{\partial k_x}. \tag{6.1}$$

Using the dispersion relation for $\omega_i << \omega << N$ where ω_i is the inertial frequency [*Hines*, 1960],

$$\omega = \frac{N k_x}{\sqrt{k_x^2 + k_z^2}}, \tag{6.2}$$

one obtains

$$v_{g_x} = \frac{N k_z^2}{\left(k_x^2 + k_z^2\right)^{3/2}}. \tag{6.3}$$

Substituting $\omega \equiv 2\pi/\tau$, $N \equiv 2\pi/\tau_B$ into Eq. (6.2), where τ is the wave period and τ_B is the buoyancy period, and solving for k_z, we obtain

$$k_z^2 = k_x^2 \left[\left(\frac{\tau}{\tau_B} \right)^2 - 1 \right]. \tag{6.4}$$

Using this in Eq. (6.3) to eliminate k_z and using $k_x \equiv 2\pi/\lambda_x$, we obtain the horizontal group velocity,

$$v_{g_x} = \frac{\lambda_x}{\tau}\left[1 - \left(\frac{\tau_B}{\tau}\right)^2\right]. \tag{6.5}$$

Similarly, the vertical group velocity is

$$v_{g_z} = \left(\frac{-\lambda_x}{\tau}\right)\left(\frac{\tau_B}{\tau}\right)\sqrt{1 - \left(\frac{\tau_B}{\tau}\right)^2}. \tag{6.6}$$

The phase and group velocities are mutually orthogonal, and for present purposes, we can ignore the minus sign. For details, consult *Gill* [1982]. For modelling purposes, we assume that the bore velocities for the two cases (upper and lower) are similar and taken to be U. This assumption implies that the upper and lower inversion layer thicknesses are similar, and is in keeping with our goal of generating concurrent bores with comparable amplitudes. The observed values of U for the inverse events cited here are 39 m/s (6 March 1997 event over Puerto Rico) and 64 m/s (24 December 2000 event over Peru). The overall range of U for both standard and inverse bore events varies from 24 to 94 m/s as tabulated in Table 5.1, detailing sharp front observations.

Applying the gravity wave parameters modelled above to actual data, we now estimate the relative displacement of theoretical bores resulting from conditions observed in actual gravity wave sources. To provide characteristic gravity wave source data, we recall two observations of thunderstorm-generated gravity waves described in *Dewan et al.* [1998]. The two observed thunderstorms occurred on 2 October 1996 and 13 November 1996. The parameters of these waves will be used to explore possible dual-bore manifestations. First, we consider the 2 October 1996 thunderstorm event. The parameters for that event were $\lambda_x = 50$ km and $\tau = 15$ min. We take the buoyancy period to be $\tau_B = 5$ min. Using these values in Eqs. (6.5) and (6.6) we obtain $v_{g_x} = 49.4$ m/s or about

50 m/s and v_{g_z} = 17.5 m/s. Similarly, for the 13 November 1996 thunderstorm, λ_x = 25 km and τ = 9 min; this leads to v_{g_x} = 32 m/s and v_{g_z} = 21 m/s.

With these values, we now estimate the resulting relative *horizontal* displacement between two theoretical bores (upper and lower) for each of these two representative thunderstorm occurrences. Figure 6.2 depicts two inversion layers separated vertically by 20 km. Let A be the location where the gravity waves intersect the lower layer, and let B be the location where the same waves intersect the upper layer at a later time. Note that, in reality, the wave field covers a very large horizontal area; points A and B must refer to certain selected representative waves within the larger wave field. We begin by calculating the time needed for the gravity wave to travel the distance D between the two layers (D = 20 km), given by

$$t = \frac{D}{v_{g_z}}. \tag{6.7}$$

During that time the gravity waves would also travel a horizontal distance and arrive at B. Letting that horizontal distance be d,

$$d = t * v_{g_x}. \tag{6.8}$$

Meanwhile, the lower bore would travel a horizontal distance,

$$d_B = t * U. \tag{6.9}$$

Therefore, the relative horizontal displacement between the upper and lower bores, d_{BB}, would be

$$d_{BB} = d - d_B = t(v_{g_x} - U). \tag{6.10}$$

For the 2 October 1996 thunderstorm event, by using Eq. (6.7), noting that v_{g_z} = 17.5 m/s, and considering the full range of observed bore velocities from Table 5.1, we find that t = 18.5 min and $d_{BB} \doteq -49$ km to 29 km. Reducing

this range to consider only the values of observed *inverse* bore velocities, we calculate $d_{BB} \doteq -16$ km to 12 km. Therefore, the upper bore could *lead* the lower bore by approximately 16 km, or *lag* the lower bore by approximately 12 km. In the case of the thunderstorm which occurred on 13 November 1996, we find that $t = 15.9$ min and $d_{BB} \doteq -60$ km to 8 km for the full range of U. Limiting the velocity range once again to inverse bore observations only, we calculate $d_{BB} \doteq -31$ km to -7 km. This is similar to the conditions observed for the inverse bores where the upper front lagged the lower by approximately $4 - 8$ km. Since the observed values for d_{BB} are in reasonable agreement with our example calculations, we believe that the existence of dual bores could be explained in the context of the models in *Dewan and Picard* [1998]. Interestingly, the observations of *Dao et al.* [1995], shown here in Figure 6.1, suggest that with the influence of the tides, even triple bores may be possible.

6.3 Comparison to Nonlinear Theory and Simulations

Seyler [2005] has developed a nonlinear theory for mesospheric bores which we now compare to our observations. This work further develops the original symmetric bore theory for stratified bores in the stably stratified mesosphere put forth by *Dewan and Picard* [1998]. A simplified form of the incompressible, hydrostatic, gravity-wave equations are first presented as the basic model. Applying the Boussinesq approximation reduces this model to numerically solvable equations for vorticity and potential temperature:

$$\partial_t \nabla_\perp^2 \psi + [\psi, \nabla_\perp^2 \psi] = -\frac{g}{\bar{\theta}} \partial_x \theta'. \tag{6.11}$$

$$\partial_x \theta' + [\psi, \theta'] = -\frac{d\bar{\theta}}{dz} \partial_x \psi. \tag{6.12}$$

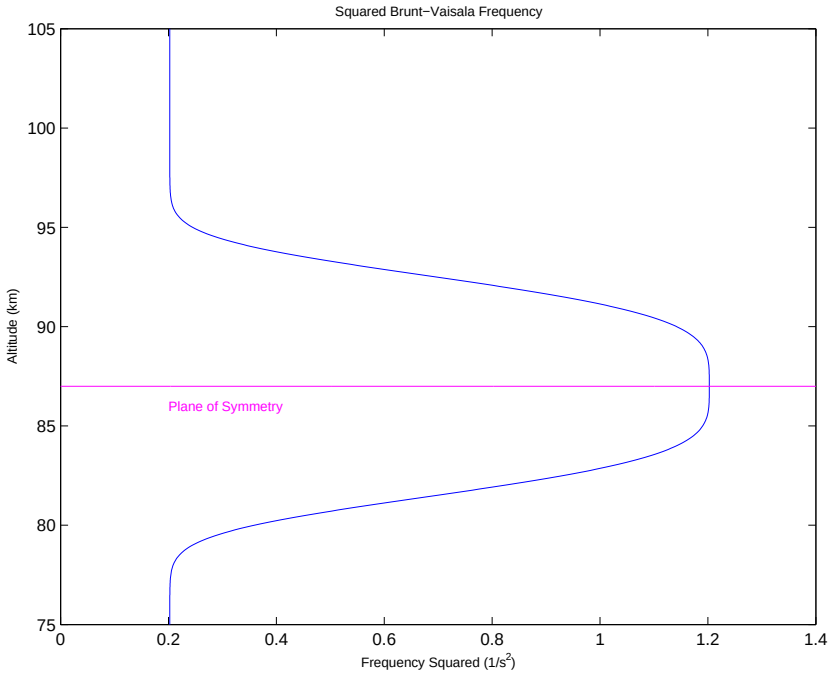

Figure 6.3: Smooth Brunt-Väisälä profile used in numerical solutions to nonlinear theory [*Seyler*, 2005].

where ψ is the velocity stream function, g is gravity, and θ is the potential temperature which can be written as $\theta = \overline{\theta}(z) + \theta'$, that is, the basic equilibrium state profile plus the relative potential temperature perturbation. Note $\nabla_\perp^2 = \partial_x^2 + \partial_y^2$; and $[A, B] = \partial_x A \partial_z B - \partial_z B \partial_x A$ is the Jacobian or Poisson bracket.

In order to understand the propagation characteristics and mode structure of mesospheric bores, this model is extended to the linear theory of gravity waves trapped in thermal inversion layers for an analytically solvable layer represented by a sharp Brunt-Väisälä profile. The resulting eigenvalue problem of *Seyler* [2005] is then

$$\frac{d^2\psi_1}{dz^2} + k^2\left(\frac{N^2}{\omega^2} - 1\right)\psi_1 = 0. \tag{6.13}$$

where perturbation space and time variations of the stream function are given as $\psi_1(z)exp(ikx - i\omega t)$.

Two-dimensional numerical simulations are developed from a dimensionless model considered in a smoothed buoyancy-frequency atmospheric profile given by $N^2(z) = \delta^2 + exp(-z^4)$, where $\delta = N_1/N_0$, as depicted in Figure 6.3. The non-dimensional model is represented as

$$\partial_t \nabla_\perp^2 \psi + [\psi, \nabla_\perp^2 \psi] = -\partial_x \theta + \mu \nabla_\perp^4 \psi. \tag{6.14}$$

$$\partial_x \theta + [\psi, \theta] = N^2(z) \partial_x \psi. \tag{6.15}$$

where the dimensionless parameters are: ψ, the velocity stream function; θ, the potential temperature; μ, the kinematic molecular viscosity; and N, the Brunt-Väisälä frequency.

Results from this reduced set of dimensionless parameters using initial conditions leading to bore formation are then compared to the existing data. Reverting back to physical space and time, the solutions found for the number of peaks, wavelength, bore formation time, and phase speed are consistent with both the observations and the values predicted by *Dewan and Picard* [1998], as tabulated in Table 5.3. Offering another way of looking at mesospheric bores, this nonlinear analysis concurs with the notion of *Dewan and Picard* [1998] that mesospheric bores are likely nonlinear structures propagating within an inversion layer.

In addition to the observed and the predicted bore characteristics noted above to concur, the numerical simulations address a number of other features observed in the bore image data, including persistence of an initial low frequency gravity wave, separation of bore peaks, and the inverse complementarity feature distinguishing the inverse bore phenomenon.

Results from several simulation runs show the persistence of the initial low

frequency wave and the effect of this wave superimposed with the crests of the bore. This superposition can manifest itself by lowering the amplitude of the leading peak with respect to successive peaks. The naked-eye bore event from 14 November 1999 [*Smith et al.*, 2003] provides a good example of this persistent low frequency wave. Evidence of the initial low frequency gravity wave can still be seen in the naked-eye bore observation even one to two hours after initial development of the bore. Again in the 6 January 1997 event over Puerto Rico, we see that the leading edge of the sharp front does not always correspond to the highest amplitude peak with respect to intensity. In Figure 5.4 from Chapter 5, the plot of relative intensity versus position taken normal to the wavefront for the OH emission layer in this event from Puerto Rico, shows the first two bright intensity peaks to be very close in amplitude; the second peak is actually larger. From the simulations, these large low frequency waves emerge initially from the interaction within a MIL of both upward and downward obliquely propagating gravity waves; the result is a ducted low frequency wave which further develops into the bore. This requirement for merging upward and downward obliquely propagating gravity waves to exist for bore formation to occur could have an impact on the distance a bore may form from the gravity wave source(s).

A property of the basic model is that the separation between successive peaks is constant [*Dewan and Picard*, 1998], whereas the nonlinear simulations show that separation between peaks actually can increase with time [*Seyler*, 2005]. In the simulations, the bore crest speed is dependent on amplitude and, from the leading edge, each successive peak has decreasing amplitude. This phenomenon is illustrated in the naked-eye bore [*Smith et al.*, 2003] in which the leading wavefronts travel faster than the trailing fronts. By comparing the

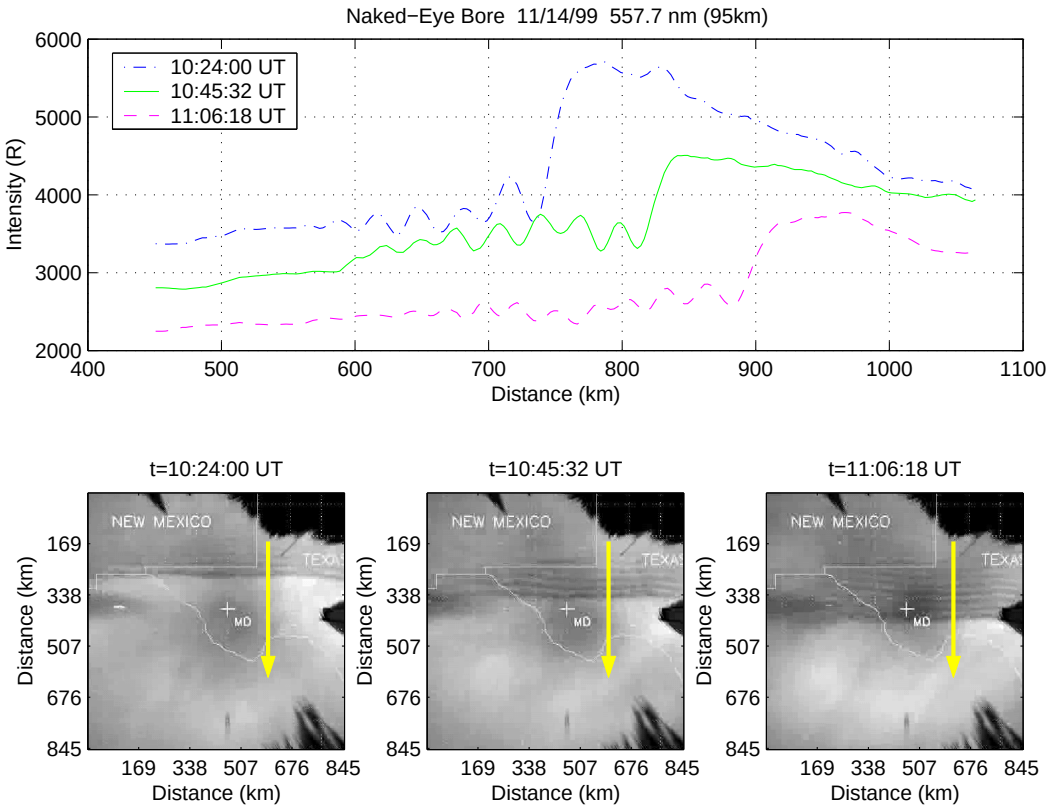

Figure 6.4: A series of three 557.7-nm (OI) intensity scan lines for the naked-eye bore event on 14 November 1999 over McDonald Observatory (MDO), TX. The scan lines show brightness variation perpendicular to the wavefront as indicated by the arrows in the corresponding unwarped images below the plot. Comparing the first three peaks for 10:45:32 UT and 11:06:18 UT shows separation between peaks increases with time. Separation between successive peaks at a given time can be seen in the 10:24:00 UT time slice; i.e. the distance between the first and second peaks is larger than the distance between the second and third peaks in this time slice. (Adapted from *Smith et al.* [2003].)

first three peaks in intensity scan lines taken perpendicular to the front at time 10:53:40 UT with the same data at time 11:33:58 UT, we can show that the peak separation has increased by the second time slice (see Figure 6.4). This event also shows clear evidence of the variable separation between sets of successive crests at a given time, as shown in the intensity plot from 10:24:00 UT in Figure 6.4. While this feature is clearly evident in the naked-eye bore, most analyzed bore events indicate little to no separation and appear to contradict the simulations at

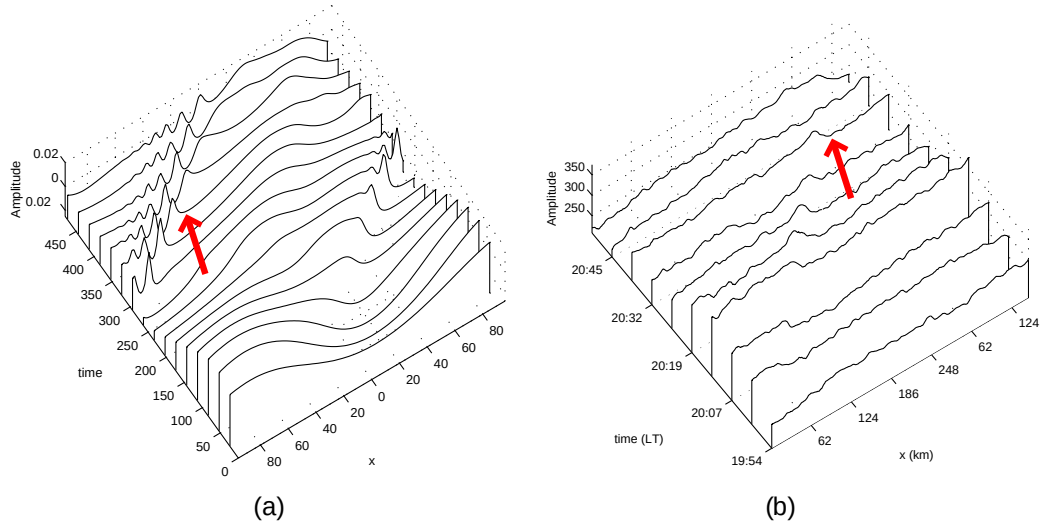

Figure 6.5: (a) Inverse bore simulation: Averaged potential temperature above the center of the simulation for the following parameters: $L_x = 50$, $d = 2\pi$, $\mu = 0.001$, $N_0 = 1$, $h = 1$, $N_1 = 0.1$, and $A = 0.25$. (Adapted from *Seyler* [2005].) (b) Inverse bore data: Relative intensity versus position over time for a scan line normal to the wavefront of the 24 December 2000 bore event from Peru. Scan lines shown are for the 557.7-nm (OI) emission. Notice the decrease in intensity indicated by the arrows just ahead of the bore in both the data and the simulation.

late times. *Seyler* [2005] found the rate of peak separation to be very dependent on initial conditions, particularly the leading edge amplitude. With low amplitude initial conditions, the rate of peak separation in simulations was found to be slow during the typical bore observation period of about two hours. By contrast, the naked-eye bore was observed over twice this duration (5.5 hrs), and the zenith emission intensity more than doubled as the bore passed overhead [*Smith et al.*, 2003]. These two features, added to the fact that this is the only documented bore event known to be visible to the naked-eye, support the fact that this event had an atypically large amplitude consistent with predicted late-time peak separation [*Seyler*, 2005].

Two-dimensional numerical simulations offer a two-node vertical eigenfunction solution which might provide an alternate explanation for the "in-

verse" complementarity observed in two of the bore events documented in Sections 5.3.0.11–5.3.0.12. Plots of this solution (see Figure 6.5) bear a striking resemblance to inverse bore observations. In Figure 6.5, a waterfall plot showing relative intensity variation normal to the bore wavefront over time for the 557.7-nm (OI) layer of the 24 December 2000 event is shown opposite to the simulation results. Note the decrease in intensity just prior to the first jump in intensity at the leading edge of the bore; this intensity dip is effectively reproduced in the simulation. With this proposed two-node explanation, an inverse bore could form and develop with the existence of only *one* inversion layer, as compared to the dual bore theory, which requires *two* critical layers with corresponding resultant inversion layers. The original symmetric bore theory precluded the formation of an inverse bore, which required sinking flow above the centerline with corresponding rising flow below the centerline in this scenario [*Dewan and Picard*, 1998]. However, the nonlinear simulations based on one MIL do not account for the lateral offset between inverse bore fronts at different altitudes.

6.4 Conclusion

In this chapter we addressed new sharp airglow front observations, some of which appear to confound classical theory. We extended the basic symmetric bore theory of *Dewan and Picard* [2001], proposing here the possibility of multiple bores to explain the inverse intensity relationship exhibited by some of the new bore events. A paper by *Seyler* [2005] offers an alternate theory against which we also compare the data. These comparisons show that some features in the data, such as the separation between small-scale wave peaks, are characterized by the nonlinear theory proposed by *Seyler* [2005], while other fea-

tures, such as the phase shift between emission layers, are best described by the dual-bore theory. If, however, there is essentially no horizontal phase difference found in further analysis of inverse bore events, there would no longer be a need to postulate two bores. In this case, a simpler explanation, such as that of *Seyler* [2005] requiring only one inversion layer, might predominate. A thorough examination of the lateral offset measurement emerges as a crucial property for understanding inverse bore phenomena.

CHAPTER 7

FUTURE RESEARCH

Sharp airglow fronts, the intriguing mesospheric phenomenon described in this study, were once thought to be extremely rare. In recent years, thanks in part to this research, many examples have now been observed by imaging systems at a number of locales. With the initiation of the jointly sponsored NSF/AFOSR Maui-Mesosphere And Lower Thermosphere (Maui-MALT) campaign in late 2001, many of these events have been captured above the Hawaiian Islands where the first spectacular event was observed during the Airborne Lidar and Observations of Hawaiian Airglow (ALOHA-93) campaign of 1993. While this first event was characterized by small-scale waves tracking behind the sharp onset of a large-scale front, some new observations exhibit variations from this classic example. This ever-increasing dataset of sharp airglow fronts with diversified "bore-like" features offers a wealth of information against which to test existing theories, such as those pioneered by *Dewan and Picard* [1998] as well as those developed and presented here. The expanded dataset also affords theorists the opportunity to develop new models.

7.1 Planned Postdoctoral Research Study

A planned post-doctoral fellowship, funded by the National Science Foundation, is scheduled to continue the research effort aimed at deciphering the enigmatic sharp-front events. The goal of the proposed investigation is to perform a multi-faceted study of the various mesospheric bore phenomena, combining analysis of multiple layer airglow observations with modelling in order to evaluate existing theories. The project includes data analysis from multiple instru-

ments, including airglow imagers, lidar, and meteor radar which are currently participating in the CEDAR-supported Maui-MALT campaign.

The proposed definitive bore study would employ a 4-part approach:

(1.) Analyze data from multiple instruments, and use it to compare existing theories. As was shown in the airglow images, the characteristics of the bore structures vary in different airglow layers implying that the vertical dimension of the bore structures differs with altitude. While our observations continue to be made over multiple airglow layers, which provides us with the basic information necessary to determine the apparent location of a bore, to take full advantage of the imager data, supporting instrumentation is highly desirable. We propose to analyze concurrent airglow images with vertical temperature and wind profiles from lidar and/or MF radar, to look for correlation between mesospheric bores and corresponding thermal inversion layers or wind shears, both of which might act as a guiding feature for bore propagation. This correlative information would be used to compare competing bore theories. In particular, we would like to evaluate inverse bore theories which propose one or two inversion layers to explain the inverted contrast feature seen in the airglow images. To gain information on potential coupling effects between atmospheric layers, weather archives could be checked for associated tropospheric fronts.

(2.) Model airglow response using 2-D chemistry and 2-D time-dependent dynamics models, and compare to existing theories. Hickey et al. have developed a full-wave model that can simulate a linear time-dependent wave packet [*Hickey et al.*, 1997, 1998]. Using this model in conjunction with their 2-D chemistry model to explore the airglow response to ducted gravity waves, we may investigate the airglow observations, and consider Seyler's theory of obliquely

propagating gravity waves (which become ducted to generate bores), as well as other theories for upwardly propagating gravity waves sourcing mesospheric bores. The coupling relationships these internal bores may have both geographically with respect to ducting effects and vertically through potential gravity wave sourcing from atmospheric layers both above and below the mesosphere could well affect the energetics of the region.

(3.) Analyze new bore events, including bore trains and crossing bores. Still more examples of mesospheric bores with astounding new features exist in the current database. Recent airglow observations show internal undular bores at mesospheric altitudes appearing to occur in succession one after another, as if in a train. Other observations show bores entering the field of view of the imager from nearly opposing azimuths and propagating obliquely, crossing overhead at zenith, and continuing to propagate out of the field of view. These types of events have not been documented in the literature, and appear rare in our airglow image databases prior to 2000.

(4.) Continue to maintain airglow database for bore analysis. In order to facilitate the bore analysis, we must maintain and process the airglow database to find bore events. Quantitative analysis of this database includes preprocessing (subtraction of background signal, star removal, flat-fielding, geographic projection, etc.) and determination of azimuthal propagation direction, apparent velocity, horizontal wavelength, etc.

7.2 Concluding Remarks

In addition to the specifics outlined above in the planned postdoc research, other project opportunities abound. We have focused primarily on the sharp-front events in the airglow imager datasets discussed. These datasets are also rich with other phenomena to analyze, both already identified and as-yet undiscovered. Additionally, these datasets – even coupled with the data available in the larger airglow science community – represent only a very limited geographic scope of the big picture. Expanding this coverage through future multi-instrument campaigns set in untapped regions of the world would help address questions regarding the morphology and dynamics of these sharp-front events, their effects on the background flow, and their relationship through sourcing and energy deposition on other regions.

Developing and applying new techniques to analyze the data would also be a challenging and beneficial project. Further refining and automating the existing techniques would provide valuable tools to speed and to improve the analysis. While the GUI software for operating the imager system and for basic pre-processing analysis exists from previous graduate student efforts, most of the parametric processing of images for particular events is still performed by developing Matlab code as-needed. Folding these many routines into an expanded GUI version would pose a challenging, but highly beneficial, project. Since the contrast is extremely low in much of our data, determining and incorporating any techniques – in addition to the ones already employed – to enhance contrast would be invaluable. While some research groups use keograms and difference images for this purpose, these techniques can mask some parametric data, and have not been preferred at Cornell. Although not specifically

presented in this dissertation write-up, many 2-D and 3-D signal processing techniques have been applied in the analysis of the sharp-front images. Many more are left to try! The effort to model sharp fronts is just taking off, with many opportunities unfolding to describe these events.

The calibration effort for this study required quite a bit of programming, and was implemented through a series of interconnected Matlab functions. Developing a GUI version of this overall process would preclude many "reinventions of the wheel", and provide a valuable service to the airglow imager community as a whole!

APPENDIX A

CONTEXTUAL PERSPECTIVE

A.1 Environmental Context

The geophysical phenomena studied in this graduate research take place in the lower region of the ionosphere within the upper terrestrial atmosphere. The ionosphere can be described by several classification systems, each based on variable parameters of the vertical structure of the atmosphere. Some of the classification conventions for these atmospheric layers are based on specifications such as: composition of constituent particles, diffusive stratification versus mixing, density of electrons, and temperature structure. Given all this, a fundamental understanding of the environmental context of the atmosphere as a whole is warranted. We take the perspective of looking outward from the surface of the Earth. Figure A.1 illustrates the location of, and relationship between, atmospheric layers based on vertical profiles of temperature and density. Note that these vertical profiles hold for all geographical regions, even though different physical processes dominate at different latitudes. The lowest layer of the atmosphere is the *troposphere*, which starts at the Earth's surface and extends upward a mere 10 km – only 0.16% of the radius of the Earth! This tiny, fragile shell houses the air we breathe and our "ordinary" atmospheric weather. Situated just above the troposphere and extending up to 45 km is the other commonly, well-known layer of the atmosphere – the *stratosphere* – home of the ozone layer, the onus of its recent claim to fame. One primary distinction between these first two layers is temperature variation. The temperature decreases with height from the surface of the Earth until it reaches a local minimum at a

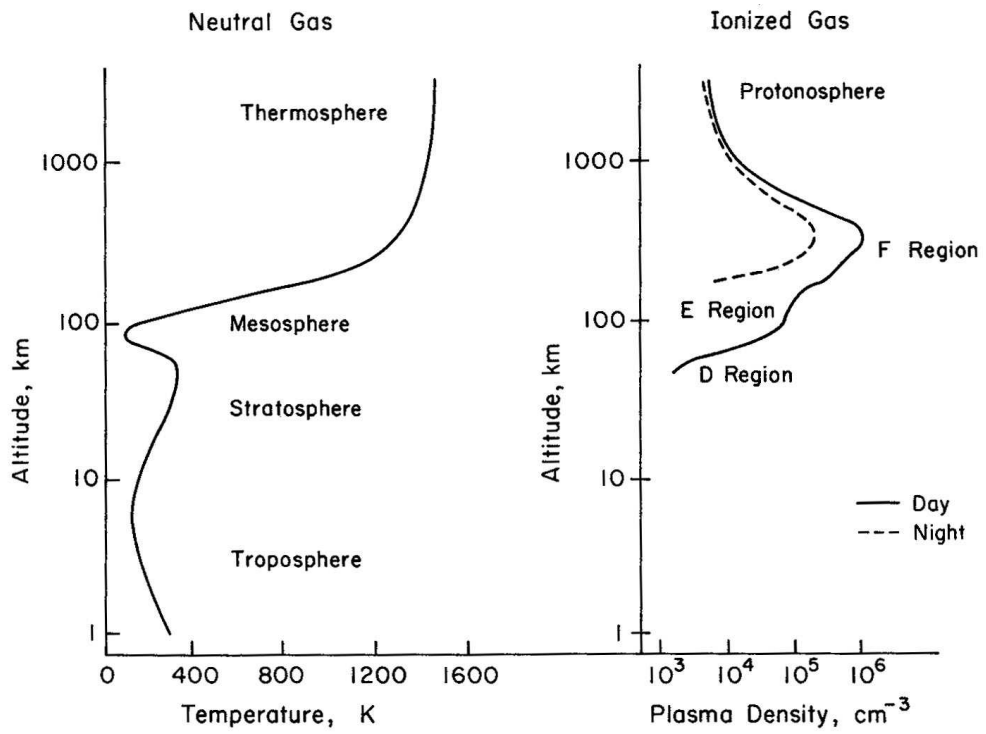

Figure A.1: Temperature and density profile of the atmosphere of the Earth. (Figure courtesy of M.C. Kelley, Cornell University.)

boundary termed the *tropopause*. Above this boundary in the stratosphere, the temperature increases until a local maximum is reached at the next boundary, termed the *stratopause*. The next layer encountered – the *mesosphere* – is the primary target region for the focus of this dissertation. The mesosphere extends from 45 km up to 95 km where the *mesopause* occurs, having the highly unique distinction of being the coldest region of the entire atmosphere – in fact, in the entire terrestrial environment! This region is home to shooting stars which, in reality, are meteors seen streaking across the nighttime sky. The mesosphere is a fascinatingly interesting region of transition. The *ionosphere*, the ionized portion of the atmosphere, begins in the mesospheric region at about 60 km where the ionized gases begin to overtake the neutrals. Above the mesopause, the temperature increases yet again, finally levelling off to the overall maximum which

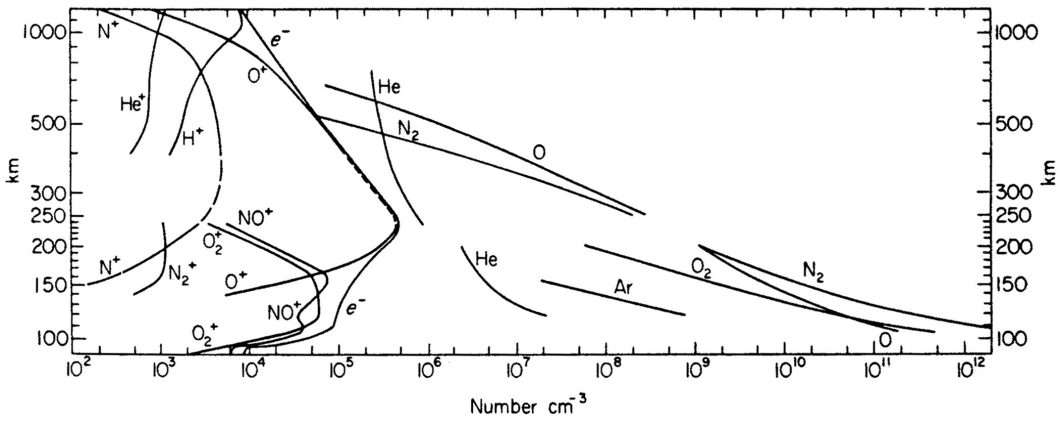

Figure A.2: Number density profile of the ionosphere of the Earth. (Figure courtesy of M.C. Kelley, Cornell University.)

then holds constant with height. This hottest region of the atmosphere, extending from about 95 km up to 500 km, is rightly termed the *thermosphere*.

The neutral composition of the entire atmospheric region is for the most part horizontally stratified; the ionized composition, that is, the plasma, typically is not. The lower portion of the terrestrial atmosphere, i.e., the neutral atmosphere, is restricted to neutral gases only, and includes both the troposphere and stratosphere. Above this altitude, beginning in the mesosphere, we move into the ionosphere, comprised of both neutral and ionized gases and characterized by the collective number density profile of its constituents, which are illustrated in Figure A.2. Below 100 km, turbulence mixes the atmospheric constituents; this region dominated by mixing is called the *homosphere*. Above 125 km, molecular diffusion prevails; this resulting stratified region is called the *heterosphere*. Whereas in the past there was thought to be a sharp boundary, called the homopause or turbopause, separating the regions, now the consensus is that a transition region exists where both processes are significant. Once again we find the region of transition to reside in the mesosphere.

As stated above, an important feature of the ionosphere from about 100 km on up is that, due to diffusive stratification, the composition changes with altitude. This variation controls the types of and rates at which chemical reactions occur, which in turn affects the resultant density profile. The lower portions of the ionosphere, from about 60 to 150 km (termed the D and E regions), are comprised of mostly molecular ions; N_2, O_2, and O are the most abundant neutral species; and chemical processes are most important [*Schunk and Nagy*, 2000]. Characterizing the D region (60-100 km), specifically, are both positive and negative ions, water-cluster ions, and three-body chemical reactions. In the weakly-ionized E region (100-150 km), the chemical reactions become less complicated, and, with the neutral density still about 7 orders of magnitude greater than the total ion density, collisions between charged particles are not yet important. Contrasting the D and E regions of the ionosphere, the F region above contains mostly atomic ions. In the F1 region (150-250 km), ion-atom interchange and transport come into play. The peak ion density occurs in the F2 region at approximately 300 km; collisions involving charged particles must be taken into account here. The plasma in this region is considered partially-ionized as the neutral density is still 2 orders of magnitude greater than the total ion density.

One of the primary sources for the ions in these ionospheric regions is the absorption of extreme ultraviolet (EUV) radiation from the sun, which blasts the neutral atmosphere during the day. This process, called *photoionization*, absorbs the highly-energized incoming photons. The process can only extend down to about 90 km above the surface of the Earth before all the bombarding, highly-energetic photons are used up. At night the onslaught ceases, chemical recombination reactions take over, and vast differences emerge between the upper regions with atomic ions and the lower ionosphere with molecular ions. The

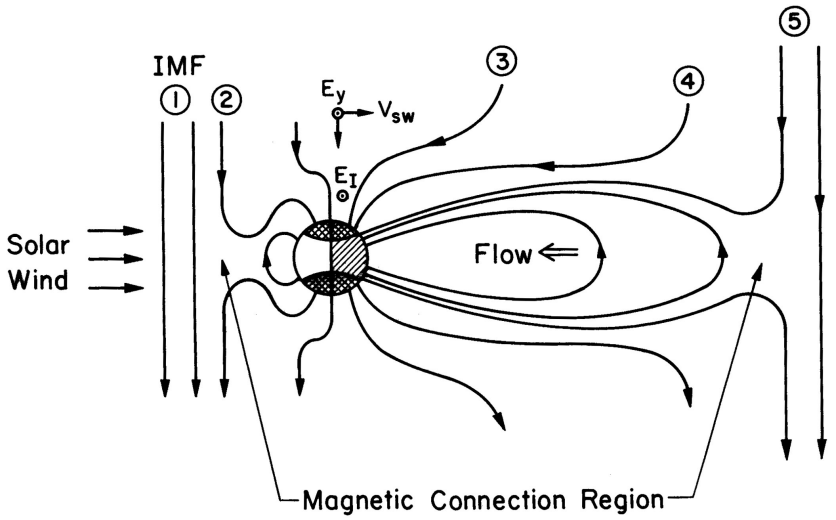

Figure A.3: Schematic diagram of the magnetic field lines of the Earth oriented as a result of interaction with the interplanetary magnetic field and solar wind. (Figure courtesy of M.C. Kelley, Cornell University.)

recombination rate for molecular ions is 1000× faster than that for atomic ions! The result is that while all the atomic ions above are working on recombining, the molecular ions below speedily recombine with electrons to form neutrals, thus eliminating the plasma concentration at these lower levels. The plasma density profile variation for the day and night is attributed to this effect.

To complete the environmental context of the upper atmosphere, we must incorporate the Earth's intrinsic magnetic field which, in turn, is enveloped in the interplanetary magnetic field (IMF) of the solar system which directs the solar wind. In reality, the resultant geometry resembles a comet, as illustrated in Figure A.3, with the magnetic field lines of the Earth shaped by their interaction with the supersonic solar wind. The solar wind is a fully-ionized plasma constantly flowing out from the sun and lambasting all in its path; this plasma is composed of hydrogen and helium which get hot enough to escape the Sun's gravitational attraction. Since collisionless plasmas such as the solar wind cannot readily flow across magnetic field lines, the Earth's strong, intrinsic mag-

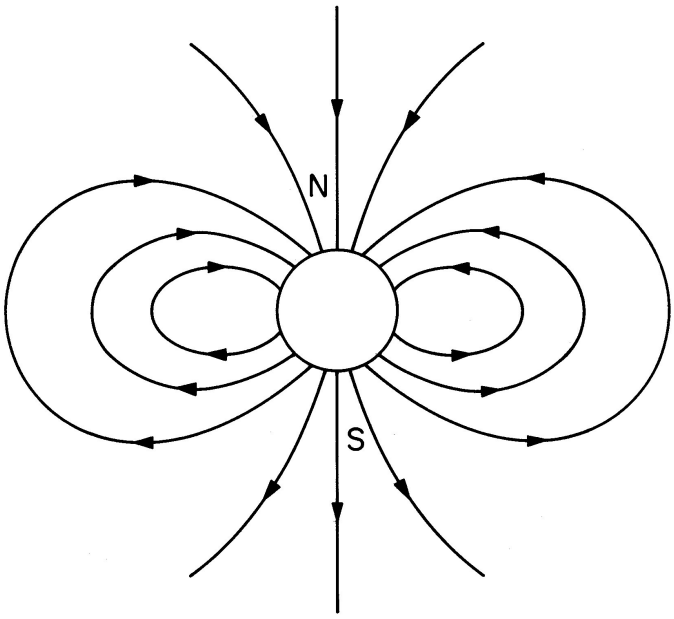

Figure A.4: Schematic diagram of the magnetic field lines of the Earth. At low latitude they can be approximated by a dipole. (Figure courtesy of M.C. Kelley, Cornell University.)

netic field deflects the bulk of the solar wind, creating a protective magnetic barrier around the Earth. This resultant magnetosphere and its coupling interaction with the ionosphere are the subjects of whole fields of study unto themselves. Fortunately, at ionospheric altitudes, the Earth's magnetic field can be approximated by a dipole, as shown in Figure A.4, which depicts a dipole in a hypothetical vacuum where the field lines are uniformly shaped in all directions and are symmetric about the magnetic axis. Note that, although not reflected in this simplified schematic, the dipole axis is actually tilted with respect to the Earth's spin axis by approximately 11 degrees. This feature is seen in many of the other planets with varying degrees of tilt. Currently in the history of our planet, the tilt is aimed approximately at North America. Some phenomena occurring at the magnetic equator follow the magnetic field lines, mapping along these field lines such that the phenomena can then be seen at mid-latitude regions almost a thousand kilometers away. This pronounced effect allows us

Figure A.5: The northern lights as viewed from the Poker Flat Research Range, Alaska. (Photograph courtesy of M.J. Nicolls, Cornell University.)

to study an equatorial phenomenon while operating imagers in mid-latitude regions. In the specific study of mesospheric bores covered in this dissertation, the environmental context is simplified with the primary focus restricted to neutral dynamics.

A.2 Historical Context

Events such as the one narrated at the opening, in Section 1.1, have been recorded in the scientific literature for over a decade. However, similarly intriguing events occurring in the ionosphere have been recorded throughout human history dating all the way back to Stone Age man's crude cave drawings resembling depictions of the northern lights, splendidly captured in present times through photographs (see Figure A.5). In a fascinating account, *Eather* [1980] traces the history of the aurora from the fearful descriptions spanning prehistoric times through ancient Chinese writings; Biblical references; early

civilizations' myths, folklore, and legends; and Greek philosophy; to the period of scientific inquiry beginning in the seventeenth century.

Schunk and Nagy [2000] expand the historical account of ionospheric research beyond the scope of the aurora, providing an interesting narrative of many of the central discoveries. Outside the aurora, the time-line of scientific inquiry begins with Galileo's discovery of sunspots in the early 17^{th} century, leading shortly to the realization that the Sun rotates, and centuries later to the determination of periodicity in the solar cycle. The first suggestion of the existence of an ionosphere came in the 19^{th} century with the hypothesis that electric currents in the atmosphere explained variations in the magnetic field at the Earth's surface, but it wasn't until the very early 20^{th} century that this notion of the existence of an ionosphere was clearly established – first, with the successful transmittance of radio signals across the Atlantic, followed by suggestions that these radio waves were reflected by upper atmospheric free electrons originating from solar radiation.

Rapid scientific growth finally ensued following World War II when, simultaneous with major advances in ground-based instrumentation, rocket technology became available allowing space-borne satellite studies. The International Geophysical Year (IGY), 1957 – 1958, organized to take advantage of the new capabilities, generated vast amounts of data and led to the birth of the field of solar-terrestrial physics. The field of ionospheric physics benefited from the new technologies as well, and continued to flourish as the general morphology of the upper atmosphere was studied with increasingly sophisticated models and a new proliferation of instruments. Study of the MLT region, however, remained somewhat of a challenge.

While balloons and high-altitude airplanes provide in-situ measurements of the lower atmosphere, they cannot reach up to the MLT. In contrast, satellite-borne instruments cannot penetrate down to the MLT. Sandwiched in between, the MLT remained relatively inaccessible due to instrument and cost constraints, with expensive, short-duration, rocket-borne experiments being the only in-situ option for the region. As a result, remote sensing of the MLT became a viable, even preferable, alternative; the post-IGY onslaught of instruments bolstered this approach. The suite of instruments included active-probing devices such as radars and lidars. Commensurate with the development effort, the second half of the 20th century saw the construction of the largest, most advanced instruments on the planet, such as the Arecibo radio telescope in Puerto Rico, dedicated to the study of the ionosphere.

Much smaller in physical stature, some of the suite of instruments, such as spectrometers and interferometers, advanced the passive study of the MLT. While all of these remote-sensing devices, both active-probes and passive-optical instruments, benefited the study of the MLT and provided limited spatial context through scanning techniques, their common disadvantage was their inability to provide spatial information on a broad scale. This broad spatial element was joined to the mix by a progression of instruments dedicated to imaging airglow – chemiluminescent light fortuitously concentrated in the MLT. The capability of these instruments improved from instantaneous photographs [*Peterson and Kieffaber*, 1973], to temporally-resolved low-light television images [*Crawford et al.*, 1975], and finally to highly-sensitive charge-coupled device (CCD) camera images which lent themselves to quantitative analysis. Airglow imagers and data collected by them are primary focuses of this dissertation.

Towards the end of the 20th century, the researchers pursuing upper atmospheric studies formalized their mission, organizing as a collective, coordinated body – the CEDAR scientific community – sponsored by the Aeronomy and Upper Atmospheric Facilities Programs of the National Science Foundation (NSF). CEDAR participants investigate the coupling, energetics, and dynamics of atmospheric regions, very often engaging in coordinated experimental and theoretical approaches involving collaborative efforts with other national and international research programs. From its early origins, the CEDAR program figured prominently into the UCAR (Universities Consortium for Atmospheric Research) long-range plan for the NSF atmospheric research programs [*CSSC*, 1987]. It is also part of the NSF Global Geosciences initiative that seeks to study the Earth and its environment as an integrated system of interrelated processes. In addition, CEDAR constitutes one element of the National Solar Terrestrial Program (NSTP) as defined by the National Academy of Sciences, filling the gap between and complementing several NASA (National Aeronautics and Space Administration) programs (GGS, ISTP, UARS), and providing an important ground-based and interpretive element to the national thrust of this initiative. The conviction of the CEDAR community to utilize and to develop various optical, radar, and theoretical techniques enabled important progress as the 20th century drew to a close, leading to the emergence of a more thorough understanding of ionospheric climatology.

Now as we embark at the dawn of the 21rst century, our focus turns to "space weather" as the space-physics community, building upon this firm foundation of scientific progress, endeavors to elucidate the nature of short-term ionospheric variability. While this spotlight on variability is perhaps an obvious next step in the evolution of our understanding of the ionosphere, it is also

very timely given the recent explosion in satellite communications and navigation systems. Our military's continued dependence on these systems, coupled with society's newfound reliance on satellite linkages, drives our need to understand the atmospheric disturbances which translate to satellite-system disruptions and outages. With severe space weather inarguably situated at the polar and equatorial regions, as illustrated by the turbulent flow, plasma instabilities, and the aforementioned northern lights occurring there, the mid-latitudes, housing the bulk of the world's population, were thought to be quiet regions sandwiched between. To the contrary, however, recent research has revealed the mid-latitudes to be quite active regions, both in terms of ionospheric phenomena such as mid-latitude spread-F and travelling ionospheric disturbances (TIDs), as well as neutral wave dynamics.

While the fantastic, visual light display of the aurora borealis – still marvelled at today – is understandably the most well-known and chronicled phenomenon from the ionospheric region, the depth and breadth of intriguing mysteries spawning from this active region are still growing today with new wonders unveiling themselves as our resources for exploring the upper atmosphere expand.

APPENDIX B

REMOTE POWER SWITCH OPERATIONS

B.1 Introduction

The RPS-10 remote AC power switch manufactured by Western Telematics, Inc. is used in conjunction with each of the Cornell imager systems to provide remote hard reboot capability for the camera equipment. The device is designed to remotely switch AC power on or off, or to initiate a toggle sequence with a user-defined delay period. It allows for PC Control of AC power, that is, the capability to switch any AC powered device on or off, using ASCII commands sent via modem or direct connection. The basic commands for operation of the RPS-10 device are rather cryptic, and not at all intuitive, so the key instructions are included in this appendix as reference. Also included in the sections to follow are brief descriptions of the device, installation or setup procedures, and a procedure to check for proper installation. The complete user's guide is currently available online at the Western Telematics, Inc. website: www.wti.com., specifically at the following location: http://www.wti.com/guides/rps10usr.pdf

The company's contact information is as follows:

Western Telematics, Inc.	(949) 586-9950
5 Sterling	Toll Free: 1-800-854-7226
Irvine, CA 92618	Fax: (949) 583-9514

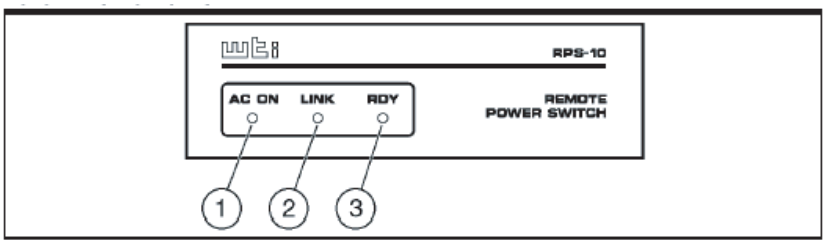

Figure B.1: Front panel of remote power switch, RPS-10, manufactured by Western Telematics, Inc.

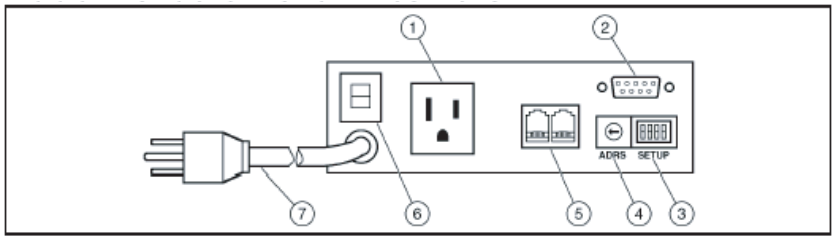

Figure B.2: Back panel of remote power switch, RPS-10, manufactured by Western Telematics, Inc.

B.2 Product Description

The front panel of the RPS-10 device is shown in Figure B.1. The panel indicator lights are described below:

1. AC ON: Lights when power to the Switched Outlet is ON.
2. LINK: Flashes when command data is received.
3. RDY: Lights when AC power is applied and the module is ready to receive commands. Does not indicate the ON/OFF condition of the Switched Outlet.

Similarly, the back panel of the RPS-10 device is illustrated in Figure B.2. Individual back panel components are identified below:

1. Switched AC Outlet
2. RS232 Control Port (Master Module Only)
3. SetUp Switches
4. Rotary Address Switch
5. RJ11 Link Ports
6. Circuit Breaker (RPS-10 = 10 Amps)
7. Power Cable

B.3 Installation

The RPS-10 is installed on each imager system as follows:

- The module address is set to '0'. As there is only one RPS-10 module per imager system, it serves as the "master" module. The RPS-10 devices have the capability to be expanded to provide control to up to 10 individual modules linked together. For our application, only one module or device is required for each imager system, and each is accessed individually.
- The setup switches on the back of the RPS-10 module are configured with all four switches in the "down" position. In this configuration, switch-1 Data Rate which controls the communication speed (baud rate) between the RPS-10M master module and ASCII control device (i.e. the host computer) is set to 9600 bps; switch-2 Toggle Rate which determines the length

of time power will remain OFF when a toggle sequence is initiated, is set to 5 sec; switch-3 Power-Up Default which determines how each switched outlet will react after an interruption in AC power is set to return the switched outlet, or terminal block, to the state that it was in prior to the power interruption; and switch-4 Spare has no effect.

- The PC is connected to the control port on the back panel of the RPS-10 module.
- The switched devices (the camera, the CEU, and the LCU) are all connected to a power strip which is then connected to the RPS-10 module's switched outlet (or terminal block).
- The RPS-10 module is connected to the AC power supply through a UPS device. Also connected to the UPS device is the monitor and harddrive for the computer.

B.4 Installation Verification Check

After installation, the following test should be performed to ensure the RPS-10 module is operating correctly.

1. Establish a connection with the RPS-10 module.
    - Direct Connect: Once a VNC connection is established, so that you are linked to the PC which is connected directly to the RPS-10 control port, start your terminal emulation software.
    - Make certain the terminal emulation software is set for the correct

baud rate to match the RPS-10 module (i.e. 9600 bps). Terminal emulation software should also be set for 8 bits, no parity.

2. After connection is established, tap the Space Bar several times. When the Space Bar is pressed, the LINK indicator on each RPS-10 Module should flash briefly. If the LINK indicator does not flash indicating that the Space characters have been received, refer to the users' manual for a list of items to check to verify proper installation.

B.5 Operation Procedures

Each RPS-10 module can be switched or toggled by an ASCII command string sent to the Master Module control port. The Control Device must send ASCII characters at the same data rate as the RPS-10 Module(s). The RPS-10 will accept any parity, but will always answer back at 8 bits, no parity. The command string consists of nine contiguous characters. The first six characters are ASCII control codes. These six characters constitute a "fixed password" that restricts access to the RPS-10. The seventh character is the address of the Module(s) that will receive the command, and the eighth character is the operation code. The last character in the command string is an ASCII Carriage Return (^M). The operation procedures are as follows:

1. Establish connection with the RPS-10M Master Module. If you are communicating via modem, the system will pause briefly while connecting, and then send the "RPS-10 READY" message. Currently our systems are set up to connect via a hyper-terminal connection (accessible either from a pre-established desktop icon or by selecting "All Programs →

Accessories → Communications → HyperTerminal") from the host computer after a VNC connection has been established.

2. Enter the desired ASCII command string. The command string uses the following format, described in detail below:

   ^B^X^X^B^X^Xac^M (^ = Control Code),

   where:

   - **^B^X^X^B^X^X** is the RPS-10's "fixed password".
   - **a** is the Module Address. This indicates the address of the module that will receive the command.
     - **a** = 0 – 9 indicates the address of the module that will receive the command.
     - **a** = * indicates that the command should be sent to all modules.
     - For our purposes with our current setup, **a** should remain set equal to 0 (zero).
   - **c** is the Operation Code. This indicates the task to be performed:
     - **c** = 0 Switch AC OFF - Instructs RPS-10 to switch OFF the Outlet for the selected Module(s)
     - **c** = 1 Switch AC ON - Instructs RPS-10 to switch ON the Outlet for the selected Module(s)
     - **c** = T Toggle AC (OFF - Delay - ON) - Instructs the RPS-10 to initiate a toggle sequence at the selected Module(s). Note that this command is case sensitive, and must always be entered as an upper case "T".
     - **c** = ? Read and Display Status - Instructs RPS-10 to display status of selected Module(s).

- **^M** Is the ASCII code for a carriage return.

3. Examples:

   - To toggle the Switched AC Outlet on the RPS-10 Module at Address "3", send the following command: **^B^X^X^B^X^X3T^M**
   - To set the Switched Outlet on the RPS-10 Module at Address "4" to the Off position, send the following command: **^B^X^X^B^X^X40^M**

4. After executing each command, the RPS-10 will send a "COMPLETE" message. Do not enter additional commands until the previous command is complete. When operating at 9600 bps, there will be a 0.5 second delay before the next command may be entered. At 2400 bps, there will be a 1.5 second delay.

APPENDIX C

FILTERS

C.1 Construction

The overall interference filter construction, as shown in Figure C.1, includes a multi-cavity bandpass filter and a multi-layer blocking filter sandwiched between two glass substrates, all held together by a protective metal ring. The bandpass functionality is achieved by a collection of structures, called "cavities", which comprise a multi-layer deposition of thin films on a single substrate. The number of cavities can vary, driven by the usual cost versus performance trade-off; Cornell filters, typically, have only about three cavities. In this trade-off scenario, as the number of cavities increases, the pass-band cut-off edges steepen (as shown in Figure C.2), but the cost increases. The design of each individual cavity is essentially a thin-film Fabry-Perot interferometer formed by vacuum deposition techniques, and consisting of two reflecting stacks separated by a spacer layer, as illustrated in Figure C.3.

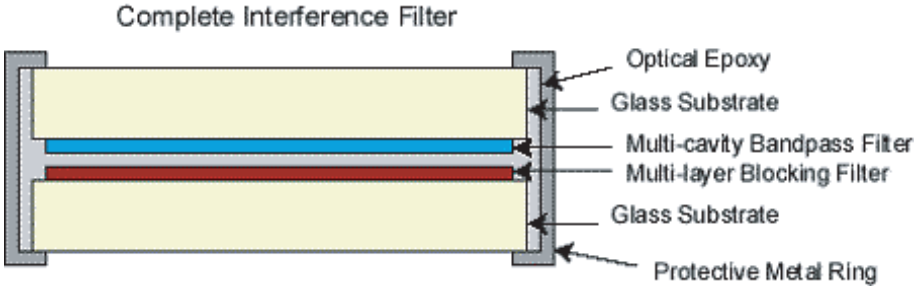

Figure C.1: Diagram of a complete interference filter illustrating the overall design in which the blocking layers and bandpass layers are held together in a protective metal case using optical epoxy. (From *C&L-Instruments*)

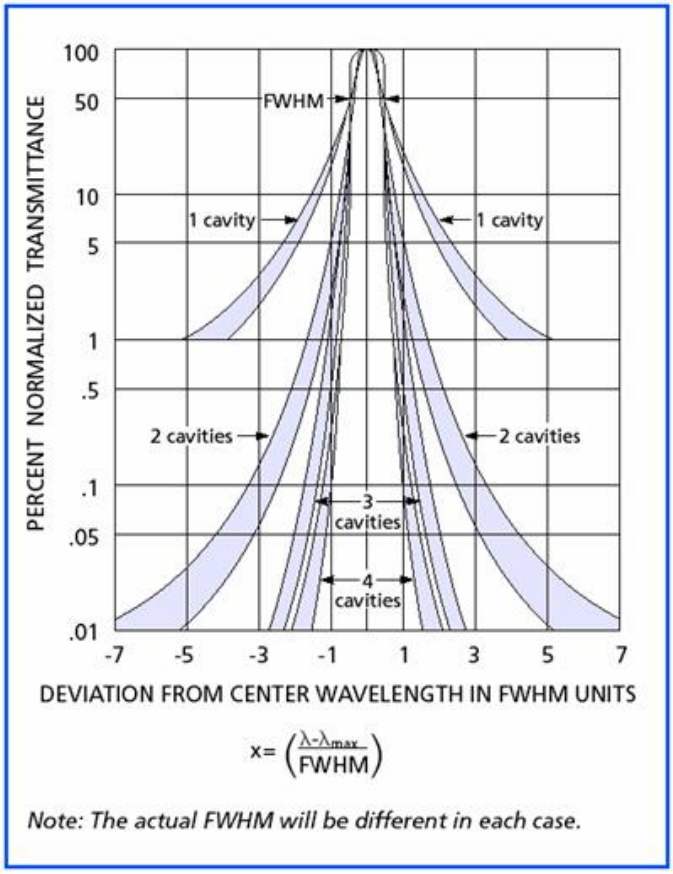

Figure C.2: Normalized log scale transmittance curves for zinc sulfide (ZnS)/cyolite (Na_3AlF_6) bandpass interference filters of 10-nm FWHM as functions of the number of cavities used in the filter construction. The graph gives a qualitative comparison depicting the improvement in performance with an increasing number of cavities incorporated into the construction process. (From *Melles Griot*).

C.2 Design

Delving further and considering the basic building blocks of the cavity, itself, we find the multi-layer thin films – usually composed of metals and dielectric materials such as magnesium fluoride (MgF_2), zinc sulfide (ZnS), or cryolite, each with unique refractive index properties – are deposited to create very precise optical depths, or thicknesses, which control and modify the reflection and

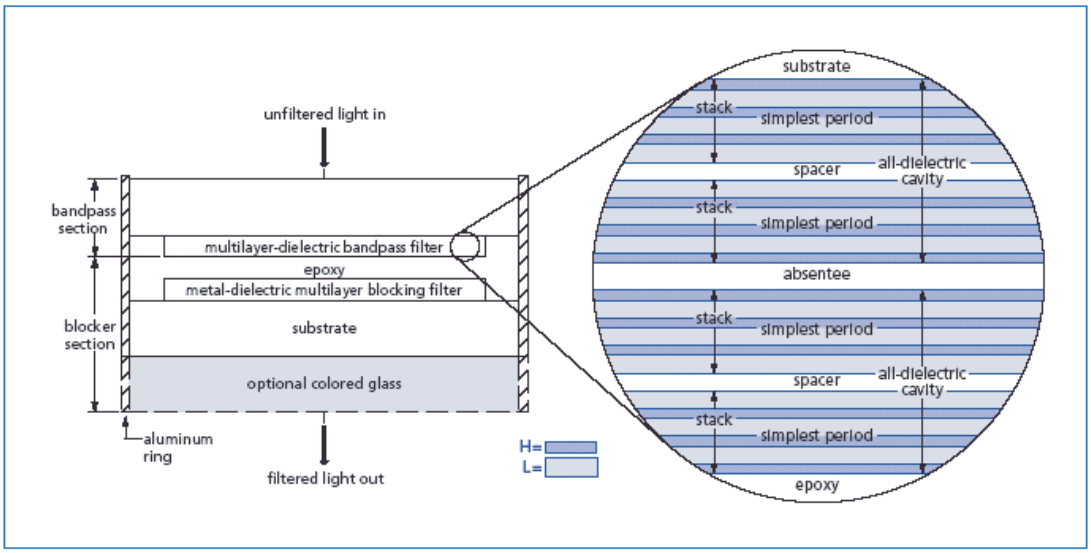

Figure C.3: Cross-section of a typical 2-cavity pass interference filter. (From *Melles Griot*).

transmission characteristics of the surface. For example, given a single layer film with a typical optical thickness of one-quarter wavelength and light entering the film at normal incidence, the wave reflected from the second surface of the film is exactly one-half wave out of phase with the light reflected from the first surface. The result is destructive interference – the filter's namesake. If, additionally, the amplitudes reflected at both surfaces are equal, then complete cancellation occurs, no light is reflected, and all the incident energy is transmitted, forming the basis of the universally-used "quarter-wave" low-reflection coating. Applying suitable combinations of optical coatings of different indices and thickness allows the creation of a variety of transmission effects – bandpass filters being one example. Once the functionality has been designed based on the particular film combination producing the desired characteristics, the target wavelength region can be changed by modifying all the film thicknesses in proportion. The crux to digest from this overview of filter construction is that since the characteristics of interference filters depend on the thickness of the layers, the filter characteristics will change as the distance that incoming rays travel

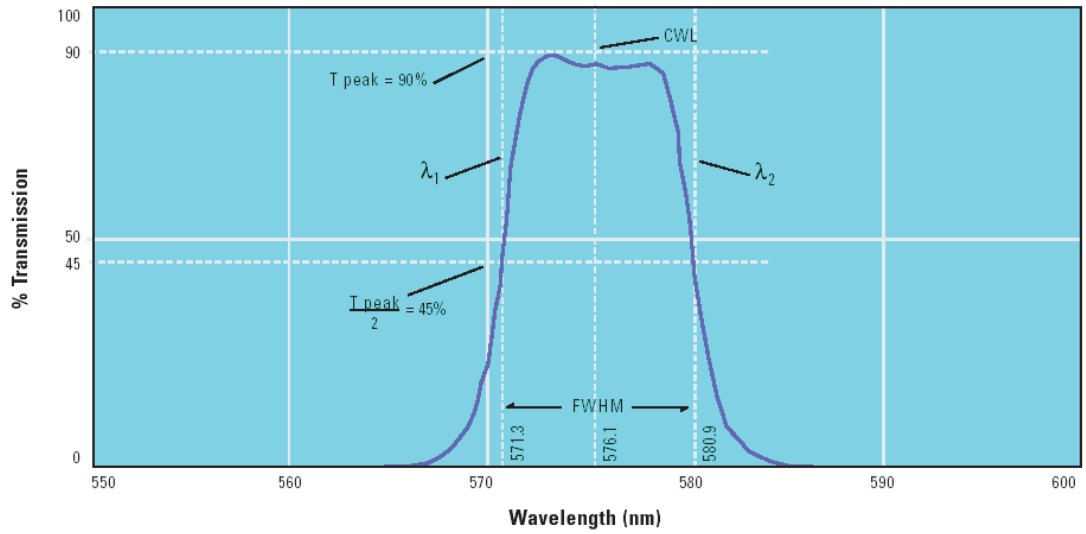

Figure C.4: The characteristic curve of a bandpass filter that was manufactured by depositing alternating layers of zinc sulfide and cryolite on a glass substrate according to a 3-cavity Fabry-Perot interferometric design. The CWL of the filter is located at 576.1 nm; the FWHM is located at 9.6 nm. (From *Omega* [2006])

through the filter material vary as a result of changes in the angle of incidence of incoming radiation.

C.3 Performance

The performance features of each filter are described by a characteristic curve; Figure C.4 illustrates the spectral performance of a 3-cavity bandpass filter. Three features used to identify bandpass filters are center wavelength (CWL $\equiv \frac{\lambda_1+\lambda_2}{2}$); full width at half maximum transmission (FWHM $\equiv \lambda_2 - \lambda_1$), which characterizes the width of the passband; and peak transmission (%T). Table C.1 indicates key parameters for the filters commonly used throughout our ionospheric studies.

Several factors are known to have considerable effect on the performance of

Table C.1: Parameters of interference filters typically used by the upper atmospheric science community. Cornell imagers operate using all but the $O_2(0,1)$ filter. Note that all the filters are narrow-band, except for the broadband OH which differs both in bandwidth and required integration time. More details (such as percent transmission, CWL, and identifying lot numbers) on the filters owned and operated by Cornell are given in Table F.1.

Filter	Wavelength λ_c (nm)	Bandwidth FWHM (nm)	Integration Time (sec)	Altitude (km)	Name	Application
BGND	541.0	2.0-2.2	90		Background	Subtract background sky emissions
OI [1]	557.7	2.0	90	96	Greenline	Mesospheric studies Equatorial spread-F
Na	589.0	5.0	90	90	Sodium	Mesospheric studies Meteor trail studies
$O(^1D)$ [2]	630.0	2.0	90	250-300	Redline [3]	Thermospheric studies Equatorial spread-F
NIR	777.4	2.0	90		Near IR	Thermospheric studies Equatorial spread-F
$O_2(0,1)$ [4]	865.5	12.0	90	94	NIR O_2	Mesospheric studies
OH [5]	871-895 [6]	23.8	8	87	Hydroxyl	Mesospheric studies

[1] also referred to as: $O(^1S)$, or $[OI_{32}]$.
[2] also referred to as $[OI_{21}]$
[3] also referred to as oxygen Redline.
[4] not monitored by Cornell University.
[5] also referred to as OH Meinel Bands, or NIR OH.
[6] with a notch at 865 nm to suppress the $O_2(0,1)$ emission.

interference filters, and, as such, should be considered when selecting or specifying bandpass filters to order. These factors include: degradation over time, exposure to the elements (temperature, humidity, light), and inherent optical path geometry (specifically, angle of incidence of incoming light). Although none of the Cornell filters have been replaced due to aging effects, it is important to keep in mind that filter performance – particularly for narrow-band filters – is subject to degradation over time resulting primarily in a blue shift of the center wavelength of the filter. To prevent drift of peak wavelength with age, bandpass filters are stabilized during manufacturing by a curing process of repeated, short duration, heat cycling at moderately high temperatures. To safeguard against damage resulting from rough handling and moisture penetration, each filter is hermetically sealed and mounted in a protective aluminum ring. However, even with this construction, the manufacturers advise against prolonged exposure to high humidity conditions and large temperature variations. Apart from irreversible changes at high temperatures, the predominant temperature effect reported is the increase in central wavelength at increased temperatures. Filters are typically designed for operating temperatures of 20° – 23°C. Very slight changes in bandwidth (about 0.001 nm/°C) and peak transmittance (about 0.01%T/°C) can occur with increasing temperature [*Oriel-Instruments*, 2003]. Even so, filters will withstand repeated thermal cycling, provided the temperature transitions are small and gradual. Although the filer is fully functional no matter which side faces the radiation source, the thermal stress on the filter assembly is minimized when the filter is oriented within the filter wheel with the most reflective, highly-mirrored surface facing the source of radiation, i.e. the sky. (By comparison, the other surface of the filter has a more colored or opaque appearance.) Positioned thus, most of the rejected radiation is reflected

and does not heat the internal components of the filter. Note that, apart from reduction of thermal effects, spectral performance is unaffected by filter orientation. Manufacturers also recommend protection from intense light when a filter is not in use. Prolonged exposure to light, particularly ultraviolet wavelengths, results in solarization and reduced transmission.

The final contributing factor to be discussed affecting filter performance – angle of incidence of incoming radiation – is particularly important as it plays a significant role in specifying the filter design parameters for targeting the desired emission. Cast in a positive light, this feature can be very useful in tuning a narrow-band filter to the desired central wavelength; overlooked, this performance-degrading factor can doom your data. The effects of off-normal radiation are three-fold: the central wavelength decreases; the peak transmittance decreases; and the bandwidth increases. For incident angles less than 2.5°, the effect on transmittance and bandwidth are minimal. The primary effect caused by an increase in the incident angle of radiation impinging on the interference coatings of a filter is a shift in passband toward shorter wavelengths. In other words, the principal wavelength of the interference filter decreases as the angle of incidence increases. This follows from the fact that changing the angle of incidence increases the apparent thickness of the deposited thin-film layers. As a result, for radiation incident on these interference coatings at oblique angles, a reduction in phase difference occurs between transmitted and reflected waves at the filter interfaces. The amount of wavelength shift is a function of the incident angle and the refractive indices of the deposited films. Alternatively, for simplification, the effective refractive index (N^*) of the filter is used. For parallel

beams in a collimating system, the relationship is defined as follows:

$$\lambda = \lambda_0 \sqrt{1 - \frac{\sin^2 \theta}{(N^*)^2}} \tag{C.1}$$

where λ is the peak wavelength at angle of incidence θ, λ_0 is the peak wavelength at normal incidence (i.e., at 0° angle of incidence), and N^* is the effective refractive index of the filter. In this equation, the ratio of effective refractive indices is $1/N^*$ with the value of one – indicative of the index of refraction for a vacuum – implied in the numerator. A more formal equation, incorporating the index of refraction for air, is:

$$\lambda = \lambda_0 \sqrt{1 - \left(\frac{N_o}{N^*}\right)^2 \sin^2 \theta} \tag{C.2}$$

where the variables are the same with the addition of N_o for the effective refractive index of air.

In a converging beam or cone of light, only the central ray is normal to the surface and all others are increasingly off-angle. When interference filters are used in a converging beam, such as in the case of a telescope, the new shifted transmission curve results from integrating the wavelength shift over the entire range of angles. In the case of telecentric optical systems, the resulting new transmission curve is based on the integration of the shift effect for the rays at all angles within each of the image-forming cones whose principal rays are parallel. To avoid the lengthy integration process, a good approximation can be predicted from the above tilted-collimated-beam formula by dividing the results in half and using the maximum half-cone angle. If λ_m is the new, shifted, central peak wavelength when the filter is inserted into a converging (i.e., non-collimating) beam or telecentric optical system, we have the following approximate relation:

$$\lambda_m = \lambda_0 \left(1 - \frac{\beta^2}{4} \left(\frac{N_o}{N^*}\right)^2\right) \tag{C.3}$$

where λ_0 is the peak wavelength at normal incidence (i.e., at 0° angle of incidence), N^* is the effective refractive index of the filter, N_o is the effective refractive index of air, and β, the maximum off-axis ray angle, is derived from the following relationship between the numerical aperture, *N.A.*, and the F number, F:

$$N.A. = N^* \sin\beta = \frac{1}{2F} \tag{C.4}$$

Assuming the effective refractive index is approximately equal to one ($N^* \sim 1$), and solving for $\sin\beta$, we get the following estimate:

$$\sin\beta \approx \frac{1}{2F} \tag{C.5}$$

based on the F number, F. For our all-sky applications with F4.0, the maximum ray angle β comprising the image-forming cones is determined to be ±7.1°.

Using small angle approximations, the shift in wavelength of peak transmission for parallel light incident on a filter at angle θ (radians) is given by (modified from *Eather* [1993]):

$$\frac{\Delta\lambda}{\lambda} = \frac{-\theta^2}{2}\left(\frac{N_o}{N^*}\right)^2 \tag{C.6}$$

where N^* is the effective refractive index, and N_o is the effective refractive index of air. Similarly, the shift in peak transmission for a cone of light of semi-angle β (radians) incident on a filter with the cone axis at normal incidence is given by:

$$\frac{\Delta\lambda}{\lambda} = \frac{-1}{2} \cdot \frac{\beta^2}{2}\left(\frac{N_o}{N^*}\right)^2 \tag{C.7}$$

The effective refractive index is determined by the coating materials used and the sequence of thin-film layers, both of which are variables in the design process. For filters with common coating materials such as zinc sulfide and cryolite, effective refractive index values are typically 1.45 or 2.0 [*Oriel-Instruments*, 2003; *Omega-Optical*, 2006].

Variation in the angle of incidence of incoming light can be realized either by tilting the filter – which is not expected in our applications unless the filter is improperly aligned within the filter-wheel housing – or due to the inherent effect of the optical path. With telecentric optics, one might expect that the incoming light rays have been properly refracted by the telecentric lens such that they are all, inclusively, parallel both to each other and to the principal axis of the telecentric lens, as well as perpendicular to the image plane. In reality, as noted in Section 2.2.1.2, it is the *principal rays* of all image-forming cones that are oriented parallel to each other. The maximum ray angle comprising the image-forming cones is determined by the F number of the objective lens, and for our all-sky applications with F4.0, this maximum angle is $\pm 7.1^{\circ}$. To see the impact the image-forming cones have on the filter design specifications, consider the case of a 7774 filter with the CWL designated to be the desired 777.4-nm airglow emission. We can apply Eq. C.7 to determine the expected shift, $\Delta\lambda$. Substituting both effective refractive index values (1.45 and 2.0) in for N^* to determine a range for the wavelength shift, we find $\Delta\lambda = 0.7 - 1.4$ nm for the 777.4-nm filter. Given that the FWHM is only 2.0 nm for the entire pass-band, Figure C.5 illustrates that blue-shifting the idealized CWL will reduce the transmission of the 774.4-nm emission line to below 40% in the best case ($\Delta\lambda = 0.7$ nm), and will effectively remove (< 10% transmission) the 777.4-nm emission line in the worst case ($\Delta\lambda = 1.4$ nm), such that the filter no longer functions to isolate our target airglow emission. If, however, we design the filter with a CWL of 778.1-778.8 nm, such that the CWL is red-shifted from our desired emission, then for the given N^* values, we obtain our desired transmission curves, shown in green in Figure C.5.

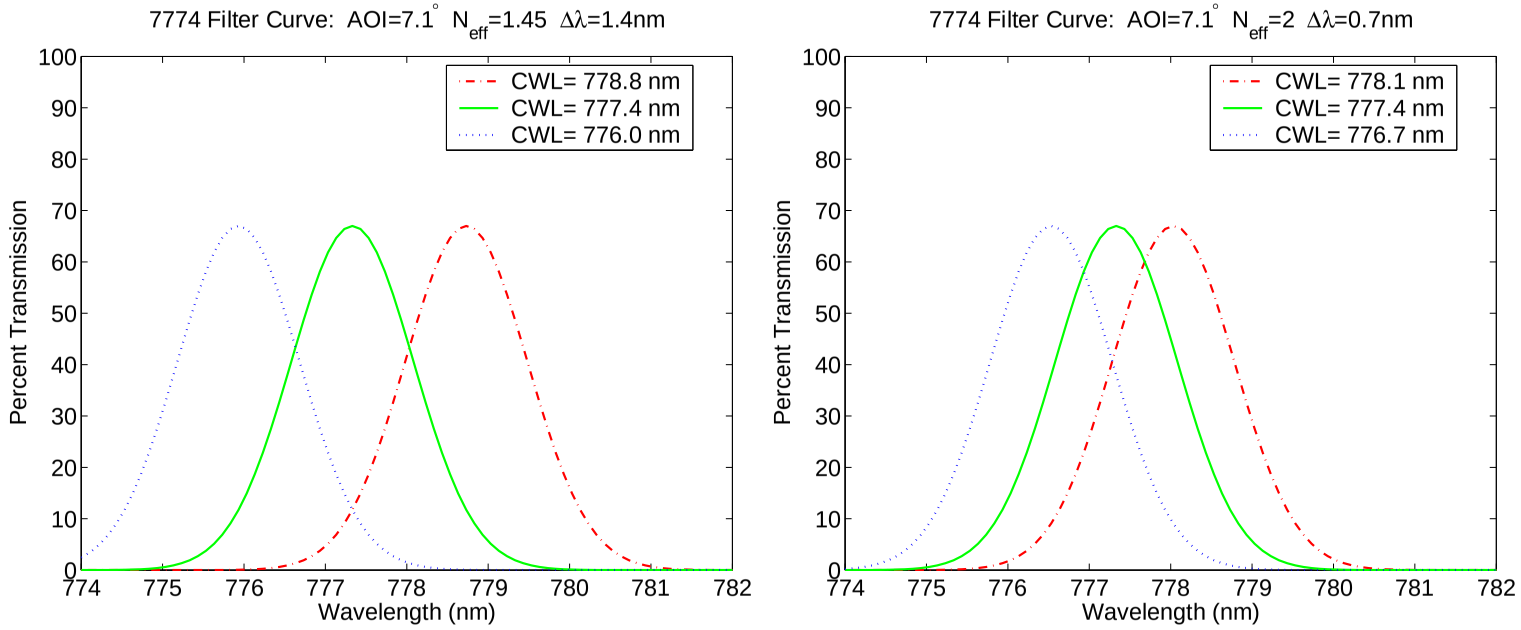

Figure C.5: This plot illustrates the impact of telecentric image-forming-cone effects on filter performance. Due to the range of angles associated with the image-forming cones, most of the light passing through the interference filters is blue-shifted. This blue-shifting of the idealized CWL will reduce the transmission of the 774.4-nm emission line to below 40% in the best case ($\Delta\lambda$ = 0.7 nm), and will effectively remove (< 10% transmission) the 777.4-nm emission line in the worst case ($\Delta\lambda$ = 1.4 nm), such that the filter no longer functions to isolate our target airglow emission. If, however, we design the filter with a CWL of 778.1-778.8 nm, such that the CWL is red-shifted upfront, then for the given N_{eff} values, we obtain our desired transmission curves, shown in green .

C.4 Cleaning Guidelines

All optical elements are delicate and should be handled as carefully as possible. The filters we use in our airglow studies are no exception. The glass and anti-reflective (AR) coated surfaces will be damaged by any contact, especially if abrasive particles come into contact with the surface. In most cases, it is best to leave minor debris on the surface. Historically we have tried to clean the filters after transport and before loading them into the filter wheel for a campaign run. For those times when cleaning is required, following are guidelines suggested by Omega Optical, Inc. as posted on their website: https://www.omegafilters.com/index.php?page=tech_cleaning

Use of oil-free dry air or nitrogen under moderate pressure is the best tool for removing excessive debris from an optical surface. In the case that the contamination is not dislodged by the flow of gas, please use the following protocol for cleaning the part:

1. Clean the filter using an absorbent towel such as Kimwipes, not lens paper. Use enough towelling so that solvents do not dissolve oils from your hands which can make their way through the towelling onto the coated surface.
2. Wet the towel with an anhydrous reagent grade ethanol.
3. The use of powder-free gloves will help to keep fingerprints off the part while cleaning.
4. Drag the trailing edge of the ethanol soaked Kimwipe across the surface of the component, moving in a single direction. A minimal amount of

pressure can be applied while wiping. However, too much pressure will damage the component.

5. If the surface requires additional cleaning, always switch to a new Kimwipe before repeating the process.
6. The purpose of the solvent is only to dissolve any adhesive contamination that is holding the debris on the surface. The towel needs to absorb both the excessive solvent and entrap the debris so that it can be removed from the surface. Surface coatings on interference filters and dichroics are typically less hard than the substrate. It is reasonable to expect that any cleaning will degrade the surface at an atomic level. Consideration should be given as to whether the contamination in question is more significant to the application than the damage that may result from cleaning the surface. In many cases, the AR coatings that are provided to give maximum light transmission amplify the appearance of contamination on the surface.

APPENDIX D

IMAGER INVENTORIES

Table D.1: CARI equipment inventory.

Part	Manufacturer	Model #	Serial #	P.O. No.	Contact	Purchase Date
Camera Head	Photometrics CCD	CH250	A96E5007			
Optical System	KEO Consultants		E138856			
Primary Lens	Mamiya Sekor 24mm/F4.0	180° FOV				
Camera Lens	Canon or Nikon 50mm/F1.2					
Liquid Cooling Unit	Photometrics	LCU1	A96E385			
Electronics Unit	Photometrics	CE300	A98E9122			
UPS	APC Back UPS	BK650M/P9710050	NB9916162182			
Computer	Dell	Dimension B110				
Flat Panel Monitor	Gateway	FPD1520	QH5215005987			
Keyboard	Gateway	SK-9921	A156911			
Mouse	Gateway		LNA21406704			
Remote Pwr Switch	Western telematics, inc.	RPS-10	#30304332			
Filters:		CWL/BW	Lot #			
6300	Barr #1	630.4/2.0NM	4699	435684	Philip Nickolson	11/1999 by JJM
5577	Barr #2	558.1/2.0NM	3291	none	none	
BGND	Barr	541.0/2.2NM	4499	435684	Philip Nickolson	11/1999 by JJM
OH	Barr	865 NM	2196	none	none	05/24/1996
7774	Barr #2	777.8/2.0NM	3191		on loan from NRL [1]	returned 07/24/2002 [2]
7774	Andover Corporation	777.4/2.0NM	ANDV8485	AM-50324-01 I.Q.		09/12/2002

[1] P.Bernhardt, C. Siefring

[2] via FedEx #831654194953

[3] previous computer was a Gateway S/N 0027164609.

Table D.2: CASI equipment inventory.

Part	Manufacturer	Model #	Serial #	P.O. No.	Contact	Purchase Date
Camera Head[1]	Achromatic Diopter	C12434	101 6 85 WK0641	PNR Supply		
Optical System	KEO Consultants		E138856			
Primary Lens	Mamiya Sekor	180° FOV				
Camera Lens						
Liquid Cooling Unit[2]	Princeton Instruments	CC-100 115V	D129323			
Electronics Unit	Princeton Instruments	ST-138S	#01094262			
UPS	APC Back UPS	600	PB9647172981			
Computer[3]	Dell	Windows	CN-0YD544-70821-61C-X8K0 [4]			
Monitor	Optiquest	Q71	#11472478			on loan from Boeing
Keyboard	ORTEK Technology, Inc.	MCK-600W	#00291438			
Mouse	Gateway	MOSUJ	#3863872A057			
Remote Pwr Switch	Western telematics, inc.	RPS-10	#30916506			
Filters:		CWL/BW	Lot #			
6300	Barr	630/2NM	1396			03/27/1996
5577	Barr #1	558.2/2.0NM	1697			04/24/1997
BGND	Barr	541/2NM	1396			03/28/1996
Na	Barr #1	590.0/5NM	4289			
7774	Barr	777/2NM	3990			

[4]previous camera head was a Princeton Instruments, Model# TEA/CCD-1024TKB/1, S/N 109414.
[5]LANL #917319.
[6]previous computer was ABS Win2000.
[7]Boeing skew# 57MVZ91.

Table D.3: CNFI equipment inventory.

Part	Manufacturer	Model #	Serial #	P.O. No.	Contact	Purchase Date
Camera Head	Photometrics[1] CCD	CH350	A00K2103[2]			
Optical System	KEO Consultants		E138856			
Primary Lens	Mamiya 80mm/F4.0	47° FOV				
Camera Lens	Canon 85mm/F1.2					
Filter Wheel	KEO Consultants	Serial Port				
Liquid Cooling Unit	Roper Scientific, Inc.	LCU	A00G302			
Electronics Unit	Roper Scientific, Inc.	CE300	A00K9125			
UPS	APC Back UPS 650	BK650M	PB0134223097(APC)			
Computer	ABS	Win2000				
15" Monitor	Gateway 2000	DX15FG	HD3345031813[3]			
Keyboard	Gateway 2000	SK8000	3882A277	replaced by loaner from Boeing		
Mouse	MS IntelliMouse 1.1A PS/2	X03-65047	#63618-OEM-1326045-00000			
Remote Pwr Switch	Western telematics, inc.	RPS-10	30916507			
USB/Serial Converter	Allied Telesyn Int'l	AFMC13	G1C603078			
External H/D[5]	West Digital	WD1200B008-RNN	WMAET2129654			
Filters:[6]		CWL/BW	Lot #			
1 - 6300	Barr #2	6311/25A	5086			
4 - 5577	Barr					
5 - BGND	Barr					
2 - 7774	Barr #1	777.8/2.0NM	3191			

[8]now Roper Scientific, Inc.
[9]Cornell University skew# E160555.
[10]old S/N(?) MON015007ABWW.
[11]old Model# 2196001-00-102; old S/N #19520046.
[12]AMOS #11473456; skew# A01476. [13]Filter position #3 is currently empty.

APPENDIX E

IMAGER TRAVEL LOGS AND DOCUMENTS

E.1 Carnet

Information regarding Carnet documents can be found online at the following website: www.atacarnet.com . An application process is now also available via the internet through the same website. The information in the first three sections of this appendix was extracted from this site.

E.1.1 Purpose

A Carnet or ATA Carnet is an international customs document issued by 70 countries. It is presented when entering a Carnet country with merchandise or equipment that will be re-exported within 12 months. Upon presentation, the Carnet permits the equipment or merchandise to clear customs without the payment of duties and taxes. Payment is not necessary because the Carnet guarantees that the merchandise or equipment will be re-exported within a year. Thus the use of a Carnet is a way of temporarily importing into foreign countries without payment of duties and taxes. Carnets also serve as the US registration of goods so that the goods can re-enter the US without payment of duties and taxes.

The Carnet General List is an itemized list of all the merchandise or equipment that is to be temporarily imported into one or more Carnet countries. It includes a description of each item, including amount and weight, and any se-

rial numbers that apply.

E.1.2 Process

The following outlines a simple, 4-step process to getting an ATA Carnet:

1. Prepare the ATA Carnet form with your export shipment information.
2. Submit an ATA Carnet application with your export shipment information securely online.
3. Update the Carnet form's shipment information, if necessary, by calling the CIB Carnet HelpLineSM at (800) ATA-2900 or (800) 282-2900 or by emailing them through the online (www.atacarnet.com) contact info.
4. Receive the ATA Carnet and related international customs documents: carnet bond, insurance for your goods, lost carnet document warranty and shipper's export declaration.

E.1.3 Application Checklist

Prior to logging in to Carnets-By-Internet, prepare the following information to complete your application:

1. Purpose for which the equipment is being temporarily imported to another country(ies).
2. EIN (Employer Identification Number) or Taxpayer Identification Number.

3. Name(s) of individual(s) responsible for carnet documents while en route.
4. List of countries the goods will be transiting. That is, countries that are being passed through en route to a destination.
5. List of destination countries.
6. Complete list of equipment that will be travelling (including model and serial numbers if applicable). Note: If you have the list of items in an electronic record (Excel or database), call the Carnet company for details on how to import the list to avoid data re-entry.
7. Number of items, values and serial numbers of equipment that will be travelling.
8. Desired date of delivery of your Carnet document.
9. Visa, American Express or MasterCard number and expiration date unless you are going to pay by ACH (Automated Clearing House).
10. Temporary Transit and Storage insurance information: Name of insurance company, expiration date of policy, policy limit. (If this is unavailable you may bypass this step and provide evidence of insurance at a later date.)

E.1.4 FAQs

The following is a U.S. government document which addresses many basic, common questions regarding the purpose and usage of an ATA Carnet. It was downloaded from http://www.osec.doc.gov/ogc/occic/atacarnet.html and is included here both for immediate reference and in case it becomes unavailable online at a future date.

The ATA Carnet Simplified Customs Procedures for "Tools of the Trade"

Businesspersons travelling outside the United States often find the arduous task of clearing customs to be one of the most frustrating parts of their travels. Fortunately, the customs process can be simplified by using an ATA Carnet (pronounced car-ney) for temporary importation of goods that can be described as a "tool of the trade." (The term ATA is an acronym for the descriptive title written in French as "Admission Temporaire" and English "Temporary Admission", respectively.)

Q. What is an ATA Carnet?

The United States acceded to the Customs Convention on the ATA Carnet for the Temporary Admission of Goods (known as the ATA Convention) in December 1968 and began issuing ATA Carnets at the end of 1969. ATA Carnets are intended to reduce the burdensome customs paperwork confronting the commercial traveler. The ATA Carnet is a global customs document used to obtain temporary admission of certain goods into the territories of countries that belong to the ATA Convention, without paying duty or value-added taxes on those goods. The ATA documentation accompanying the goods bypasses the time-consuming task of filing numerous customs documents otherwise required by each of the individual ATA member countries into which the goods are temporarily imported. The Carnet also provides a financial guarantee to foreign customs officials that, in the event the goods which have been temporarily

admitted are not re-exported, import duties and taxes will be paid.

Q. What is contained in an ATA Carnet document?

The Carnet document has a green cover page which provides the names of the Carnet holder and issuing association, the Carnet issue date, the Carnet number, the countries in which the Carnet may be used and a complete description of the goods covered. Two yellow sheets in the package are to be used upon exportation from and re-importation back into the issuing country. White sheets are used for the temporary importation into and re-exportation from the second or additional countries. Blue sheets are used when transiting through countries. Each sheet contains two parts - a counterfoil, which remains in the Carnet and describes the actions taken by Customs officers each time goods enter or leave a country, and a detachable voucher, which contains a list of the goods covered by the Carnet and serves as the required Customs document.

Q. How is a U.S.-issued ATA Carnet processed by Customs?

When leaving the United States, the holder of a U.S.-issued ATA Carnet presents the Carnet and the covered goods to a Customs officer. The Carnet is reviewed for completeness and accuracy and the goods are examined to ensure that they match the Carnet list. The officer then validates the Carnet document and certifies the appropriate exportation counterfoil and voucher. The Carnet and the U.S. Customs-certified export voucher are returned to the Carnet holder who retains the voucher as the permanent record of the Customs transaction. (Note: The Carnet does not affect export control requirements such as the filing of a shipper's export declaration or the requirement to obtain export licenses). Upon return to the United States, the holder of a U.S.-issued Carnet presents the Car-

net and covered goods to a Customs officer for examination. The officer certifies the appropriate re-importation counterfoil and voucher and returns the Carnet to the holder for further use or surrender to the issuing association. (Note: On U.S.-issued Carnets only, the vouchers of the yellow exportation/re-importation sheets will not be detached, but will remain with the document when departing or returning to the United States). It is the responsibility of the Carnet holder to present the Carnet to the Customs authorities when entering or leaving a country in order that the necessary verification and certification of the appropriate vouchers and counterfoils can take place. Failure to do so may result in a claim being made. A claim is a notice from a Customs authority of the country of import that a violation of the Carnet system has occurred and payment of duties, taxes, and penalties are required.

Q. What kinds of goods are covered?

Virtually all goods are covered by ATA Carnets. Ordinary goods including vehicles, apparel and jewelry, computers, photography/video and sound equipment, repair tools, and industrial equipment, or extraordinary items such as philharmonic orchestras and Olympic horses can all be covered if they qualify as a "tool of the trade." Examples of tools of the trade include goods for exhibitions and fairs, commercial samples, and professional equipment.

Q. What goods are not covered?

Merchandise that does not qualify as a tool of the trade is not eligible to be covered by an ATA Carnet. ATA Carnets also do not cover such items as: postal traffic, disposable and hazardous items, and consumable goods (food and agriculture products).

Q. Who issues ATA Carnets?

In each member country, organizations affiliated with the International Bureau of Chambers of Commerce are designated to issue Carnets to residents for use abroad. In the United States, that function is performed by the U.S. Council for International Business (USCIB). More information on the USCIB can be found at their web site at http://www.uscib.org/ .

Q. Are there fees associated with the ATA Carnet?

Certain fees are connected with applying for an ATA Carnet. In addition, other additional costs including security and expedited service may also apply. More information about associated costs can be found on the USCIB web site at http://www.uscib.org/ .

Q. Where are ATA Carnets accepted?

An updated listing off all countries and territories that accept ATA Carnets can be found on the USCIB web site at http://www.uscib.org./ .

Q. How long is the ATA Carnet valid?

The ATA Carnet is valid for up to one year from the date of its issuance, during which the Carnet may be used for an unlimited number of exits from the United States and entries into foreign countries. The ATA Carnet will only cover goods that are returned to the United States within 12 months.

Q. What if the ATA Carnet is expired?

Although no penalties or duties will be assessed by the United States for an expired U.S.-issued Carnet, a foreign government may assess penalties if the

Carnet expires before the U.S. merchandise is exported from that country. The U.S. Customs Service will assess liquidated damages for foreign-issued Carnets that expire before the merchandise is exported from the United States.

Q. Under what circumstances might a claim be filed?

A claim consists of a notice issued by the customs authority of a foreign country in cases where there is no record that merchandise was re-exported. Examples of this would be: where the Carnet certificates have not been properly validated by either U.S. or foreign customs; where goods have been lost, stolen, or destroyed; where there is an improper or inadequate description of the merchandise on the general list; or where goods have not been re-exported in a timely fashion.

Q. What happens if the goods are not exported?

ATA Carnet holders who sell, donate, or otherwise dispose of any goods listed on the Carnet will cause the issuing organization to be assessed liquidated damages equaling 100 percent of the import duties and taxes (the issuing organization will then attempt to collect all such moneys from the Carnet holder that violated the terms). Additional charges may also apply in some cases, since some countries where violations occur hold the Carnet issuer and holder equally responsible (including normal duties and taxes as well as liquidated damages).

For additional information, contact: Carnet Headquarters, U.S. Council for International Business (USCIB), 1212 Avenue of the Americas, New York, NY 10036; Tel: (212) 354-4480, Fax: (212) 944-0012; or visit the USCIB web site at www.uscib.org . Further information may also be obtained from the Importing and Exporting link on the U.S. Customs Service website, at www.customs.ustreas.gov . Revised August 2002

E.2 Travel Logs and Sample Shipping Documents

351 Rhodes Hall
Cornell University
Ithaca, NY 14853

June 27, 2002

Steve Hoskins
A.T.A. Carnet Service Center
Corporation for International Business
118 Barrington Commons
Suite 236
Barrington, IL 60010

Dear Steve,
Enclosed please find the filled out *Application for waiver of security* for carnet number US89/02-18198. The form has been filled out and signed by Zhila Sadri who is the account representative for the grant paying for the shipment.

Please contact me if there are any questions. I can be reached at (607) 255-8298 or by email at demi@ece.cornell.edu.

Sincerely,

Pamela J. Loughmiller
Enclosure (1)
pjl

Figure E.1: Sample letter requesting a waiver of security for a given Carnet number.

Table E.1: Imager travel logs.

Name	Site	Location	Date In	Date Out	Carnet A.T.A. No.	Shipping Carrier	Purpose	Grad Students
CASI[1]	Arecibo	Puerto Rico	01/05/1997	03/31/1998	n/a			FJG
CASI[1]	Paia, Waimea Canyon	Kauai, HI	07/01/1998		n/a		feasibility test	FJG, PJL
CASI[1]	AEOS @ MSSC	Haleakala, Maui, HI		08/01/1998	n/a		Maui-MALT precursor	FJG,PJL
CASI[1]	M.C.Kelley's dock	Ithaca, NY	10/03/2000	11/02/2000	n/a			FJG,PJL
CASI[1]	Jicamarca	Colan-Piura, Peru	12/01/2000	01/01/2001 ??	??			Huaman
CARI[1]	RAAF BASE Tindal, N.T.	Australia	09/06/2001	06/14/2002	US 89/01-19631/S	Danzas AEI		JJM
CARI[1]	Univ. of Crete	Crete/ Milos, Greece	06/17/2002		US89/0218198	Danzas AEI		MJN, PJL
CARI[1]	NRL	Washington, DC	06/13/2003	08/20/2003	n/a	FedEx[4]	Radiometric calibration	JJM
CARI[1]	VLA, NRAO	Soccorro, NM	08/21/2003	09/01/2003	n/a	FedEx	NRL campaign	PJL
CARI[1]	Michigan Aerospace Corp.	Ann Arbor, MI	09/02/2003	04/12/2004	n/a	FedEx	SOFDI	PJL
CARI[1]	A.Gerrard's backyard	Oneida, NY	04/2004	ongoing	n/a	via truck	SOFDI	MJN, PJL
CASI[2]	J. Otten's roof	Placitas, NM	11/1998	11/1998	n/a	via truck	Leonid's meteor shower	PJL, CAK
CASI[3]	LBD Trailer on MSSS @ MSSC	Haleakala, Maui, HI	10/11/2001	ongoing	n/a	FedEx[5]	Maui-MALT	PJL, JJM
CNFI[1]	doghouse @ MSSC	Haleakala, Maui, HI	10/11/2001	ongoing	n/a	FedEx[5]	Maui-MALT	PJL, JJM

[1] owned and operated by Cornell University

[2] owned and operated by Los Alamos National Laboratory, Tom Armstrong

[3] originally owned by LANL and operated by Cornell; currently owned and operated by Cornell

[4] #833447232302

[5] #827488328-855 -866-877-888 #829381539154

CASI and CNFI Packing List

Box 1

Item	*Camera*	*Manufacturer*	*Value*
40 deg camera	NF	KEO	$30,000.00
misc parts	NF		
Filters:			
5577	AS	Barr Associates	$1,000.00
7774	AS	Barr Associates	$1,000.00
BGND	AS	Barr Associates	$1,000.00
Na	AS	Barr Associates	$1,000.00
6300	NF	Barr Associates	$1,000.00
7774	NF	Barr Associates	$1,000.00
lens	NF	Cannon	$2,400.00
cables:			$250.00
power strip	NF		
CEU->CCD cable	NF		
CEU power cable	NF		
KEO power cable	NF	KEO	
serial cable	NF		
serial Y cable	NF		
CEU->computer	NF		
extra (short) CEU->computer cable			
cooling power cable			
computer cable	NF		
		subtotal:	$38,650.00

contact info:
Cornell University
Electrical and Computer Engineering
Space Physics Research Group
Attn: Pamela J. Loughmiller
351 Rhodes Hall
Ithaca, NY 14853
(607) 255-8298

Figure E.2: Sample box packing list for the combined shipment of CASI and CNFI research material bound for Maui-MALT campaign site.

Box 5 of 5

FROM: Cornell University
Electrical and Computer Engineering
Space Physics Research Group
Pamela J. Loughmiller
351 Rhodes Hall
Ithaca, NY 14853
(607) 255-4183

TO: Boeing Company
358 Papa Place #3
Kahului, Maui, HI 96732
Attn: Maui Malt Russ Taft
(808) 874-1557
(808) 874-1600 fax

Figure E.3: Sample box shipping label for research material container bound for Maui-MALT campaign site.

APPENDIX F

CALIBRATION FIGURES

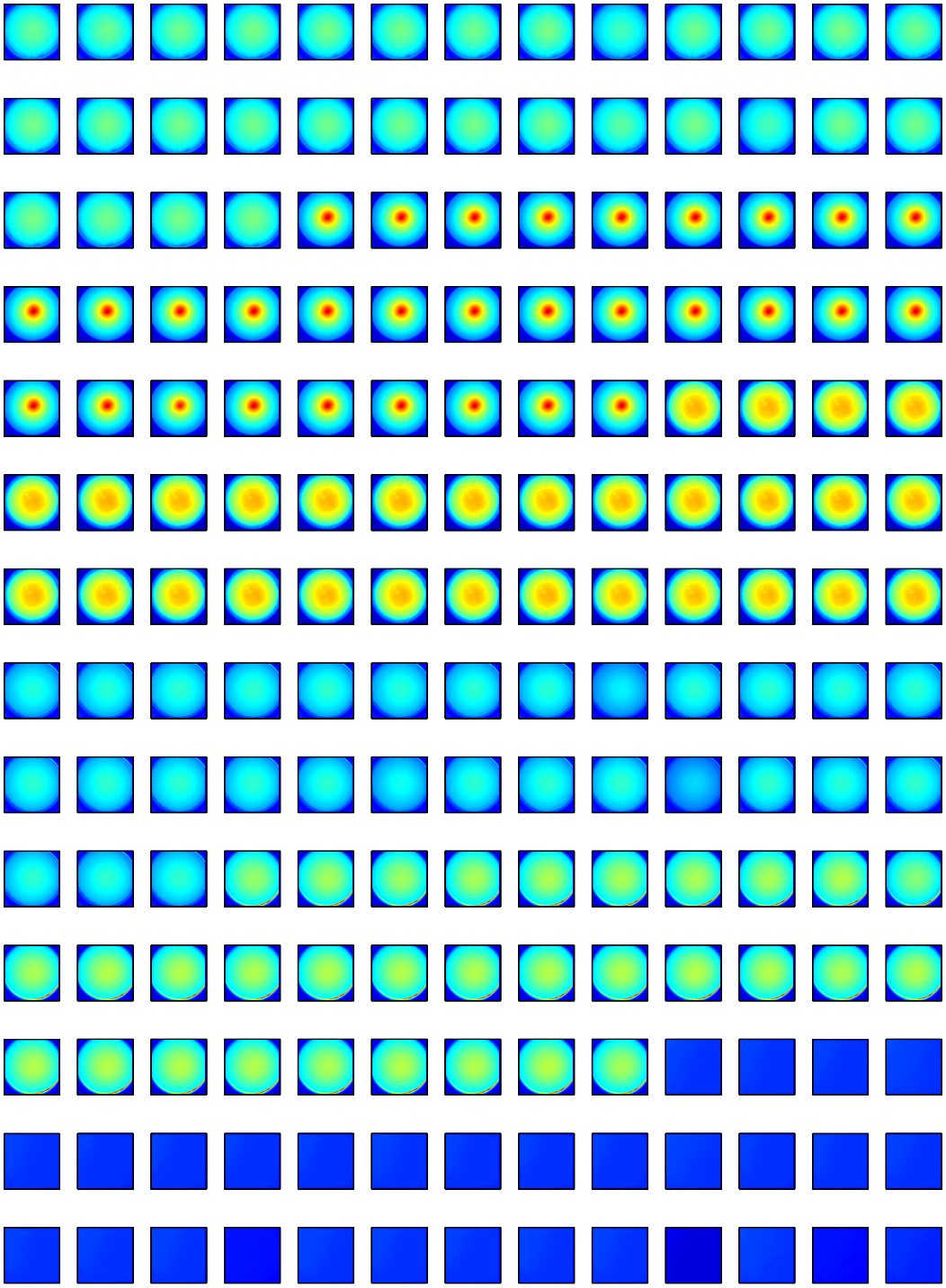

Figure F.1: Flat-fielding raw data images taken of the PCLS for CASI filters. In order from top to bottom, multiple images are shown for the following filters: 5577, 6300, 7774, BGND, Na, and Dark.

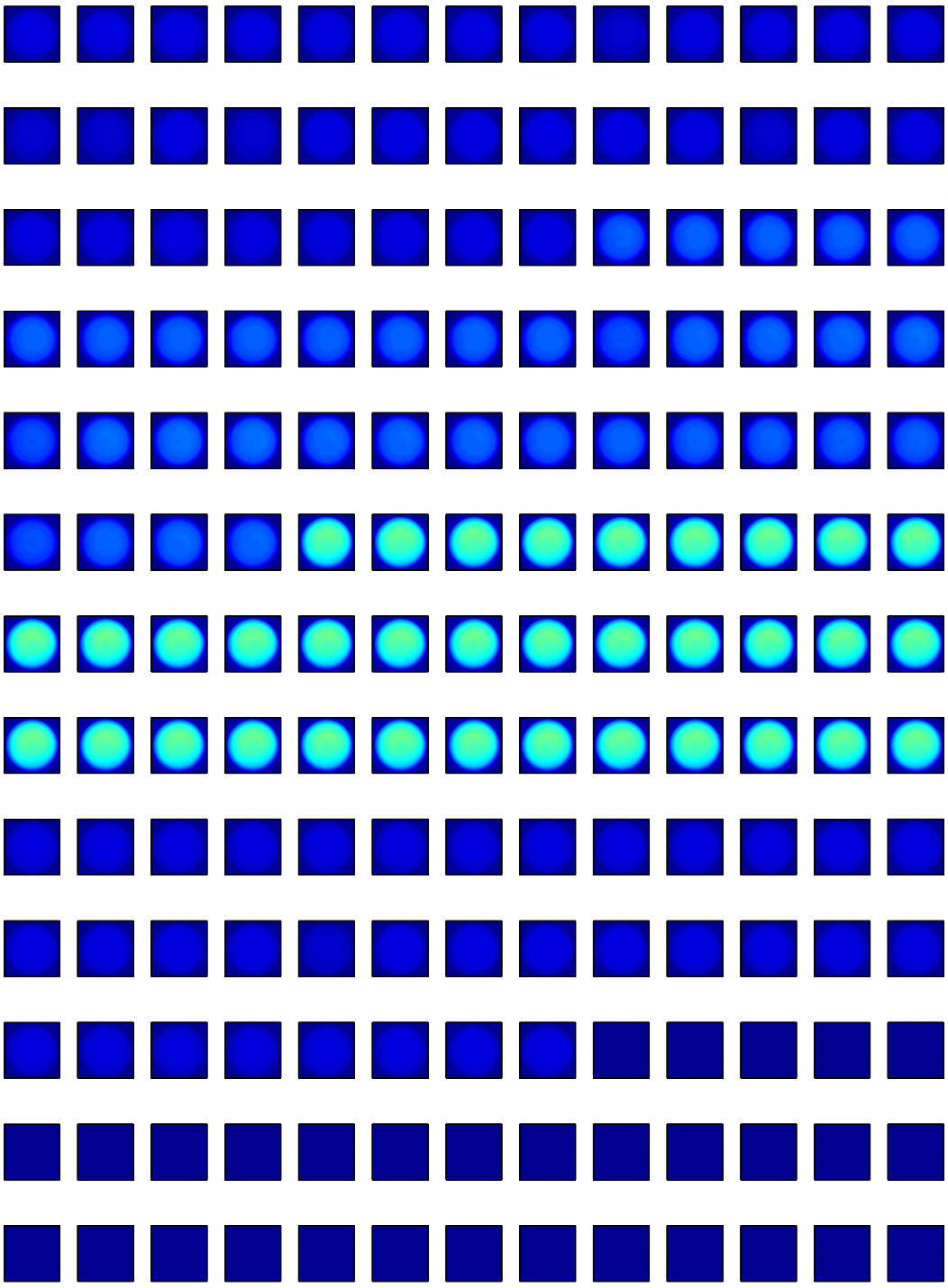

Figure F.2: Flat-fielding raw data images taken of the PCLS for CNFI filters. In order from top to bottom, multiple images are shown for the following filters: 5577, 6300, 7774, BGND, and Dark.

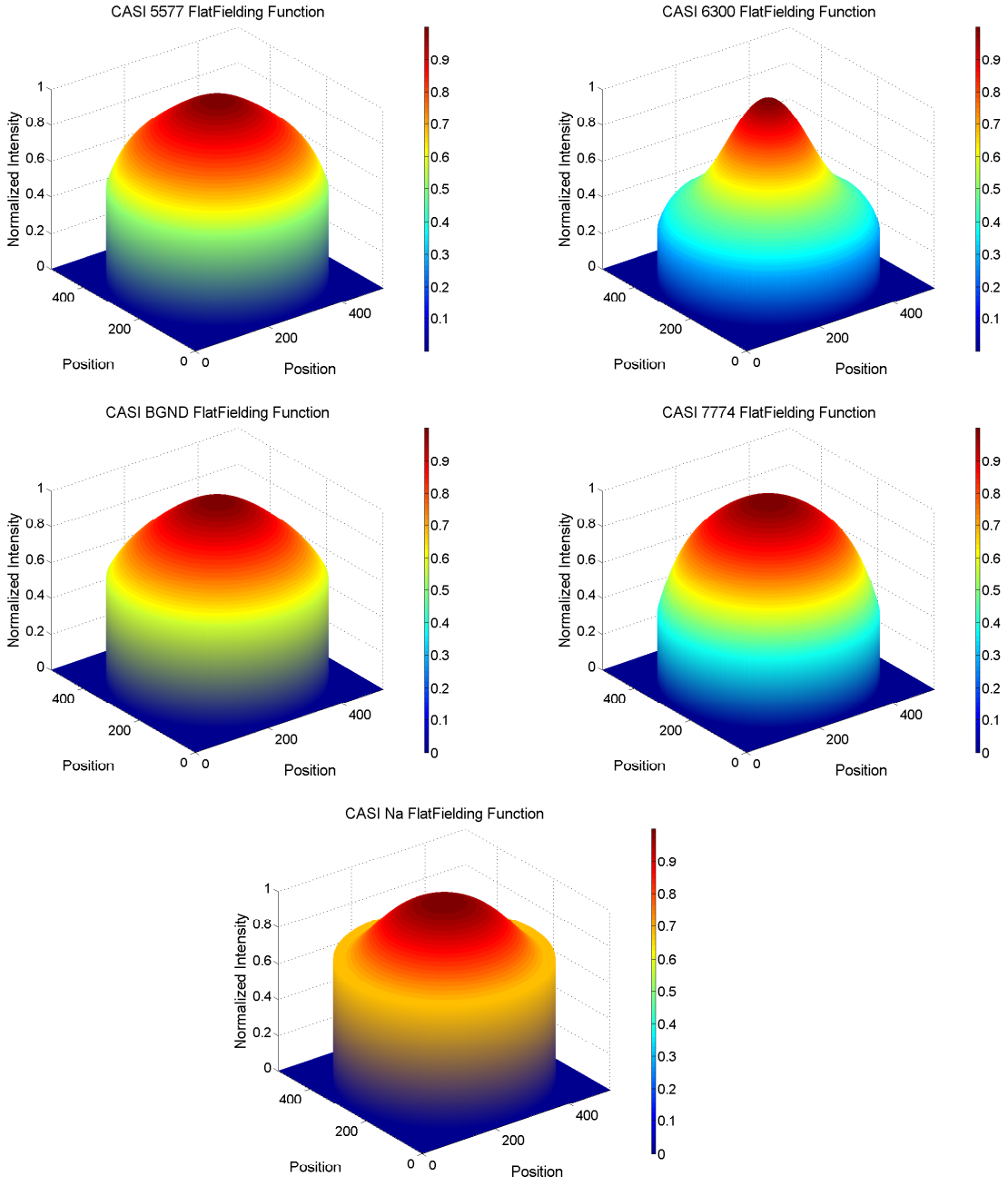

Figure F.3: 3-D plots of the flat-fielding functions for the five filters in CASI.

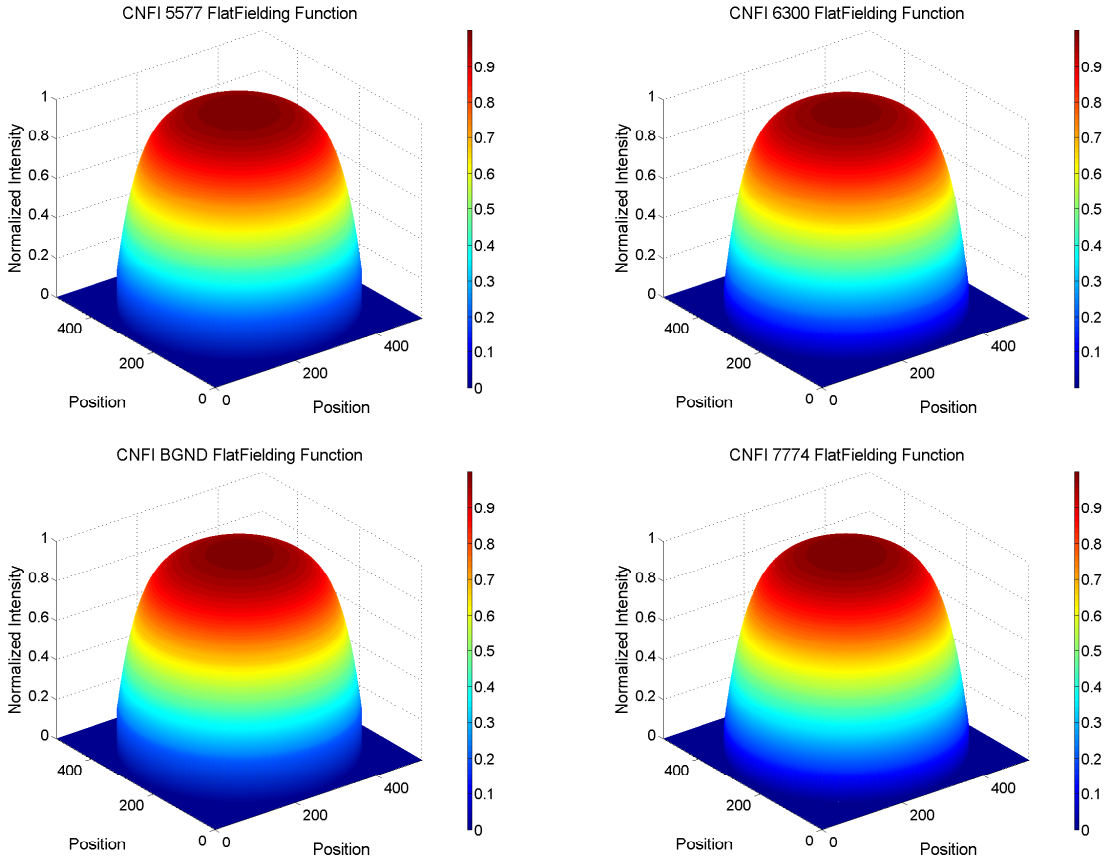

Figure F.4: 3-D plots of the flat-fielding functions for the four filters in CNFI.

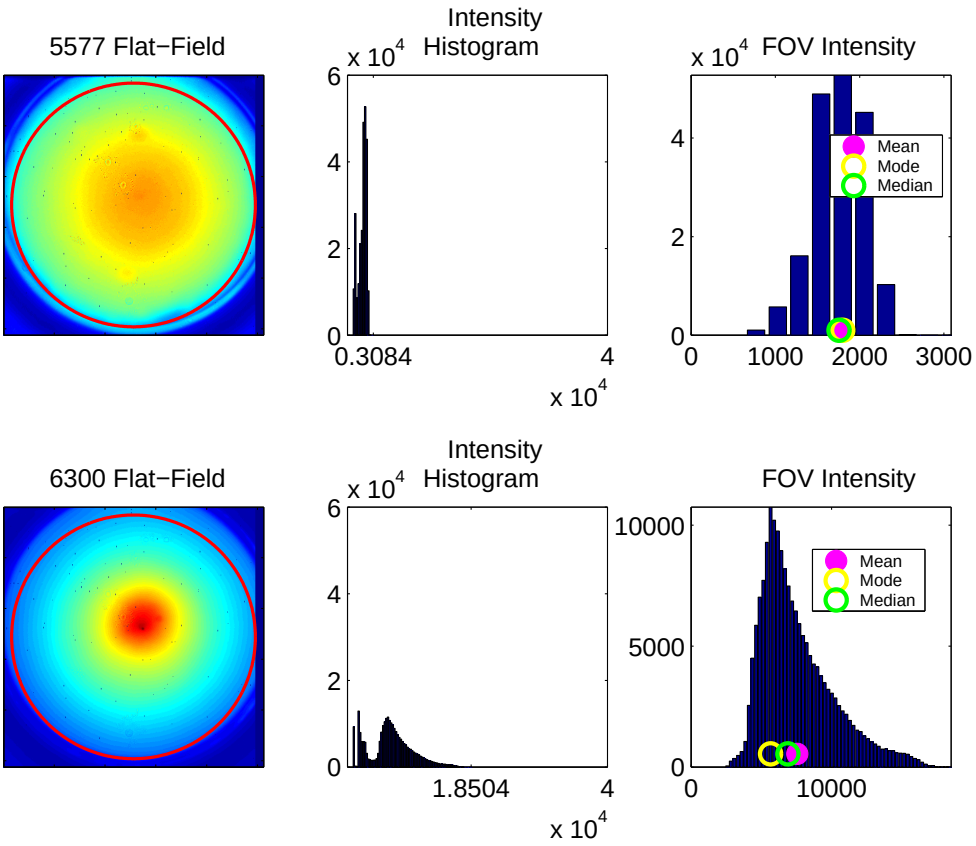

Figure F.5: Flat-fielding statistical summary for CASI filters: 5577 and 6300 are included in this figure; 7774 and BGND are shown in Figure F.6; and Na is shown in Figure F.7. Three panels are shown for each filter. On the left is the normalized, average flat-field image with the master dark removed. The red circle indicates the field of view of the primary lens, removed for this data-collection series. However, calculations for the statistics summarized in the panel on the right were confined to this area. In the middle panel is a histogram of the flat-field image on the left, with all histograms shown on the same scale for comparison. On the right, the histograms are expanded to suitable scales for the individual plots, and basic statistics of mean, median, and mode are indicated. For both histogram representations, intensity values are shown on the x-axis and pixel counts are depicted on the y-axis.

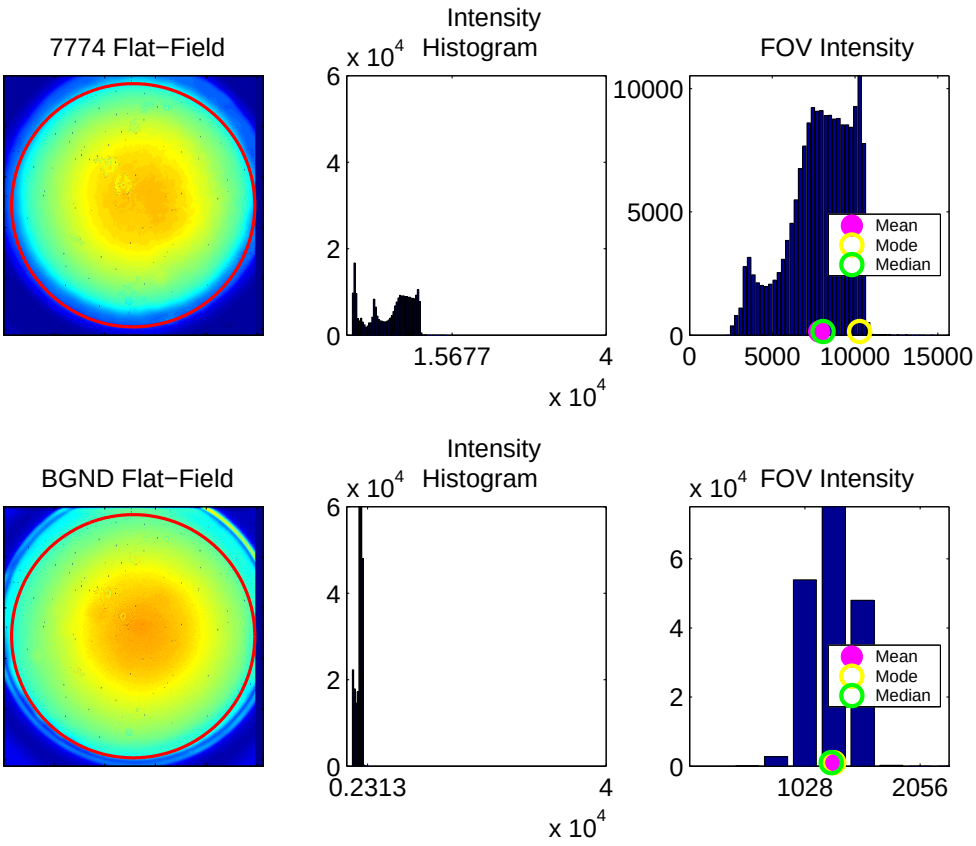

Figure F.6: Flat-fielding statistical summary for CASI filters continued: 7774 and BGND are shown above. See Figure F.5 caption for description.

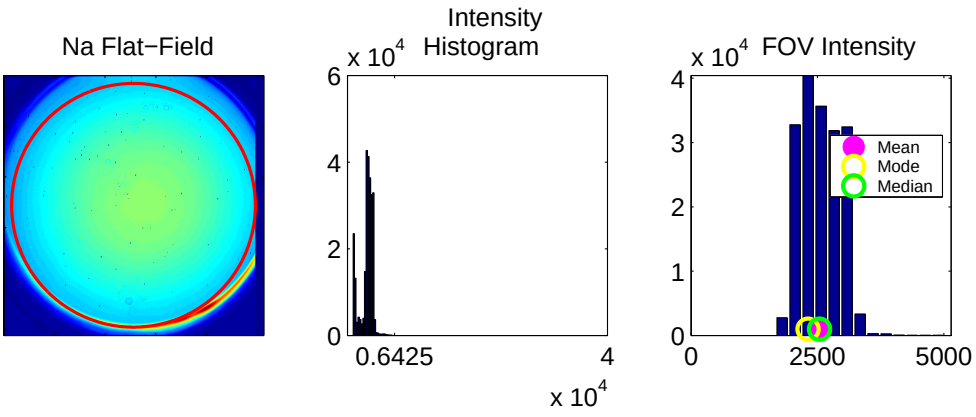

Figure F.7: Flat-fielding statistical summary for CASI filters continued: Na is shown above. See Figure F.5 caption for description.

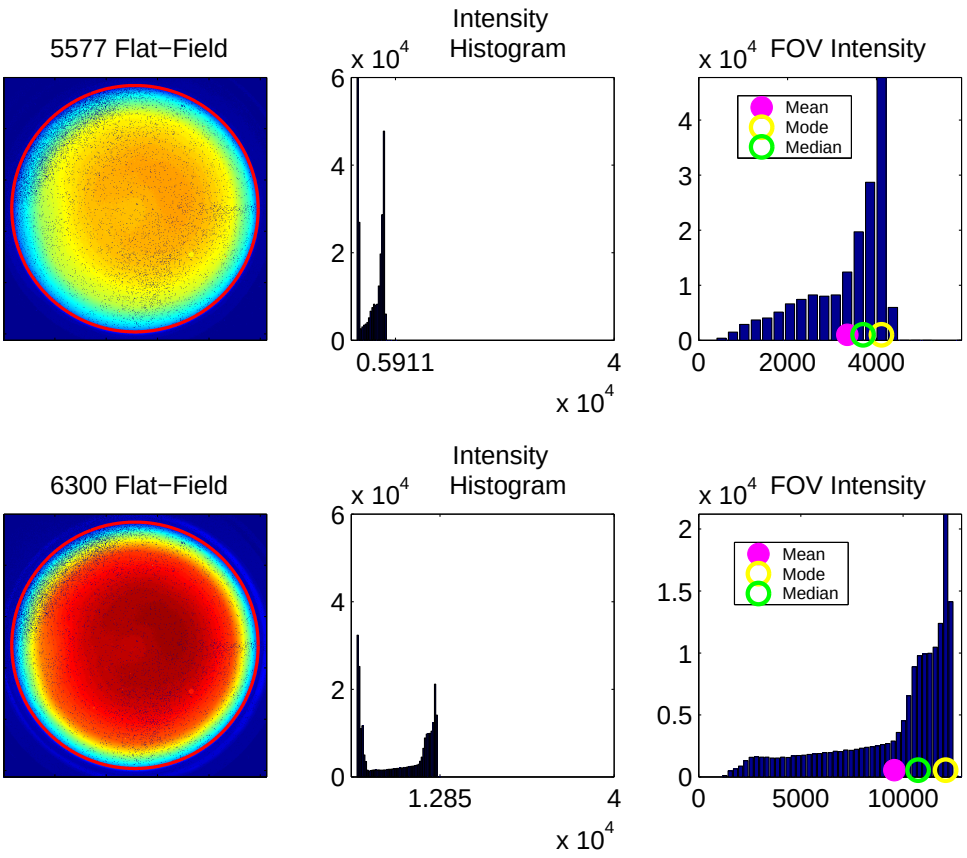

Figure F.8: Flat-fielding statistical summary for CNFI filters: 5577 and 6300 are included in this figure; 7774 and BGND are shown in Figure F.9. Three panels are shown for each filter. On the left is the normalized, average flat-field image with the master dark removed. The red circle indicates the field of view of the primary lens, removed for this data-collection series. However, calculations for the statistics summarized in the panel on the right were confined to this area. In the middle panel is a histogram of the flat-field image on the left, with all histograms shown on the same scale for comparison. On the right, the histograms are expanded to suitable scales for the individual plots, and basic statistics of mean, median, and mode are indicated. For both histogram representations, intensity values are shown on the x-axis and pixel counts are depicted on the y-axis.

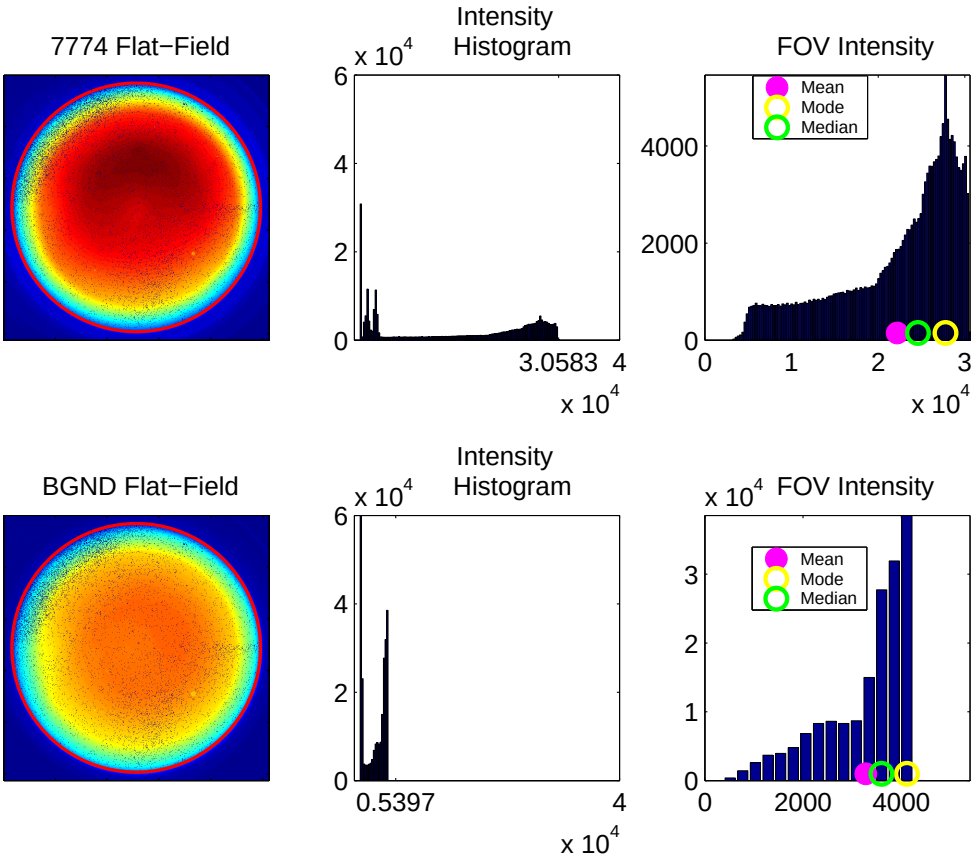

Figure F.9: Flat-fielding statistical summary for CNFI filters continued: 7774 and BGND are shown above. See Figure F.8 caption for description.

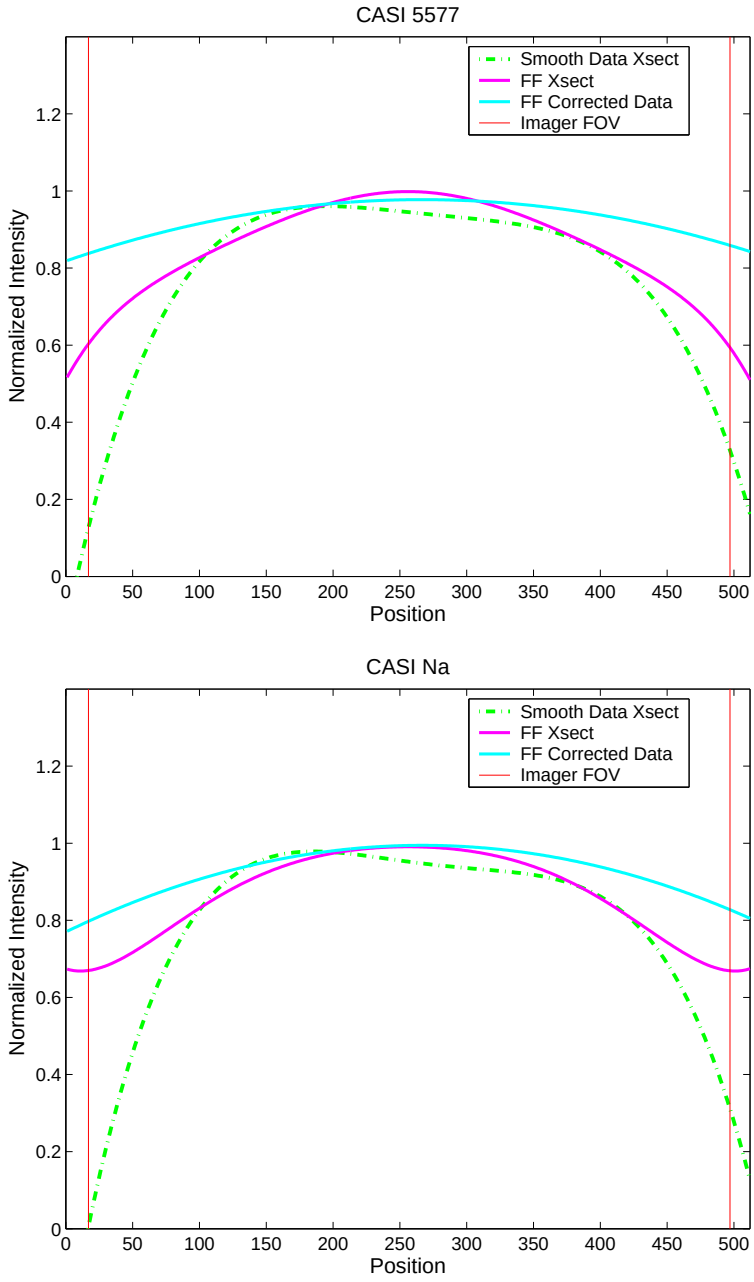

Figure F.10: These example plots illustrate the application of the flat-fielding functions for CASI. In both the 5577 plot in the top panel and the Na plot in the bottom panel, cross-sections are shown for an example dataset (green dash-dot line), and the same dataset corrected by the flat-fielding function for the associated filter (in light blue). Note the attenuation evident on both the left and right in the original datasets has been rectified following flat-fielding.

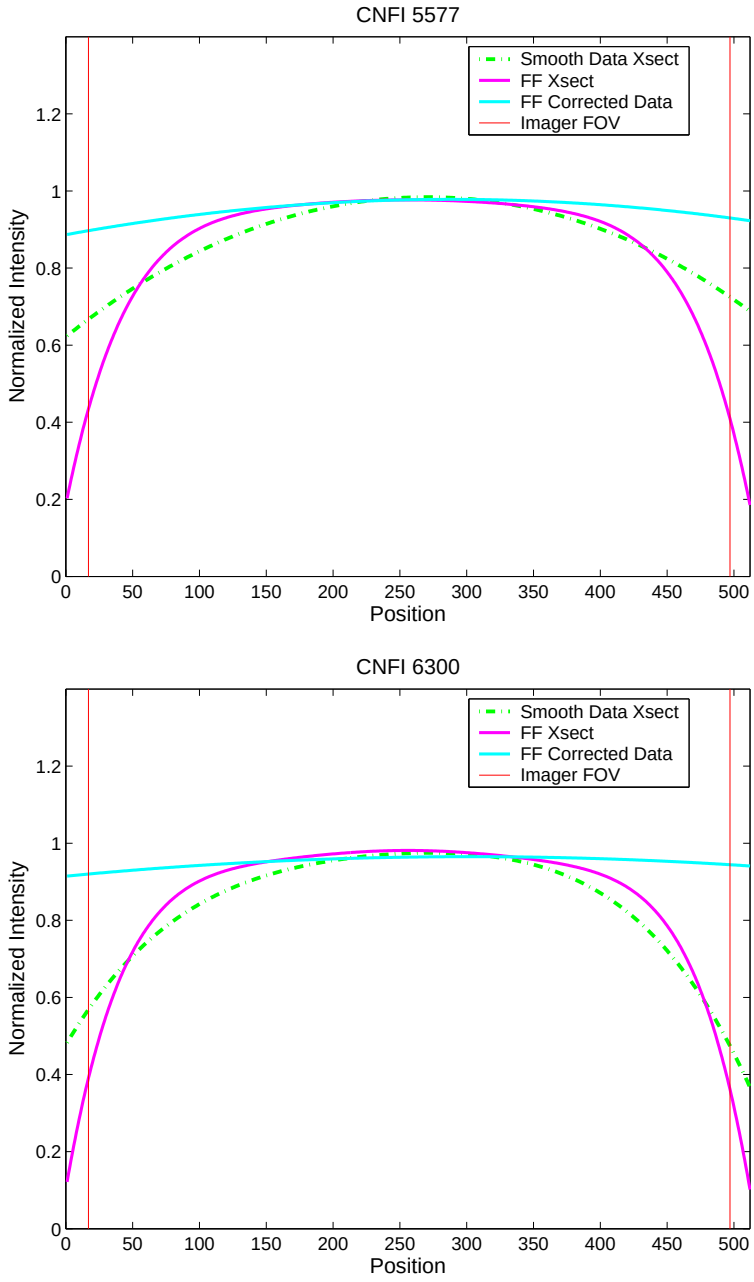

Figure F.11: These example plots illustrate the application of the flat-fielding functions for CNFI. In both the 5577 plot in the top panel and the 6300 plot in the bottom panel, cross-sections are shown for an example dataset (green dash-dot line), and the same dataset corrected by the flat-fielding function for the associated filter (in light blue). Note the attenuation evident on both the left and right in the original datasets has been rectified following flat-fielding.

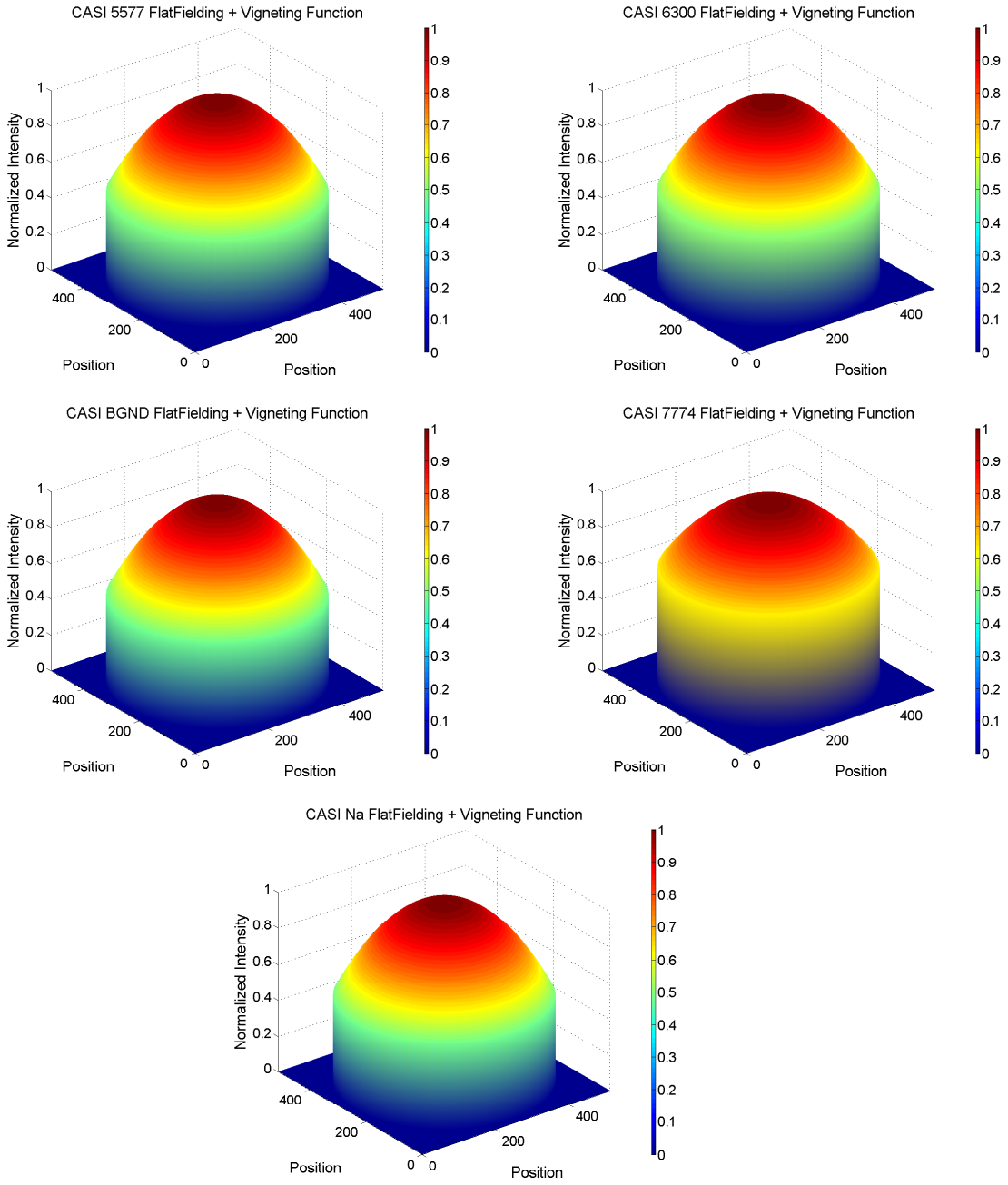

Figure F.12: 3-D plots of the vignetting with flat-fielding functions for the five filters in CASI.

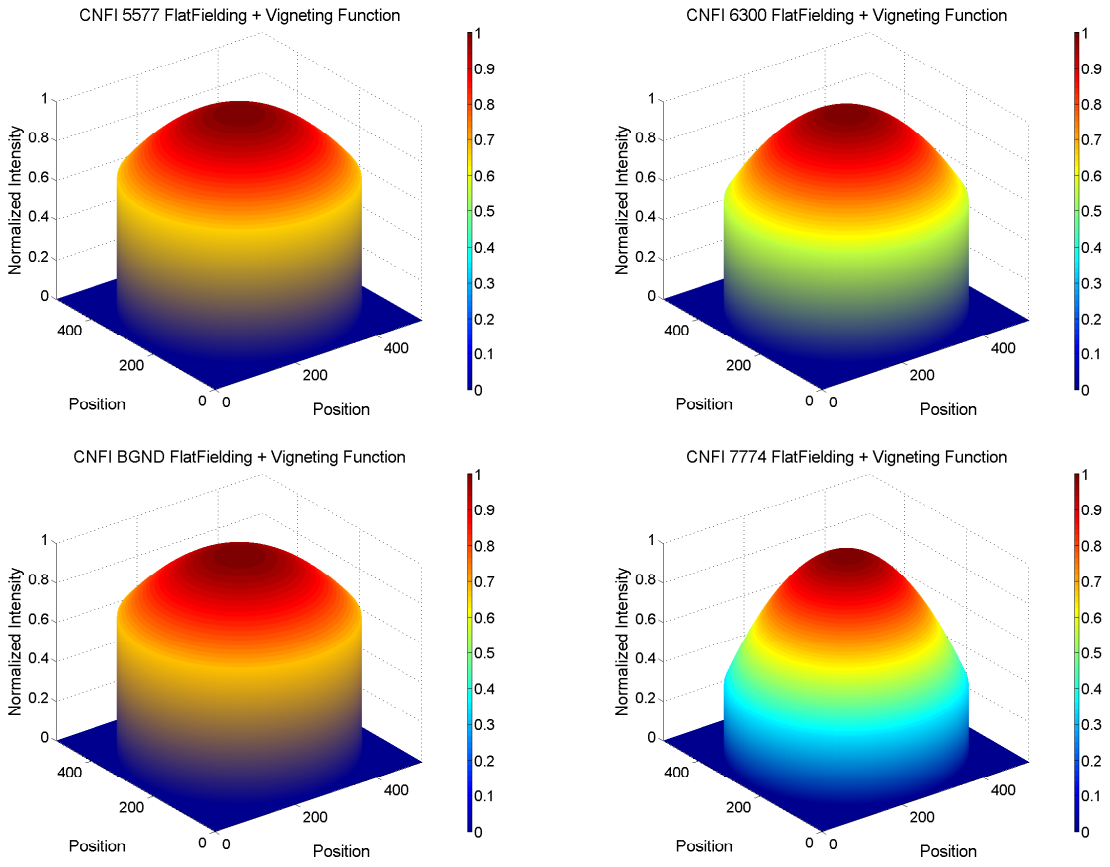

Figure F.13: 3-D plots of the vignetting with flat-fielding functions for the four filters in CNFI.

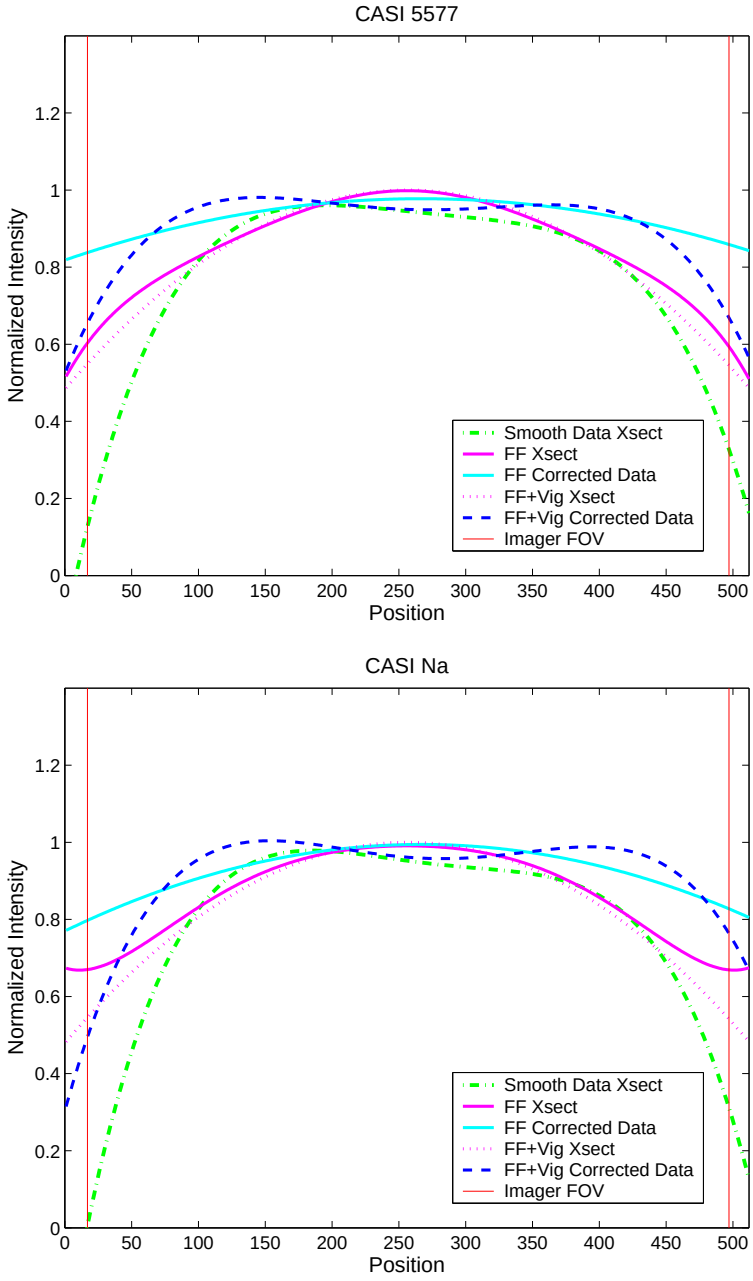

Figure F.14: These example plots illustrate the application of coupled vignetting with flat-fielding functions for CASI. In both the 5577 plot in the top panel and the Na plot in the bottom panel, cross-sections are shown for an example dataset (green dash-dot line), and the same dataset corrected by the coupled vignetting with flat-fielding function for the associated filter (dark blue dashed line). Note the attenuation evident on the sides in the original dataset has been rectified following application of the coupled vignetting correction function (dotted magenta line). Cross-sections for the flat-fielding correction function (solid magenta line) and flat-field-corrected data (solid light blue line) are shown for comparison.

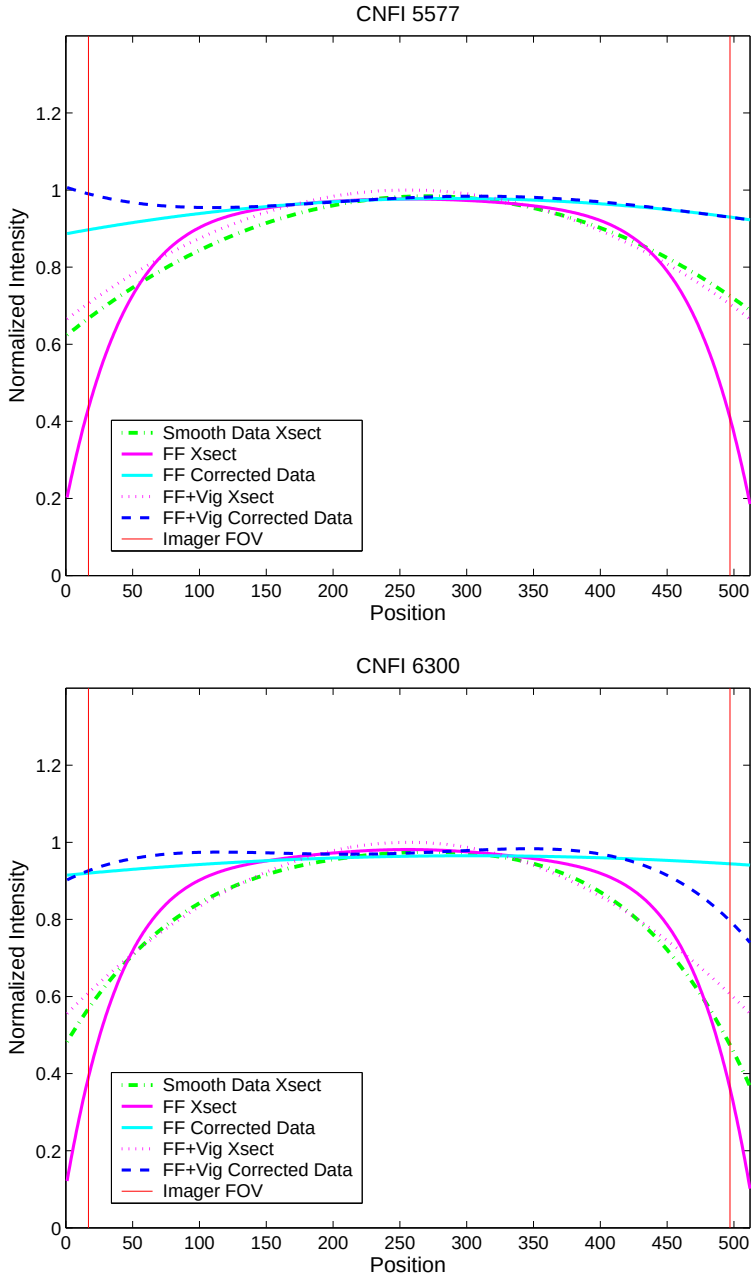

Figure F.15: These example plots illustrate the application of coupled vignetting with flat-fielding functions for CNFI. In both the 5577 plot in the top panel and the 6300 plot in the bottom panel, cross-sections are shown for an example dataset (green dash-dot line), and the same dataset corrected by the coupled vignetting with flat-fielding function for the associated filter (dark blue dashed line). Note the attenuation evident on the sides in the original dataset has been rectified following application of the coupled vignetting correction function (dotted magenta line). Cross-sections for the flat-fielding correction function (solid magenta line) and flat-field-corrected data (solid light blue line) are shown for comparison.

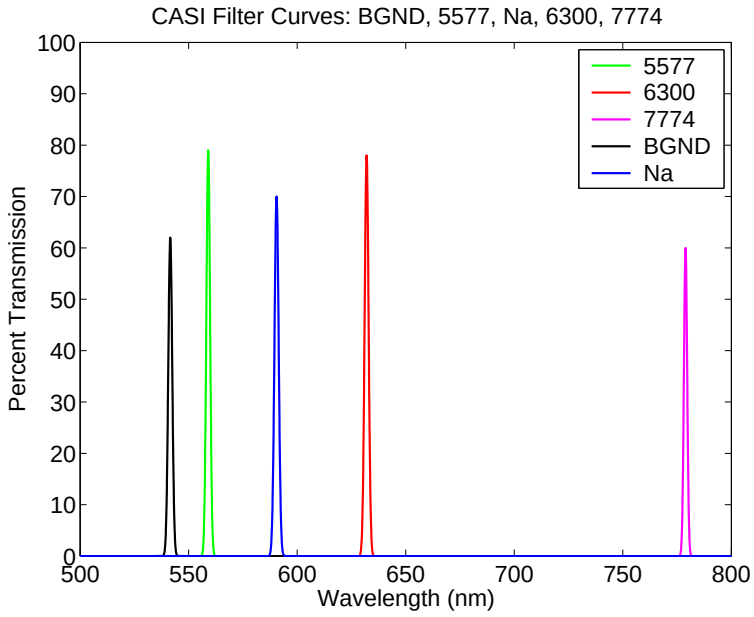

Figure F.16: Profile curves for the five filters in CASI plotted together on the same scale for comparison. The data were taken using the spectrograph at the Maui Space Surveillance Site in November 2004.

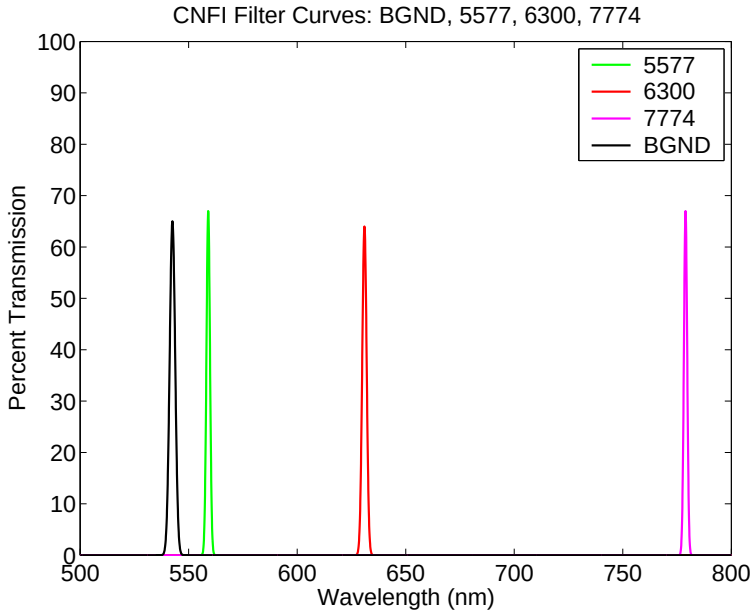

Figure F.17: Profile curves for the four filters in CASI plotted together on the same scale for comparison. The data were taken using the spectrograph at the Maui Space Surveillance Site in November 2004.

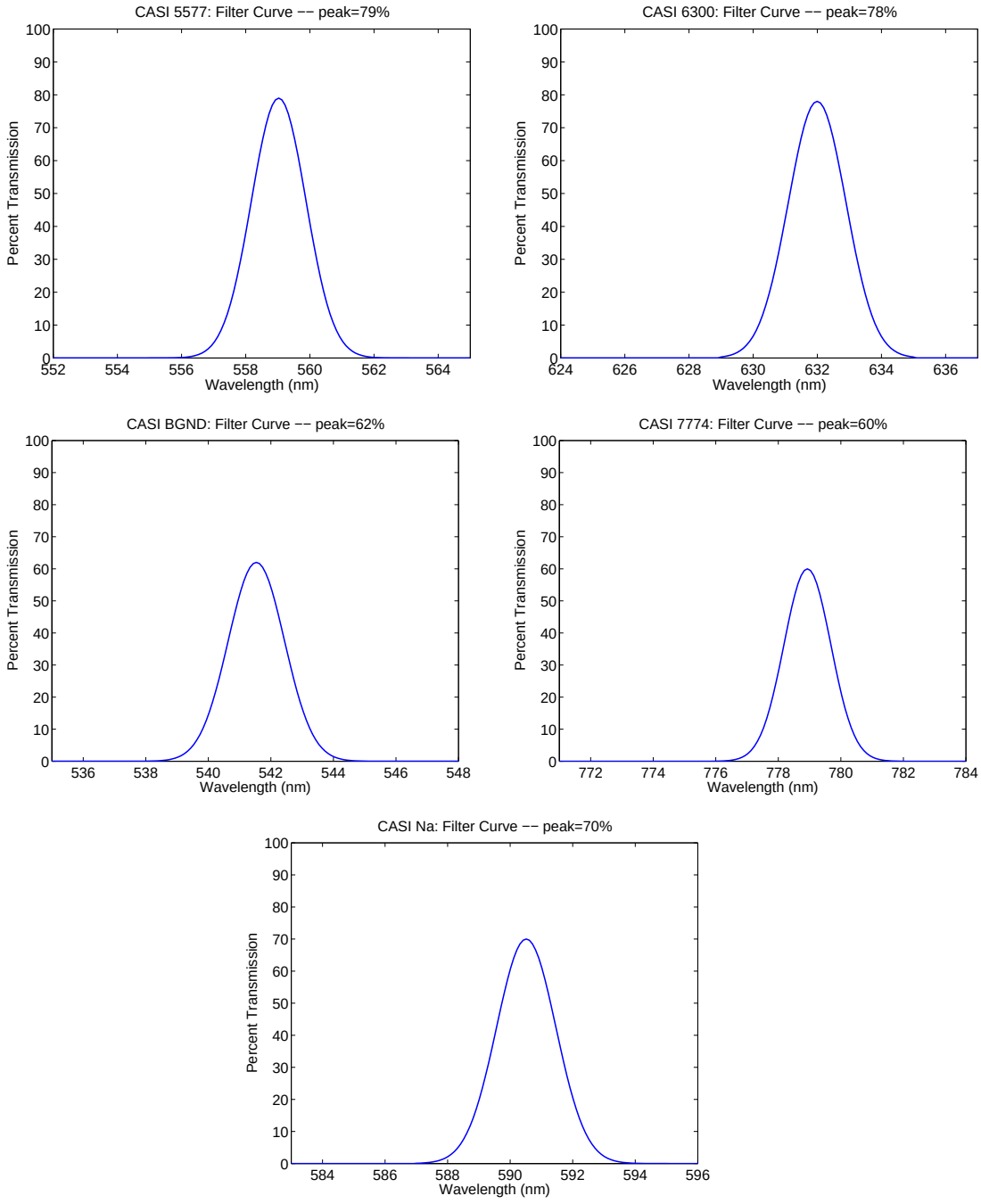

Figure F.18: Profile curves for the five filters in CASI. The data were taken using the spectrograph at the Maui Space Surveillance Site in November 2004.

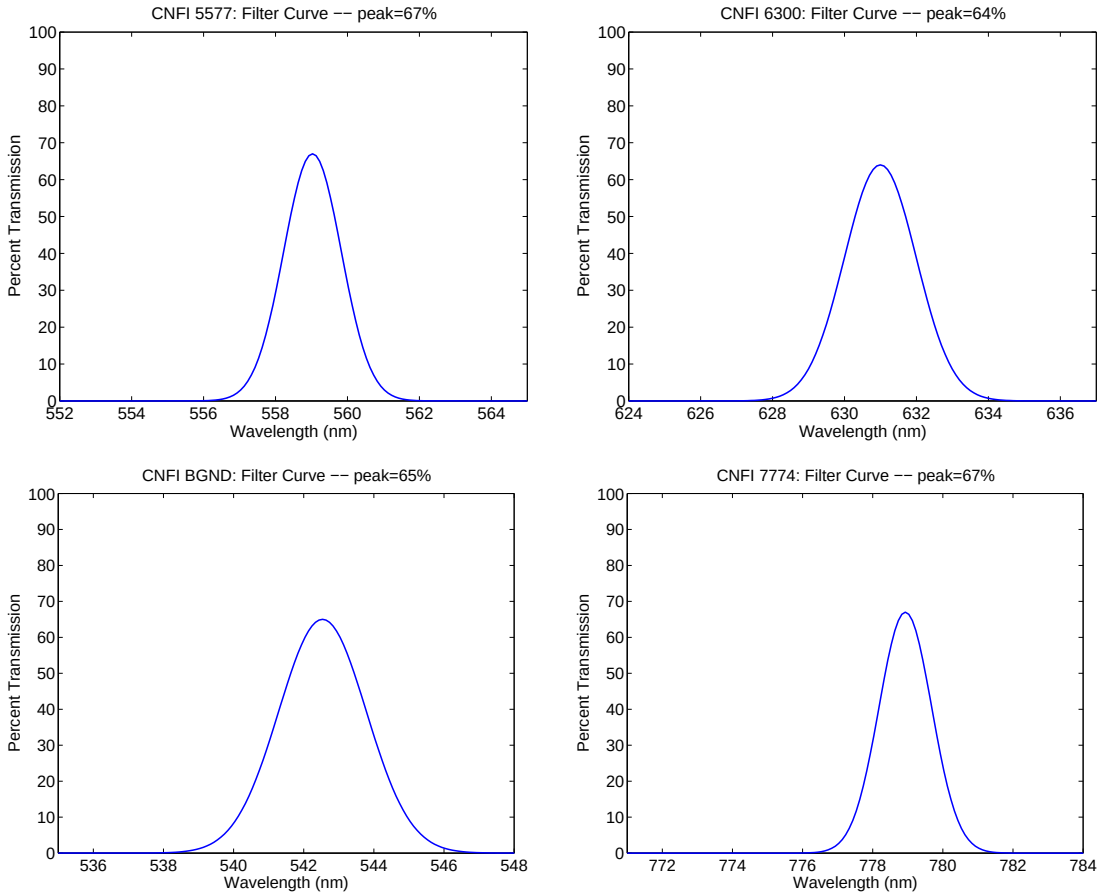

Figure F.19: Profile curves for the four filters in CNFI. The data were taken using the spectrograph at the Maui Space Surveillance Site in November 2004.

Table F.1: Peak and integrated (over the entire passband) filter transmission values.

Imager	Filter Wavelength	Filter ID	Peak Transmission [%]	$\int T(\lambda)\, d\lambda$
CASI	541.0 nm	541/2NM 1396 BARR	62	0.93
CASI	557.7 nm	558.2/2NM 1697 BARR#1	79	2.11
CASI	630.0 nm	630/2NM 4501 BARR #2	78	2.93
CASI	777.4 nm	778/2NM 3990 BARR	60	1.88
CASI	589.0 nm	590/3NM 4897 BARR #1	70	2.09
CNFI	541.0 nm	541/2NM 4601 BARR	65	1.36
CNFI	557.7 nm	557.7/2.0NM 3901 BARR #1	67	1.68
CNFI	630.0 nm	630/2NM 1396 BARR	64	3.85
CNFI	774.4 nm	777.8/2.0NM 3191 BARR #1	67	2.10
CARI[1]	541.0 nm	541.0/2.2NM 4499 BARR	69.8	1.61
CARI[1]	557.7 nm	558.1/2.0NM 3291 BARR #2	47.6	1.51
CARI[1]	630.0 nm	630.4/2.0NM 4699 BARR #1	40.5	1.49
CARI[1]	774.4 nm	ANDV8485 (777.4/2.0NM) AM-50324-01 I.Q.	18.5	n/a

[1] included for reference; results from [*Makela*, 2005 personal communication]

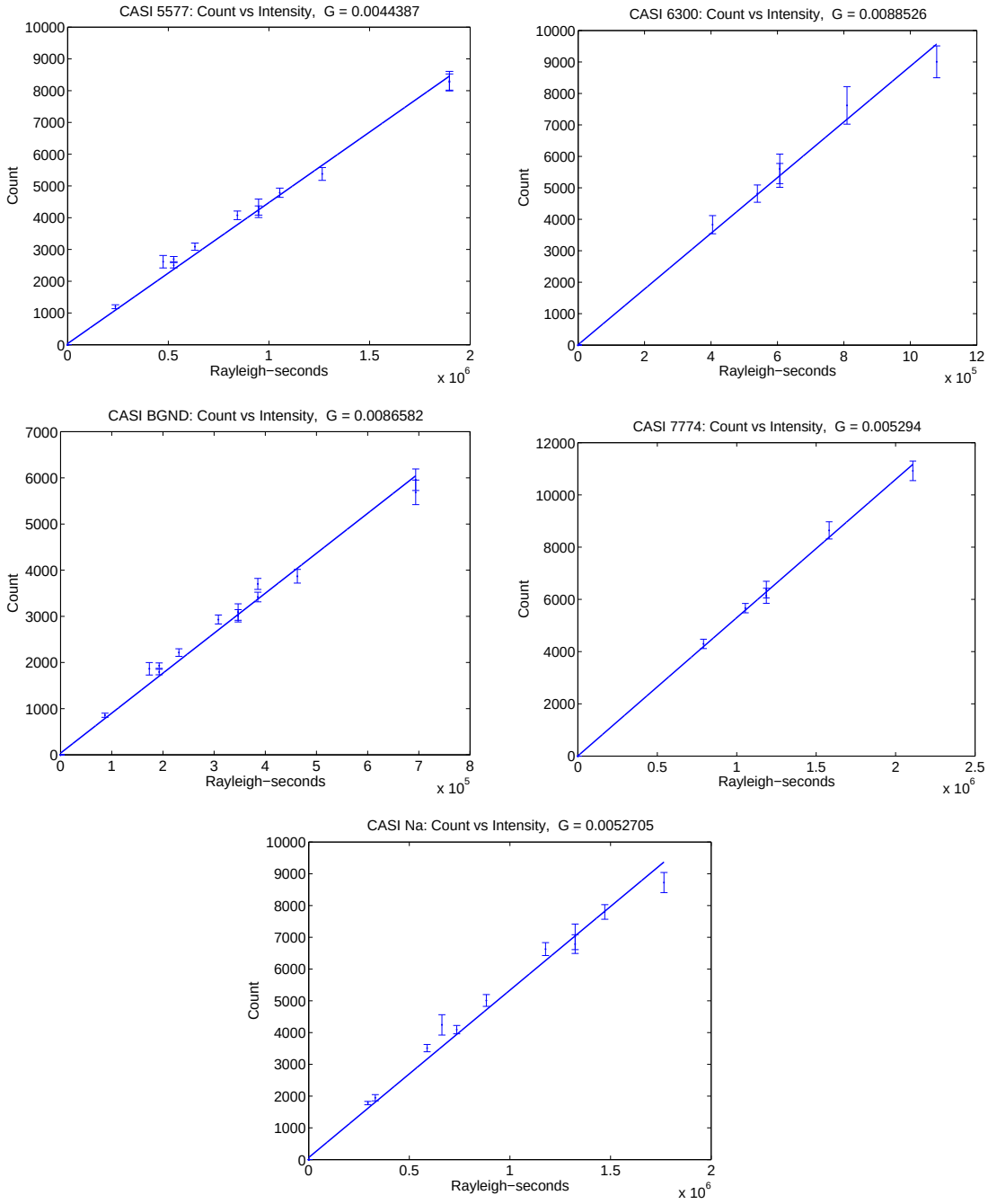

Figure F.20: Count versus brightness plots for the five filters in CASI. Each point and associated error bar on each graph are derived from the set of images taken for a particular PCLS intensity setting and exposure time. Data from at least three images are used for each point. The least squares best fit line is plotted for each filter, and corresponds to the *G* factor noted in each title.

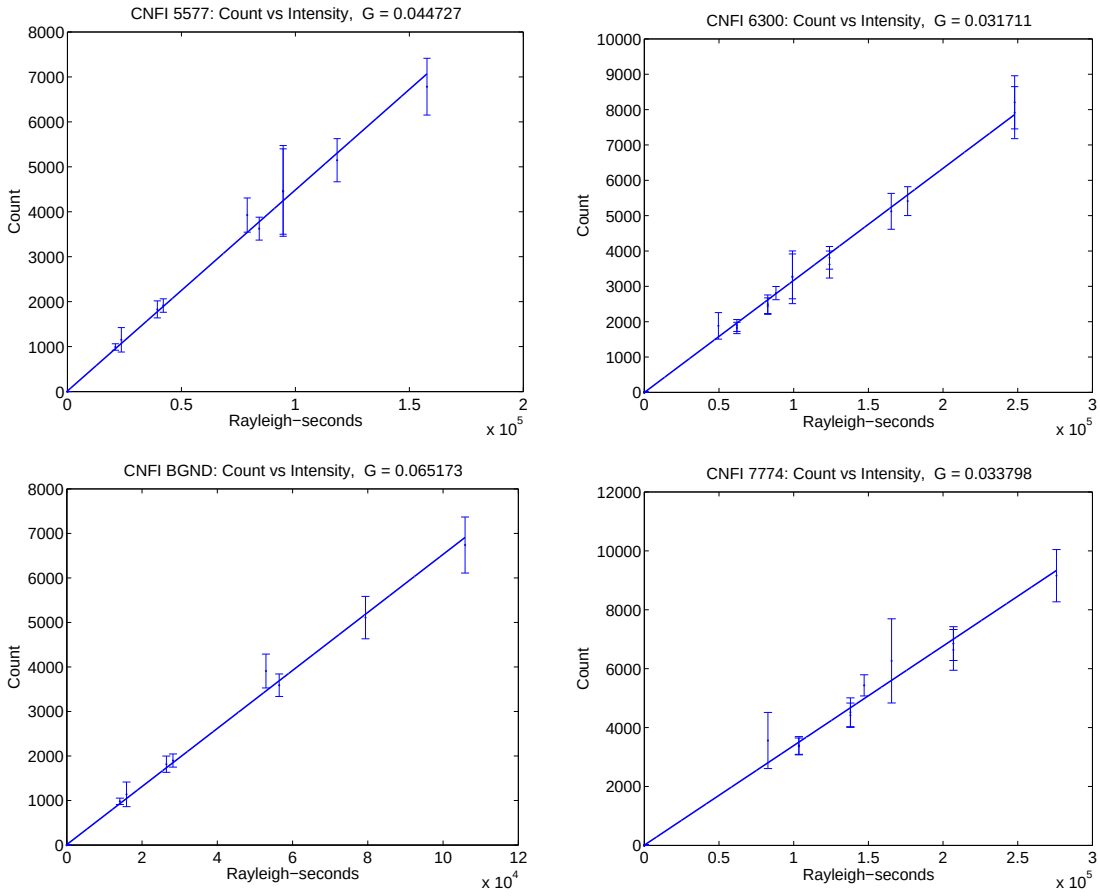

Figure F.21: Count versus brightness plots for the four filters in CNFI. Each point and associated error bar on each graph are derived from the set of images taken for a particular PCLS intensity setting and exposure time. Data from at least three images are used for each point. The least squares best fit line is plotted for each filter, and corresponds to the *G* factor noted in each title.

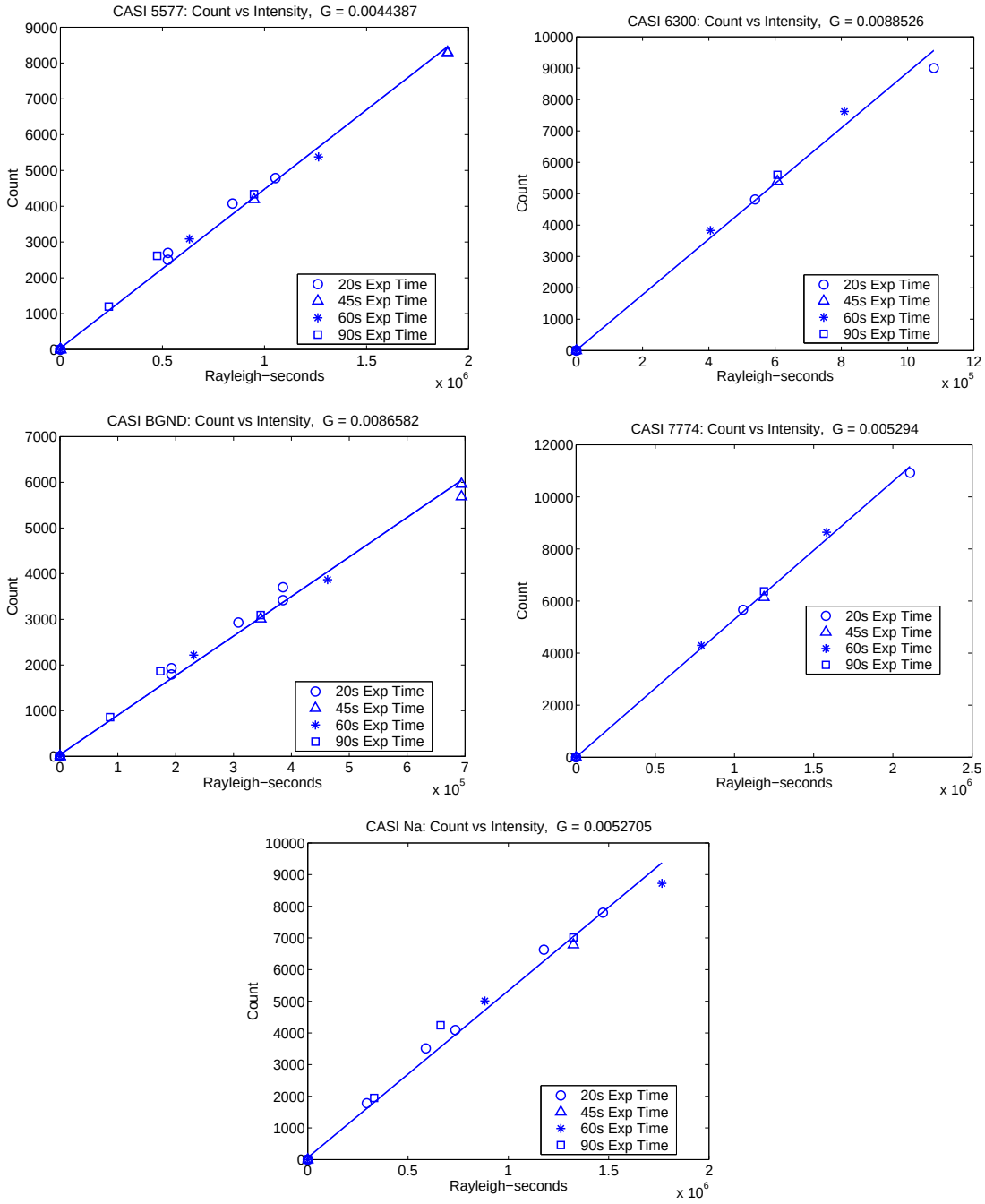

Figure F.22: Count versus brightness plots for the five filters in CASI. Each point on each graph is derived from the set of images taken for a particular PCLS intensity setting and exposure time. Exposure times are noted in the legends, and are indicated by the plot-point style. Data from at least three images are used for each point. The least squares best fit line is plotted for each filter, and corresponds to the *G* factor noted in each title.

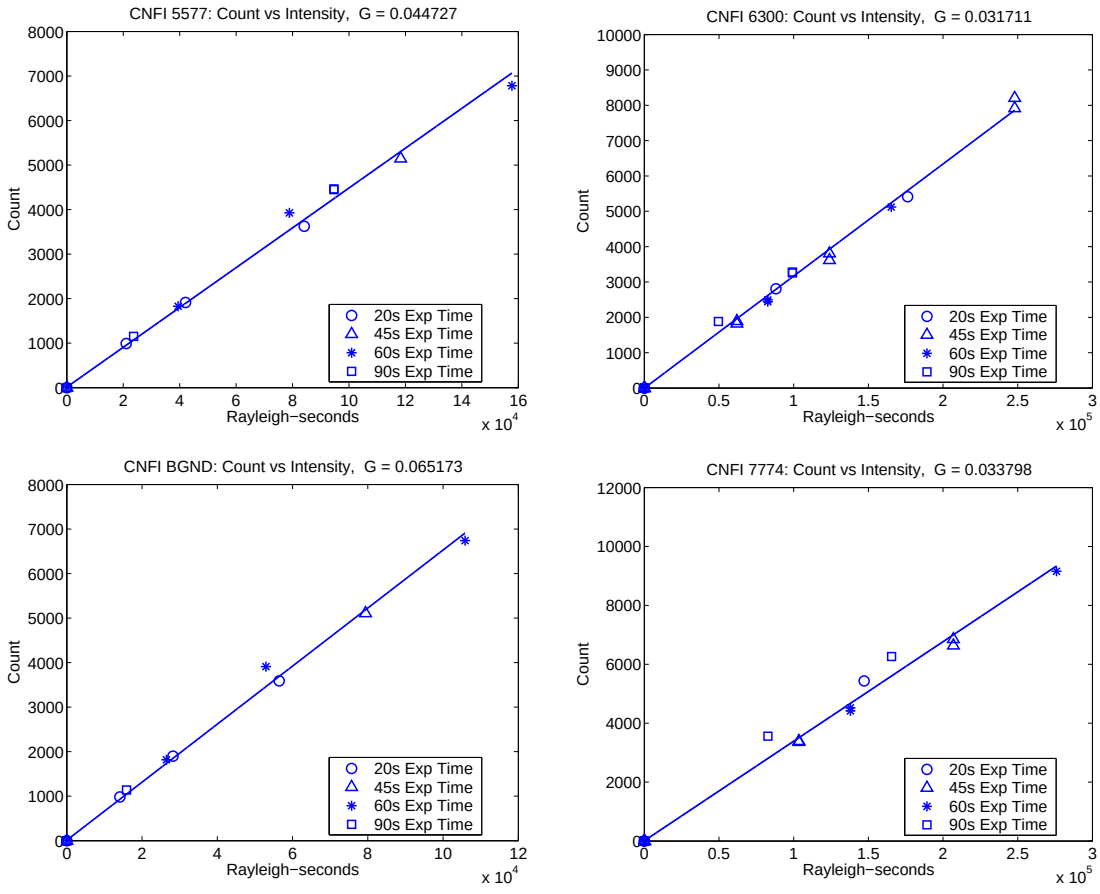

Figure F.23: Count versus brightness plots for the four filters in CNFI. Each point on each graph is derived from the set of images taken for a particular PCLS intensity setting and exposure time. Exposure times are noted in the legends, and are indicated by the plot-point style. Data from at least three images are used for each point. The least squares best fit line is plotted for each filter, and corresponds to the *G* factor noted in each title.

Table F.2: G factors and Errors

Imager	Filter "Name"	Filter Wavelength	Year	Calibration Source	**G** $[\frac{counts}{R \cdot s}]$	Error[4] $[\frac{counts}{R \cdot s}]$
CASI	BGND	541.0 nm	2004	PCLS	**0.0087**	9.0×10^{-4}
CASI	5577	557.7 nm	2004	PCLS	**0.0044**	4.6×10^{-4}
CASI	6300	630.0 nm	2004	PCLS	**0.0088**	7.4×10^{-4}
CASI	7774	777.4 nm	2004	PCLS	**0.0053**	2.4×10^{-4}
CASI	Na	589.0 nm	2004	PCLS	**0.0053**	5.4×10^{-4}
CNFI	BGND	541.0 nm	2004	PCLS	**0.0652**	1.0×10^{-2}
CNFI	5577	557.7 nm	2004	PCLS	**0.0447**	7.8×10^{-3}
CNFI	6300	630.0 nm	2004	PCLS	**0.0317**	4.9×10^{-3}
CNFI	7774	774.4 nm	2004	PCLS	**0.0338**	6.6×10^{-3}
CARI[1]	BGND	541.0 nm	2003[2]	Integrating Sphere	**0.0337**	2.1×10^{-4}
CARI[1]	5577	557.7 nm	2003[2]	Integrating Sphere	**0.0656**	2.8×10^{-4}
CARI[1]	6300	630.0 nm	2003[2]	Integrating Sphere	**0.0109**	2.6×10^{-5}
CARI[1]	7774	774.4 nm	2003[2]	Integrating Sphere	**0.0075**	1.4×10^{-5}
CARI[1]	5577	557.7 nm	1999[3]	C14	**0.0714**	n/a
CARI[1]	6300	630.0 nm	1999[3]	C14	**0.0526**	n/a

[1] included for reference

[2] [*Makela*, 2005 personal communication]

[3] [*Garcia*, 1999]

[4] wrt the linear fit

BIBLIOGRAPHY

Babcock, H. D., *Astrophys. J.*, *57*, 1923.

Baggaley, W. J., Sodium emission in persistent meteor trains, *Nature*, *267*, 1977a.

Baggaley, W. J., The source of enduring meteor train luminosity, *Nature*, *289*, 1981.

Bates, D. R., The green light of the night sky, *Planet. Space Sci.*, *29*, 1061–1067, 1981.

Batista, P. P., B. R. Clemesha, D. M. Simonich, M. J. Taylor, H. Takahashi, D. Gobbi, I. S. Batista, R. A. Buriti, and A. F. de Medeiros, Simultaneous lidar observation of a sporadic sodium layer, a "wall" event in the OH and OI5577 airglow images and the meteor winds, *J. Atmos. Sol. Terr. Phys.*, *64*, 1327–1335, 2002.

Baumgardner, J., All-sky camera calibration techniques, CEDAR Workshop, 2005.

Baumgardner, J., B. Flynn, and M. Mendillo, Monochromatic imaging instrumentation for applications in aeronomy of the earth and planets, *Optical Engineering*, *32*, 3028–3032, 1993.

Beer, T., *Atmospheric Waves*, Halsted Press, a Division of John Wiley and Sons, Inc., New York, 1974.

Booker, J. R., and F. P. Bretherton, The critical layer for internal gravity waves in a shear flow, *J. Fluid Mech.*, *27*, 513–539, 1967.

Broadfoot, A. L., and K. R. Kendall, The Airglow Spectrum, 3100–10,000Å, *J. Geophys. Res.*, *73*, 426–428, 1968.

Brown, L. B., A. J. Gerrard, J. W. Meriwether, and J. J. Makela, All-sky imaging observations of mesospheric fronts in OI 557.7 nm and broadband OH airglow emissions: Analysis of frontal structure, atmospheric background conditions, and potential sourcing mechanisms, *Geophys. Res. Lett.*, *109, D19104, doi:10.1029/2003JD004223*, 2004.

Chamberlain, J. W., *Physics of the Aurora and Airglow*, Classics in Geophysics, American Geophysical Union, 1995.

Chapman, S., Notes on atmospheric sodium, *Astrophys. J.*, *90*, 309–316, 1939.

Chapman, S., *The Airglow and the Aurorae*, chap. Note on persistent meteor trails, pp. 204–205, NY: Pergamon Press, NY, 1956.

Chen, F. F., *Introduction to Plasma Physics and Controlled Fusion*, vol. Volume 1: Plasma Physics, 2nd ed., Plenum Press, 1984.

C&L-Instruments, Interference Filters: The Key to It All, *Tech. rep.*, C&L Instruments, Inc., 475 W. Governor Road, Suite 12, Hershey, Pa 17033, (www.fluorescence.com/tutorial/int-filt.htm).

Crawford, J., P. Rothwell, and N. Wells, Simulating experiments for Spacelab, *Nature*, *257*, 650, 1975.

CSSC, Cedar: Observation of the coupled atmospheric regions, *Volume II: The CEDAR Science Steering Committee's Detailed Facility Development*, The Aeronomy Program of the National Science Foundation, 1987.

Dao, P. D., R. Farley, X. Tao, and C. Gardner, Lidar observations of the temperature profile between 25 and 103 km: Evidence of strong tidal perturbation, *Geophys. Res. Lett.*, *22*, 2825–2828, 1995.

Dewan, E. M., and R. H. Picard, Mesospheric bores, *J. Geophys. Res.*, *103*, 6295–6305, 1998.

Dewan, E. M., and R. H. Picard, On the origin of mesospheric bores, *J. Geophys. Res.*, *106*, 2921–2927, 2001.

Dewan, E. M., R. H. Picard, R. R. O'Neil, H. A. Gardiner, J. Gibson, J. D. Mill, E. Richards, M. Kendra, and W. O. Gallery, MSX satellite observations of thunderstorm-generated gravity waves in mid-wave infrared images of the upper stratosphere, *Geophys. Res. Lett.*, *25*, 939–942, 1998.

Dewan, E. M., M. C. Kelley, P. J. Loughmiller, and R. H. Picard, On the possibility of dual mesospheric bores, *EOS Trans. AGU*, *82(47) Fall Meet. Suppl., Abstract SA41B-0722*, 2001.

Eather, R., Telecentric lens systems for wide-field low-f# monochromatic imaging, *Tech. rep.*, Keo Consultants, 27 Irving Street, Brookline, MA 02146, 1993.

Eather, R. H., *Majestic Lights: The Aurora in Science, History, and the Arts*, American Geophysical Union, 1980.

Fechine, J., A. F. Medeiros, R. A. Buriti, H. Takahashi, and D. Gobbi, Mesospheric bore events in the equatorial middle atmosphere, *J. Atmos. Sol. Terr. Phys.*, *67*, 1774–1778, 2005.

Garcia, F. J., Atmospheric studies using all-sky imaging of airglow layers, Ph.D. thesis, Cornell University, 1999.

Garcia, F. J., M. J. Taylor, and M. C. Kelley, Two-dimensional spectral analysis of mesospheric airglow image data, *Appl. Optics*, *36*, 7374–7385, 1997.

Gill, A. E., *Atmosphere-Ocean Dynamics*, Academic Press, New York, 1982.

Gossard, E. E., and W. H. Hooke, *Waves in the Atmosphere*, Elsevier, New York, 1975.

Hapgood, M. A., and M. J. Taylor, Analysis of airglow image data, *Ann. Geophys.*, *38*, 805–813, 1982.

Hickey, M. P., R. L. Walterscheid, M. J. Taylor, W. Ward, G. Schubert, Q. Zhou, F. J. Garcia, M. C. Kelley, and G. G. Shepherd, Numerical simulations of gravity waves imaged over Arecibo during the 10-day January 1993 campaign, *J. Geophys. Res.*, *102*, 11,475–11,489, 1997.

Hickey, M. P., M. J. Taylor, C. S. Gardner, and C. R. Gibbons, Full-wave modeling of small-scale gravity waves using Airborne Lidar and Observations of the Hawaiian Airglow (ALOHA-93) $O(^1S)$ images and coincident Na wind/temperature lidar measurements, *J. Geophys. Res.*, *103*, 6439–6453, 1998.

Hines, C. O., Internal atmospheric gravity waves at ionospheric heights, *Canadian J. Phys.*, *38*, 1441–1481, 1960.

Hines, C. O., *The Upper Atmosphere in Motion: A Selection of Papers with Annotation*, Geophys. Monogr. 18, Am. Geophys. Union, Washington, D.C., 1974.

Holton, J. R., *An introduction to Dynamic Meteorology*, Academic Press, 1979.

Howell, S. B., Two-dimensional aperture photometry: Signal-to-noise ratio of point-source observations and optimal data-extraction techniques, *Publications of the Astronomical Society of the Pacific*, *101*, 616–622, 1989.

Huang, T. Y., H. Hur, T. F. Tuan, X. Li, E. M. Dewan, and R. H. Picard, Sudden narrow temperature-inversion-layer formation in ALOHA-93 as a critical-layer-interaction phenomenon, *J. Geophys. Res.*, *103*, 6323–6332, 1998.

Huang, T. Y., M. P. Hickey, T. F. Tuan, E. M. Dewan, and R. H. Picard, Further investigations of a mesospheric inversion layer observed in the ALOHA-93 Campaign, *J. Geophys. Res.*, *107*, 4408–4415, 2002.

Kelley, M. C., *The Earth's Ionosphere*, Academic Press, Inc., 1989.

Lanchester, B. S., Relation between discrete auroral forms and magnetic field disturbances, Ph.D. thesis, University of Southampton, Southampton, U.K., 1985.

Lighthill, J., *Waves in Fluids*, Cambridge University Press, 1979.

Loughmiller, P. J., and J. J. Makela, *CU-WINS URT Manual*, Cornell University Undergraduate Research Team, version 1.0 ed., 2002.

Loughmiller, P. J., M. C. Kelley, F. J. Garcia, J. J. Makela, S. M. Smith, and E. M. Dewan, Sharp front observations of mesospheric bores: Further evidence and new classes, *EOS Trans. AGU*, *85(17) Jt. Assem. Suppl., Abstract SA21A-05*, 2004.

Loughmiller, P. J., M. C. Kelley, E. M. Dewan, J. J. Makela, F. J. Garcia, and S. M. Smith, Sharp mesospheric fronts: Observations and classes of bore phenomena, *J. Geophys. Res.*, accepted 2007.

Makela, J. J., Photometric calibration of the Cornell all-sky imager (rover), 2005 personal communication.

Makela, J. J., M. C. Kelley, S. A. González, N. Aponte, and R. P. McCoy, Ionospheric topography maps using multiple-wavelength all-sky images, *J. Geophys. Res.*, *106*, 29,161–29,174, 2001.

Makela, J. M., Midlatitude ionospheric studies using the global positioning system and airglow cameras, Ph.D. thesis, Cornell University, 2003.

Medeiros, A. F., M. J. Taylor, H. Takahashi, P. P. Batista, and D. Gobbi, An unusual airglow wave event observed at Cachoeira Paulista 23°S, *Adv. Space Res.*, *27*, 1749–1754, 2001.

Medeiros, A. F., J. Fechine, R. A. Buriti, H. Takahashi, C. M. Wrasse, and D. Gobbi, Response of OH, O_2 and OI5577 airglow emissions to the mesospheric bore in the equatorial region of Brazil, *Adv. Space Res.*, *35*, 1971–1975, 2005.

Mende, S. B., R. H. Eather, and E. K. Aamodt, Instrument for the monochromatic observation of all sky auroral images, *Appl. Optics*, *16*, 1691–1700, 1977.

Meriwether, J., and C. Gardner, A review of the mesosphere inversion layer phenomenon, *J. Geophys. Res.*, *105*, 12,405–12,416, 2000.

Meriwether, J., and M. Mlynczak, Is chemical heating a major cause of the mesosphere inversion layer?, *J. Geophys. Res.*, *100*, 1379–1388, 1995.

Meriwether, J., X. Gao, V. Wickwar, T. Wilkerson, K. Beissner, S. Collins, and M. Hagan, Correction to "Observed coupling of the mesosphere inversion layer to the thermal tide", *Geophys. Res. Lett.*, *25*, 2127–2128, 1998a.

Meriwether, J., X. Gao, V. Wickwar, T. Wilkerson, K. Beissner, S. Collins, and M. Hagan, Observed coupling of the mesosphere inversion layer to the thermal tide, *Geophys. Res. Lett.*, *25*, 1479–1482, 1998b.

Molina, A., Sodium nightglow and gravity waves, *J. Atmos. Sci.*, pp. 2444–2450, 1983.

Nappo, C. J., *An Introduction to Atmopheric Gravity Waves*, vol. 85 of *International Geophysics Series*, First ed., Academic Press, 2002.

Nielsen, K., M. J. Taylor, R. G. Stockwell, and M. J. Jarvis, An unusual mesospheric bore event observed at high latitudes over Anartica, *Geophys. Res. Lett.*, *33, L07803, doi:10.1029/2005GL025649*, 2006.

Nossal, S., Optical calibration techniques and issues, CEDAR Workshop, 2005.

Omega-Optical, Optical Filter Design Application Note, *Tech. rep.*, Omega Optical, Inc., Delta Campus, Omega Drive, Brattleboro, VT 05301, 2006.

Oriel-Instruments, Filter characteristics, *Tech. rep.*, Oriel Instruments, Stratford, CN, 2003.

Oznovich, I., R. Yee, A. Schiffler, D. J. McEwen, and G. J. Sofko, The all-sky camera revitalized, *Appl. Optics*, *33*, 7141–7150, 1994.

Pallamraju, D., Errors in airglow and auroral emission measurements, CEDAR Tutorial, 2003.

Peterson, A. W., and L. M. Kieffaber, Infrared photography of OH airglow structures, *Nature*, *242*, 321, 1973.

Photometrics, *Advanced Camera Operation*, Photometrics Ltd., 1998.

Rees, M. H., *Physics and chemistry of the upper atmosphere*, First ed., Cambridge University Press, 1989.

Rishbeth, H., and O. K. Garriot, *Introduction to Ionospheric Physics*, Academic Press, 1969.

Roper-Scientific, *Princeton Instruments TE/CCD Detector 4411-0012 Version 1.H*, 3660 Quakerbridge Road, Trenton, NJ 08619 (www.roperscientific.com), 1999.

Salby, M. L., *Fundamentals of Atmospheric Physics*, vol. 61 of *International Geophysics Series*, Academic Press, 1996.

Schunk, R. W., and A. F. Nagy, *Ionospheres: Physics, Plasma Physics, and Chemistry*, American Geophysical Union: Atmospheric and Space Science Series, Cambridge University Press, 2000.

Seyler, C. E., Internal waves and undular bores in mesospheric inversion layers, *J. Geophys. Res.*, *110, D09S05, doi:10.1029/2004JD004685*, 2005.

She, C. Y., T. Li, B. P. Williams, T. Yuan, and R. H. Picard, Concurrent OH imager and sodium temperature/wind lidar observation of a mesopause region undular bore event over Fort Collins/Platteville, Colorado, *J. Geophys. Res.*, *109, D22107, doi:10.1029/2004JD004742*, 2004.

Shiokawa, K., Y. Katoh, M. Satoh, M. K. Ejiri, and T. Ogawa, Integrating-sphere calibration of all-sky cameras for nightglow measurements, *Adv. Space Res.*, *26*, 1025–1028, 2000.

Smith, R. K., Traveling waves and bores in the lower atmosphere: The "Morning Glory" and related phenomena, *Earth Sci. Rev.*, *25*, 267–290, 1988.

Smith, S. M., M. J. Taylor, G. R. Swenson, C. Y. She, W. Hocking, J. Baumgardner, and M. Mendillo, A multi-diagnostic investigation of the mesospheric bore phenomenon, *J. Geophys. Res.*, *108*, 1083–1101, 2003.

Stimson, A., *Photometry and Radiometry for Engineers*, John Wiley and Sons, Inc., New York, 1974.

Swenson, G. R., J. Qian, J. M. C. Plane, P. J. Espy, M. J. Taylor, D. N. Turnbull, and R. P. Lowe, Dynamical and chemical aspects of the mesospheric Na "wall" event on October 9, 1993, during the Airborne Lidar and Observations of Hawaiian Airglow (ALOHA) campaign, *J. Geophys. Res.*, *103*, 6361–6380, 1998.

Taylor, M. J., and F. J. Garcia, A two-dimensional spectral analysis of short period gravity waves imaged in the OI(557.7nm) and near infrared OH nightglow emissions over Arecibo, Puerto Rico, *Geophys. Res. Let.*, *22*, 2473–2476, 1995.

Taylor, M. J., and M. A. Hapgood, Identification of a thunderstorm as a source of short period gravity waves in the upper atmospheric nightglow emissions, *Geophys. Res. Lett.*, *21*, 2239–2242, 1994.

Taylor, M. J., M. B. Bishop, and V. Taylor, All-sky measurements of short-period waves imaged in the OI (557.7 nm), Na (589.2 nm), and near-infrared OH and O_2(0,1) nightglow emissions during the ALOHA-93 campaign, *Geophys. Res. Lett.*, *22*, 2841–2844, 1995a.

Taylor, M. J., G. R. Swenson, and V. Taylor, Height measurements of the OI(557.7 nm) gravity wave structure over the Hawaiian Islands during ALOHA-93, *Geophys. Res. Lett.*, *22*, 2881–2884, 1995b.

Taylor, M. J., D. N. Turnbull, and R. P. Lowe, Spectrometric and imaging measurements of a spectacular gravity wave event observed during the ALOHA-93 campaign, *Geophys. Res. Lett.*, *22*, 2849–2852, 1995c.

Torr, D. G., *The Photochemistry of Atmospheres: Earth, the Other Planets, and Comets*, chap. The Upper Atmosphere, pp. 165–278, Academic Press, Inc., 1985.

Torr, M. R., D. G. Torr, and R. R. Laher, The O_2 atmospheric 0-0 band and related emissions at night from Spacelab 1, *J. Geophys. Res.*, *90*, 8525, 1985.

Tricker, R., *Bores, Breakers, Waves, and Wakes*, Elsevier, 1965.

Vadas, S. L., Horizontal and vertical propagation and dissipation of gravity waves in the thermosphere from lower atmospheric and thermospheric sources, *J. Geophys. Res.*, *112, A06305, doi:10./1029/2006JA011845*, 2006.

Vadas, S. L., and D. C. Fritts, Thermospheric responses to gravity waves arising from mesoscale convective complexes, *J. Atmos. Sol. Terr. Phys.*, *66*, 781–804, 2004.

von Zahn, U., J. Höffner, V. Eska, and M. Alpers, The mesopause altitude: Only two distinctive levels worldwide?, *Geophys. Res. Lett.*, *23*, 3231–3234, 1996.

Wayne, R. P., *Chemistry of Atmospheres: An Introduction to the Chemistry of the Atmospheres of Earth, the Planets, and their Satellites*, Second ed., Oxford University Press, 1991.

Western-Telematic-Inc., *RPS-10 Series: Expandable Remote AC Power Switches, User's Guide, WTI P/N-12493 Rev.D*, www.wti.com, 2000.

Yee, J. H., E. R. Talaat, T. Woods, F. Eparvier, P. Richards, and S. C. Solomon, Solar irradiance measurements comparison and applications, CEDAR Workshop, 2005.